SDC-92-169

Conceptual Design Report for the SDC Barrel and Intermediate Muon Detectors Based on a Jet-type Drift Chamber

January 1 , 1992

(revised on January 21 , 1992)

Jet Muon Chamber Group

Y. Arai, Y. Funahashi, Y. Higashi, H. Iwasaki, N. Kanematsu, T. Kondo,
A. Maki, S. Odaka, H. Sakamoto, T. Shinkawa and S. Terada
KEK, National Laboratory for High Energy Physics

Y. Asano and S. Mori
Institute of Applied Physics
University of Tsukuba

K. Fujita, T. Okusawa, T. Takahashi, Y. Teramoto and T. Yoshida
Department of Physics
Osaka City University

Executive Summary

We propose a jet-type drift chamber for the barrel and intermediate muon detectors of SDC. The chamber system consists of large multiwire drift chambers having a simple box-type frame structure: 2.5×0.4 m^2 in cross section and maximum 9 m in length. An intermediate wire support is added for the chambers longer than 5 m in order to keep the wire sag within a tolerable level. A chamber module consists of double layers of small jet cells. The drift cell is composed of a wire plane, including 3 sense wires, and cathode plates parallel to the wire plane. The two layers in a chamber are staggered to each other by half a cell width. The jet cell is tilted such that its principle axis points to the interaction point. Such an arrangement, together with a constant drift velocity of the jet cell, allows us to design a simple and powerful trigger system for high momentum muons utilizing a drift time sum between a pair of staggered cells. A good spatial resolution and a multi-hit capability are also distinct features of jet-type chambers. The multi-hit capability will be helpful to distinguish high momentum muon tracks from associated electromagnetic debris as has been demonstrated by the Fermilab beam test T816. The chamber is operated with conventional nonflammable gas. The maximum drift time fulfills the SDC requirement. The proposed concept also has good characteristics from a mechanical point of view. The simple frame structure results in a relatively light weight of the chamber. A preliminary FEM analysis of the chamber module verified the excellent structural stiffness. It allows us to make the support structure and the alignment system relatively simple. These features will reduce the total cost as well as ensure a good performance of the chamber system.

Table of Contents

§1. Introduction

The detection of high energy muons is one of the most important characteristics of the SDC detector in pursuing exciting SSC physics. Muons have advantages over electrons in providing cleaner signature, less backgrounds, as well as detection capability inside jets. In addition, as the luminosity increases, the muon detection becomes more and more important due to potential deficiencies of inner tracking and calorimetry at luminosities well over 10^{33} $cm^{-2}s^{-1}$.

The muon detection system of the SDC detector has three major roles,

a) muon identification,
b) muon trigger,
c) improvement of momentum measurements for very high energy muons.

In order to fulfill these roles, the muon system has momentum measuring capability by means of a toroidal magnet system in conjunction with layers of drift chambers. In general, the role a) requires good track recognition capability against electromagnetic debris and other possible spurious hits. Concerning the role b), the muon trigger can be formed by scintillation counters. However, uncertainty in a rate estimate as well as triggering capability at high luminosity operation requires us to have more flexible triggers based on the drift chamber system with which the trigger threshold can be varied within a certain range, so as to be able to adjust the trigger rate at an acceptable level. The role c) naturally requires a good spatial resolution and precise alignment of the muon chambers.

The SDC muon system consists of barrel, intermediate and forward muon detectors as shown in Fig. 1.1. The system utilizes iron toroids to bend muons for momentum measurement. The detection system is composed of two layers of scintillation counters for triggering and a set of drift chamber superlayers which enables triggering with variable p_t thresholds, muon identification and momentum measurement. The thickness of the iron toroids

and drift chamber layout are determined to accomplish the p_t resolution of 20% in the barrel region and 10% in the forward region for muons below 100 GeV/c. This report describes a conceptual design of the barrel and intermediate drift chamber system.

The requirements for drift chambers are summarized more specifically as follows,

i) good multi-track separation capability particularly in such a muon system having a small number of chamber layers,
ii) tunable chamber trigger with an adjustable trigger threshold in a p_t range from 10 to 50 GeV/c,
iii) good spatial resolution of about 250 μm/station which also requires precision alignment of the chambers at the level of 100 μm.

These requirements are by no means trivial to be satisfied simultaneously, especially for a large system such as the SDC muon chamber which must cover an area of about 2,200 m^2 just for the outermost layer in the barrel section.

Simple tube chambers are most commonly used for muon chambers. However, our close examination manifested that the independent tube type chamber has difficulties to fulfill the requirements such as alignment, gas seal, spatial resolution, multi-track separation and triggering. A natural solution for tunable triggering capability turned out to be the projective drift geometry with uniform drift field. Past experiences on the construction of large systems of field-shaped tube drift chambers taught us that the main difficulty would arise from the field shaping electrodes. On the other hand, L3 muon chambers with large chamber boxes made success in accomplishing high precision measurements. Taking account of these facts and requirements, a drift chamber module based on a tilted jet cell structure with simple cathode electrodes has been proposed.

The basic cell structure proposed here has a semi-closed cell structure partitioned with thin plates used as cathode planes. As illustrated in Fig. 1.2,

the cathode plates and a row of wires in every jet cell are arranged to point the beam crossing area. These cells are furnished in a rigid box with a partition by a middle plate. The upper and lower layers in the box are staggered each other by a half cell. The total weight of the chamber is relatively light due to the open structure. This will be of great help for the precision alignment of the chambers, transportation and installation.

As demonstrated by prototype short chambers for polar angles of 90 and 30 deg., a spatial resolution of 250 μm/wire can be easily obtained for this type of jet chambers with well known safe gas (HRS gas) together with comfortably low high voltage. The details of the results are described in Appendix 1. A prototype large chamber box based on the proposed construction concept is being constructed as described in Appendix 2. It has been readily shown that a chamber box of 8 m x 3 m is technically feasible.

Superiority of the jet chamber in regard to detection of a high energy muon track in a realistic environment has been undoubtedly demonstrated by the muon test beam jet chamber prepared by the Washington group. This beam chamber happened to have a cell configuration similar to the muon jet chamber proposed here. Apparently, the good track recognition of the jet chamber is based on a local vector measurement using multi-wires with good multi-hit separation at each cell level. The preliminary results are described in Appendix 3.

By utilizing the local vector measurement together with the half cell staggered layer arrangement, powerful chamber triggers for the 1st and 2nd levels can be formed in a logically natural and simple way, which will be discussed in sections 2.2 and 4.6 and also in Appendix 4.

The R&D work is yet in a mid-way and we still have many things to do to complete a satisfactory system design. Accordingly, the data and design we present here are by no means final. Therefore, we tried to make the numbers to be on the conservative side, if not precise, so that any further progress of R&D and design optimization should more likely give us a corresponding cost reduction rather than cost escalation.

In this report, the basic concepts of the design is described in §2, while the expected performance of the muon chamber system, such as momentum resolution and trigger rates, are written in §3. Details of technical, engineering design as well as production scheme are described in §4. §6 summarizes the proposed design parameters and specific features of the proposed design.

The general outline of the proposed design can be understood by reading through §2, §3 and §6.

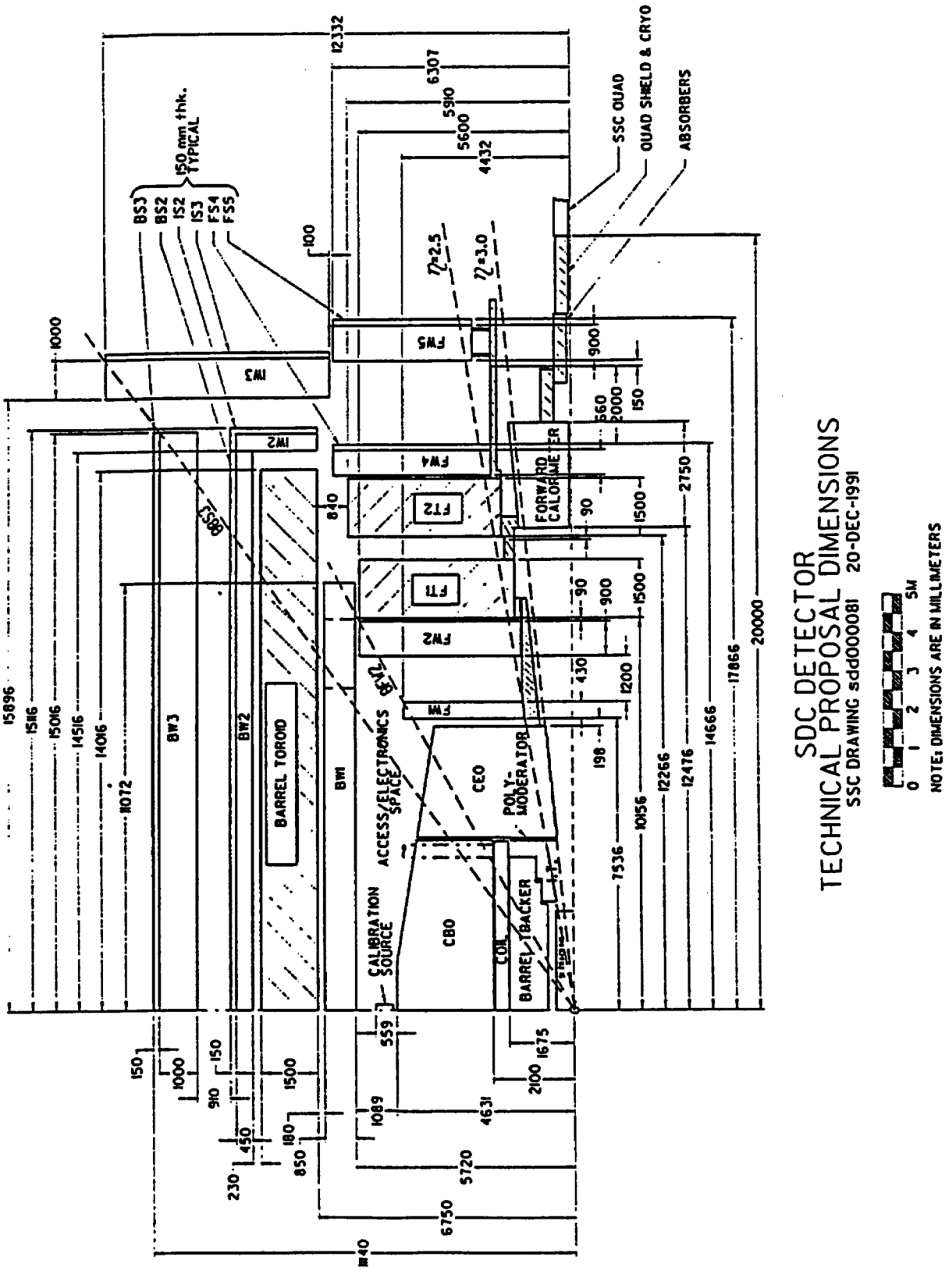

Fig. 1.1 SDC Detector layout.

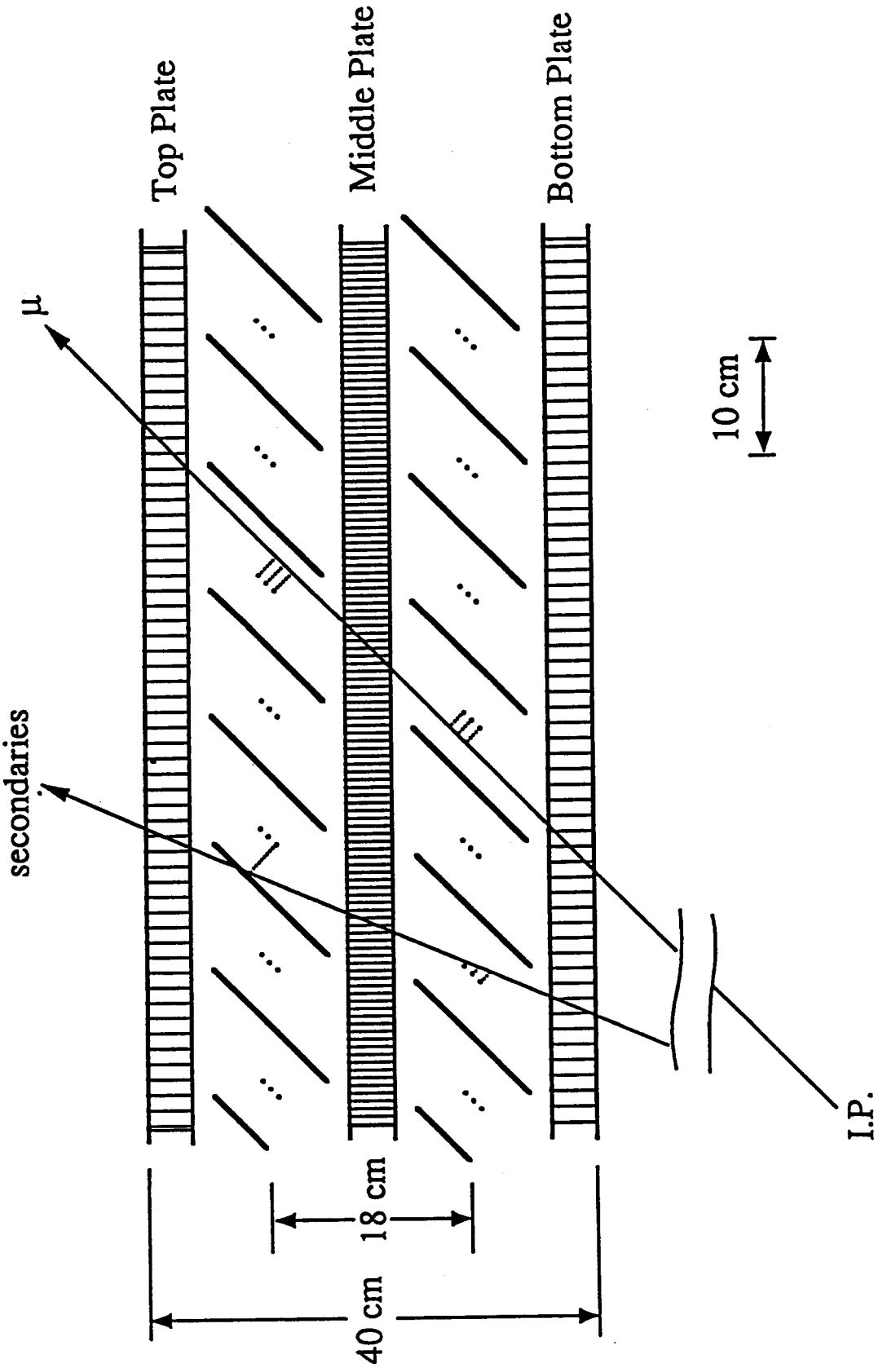

Fig. 1.2 Schematic picture of proposed jet-type drift chambers.

§2. Design Concept

2.1 Drift cell

The cell structure that we propose is schematically shown in Fig. 2.1. The structure is very simple compared to the jet-type drift chambers having been built so far. Wires are employed only in the sense plane. A simple structure will not only reduce the construction cost, but also will ensure a good performance of the chamber system since it will make the quality control easier. The sense plane is composed of 3 sense wires and 4 potential wires interleaved. The spacing between the sense wires is 1 cm. A guard wire is placed for cell termination in each end of the sense plane, 5 mm apart from the nearest potential wire. The sense plane is tilted so that the cell axis points towards the interaction point.

The cathode electrodes are planes parallel to the sense plane. The distance between the sense plane and the cathode plane, the maximum drift distance, is chosen to be 4 cm in order to fulfill the requirement on maximum drift time, < 1 μsec. The drift paths of ionized electrons are perpendicular to the sense and cathode planes ideally, and the cathode plane must be wide enough to cover the whole drift region. The situation is most severe for the cells in θ-chambers located at the edge of the barrel region, where the polar angle is nearly 30° and the tilting angle is as large as 60°. The full height of the cathode planes is chosen to be 10 cm so as to have some margin even in the most severe case. The ground planes are a part of the inner surface of the chamber structure, and play a passive role as a field-shaping electrode. We leave a 2 cm-spacing between the cathode plane and the ground plane for insulation and for cathode plane fixtures.

This cell arrangement is essentially the same as the original design [2.1]. Only the differences are that the gap between the cathode and ground planes has been widened from 1 cm to 2 cm in order to reserve enough room for fixtures of the cathode planes, and that the number of sense wires has been reduced from 4 to 3 in order to reduce the total channel count.

Table 2.1. Parameters of the electrodes.

	diameter (μm)	voltage (kV)	material	tension (kg)
sense	70	+ 2.07	W	0.40
potential	140	0	CuBe	0.69
guard	200	+ 2.33	CuBe	1.40
cathode	plane	– 3.04	—	—

The parameters of the electrodes are summarized in Table 2.1. The wire diameters and the voltages are optimized to the chamber gas that we have chosen, Ar/CO_2/Methane (89/10/1). This gas mixture (HRS gas) has many features suitable for large chambers: it is nonflammable and has an approximately saturating drift velocity for the field strength above 800 V/cm. Besides, a stability in a long term operation has been guaranteed through experiences at various collider experiments. These parameters give us a sufficiently uniform drift field with a nominal field strength of 900 V/cm and a gas gain of approximately 10^5.

It is expected that one can achieve a spatial resolution of better than 300 μm/wire and a double track separation of about 5 mm with the above configuration. Also we expect that the maximum drift time is about 800 nsec from simulation results. The expectations on the spatial resolution and the maximum drift time have been confirmed by the tests using short test chambers (Appendix 1), and the resolution of the double track separation has been proved by the beam chambers used for a beam test at Fermilab (Appendix 3).

[2.1] S. Odaka, *A Jet-cell Design for the SDC Muon Chamber*, KEK preprint 91-96, 1991.

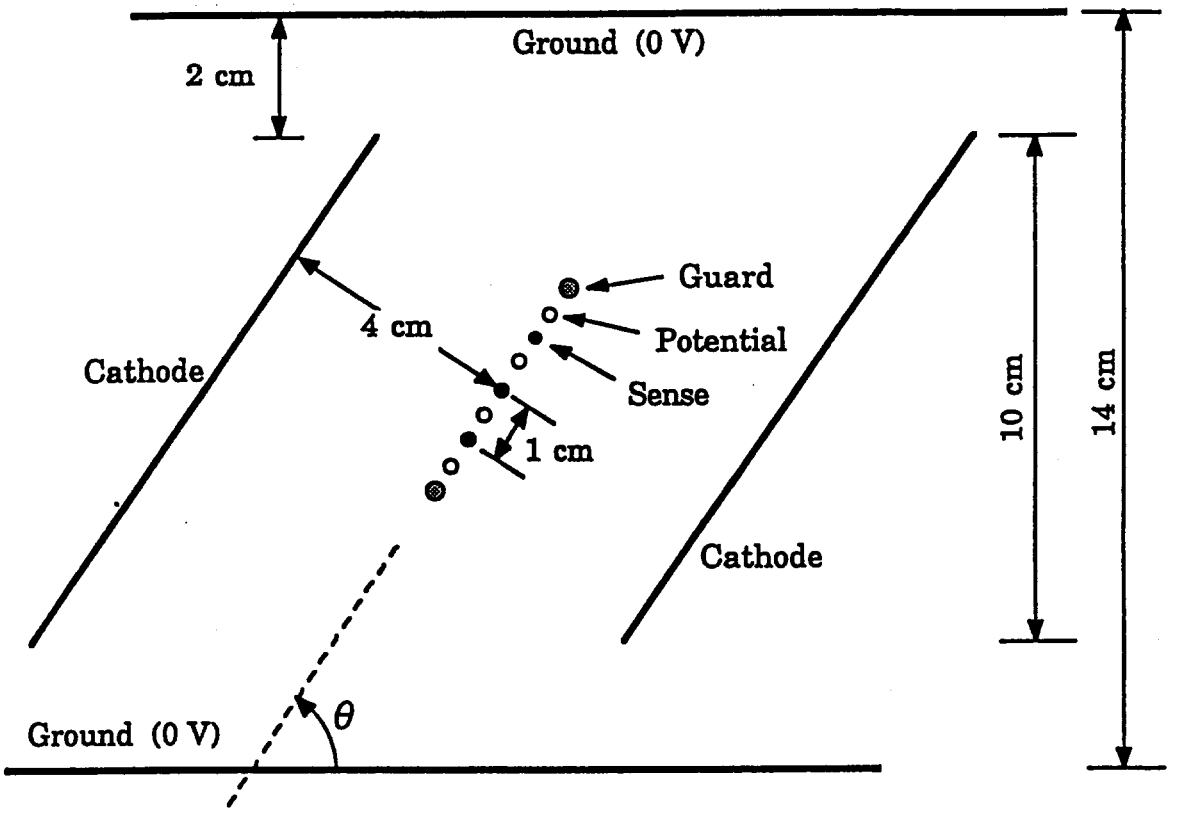

Fig. 2.1. A schematic illustration of the drift cell structure.

2.2 Cell arrangement and trigger

A primary technique of the muon trigger is a measurement of the track bend using θ-chambers placed outside of the toroid. The jet chamber design that we propose is optimum for this purpose. In our cell arrangement, as has been shown in Fig. 1.2, the projective jet cells form a half-cell staggered double layer structure in each chamber module. Since the drift velocity is practically constant through the entire drift region, the sum of the drift times between a pair of staggered cells corresponds to the maximum drift time for infinitely high-momentum tracks. A tolerance in this correspondence gives us a finite acceptance for the bending angle, *i.e.* a finite threshold value of muon momenta. The momentum threshold is smeared by the spread of the interaction point and the multiple scattering in the calorimeter and the toroid. The amount of these fluctuations relative to the bending angle determines the upper limit of the momentum threshold that we can select.

The above concept for triggering can be implemented with a pair of shift registers having a length corresponding to the maximum drift time. The circuit is schematically illustrated in Fig. 2.2. First, the wire signals from discriminator outputs are processed in each jet cell by a 2-out-of-3 coincidence in order to eliminate spurious hits. The processed signals from staggered cells are fed to a pair of shift registers from opposite sides and transmitted to opposite directions. Since each input signal has a time offset corresponding to the drift time, the signals from the staggered cells meet each other at a certain column of the shift registers when the time of around the maximum drift time has passed. The difference between time of meeting and the maximum drift time is proportinal to the deflection angle. The strobe signal that determines the coincidence timing can be generated from the scintillation counter signal using a suitable delay circuit. The width of the strobe signal determines the tolerance of the angle measurement. A programmable shift register is the best choice for this delay circuit, in which the total length and the length of the signal train are adjustable.

It is noted that the above circuits are driven by a 16 nsec clock, *i.e.* 62.5 MHz. A present ASIC technology allows us to construct such fast and sophisticated circuits without difficulty. Note that the above circuit is

basically a dead-time-less system since all components are based on shift registers. Furthermore, the column position where oppositely going signals coincide corresponds to the track position. This information can be used in higher level triggers.

Also the same circuit can be applied to ϕ-chambers in order to assure that a track originates from the interaction point. For Level-1 trigger, as will be described in detail in section 3.2, reasonable efficiency and trigger rate that meets the SDC DAQ requirements can be achieved by using the outputs from θ- and ϕ-chambers located outside the toroid. In this scheme the ϕ-chamber trigger effectively eliminates the contamination of cosmic rays.

If BW1 information can be used in the triggering, one can be free from the ambiguity of the interaction point and the multiple scattering in the calorimeters. In Level-2 trigger, though we are still in an early stage of the conceptual thought, it is possible to improve the threshold behavior and, as a result, the trigger rate can be further reduced by using the position information obtained by the trigger circuits in all superlayers. We are also considering further options for Level-2 trigger. One of them is a connection to the trackers inside the solenoid. However, this option is quite ambiguous since we do not know enough details of the triggering information available from the inner tracking detectors. Another is an isolation cut using the information from the calorimeters. This option not only has an ambiguity on the available information, but also needs some further considerations on physics requirements since this is a kind of physics cut.

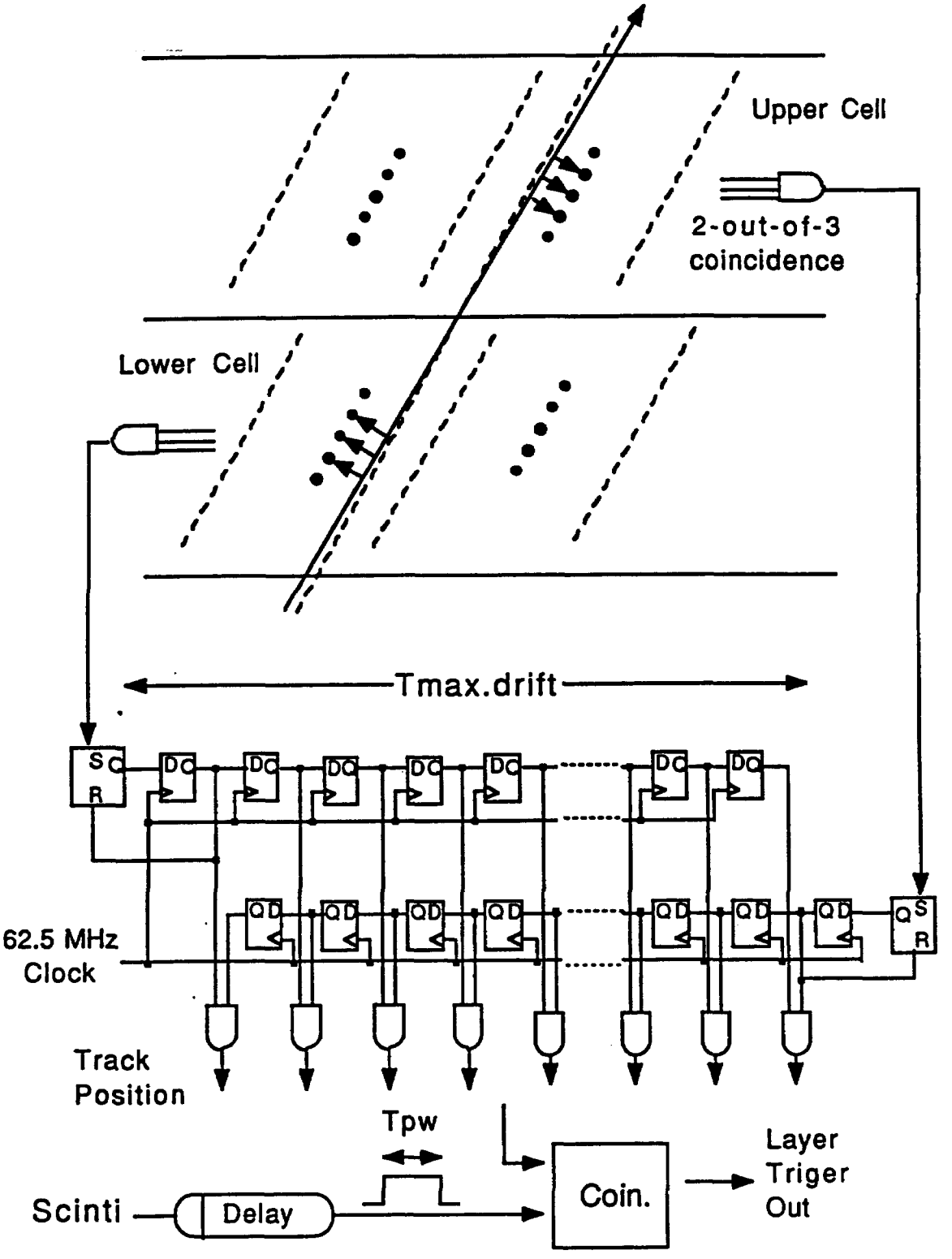

Fig. 2.2. A schematic circuit diagram to implement the mean-timer method.

2.3 Chamber module

The chamber module is essentially a rectangular flat box made of thin aluminum plates, as shown in Fig. 2.3. The outer frame of the module is composed of a pair of end frames and a pair of side frames. A set of wires are strung between plastic feedthroughs inserted in the end frames. The box is partitioned with a middle plate to furnish the double-layer cell arrangement. An intermediate wire support (center support) is located at the middle of the chamber, at least for the chambers longer than 5 m, in order to keep the wire sag within an acceptable amount. The center support is made of aluminum and the wires are supported with plastic positioning pieces inserted into precisely machined holes in the center support. This frame structure is covered with top and bottom plates to close the gas volume.

In our present design, the cathode plates are made of copper-clad GFRP plate with a thickness of 1 mm. As schematically shown in Fig. 2.4, the cathode plates are supported at both sides with narrow strips strung orthogonal to the cathode plates. The support strips are made of 2 mm thick GFRP . The cathode plates and the support strips are put in and glued to each other through notches to form a stiff matrix structure. The support strips are fixed on the side frames at both ends, and the strips in the middle-plate side are fixed on the middle plate. The cathode structure is the most important issue in our R&D program. We would like to make the cathode plane as thin as possible in order to minimize the dead area between cells while keeping the tolerance of 1 mm for the cathode positioning. This tolerance is moderate but not trivial for a thin structure.

The end frames, the side frames and the center support are made of extruded aluminum with a typical thickness of 1.6 cm, 0.8 cm and 0.8 cm, respectively. A 4 cm-thick aluminum honeycomb covered with 1 mm-thick aluminum sheets is primarily considered for the middle plate. Because the middle plate is the support base of the cathode plates, the flatness of its surface is required to be better than 1 mm. The gravitational deformation can be kept within 0.6 mm using this honeycomb plate. A corrugated aluminum plate is another candidate but the evaluation is still under way. A

similar honeycomb plate or a corrugated plate is used for the top and bottom plates. Although the tolerance required is looser for these plates (~5 mm) they must withstand the pressure difference of maximum 10 g/cm^2 between the chamber gas and the outside atmosphere.

The total thickness of the chamber module is 40 cm, *i.e.* 2 drift cells of 14 cm plus 3 structural plates of 4 cm in thickness. The length is determined to fit to the chamber layout, described in the next section, and the longest are the outermost θ-chambers, about 9 m, within the barrel region. The width of the chamber module is preferred to be maximum within a limit of fabrication, handling and transportation. We have chosen 2.5 m as an optimum width.

All the chamber components are fabricated in order to make a required precision assembly easy. The frame components including the center support and the middle plate are tightly bolted and glued to each other, so that they form a very rigid structure even without the top and bottom plates. Our experience in handling the large prototype chamber and the FEM analysis show that the chamber has excellent rigidity which allow us easy handling in assembly and transportation.. Rigidity is not a critical requirement for the chamber structure because each module is considered to be supported at 6 points, 4 corners as well as 2 middle points of the side frames.

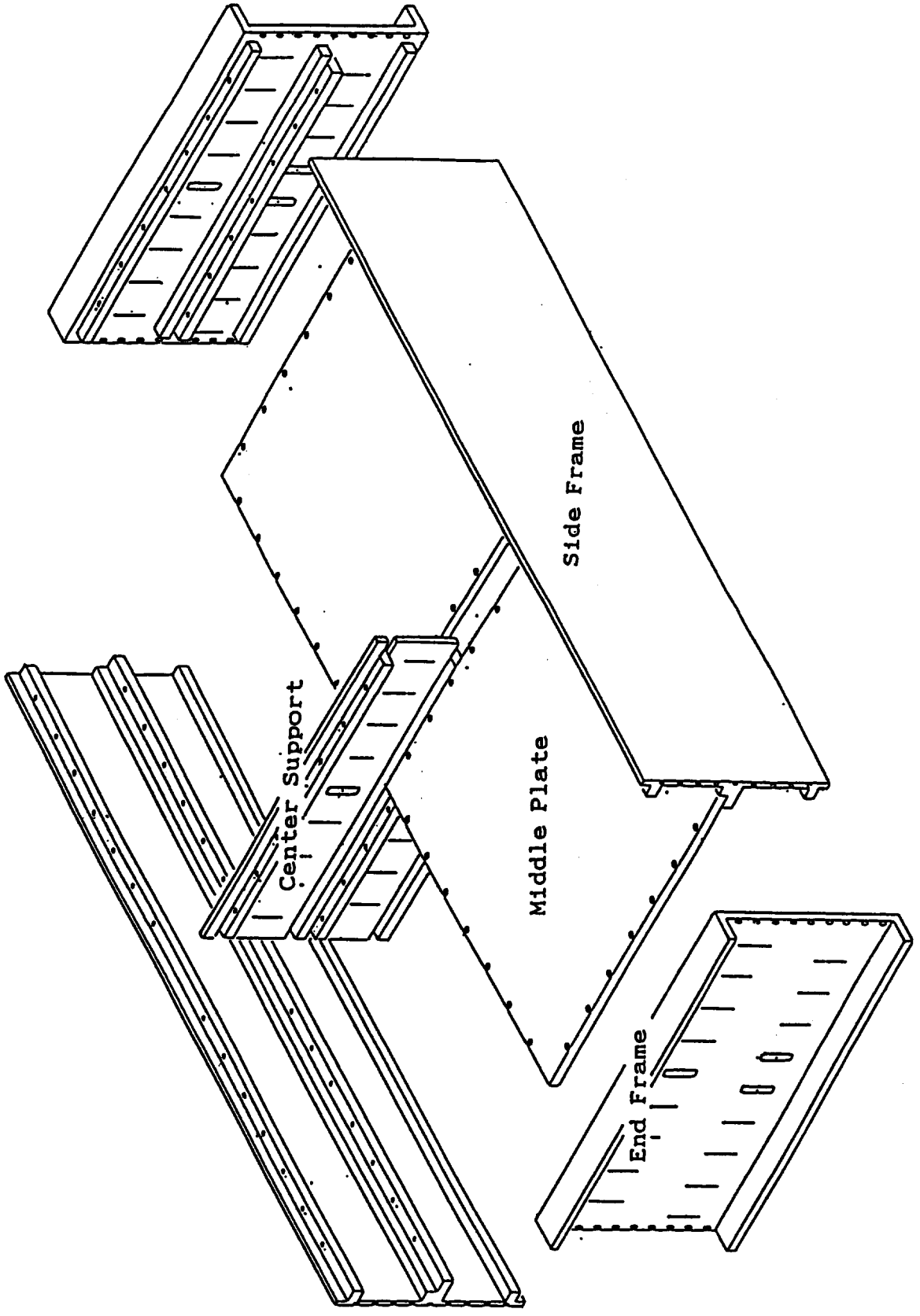

Fig. 2.3. A cutaway view of the jet chamber module.

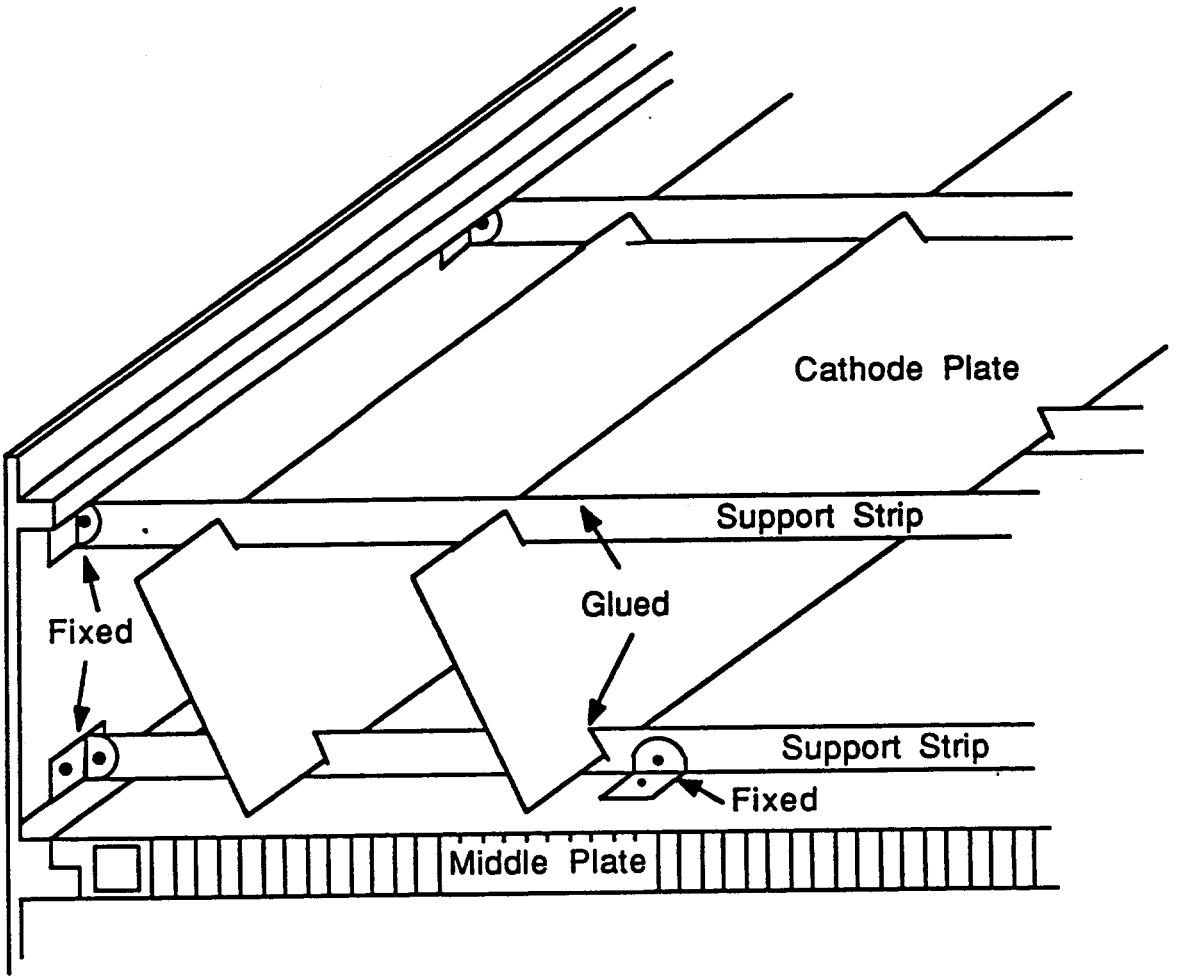

Fig. 2.4. A picture to show the cathode support structure.

2.4 Chamber layout

Based on the optimum chamber width of 2.5 m, a layout of the chamber modules and a supermodule configuration have been worked out in accordance with *the SDC detector technical proposal dimensions* (SSC Drawing SDD000081). The chamber layout for the barrel part is shown in Fig. 2.5. The arrangement is not exactly the same as the tube chamber options proposed by the other groups. We have two stereo layers in BW2 instead of in BW3. The stereo layers are assumed to be a conventional single wire drift tube with a square cross section of 8×8 cm^2 because the required resolution is not stringent. The θ and ϕ chambers are all jet chambers.

In the barrel region, the chamber system outside the toroid (BW2 and BW3) is divided into mechanically separated 4 supermodules in each octant. Each supermodule includes 3 θ-chambers both in BW2 and in BW3, and also 3 stereo chamber modules in BW2 and 4 ϕ-chambers in BW3. The support structure is a stiff box made of appropriate panels and plates. The chambers are slidden into compartments furnished in the support structure, being guided with a pair of rails precisely located in the compartments. After the positioning is completed, the chambers are held on the rails at 6 points: 4 corners and 2 middle points where the center support is placed.

The chamber system inside the toroid (BW1) is subdivided into 3 supermodules, which includes 3 θ-chambers and 2 ϕ-chambers each. The support structure is a simple box mounted on a rail system on the toroid. The chamber modules are brought into the box with a help of thin needle bearing pads and directly fixed to the inner surfaces of the box at the 6 points.

The chambers in the intermediate region are described in section 4.2.7. Their structure and arrangement are somewhat different from our basic concept because they have to cover an octagonal area.

The number of readout channels has been examined according to this chamber layout. The results are summarized in Table 2.2. The projective cell layout helps us to save the channel count by typically 25 % in the barrel

θ chambers. The stereo layers are counted with an assumption that they are slanted by 3° with respect to the theta wires. The total channel count amounts to about 72k for the barrel region and 23k for the intermediate region.

Alignment is one of the most important items for the muon detector system. In order to achieve a good stand-alone momentum resolution for several 100 GeV/c muons, the alignment of wires is required to be an order of 100 μm. However the chamber placement need not be guaranteed to this level. What we need is a precise measurement of the wire location, which can be carried out by analyzing high momentum muon tracks from *W* and *Z* decays as well as by surveying and monitoring. A monitoring system is being designed to achieve a 100 μm accuracy.

We believe that the muon chamber system proposed here is the best choice to achive a good alignment in the above aspect. The wire placement within a chamber module is trivial in our design since it is accomplished with precise machining. Even if a module suffers from a temperature change of a few degrees, the thermal deformation is kept within an order 100 μm since the thermal expansion coefficient is approximately 2×10^{-5} $degC^{-1}$ and the size of the end frame is maximum 2.5 m. Such deformation may be serious for larger modules.

There is essentially no requirement on the actual chamber placement. Even a 1 cm displacement is tolerable for the level 1 trigger. The supermodule structure is being designed to achieve a positioning accuracy of 200 μm within a supermodule in order to reduce measurement efforts. Although the structure need not be built with high accuracy, it must be stable within an order of 100 μm throughout a reasonable length of period. Otherwise, we need a highly reliable monitoring system which can measure a long term movement of the structure.

Table 2.2 Summary of the sampling layer, module and channel counts.

Barrel Chambers		BW1	BW2	BW3	Total
layers in station	θ	6	6	6	18
	ϕ	6	0	6	12
	s	0	2	0	2
	Total	12	8	12	**32**
chamber modules	θ	72	96	96	264
	ϕ	48	0	128	176
	s	0	96	0	96
	Total	120	192	224	**536**
super modules		24	32	32	**88**
readout channels	θ	10.1k	13.4k	14.8k	38.3k
	ϕ	8.2k	0k	19.3k	27.5k
	s	0k	6.1k	0k	6.1k
	Total	18.3k	19.5k	34.1k	**71.9k**
Intermediate Chambers			IW2	IW3	Total
layers in station	θ		6	6	12
	ϕ		0	6	6
	s		0	2	2
	Total		6	14	**20**
chamber modules	θ		16	48	64
	ϕ		0	64	64
	s		0	48	48
	Total		16	160	**176**
super modules			16	16	**32**
readout channels	θ		2.3k	6.1k	8.4k
	ϕ		0k	12.5k	12.1k
	s		0k	2.5k	2.5k
	Total		2.3k	19.5k	**23.0k**

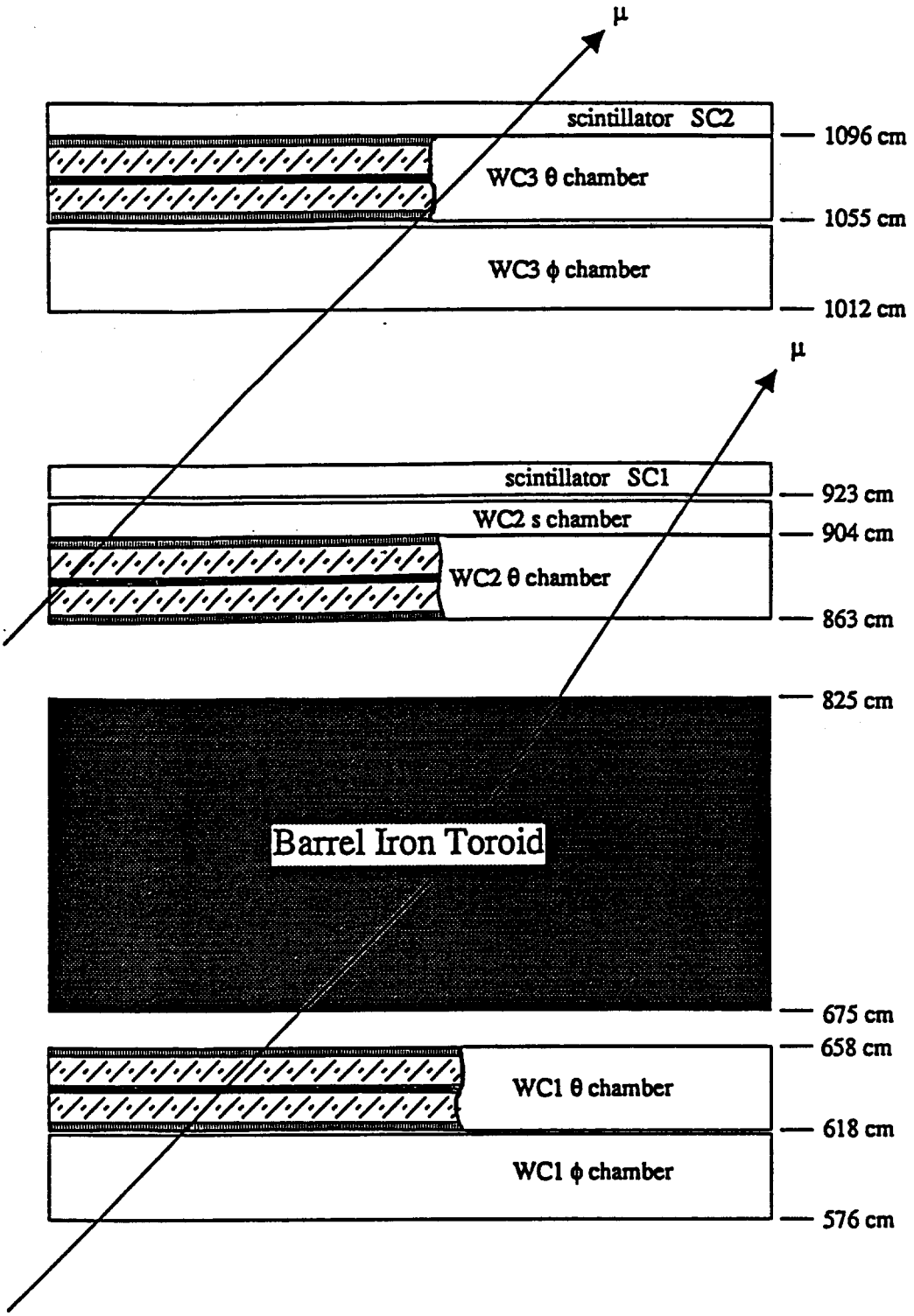

Fig. 2.5. The chamber module arrangement.

§3. System Performance

3.1 Momentum resolution

The position resolution of each sense wire is about 250 μm. Since we have six independent measurements per superlayer for one coordinate, the position resolution per station is in principle 102 μm. In this sense, the position resolution is much better than 200 μm within a module. However, the muon system is so large that a main contribution to the momentum measurement error would be caused by relative alignment errors between the superlayers. At the stage of off-line analyses we would be able to align them within 100 μm. Therefore, the position resolution of 200 μm per superlayer is regarded as a rather realistic assumption, which we will use for the estimation of the momentum resolution unless it is stated otherwise. The magnetic field in the barrel muon toroid is assumed to be 1.8 Tesla.

3.1.1 Full muon system

(1) $\sigma(p_t)/p_t$ as a function of p_t

The momentum is determined by the muon system alone with a point measurement inside the toroid and a line segment outside. We plot the momentum resolution as a function of p_t in Fig. 3.1.1 for three different angles. The solid, dashed, and dotted curves correspond to 90, 60, and 40 deg in polar angle, respectively. Definitions of the parameters given in the figure are depicted in Fig. 3.1.2. The muon tracks are assumed to enter the toroid with a normal incident angle in the rϕ-view. At 90 deg the resolution is 17 % up to about 200 GeV/c, where the multiple scattering in the toroid is dominant over the intrinsic spatial resolution. The angular dependence of the multiple scattering in the momentum resolution is proportional to $\sqrt{\sin\theta}$.

(2) $\sigma(p_t)/p_t$ as a function of pseudorapidity

The momentum resolution as a function of pseudorapidity, $\eta = -\ln(\tan(\theta/2))$, is shown in Fig. 3.1.3 for p_t = 20, 100, 500, and 1000 GeV/c. The

structure between $\eta = 1$ and 1.7 corresponds to the transition from the barrel to the forward region. In this calculation we also assume the position resolution of 200 μm per superlayer for the forward chambers, and the magnetic field of 1.8 Tesla in the forward toroid.

(3) Dependences of $\sigma(p_t)/p_t$ on the position resolution

Fig. 3.1.4a shows the momentum resolution versus the position resolution of the superlayer BW1(θ), σ_F in Fig. 3.1.2, at $\theta = 90$ deg for several transverse momenta keeping the other parameters fixed. The four curves correspond to 50, 100, 200, and 500 GeV/c starting from the lowest curve. Below p_t of about 200 GeV/c, where the multiple scattering is dominant, $\sigma(p_t)/p_t$ is almost constant up to $\sigma_F = 1$ mm. Similar plots are shown in Fig. 3.1.4b as a function of the position resolution of BW2(θ) and BW3(θ), σ_R. In this case the dependence is much larger than that of σ_F, especially at higher momenta. These results suggest that the relative alignment between BW2(θ) and BW3(θ) is important, while that of BW1(θ) and BW2(θ)/BW3(θ) is less important.

(4) Dependences of $\sigma(p_t)/p_t$ on the geometrical variables

Fig. 3.1.5a shows the momentum resolution versus the distance between BW1(θ) and the center of the barrel toroid, X_F in Fig. 3.1.2, for several momenta. Qualitatively speaking, the resolution improves as the distance increases. It is because the distance between the hit point at BW1(θ) and the extrapolated line determined by BW2(θ) and BW3(θ) becomes larger. However, its dependence is very small as indicated in the figure. Similar plots are shown in Fig. 3.1.5b as a function of the distance between BW2(θ) and the center of the barrel toroid, X_R. keeping the distance between BW2(θ) and BW3(θ) fixed. In this case, the resolution becomes slightly poor as X_R increases because the expected point at BW1(θ) becomes more ambiguous. Quantitatively, however, the dependence is also very small. In practice, we have little freedom to change these parameters. Fig. 3.1.5c shows the momentum resolution as a function of the distance between BW2(θ) and BW3(θ), L_R, for several momenta. The dependence is also not significant for p_t below 200 GeV/c.

In conclusion, the dependences on the geometrical parameters are small for p_t below about 200 GeV/c, where the multiple scattering contribution is dominant.

3.1.2 Muon system without BW1(θ) --- corresponding to the L1 trigger ---

Assuming the collision point at the center of the SDC detector, we can estimate a momentum of a muon by just measuring the exit angle outside the toroid with BW2(θ) and BW3(θ). Unfortunately, however, the beam is estimated to be spread along the beam line with $\sigma_{Beam} \cong 10$ cm. Therefore, the interaction point is also expected to be spread about 7 cm along this direction. The angular dependence of the momentum resolution due to the spread is proportional to $\sin^2\theta$. Compared to the beam spread, the effect of the multiple scattering in the calorimeter to the momentum resolution is not so significant. It is because the effect of the multiple scattering in the calorimeter to the momentum resolution is reduced by R_{cal}/R_{toroid}, where R_{cal} (R_{toroid}) is the effective mean radius of the calorimeter (toroid). The result is shown in Fig. 3.1.6 for $\theta = 90$, 60 and 40 deg. At $\theta = 90$ deg, it is flat up to only about 20 GeV/c and reach 100 % at $p_t \cong 100$ GeV/c. In fact, the deflection angle at $p_t = 100$ GeV/c is equal to the angular smearing due to the beam spread. Therefore, we are not able to increase the p_t threshold beyond about 50 GeV/c in order to keep a good trigger efficiency. The detail will be described in subsection 3.2.2.

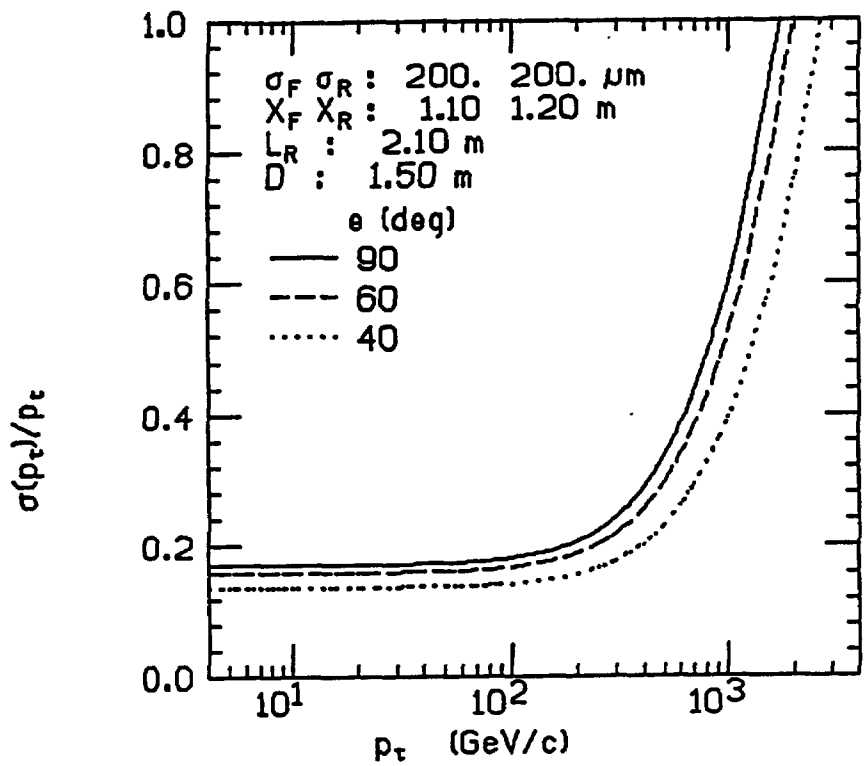

Fig. 3.1.1 Momentum resolution as a function of the transverse momentum for 90, 60, and 40 deg of polar angle. Definitions of the parameters are depicted in Fig. 3.1.2.

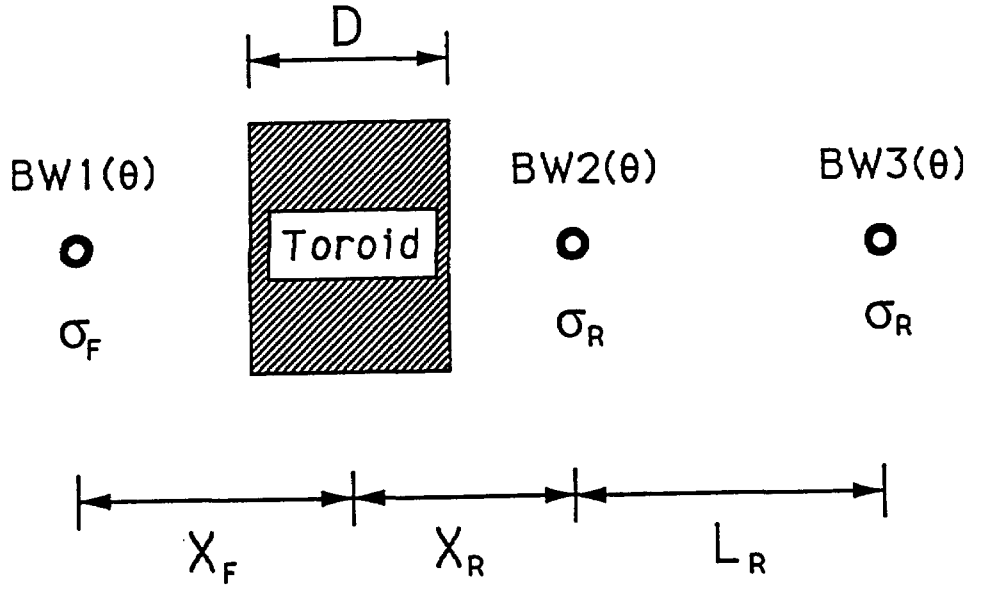

Fig. 3.1.2 Definitions of parameters, σ_F, σ_R, X_F, X_R, L_R, and D. σ_F and σ_R are the position resolutions of BW1(θ) and BW2(θ)/BW3(θ), respectively. X_F is the distance between BW1(θ) and the center of the barrel toroid. X_F is the similar definition for BW2(θ). L_R is the distance between BW2(θ) and BW3(θ). D is the thickness of the barrel toroid.

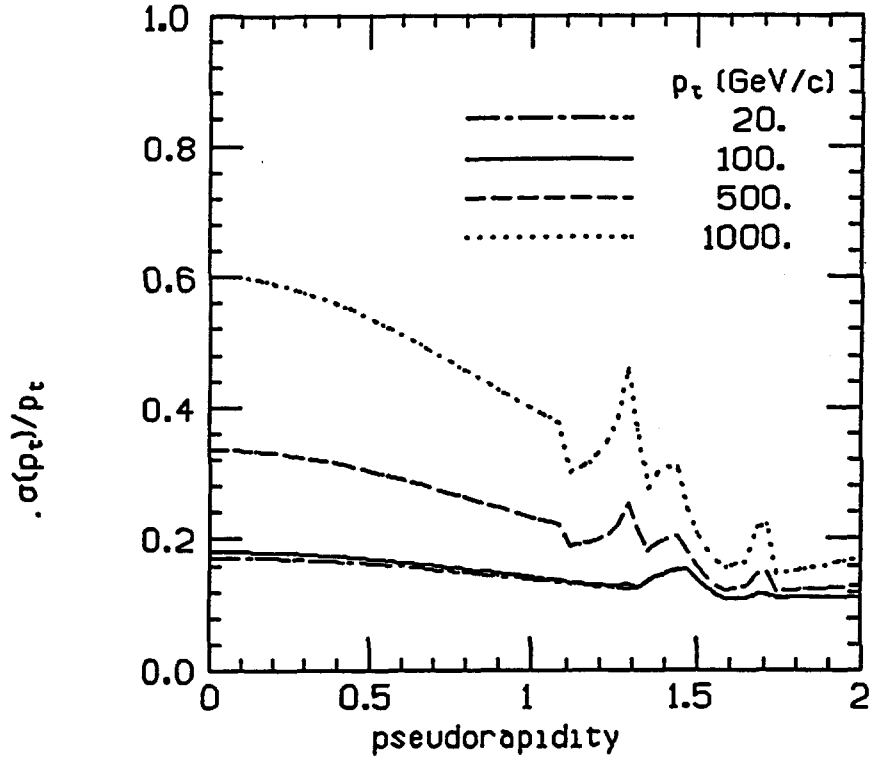

Fig. 3.1.3 Momentum resolution as a function of pseudorapidity for $p_t = 20$, 100, 500, and 1000 GeV/*c*. For the forward muon system, we assume a position resolution of 200 μm per superlayer, and assume a magnetic field of 1.8 Tesla in the relevant region.

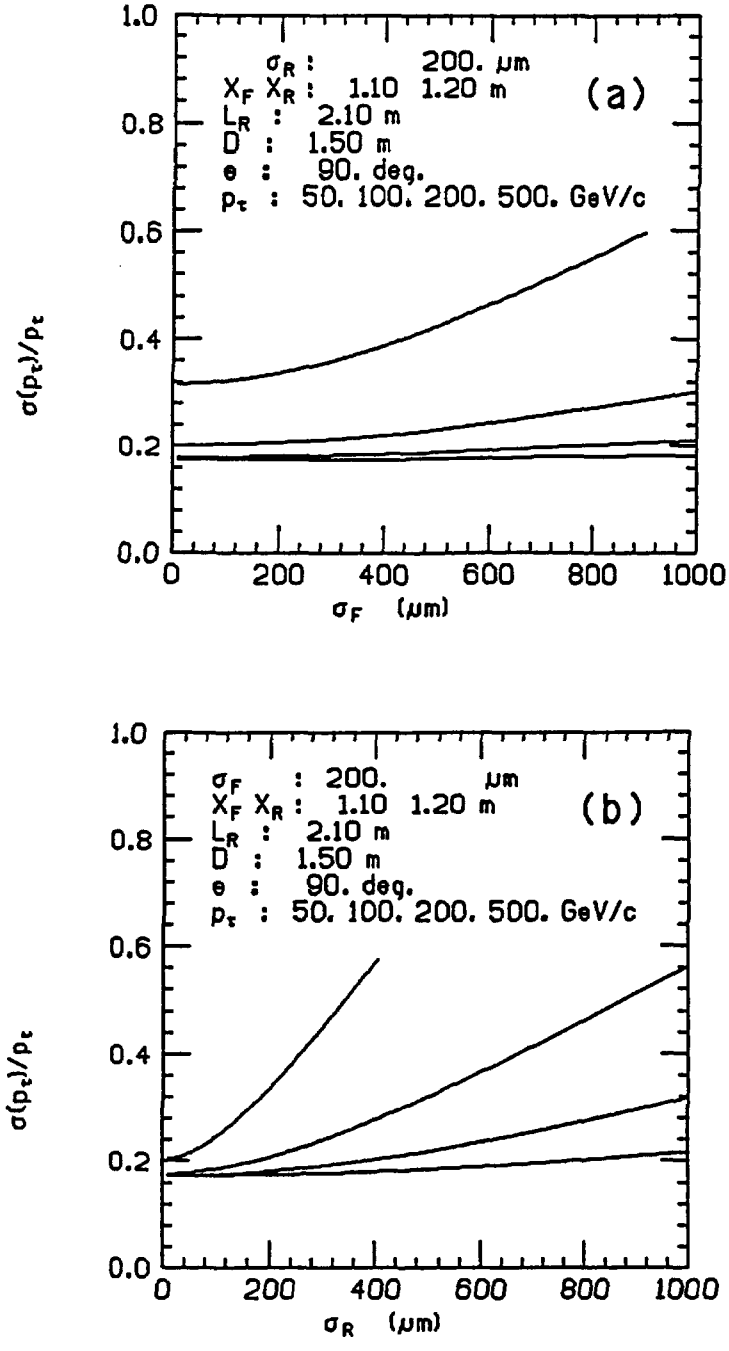

Fig. 3.1.4 Momentum resolution as a function of σ_F (a), and as a function of σ_R (b). Definitions of the parameters are shown in Fig. 3.1.2.

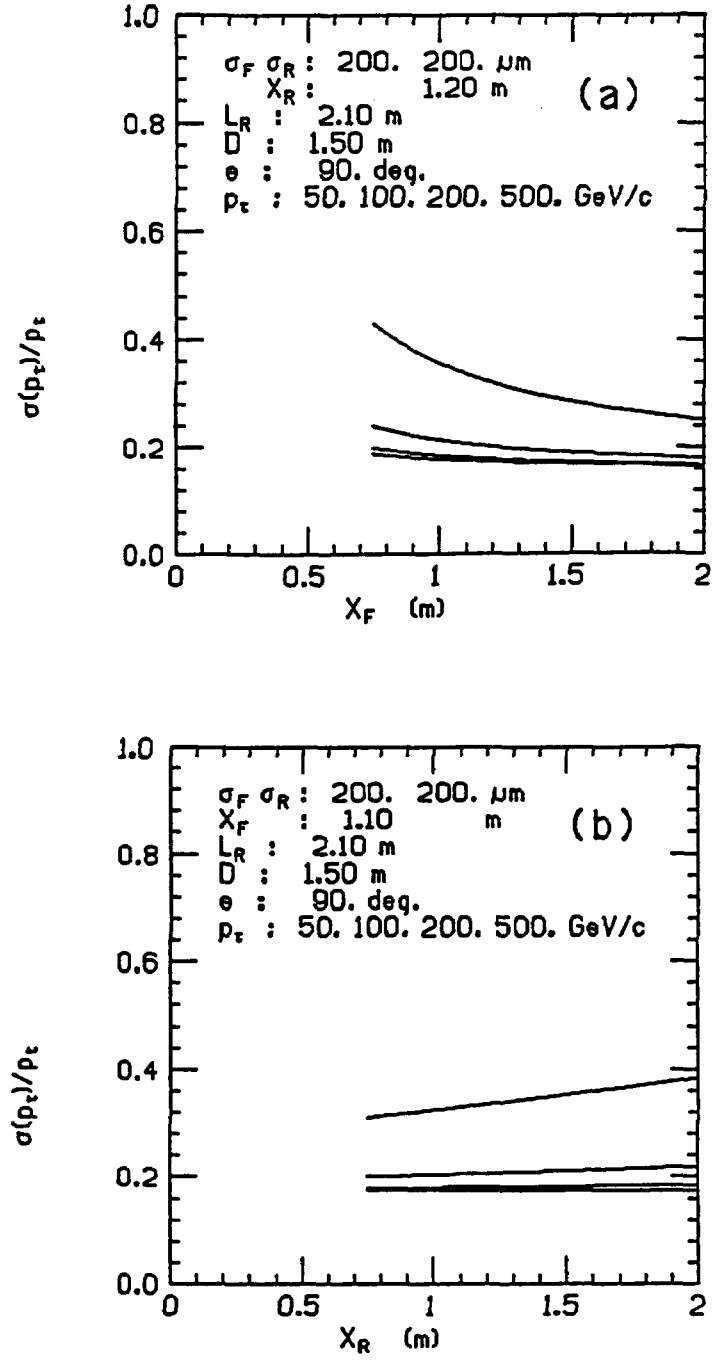

Fig. 3.1.5 Momentum resolution as a function of X_F (a), as a function of X_R (b), and as a function of L_R (c). Definitions of the parameters are shown in Fig. 3.1.2. [continue to the next page]

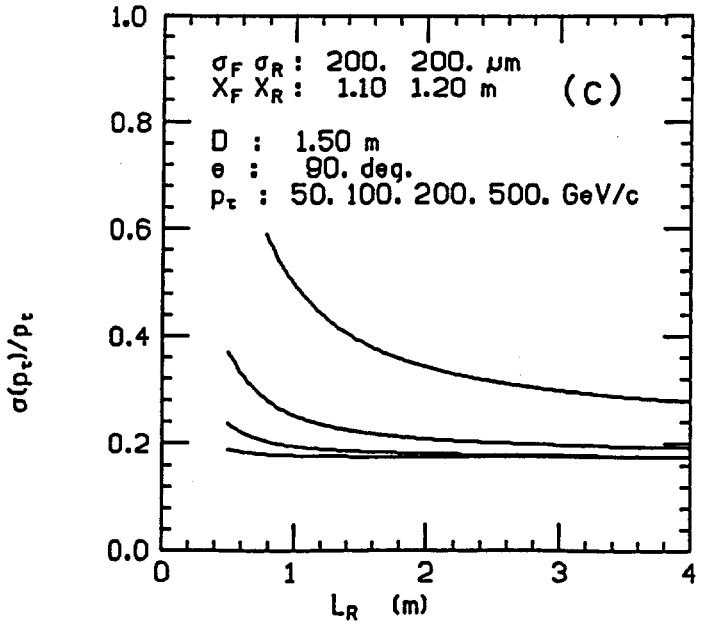

Fig. 3.1.5 [continued from the previous page]

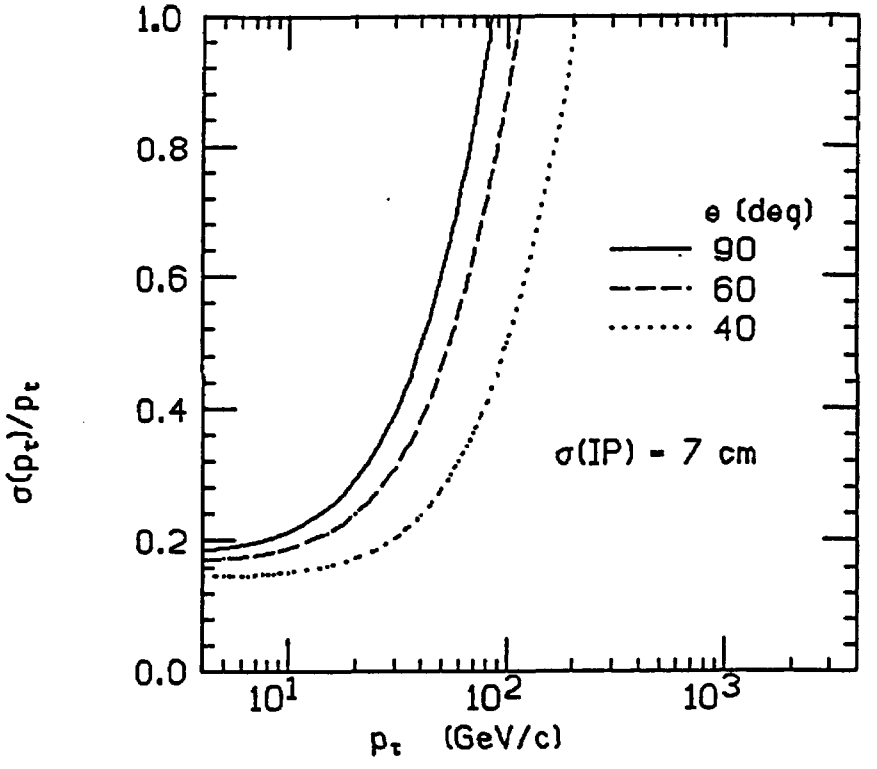

Fig. 3.1.6 Momentum resolution as a function of p_t without BW1(θ). The interaction point is assumed to be spread along the beam direction with a rms value of 7 cm.

3.2 Performance of the level-1 trigger

At level-1 trigger, we select high-p_t muons by evaluating the bending angles outside the toroid with BW2(θ) (or IW2(θ)) and BW3(θ) (or IW3(θ)). We further reject cosmic rays and punchthrough particles by requiring tracks to be extrapolated to the interaction region in rφ-plane also. For this purpose, we use BW3(φ). Because the jet cells of the IW3(φ) are not projective geometry, the layer is not used for the trigger purpose.

Muon hit rates without the trigger conditions are estimated in subsection 3.2.1 to see the noise level at the muon system. The trigger efficiency for prompt and decay muons are given in subsection 3.2.2. And the resulting trigger rates are calculated in subsection 3.2.3.

3.2.1 Muon rates

There are four kinds of particles to hit the muon chambers: prompt muons, decay muons, punchthrough particles, and cosmic rays. In this subsection, we estimate the hit rate for each source without the trigger conditions. It gives the noise level at the barrel and intermediate muon chambers. A summary of the hit rates is given in Table 3.2.1. The design luminosity of 10^{33} $cm^{-2}s^{-1}$ is assumed. Electromagnetic debris associated with a high energy muon are not considered here. The detail of such an analysis based on the real beam data is given in Appendix 3.

(1) Prompt muons

Prompt muons are the decay muons from the heavy-quark (charm, bottom) hadrons. We estimate the muon rates by using PYTHIA5.3 [3.2.1] at the SSC energy, $\sqrt{s}$ = 40 TeV. Differential cross section versus p_t at the interaction point is shown in Fig. 3.2.1 with open circles. Although the width of the plateau shrinks as p_t increases, the pseudorapidity distribution is almost flat in the barrel and intermediate regions ($|\eta| < 1.5$). The calculated points are well fitted with a function,

Table 3.2.1 Summary of muon rates at L = 10^{33} $cm^{-2}s^{-1}$.

particles	hit rate	area (η range)
1. prompt μ	1100 kHz / unit η	at BW1
	83 kHz / unit η	at BW2/BW3
2. decay μ	56 kHz / unit η	at BW1
	7 kHz / unit η	at BW2/BW3
3. punchtrough	160 kHz	at BW1 ($\|\eta\|<1.3$)
	20 Hz	at BW2+IW2 ($\|\eta\|<1.5$)
4. cosmic rays	8.2 kHz / octant	top octant of BW2 ($\|\eta\|<1.3$)
	4.8 kHz / octant	next to the top octant
	0.6 kHz / octant	side octant
	0.2 kHz / end	at IW2 ($1.3<\|\eta\|<1.5$)

$$\frac{d\sigma}{dp_t\, d\eta} = \frac{9.13\times10^7}{p_t{}^{4.88}}$$

where $d\sigma/dp_t\, d\eta$ is given in nb/GeV/c and p_t in GeV/c. Assuming that the formula is applicable below 10 GeV/c, we can estimate hit rates at BW1 and BW2/BW3. At the design luminosity of 10^{33} $cm^{-2}s^{-1}$, 1nb corresponds to 1 Hz. Since only muons with transverse momenta greater than 2.2 GeV/c can penetrate the calorimeter, the hit rate of prompt muons at BW1 per unit rapidity is estimated to be about 1.1 MHz. The minimum p_t of 4.3 GeV/c is required for muons to pass through the barrel iron toroid. At BW2 and BW3, the hit rate per unit rapidity decreases down to 83 kHz. Since the cross section must be below the extrapolation in the low-p_t region, these estimates could be considered to be the upper limits. Even though, the hit rate integrated over the entire BW1 during 0.8μs, which is the maximum drift time, is no more than 3 hits.

(2) Decay muons

Decay muons are the decay products from charged pions and kaons in flight. We estimate the muon rates also by using PYTHIA5.3. As for the decay volume, we assume a radius of 1.7 m and a half length of 4 m. The result is

also shown in Fig. 3.2.1 with x-marked points, where p_t is the transverse momentum of the muon inside the decay volume. The calculated points are well fitted with a function,

$$\frac{d\sigma}{dp_t\, d\eta} = \frac{1.95 \times 10^6}{{p_t}^{4.08}}$$

where $d\sigma/dp_t\, d\eta$ is given in nb/GeV/c and p_t in GeV/c. Assuming that the formula is applicable beyond 10 GeV/c, we can estimate hit rates at BW1 and BW2/BW3. The hit rates per unit rapidity are 56 kHz at BW1 and 7 kHz at BW2/BW3. These hit rates are much smaller than those from prompt muons.

(3) Punchthroughs

Hadrons at the interaction point are generated by using PYTHIA5.3. As for the punchthrough properties through the calorimeter and the ion toroid, we use the parametrization developed by R.McNeil *et al.*[3.2.2]. Fig. 3.2.2 shows the material thickness integrated up to the outside of the toroid in the interaction length as a function of pseudorapidity, η. The punchthrough hit rate integrated over the whole BW1 ($|\eta| < 1.3$) is 160 kHz. The corresponding hit rate over the BW2 and IW2 ($|\eta| < 1.5$) is only 20 Hz.

(4) Cosmic rays

We use a formula given in ref.[3.2.3] for the flux of cosmic rays at the sea level. In the estimation we simplify the experimental hall as an infinitely long square tube as shown in Fig. 3.2.3. We assume the density of the soil around the experimental hall to be 2.0 g/cm^3, and a constant energy loss of 2 MeV/(g/cm^2) for cosmic rays. The hit rates on the top octant of BW2 and on the octant next to the top are about 8 kHz and 5 kHz, respectively. It is less than 1 kHz for the side octant. The hit rate on the entire region on IW2 is 0.2 kHz per end.

3.2.2 Trigger efficiency

In this subsection, we evaluate the performance of the level-1 trigger based on the scheme described in sections 2.2 and 4.6.2. We discriminate low-p_t muons by measuring deflection angles outside the toroidal magnets. The bending power of the toroid for transverse momentum of p_t is $\Delta\theta = qBD/p_t$, where q is the charge of the muon, B is the magnetic field inside the toroid (B = 1.8 Tesla), and D is the thickness of the toroid (D = 1.5 m). Namely, $\Delta\theta$(rad) = 0.81/p_t(GeV/c).

(1) Efficiency of the cell trigger

Efficiency curves of the cell trigger at BW3(θ) as a function of p_t are plotted in Fig. 3.2.4 for T_{clip} = 7, 10, 20 and 30 ns. T_{clip} is the clipping time for each sense wire signal, which corresponds to "dT" in Fig. 4.6.7. For T_{clip} = 20 ns, the efficiency reaches 100% at around 14 GeV/c. We can set a higher threshold by choosing shorter T_{clip}. However, for T_{clip} = 10 ns it never reaches to 100%. Therefore, we should set T_{clip} wide enough, about 16 ns, not to loose real muons. We can reject most of muons less than 5 GeV/c of p_t at the cell trigger stage. The small bumps below 5 GeV/c are caused by those tracks which cross the sense wire plane.

(2) Efficiency of the layer trigger

From a pair of the cell triggers generated in associated upper and lower cells, a layer trigger can be made. Efficiency curves of the layer trigger at BW2(θ) and BW3(θ) are plotted in Fig. 3.2.5 for T_{clip} = 20 ns and T_{PW} = 192 ns, where T_{PW} is the gate width corresponding to "Pulse Width (Tpw)" in Fig. 4.6.8. The efficiencies become 50% at p_t= 21 GeV/c for BW2(θ) and 17 GeV/c for BW3(θ). The difference is due to the fact that the measured deflection angle, $\Delta\theta_{mes}$, depends on the measured position (see Fig. 3.2.6):

$$\Delta\theta_{mes} = \frac{R_{toroid}}{R_{BW}}\Delta\theta$$

where R_{toroid} (R_{BW}) is the mean radius of the toroid (muon chamber), and $\Delta\theta$ is the actual deflection angle at the toroid, $\Delta\theta$ (rad) = $0.81/p_t$(GeV/c). Therefore, if $\Delta\theta_{mes}$ is kept fixed, the p_t threshold is inversely proportional to R_{BW} (21 GeV/c : 17 GeV/c = 1/(8.7m) : 1/(10.8m)). Efficiencies for logical AND and OR of BW2(θ) and BW3(θ) are also plotted in the figure. The curves for logical AND and OR are similar to those of BW2(θ) and BW3(θ), respectively. Except for the curve for logical AND, the curves have bumps at around 10 GeV/c. They are caused by low p_t muons, which enter the same side relative to the wire planes in both upper and lower cells (see Fig. 3.2.7). The bumps can be removed by taking logical AND.

In the real environment, we have module boundaries where the layer trigger can not be generated. However, at least one of the cells at the boundary can cover the region as shown in Fig. 4.2.1. In order to reject muons of 10 GeV/c, the position resolution of 8cm is sufficient for the lever arm of 2 m. In the real situation, therefore, we require the layer trigger in a layer and the cell trigger within the corresponding region in the other layer. The deflection angle cuts at BW2 and BW3 are also adjusted to give the same p_t threshold.

(3) Efficiency vs p_t

In Fig. 3.2.8, efficiency curves as a function of the transverse momenta of muons in the barrel region are shown for T_{PW} = 384, 272, 224, 176, 128, 96, 80, 64 and 48 ns, which correspond to p_t(thr) = 13, 16, 18.5, 22.7, 30, 39, 46.4, 57 and 75.4 GeV/c in this order. p_t(thr) is defined as the transverse momentum where the trigger efficiency becomes 50%. For small p_t(thr), the trigger efficiency reaches almost 100 %. The resolution is dominated by the multiple scattering. However, it never reaches 100 % for higher p_t(thr). For example, it is about 90 % for p_t(thr) = 75.4 GeV/c. It is because the effect of the beam spread becomes comparable to the maximum allowed $\Delta\theta$, although the effect of the multiple scattering is the same. We plot the p_t of the muon at which the trigger efficiency becomes 90%, p_t(90%), as a function of p_t(thr) in Fig. 3.2.9.

3.2.3 Trigger rates

The level-1 trigger rates integrated over the barrel and intermediate regions ($|\eta| < 1.5$) are summarized in Table 3.2.2 and Fig. 3.2.10. Throughout this section we assume the design luminosity of $10^{33}cm^{-2}s^{-1}$. In the estimation for punchthrough particles and cosmic rays, a value $\Delta\phi_{cut} = 0.05$ for BW3(ϕ) is used, where $\Delta\phi_{cut}$ is the maximum allowed projective angle of the track in the rϕ-plane from the straight line connecting the interaction point and the hit point on the relevant muon chamber. Decay muons have a similar dependence on p_t(thr) as prompt muons. In the log-log scale, the cosmic ray and the punchthrough rates as functions p_t(thr) have a similar slope. However, the latter is two orders of magnitude smaller than the former. The cosmic-ray trigger rate becomes about six times larger if we do not have the ϕ-cut capability with BW3(ϕ).

Table 3.2.2 Summary of level-1 trigger rates (Hz).

p_t (thr) GeV/c	prompt	decay	cosmic rays	punchthru	total
10	13200	1970	210	2.5	15400
20	1420	310	110	1.6	1840
30	380	100	71	1.3	550
40	170	49	53	1.2	270
50	86	26	43	1.0	156
60	51	17	35	0.92	104
70	35	11	30	0.85	77
80	25	7.8	27	0.80	61

(1) Trigger rates for prompt and decay muons

The trigger rates for prompt and decay muons in the barrel and intermediate regions can be estimated by folding the muon rates and the trigger efficiency curve given in the previous subsection. The results are shown in Fig. 3.2.11 as a function of p_t(thr). The vertical axis is the trigger rate per unit rapidity

in Hz. The solid curve is for prompt muons, and the dashed curve for decay muons. The former is about four times larger than the latter. If we set the p_t(thr) at 20 GeV/c, which corresponds to 29 GeV/c of p_t(90%), the trigger rate becomes 1.7 kHz in the whole barrel and intermediate regions ($|\eta| <$ 1.5) from these muons.

(2) Trigger rate for punchthrough particles

For the estimation of the level-1 trigger rate for punchthrough particles and cosmic rays, we did not fully apply the trigger simulation logic. The resolution of the trigger efficiency for prompt and decay muons is dominated by the multiple scattering and the beam spread, but not due to the trigger logic. Compared with the angular distributions of punchthroughs and cosmic rays, the angular resolution by the trigger logic itself is negligibly small (order of 5 mrad). Therefore, the step function can be a good approximation as an efficiency curve for these particles.

The trigger rate integrated over BW2(θ) and IW2(θ) for punchthrough particles as a function of $\Delta\theta_{cut}$ is shown in Fig. 3.2.12, where $\Delta\theta_{cut}$ is the maximum allowed projective angle of the exiting muon from the straight line connecting the interaction point and the hit point on the relevant muon chamber. The phi-cut is not imposed at this stage. The relation between $\Delta\theta_{cut}$ and p_t(thr) is approximately given as

$$p_t(\text{thr}) = \frac{0.81}{\Delta\theta_{cut}} \frac{R_{toroid}}{R_{BW2}}$$

where R_{toroid} (R_{BW2}) is the mean radius of the toroid (BW2). R_{toroid}/R_{BW2} is the correction factor from the measured angle to the real deflection angle by the toroid. At $\Delta\theta_{cut}$ = 0.035 rad which corresponds to p_t(thr) = 20 GeV/c, the rate is about 4 Hz only.

At level-1, we apply the angular cut also in the rφ-plane by utilizing BW3(φ). Because of the axial symmetry of a hadron shower, the curve in Fig. 3.2.12 is also applicable to the phi projection. Since the hit rate is 20 Hz without the $\Delta\phi_{cut}$ cut, the reduction factor is about 4 at $\Delta\phi_{cut}$ = 0.05 rad.

Therefore, the hit rate in the barrel region is further reduced. The resulting trigger rate integrated over BW2(θ) and IW2(θ) for punchthrough particles is 1.6 Hz for p_t(thr) = 20 GeV/c and $\Delta\phi_{cut}$ = 0.05 rad.

(3) Rejection of cosmic rays

We first consider the trigger rate for the case in which only the theta-cut is required. Under this given condition, the trigger rate is proportional to the cut angle $\Delta\theta_{cut}$ as long as it is less than 0.2. We require the $\Delta\theta_{cut}$ on both W2 and W3, where W2 represents logical OR of BW2 and IW2, and W3 corresponds to the similar definition. In the case without the ϕ cut, the trigger rate is 18.2 $\Delta\theta_{cut}$ kHz. When we set p_t(thr) = 20 GeV/c, it becomes 0.64 kHz, which roughly corresponds to half of the prompt muon rate.

We can further reduce the cosmic ray rate by imposing the ϕ cut on BW3(ϕ), which is the actual trigger condition. The resulting trigger rate is parametrized as follows:

$$\text{Rate(kHz)} = (17\Delta\phi_{cut} + 2.2)\Delta\theta_{cut} .$$

If we set p_t(thr) = 20 GeV/c and $\Delta\phi_{cut}$ = 0.05 rad, the rate is 0.11 kHz, which is one order of magnitude smaller than the prompt muon rate. The trigger rate in the proposed chamber arrangement is sufficiently low.

We note, however, that the trigger rate can be further reduced to

$$\text{Rate(kHz)} = 18.8\Delta\phi_{cut}\,\Delta\theta_{cut} ,$$

when the projective cell geometry is also employed for IW3(ϕ). With the same cut values as above, it is indeed reduced to 33 Hz.

3.2.4 Discussions

We can get the absolute position at each superlayer with an error of less than 1mm after the level-1 trigger from the data in the shift registers (Fig.

4.6.8). At level-2, we are able to utilize the position information and calculate p_t. Then the resolution of the trigger efficiency is basically the multiple scattering in the muon toroid alone. In Fig. 3.2.13, we plot the trigger rates under such a trigger scheme. Compared with the rates given in Fig. 3.2.10, the cosmic ray rate is reduced down to a negligible level relative to the prompt muon rate in any p_t(thr) region. The reduction is larger for higher p_t(thr). Note that p_t(thr) is nothing to do with the momentum of a cosmic ray, but just the angular cut at the level-1 trigger. The actual momentum distribution has a peak in the low-p_t end and decreases rapidly as p_t increases. It is the reason why the reduction is larger in the higher p_t region. The trigger rates for prompt and decay muons are also reduced by about factor two to three in the p_t(thr) range from 20 to 50 GeV/c.

At the level-1 trigger, we cannot get good trigger efficiency for p_t(thr) larger than about 50 GeV/c because of the spread of the interaction point. We assume the spread to be 7cm in the present study, but it might well happen to be longer than this value in the real operation. Even in such a case, we can get a steeper efficiency at level-2, because absolute positions in the three super layers are known. If we do not have such capability, we can not improve the trigger efficiency. One of the important requirements for the trigger scheme is the robustness in case unexpected difficulties are encountered. Our trigger scheme with the jet-chamber is best suited to the requirement.

References

[3.2.1] H.-U. Bengtsson and T.Sjostrand, Computer Physics Commun. **46** (1987) 43.

[3.2.2] R.McNeil, W.Morse and H.Ma, private communication. In the parametrization, the punchthrough probability is based on the experimental data (F.S.Merritt *et al.*, Nucl. Instr. and Meth. **A245** (1986) 27.), and the exit angle and position distributions are based on the GEANT simulation.

[3.2.3] W.D.Dau, K.Carstensen and H.Jokisch, Proc. 14th Int. Conf. on Cosmic Rays, Munchen, MN p.1931, 1974. The formula in the original article is given for large zenith angles (>79 deg) and a correction for the spherical surface of the earth is made. Since it is not necessary for the present study, the correction is ignored. The parameter values given in the formula are tuned up to reproduce data better in the small zenith angle region.

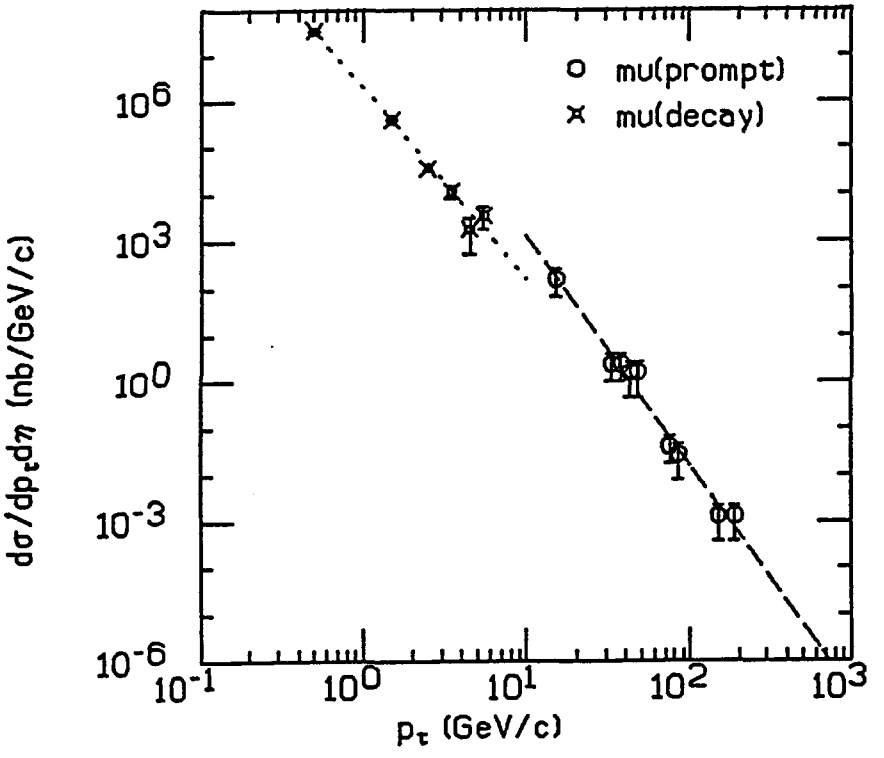

Fig. 3.2.1 Differential cross section, $d\sigma/dp_t\, d\eta$ as a function of p_t for prompt muons (open circle) and decay muons (x-mark). These points are calculated by using PYTHIA5.3. The dashed and dotted lines are the best fitted functions given in the text.

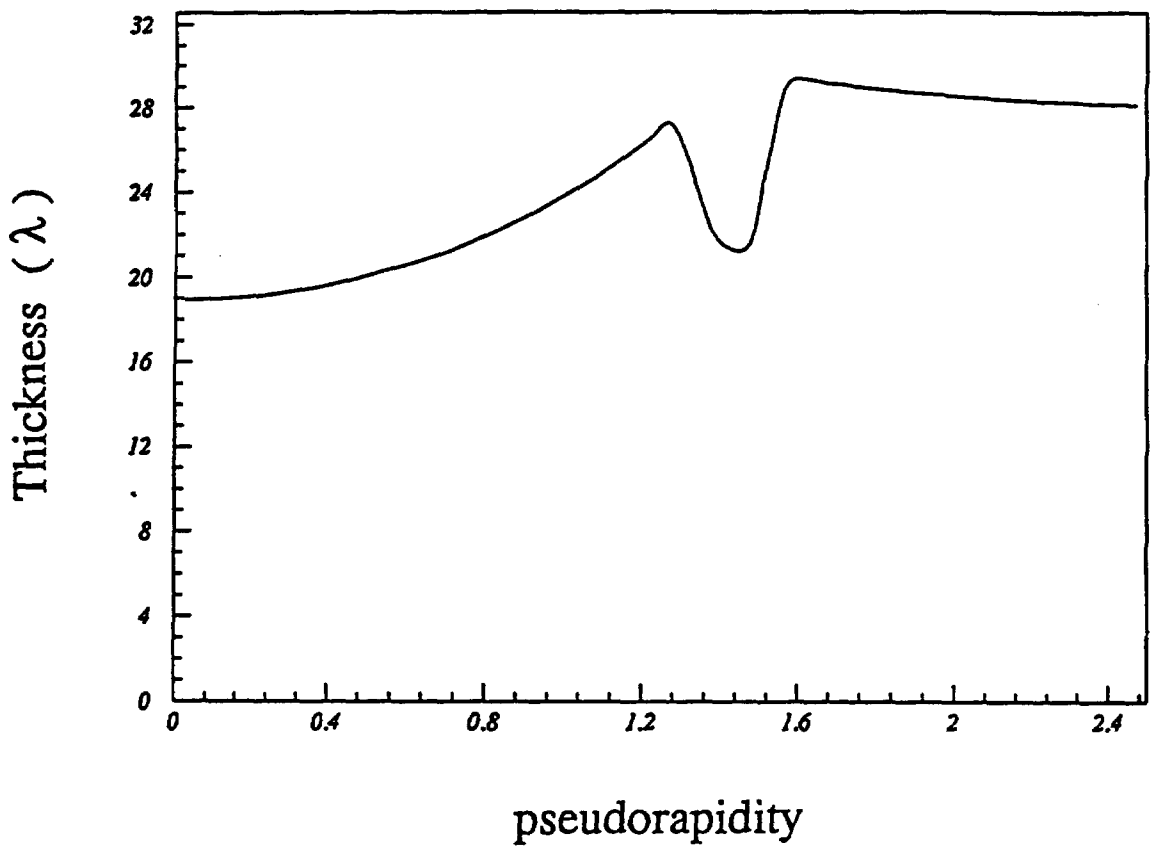

Fig. 3.2.2 Material thickness integrated up to the outside of the toroid in the interaction length as a function of pseudorapidity, η.

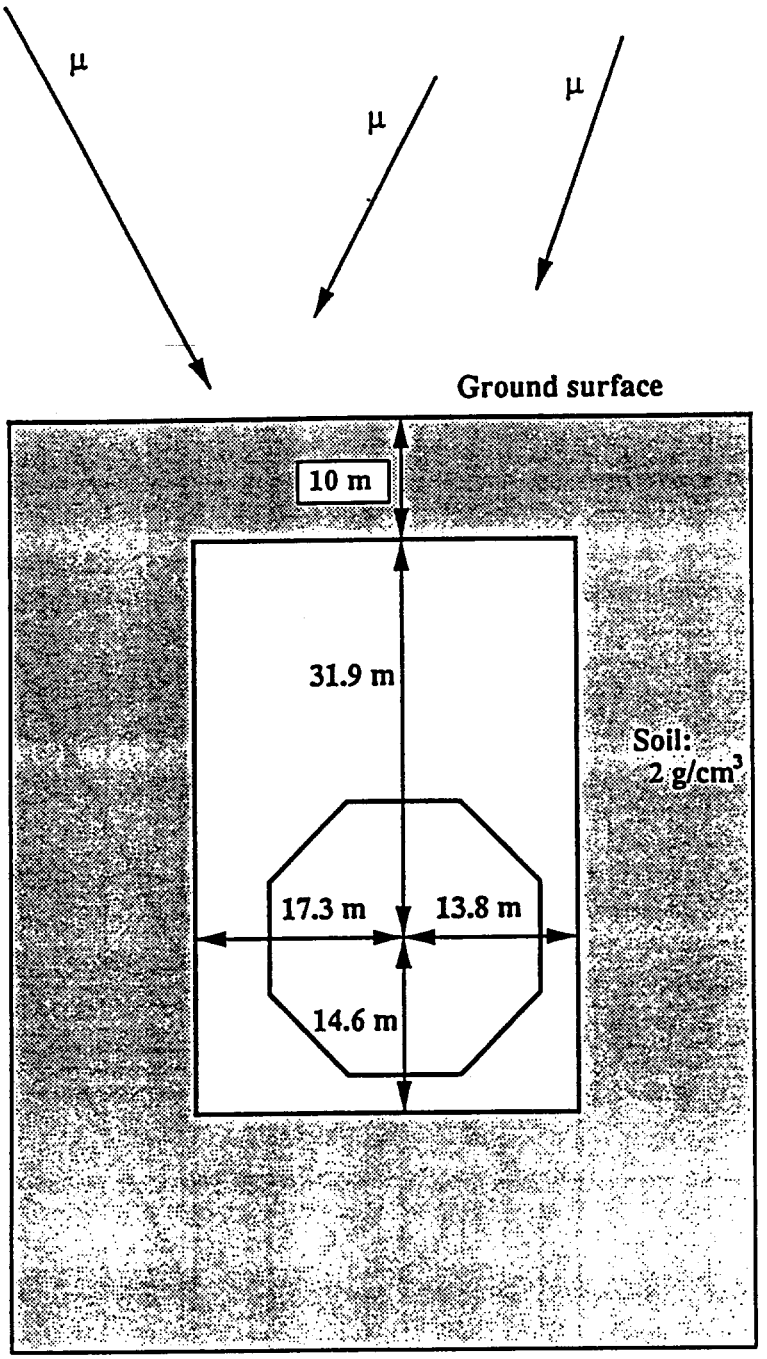

Fig. 3.2.3 Cross-sectional view of the experimental hall, which is simplified for the estimation of the cosmic ray rate.

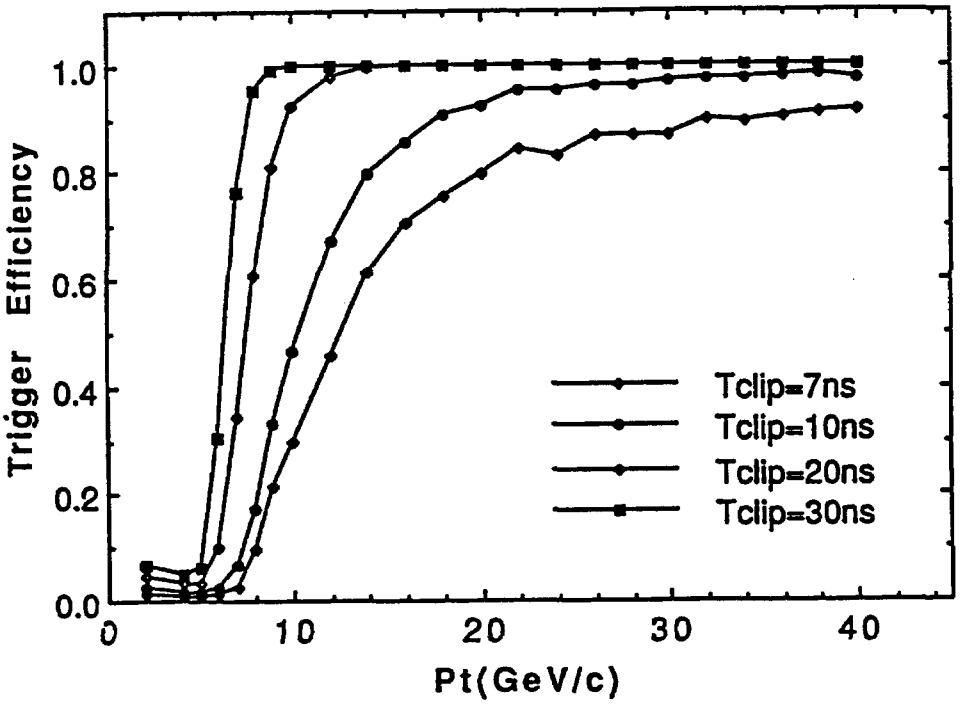

Fig. 3.2.4 Efficiency curves of the cell trigger at BW3 as a function of p_t for T_{clip} = 7, 10, 20 and 30 ns, where T_{clip} is the clipping time for each sense wire signal. The longer clipping time sets the lower threshold.

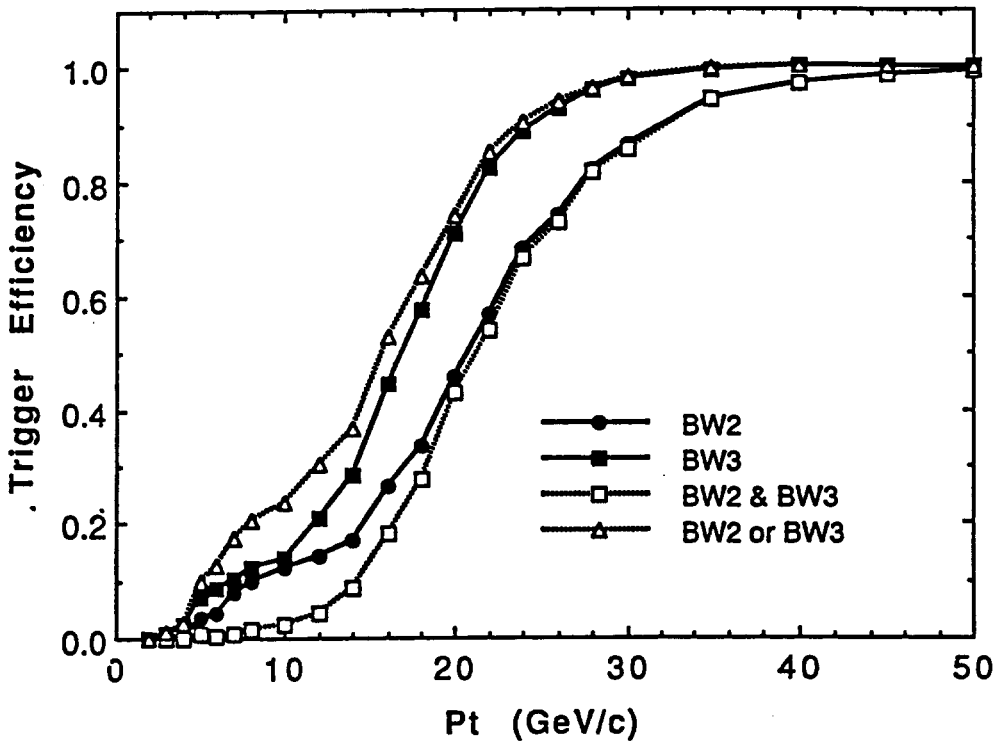

Fig. 3.2.5 Efficiency curves of the layer trigger at BW2 (closed circle), BW3 (closed box), logical AND of BW2 and BW3 (open box) and logical OR of BW2 and BW3 (closed triangle). The clipping time, T_{clip}, of 20 ns and the gate width, T_{PW}, of 192 ns are used.

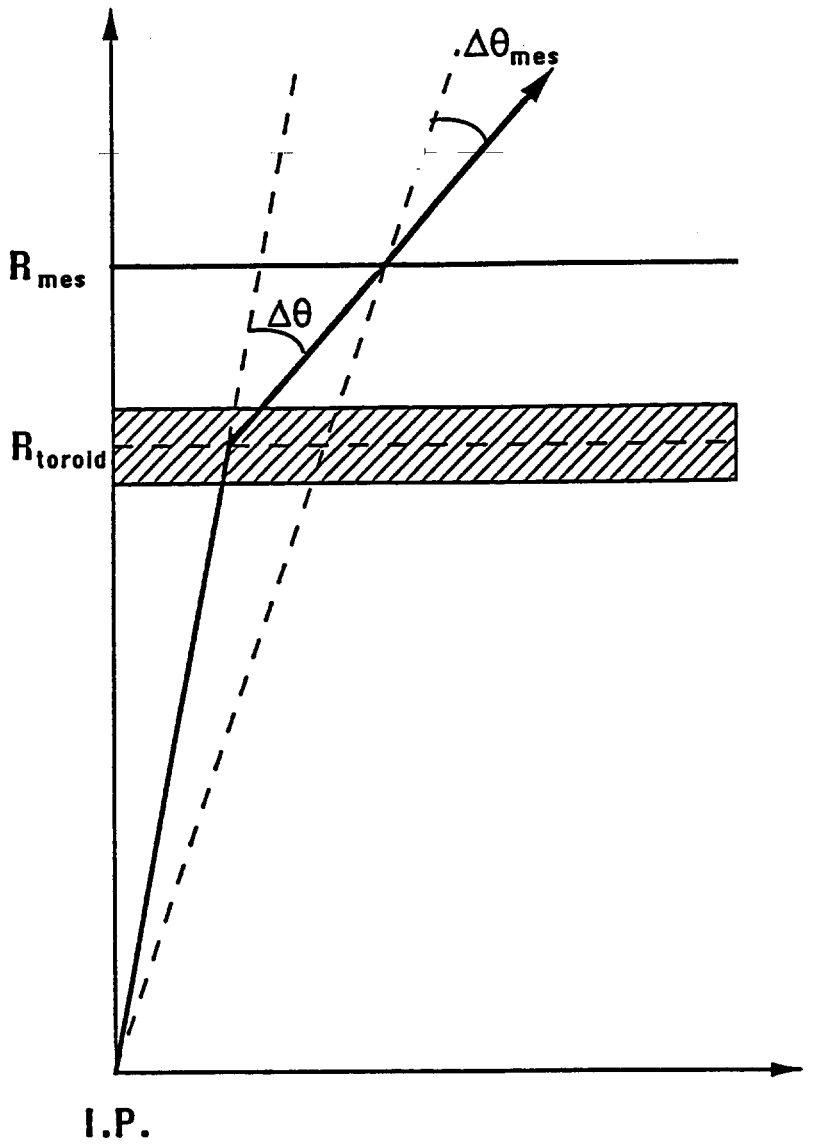

Fig. 3.2.6 Schematic drawing to show the relation between the actual deflection angle at the toroid, $\Delta\theta$, and the measured angle at the muon chamber relevant for the level-1 trigger, $\Delta\theta_{mes}$.

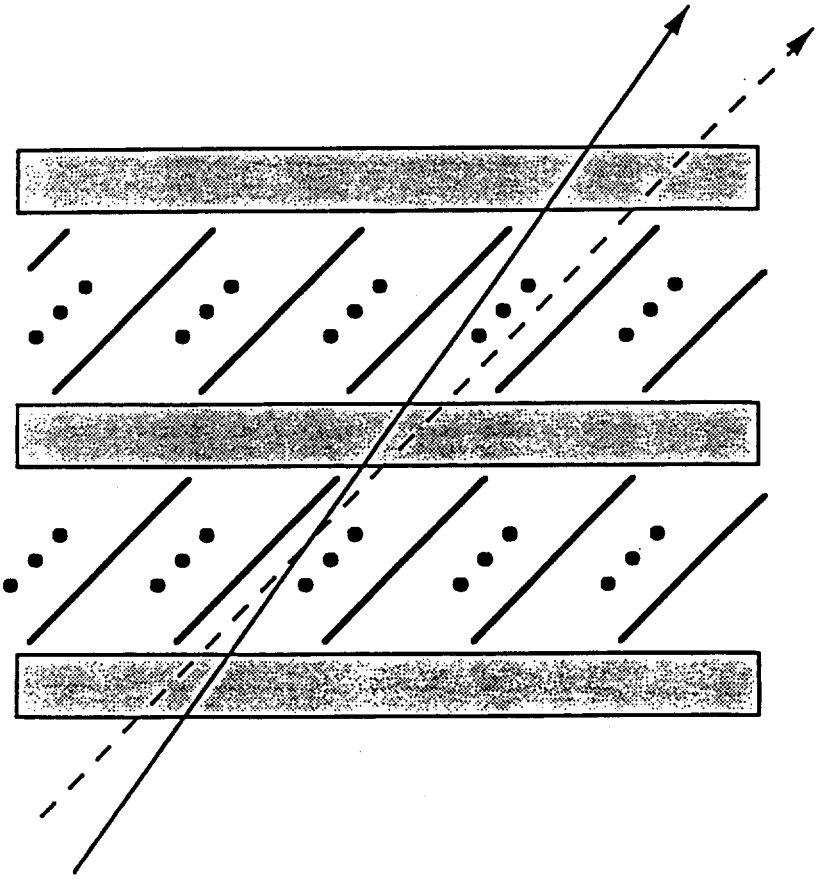

Fig. 3.2.7 An example of a track (solid arrow) which fakes high-p_t trigger. In the drawing, both track segments enter the left side relative to the wire plane in each cell. The track is misunderstood to be the dashed arrow.

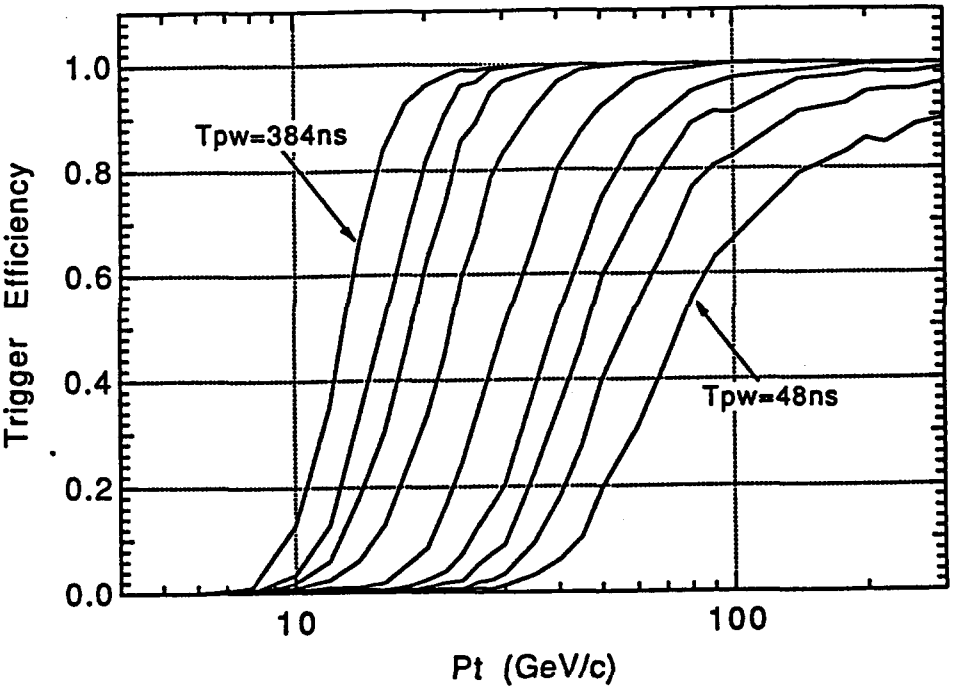

Fig. 3.2.8 Efficiency curves of the layer trigger versus the transverse momenta of muons in the barrel region for T_{PW} = 384, 272, 224, 176, 128, 96, 80, 64 and 48 ns, which correspond to p_t(thr) = 13, 16, 18.5, 22.7, 30, 39, 46.4, 57 and 75.4 GeV/c in this order. p_t(thr) is defined as the transverse momentum where the trigger efficiency becomes 50%.

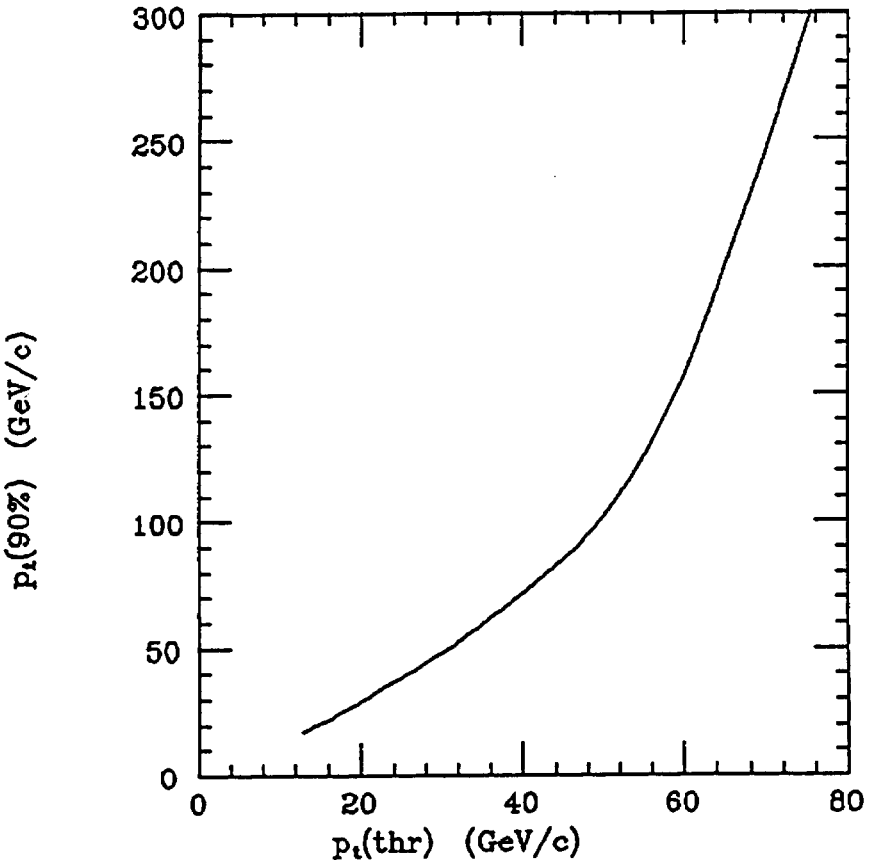

Fig. 3.2.9 Transverse momentum of the muon at which the trigger efficiency becomes 90 %, p_t(90%), as a function of p_t(thr).

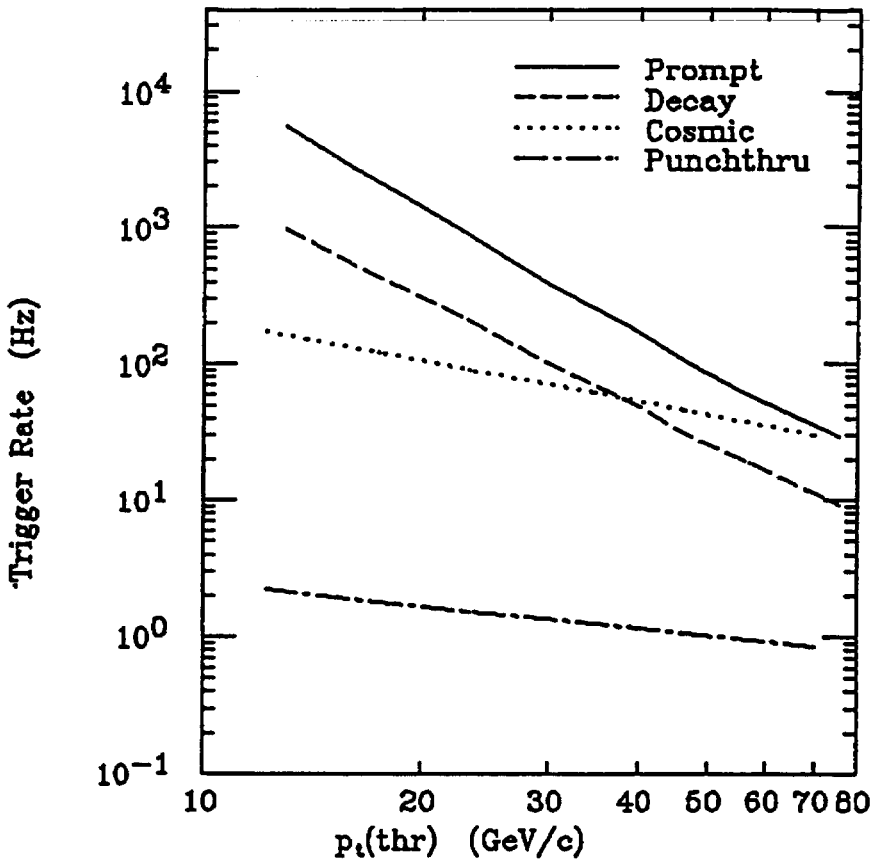

Fig. 3.2.10 Level-1 trigger rates integrated over the barrel and the intermediate regions as a function of p_t(thr). In the estimation for the punchthrough particles and the cosmic rays, a value $\Delta\phi_{cut} = 0.05$ rad for BW3(ϕ) is used.

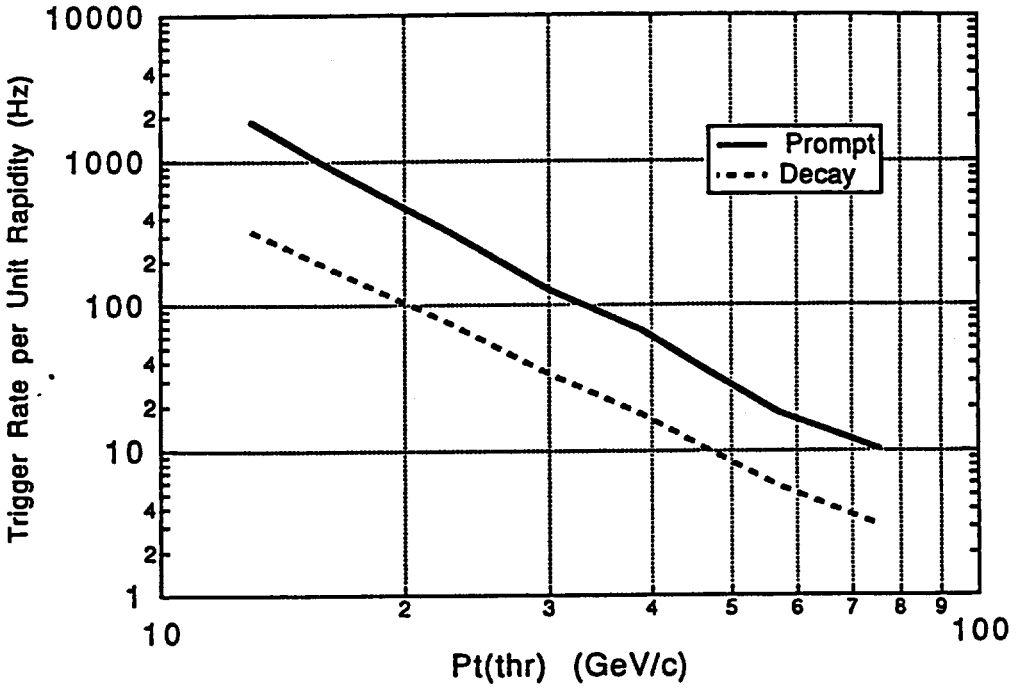

Fig. 3.2.11 Trigger rates in the barrel and intermediate regions as a function of p_t(thr). The vertical axis is the trigger rate per unit rapidity in Hz. The solid and dashed curves are the prompt and decay muon rates, respectively.

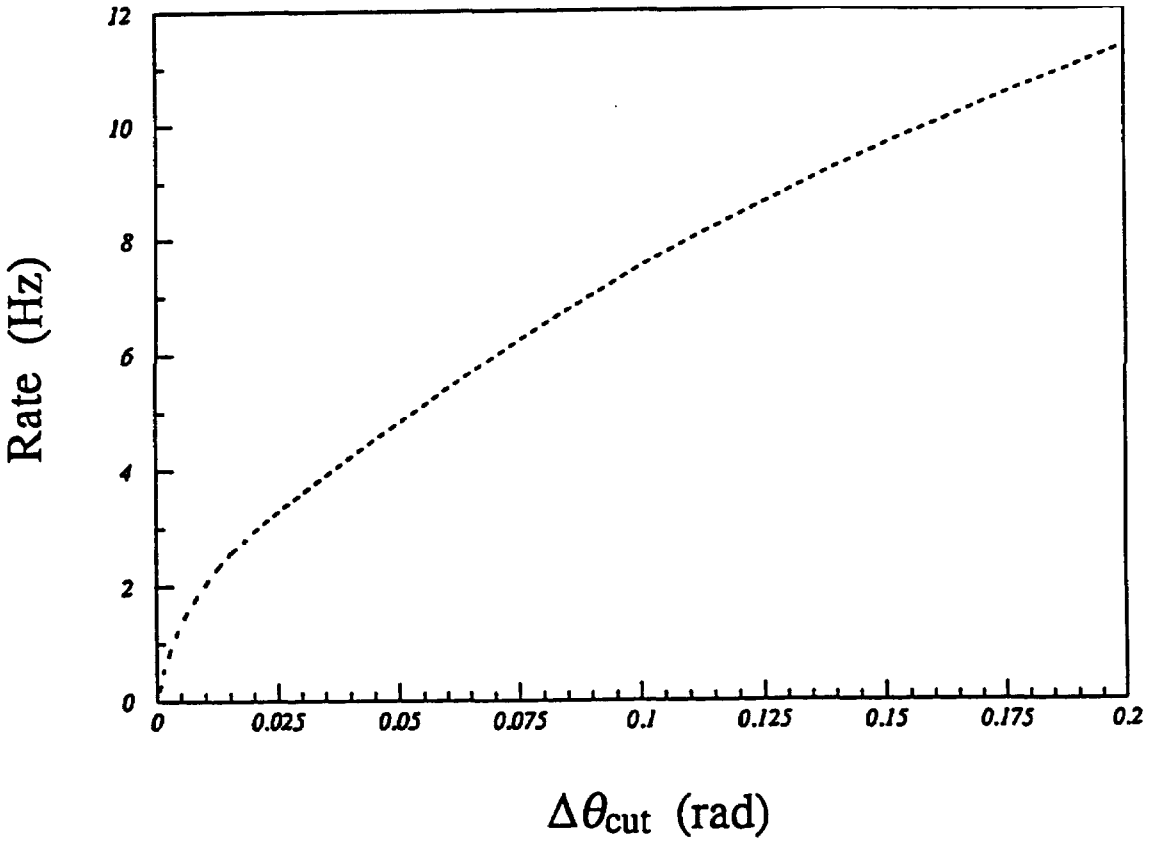

Fig. 3.2.12 Trigger rate integrated over BW2(θ) and IW2(θ) for punchthrough particles as a function of the maximum allowed projective angle, $\Delta\theta_{cut}$. The phi-cut is not imposed at this stage.

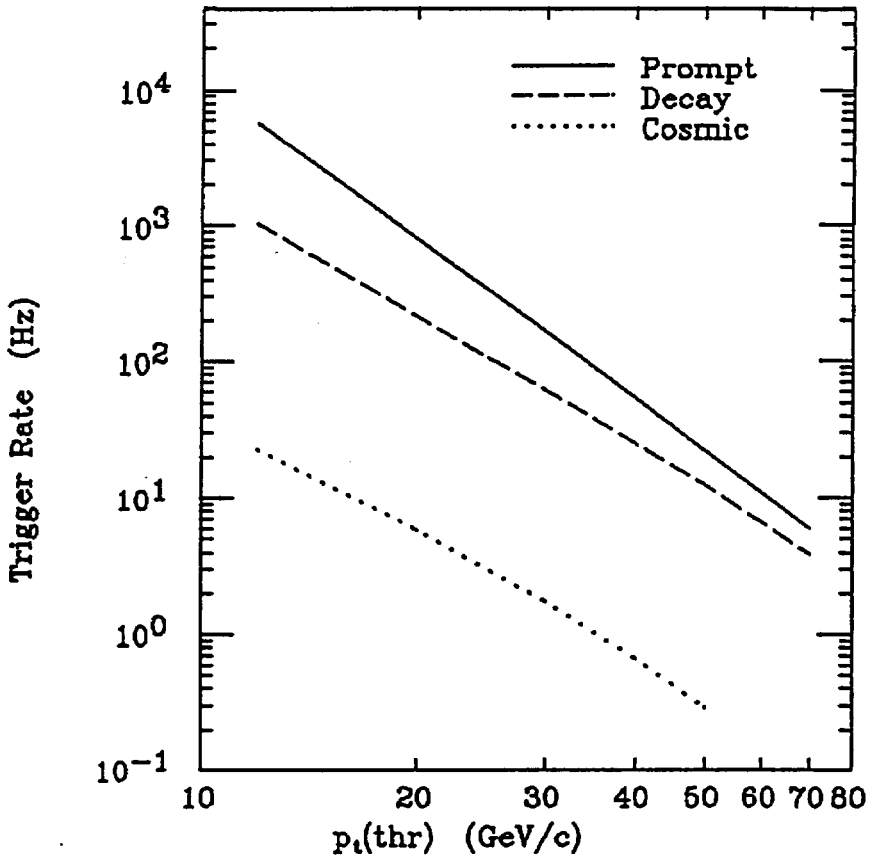

Fig. 3.2.13 Trigger rates integrated over the barrel and the intermediate regions in case the position information at all the θ-chambers is known. In the estimation for the punchthrough particles and the cosmic rays, a value $\Delta\phi_{cut}$ = 0.05 rad for BW3(ϕ) is used.

3.3 Beam test results and their implications to jet cell design

The muon collaboration of the SSC detector subsystem R&Ds has performed an extensive muon beam test using high energy muon beams at Fermilab. The test experiment is called T816. The details of the setup and some preliminary results are described in Appendix 3. The results have revealed extremely useful truth for any of future high energy muon detectors.

Among many interesting outcomes of T816, although they are very preliminary, the rates of events with the electromagnetic debris associated with penetrating muons are plotted in Fig. 3.3.1 as a function of the muon momentum. They increase with the incident muon-momentum from 15 % at 94 GeV/*c* to 23 % at 550 GeV/c in the chamber approximately 1 m downstream of the iron block with 1 inch aluminum at the upstream of the chamber. This arrangement well simulates the environment of the SDC muon chambers. The closed circles and closed boxes roughly correspond to the environment of BW2 and BW3, respectively.

The performance of the T816 jet-chambers was studied to estimate the expected behavior of jet-chambers. A typical event sample is shown in Fig. 3.3.2. The two-track separation of about 5mm has been achieved by the T816 jet-chamber as demonstrated in Fig. 3.3.3. Since two-track separation is mainly determined by the cell geometry and the chamber we propose has quite a similar geometry as the T816 chambers, one can expect similar two-track separation capability. We may get a better resolution by a better pattern recognition program. As shown in Fig. 3.3.4, even with the present program without final tuning, the efficiency of global-track-reconstruction in the downstream of the iron block is demonstrated to be better than 95 % in the muon-momentum range of 94 GeV/*c* to 550 GeV/*c*.

These samples of preliminary T816 results indicate that the probability of soft particle association is quite high at the exit of thick absorbers. Although the jet chamber and gas used in T816 was slightly different from

those proposed in this report, it can be said that, for detecting high energy muons, a set of jet type drift chambers can maintain high tracking efficiency while keeping the resolution of two track separation quite small. This is the existing proof that the type proposed has good promise for high quality performance.

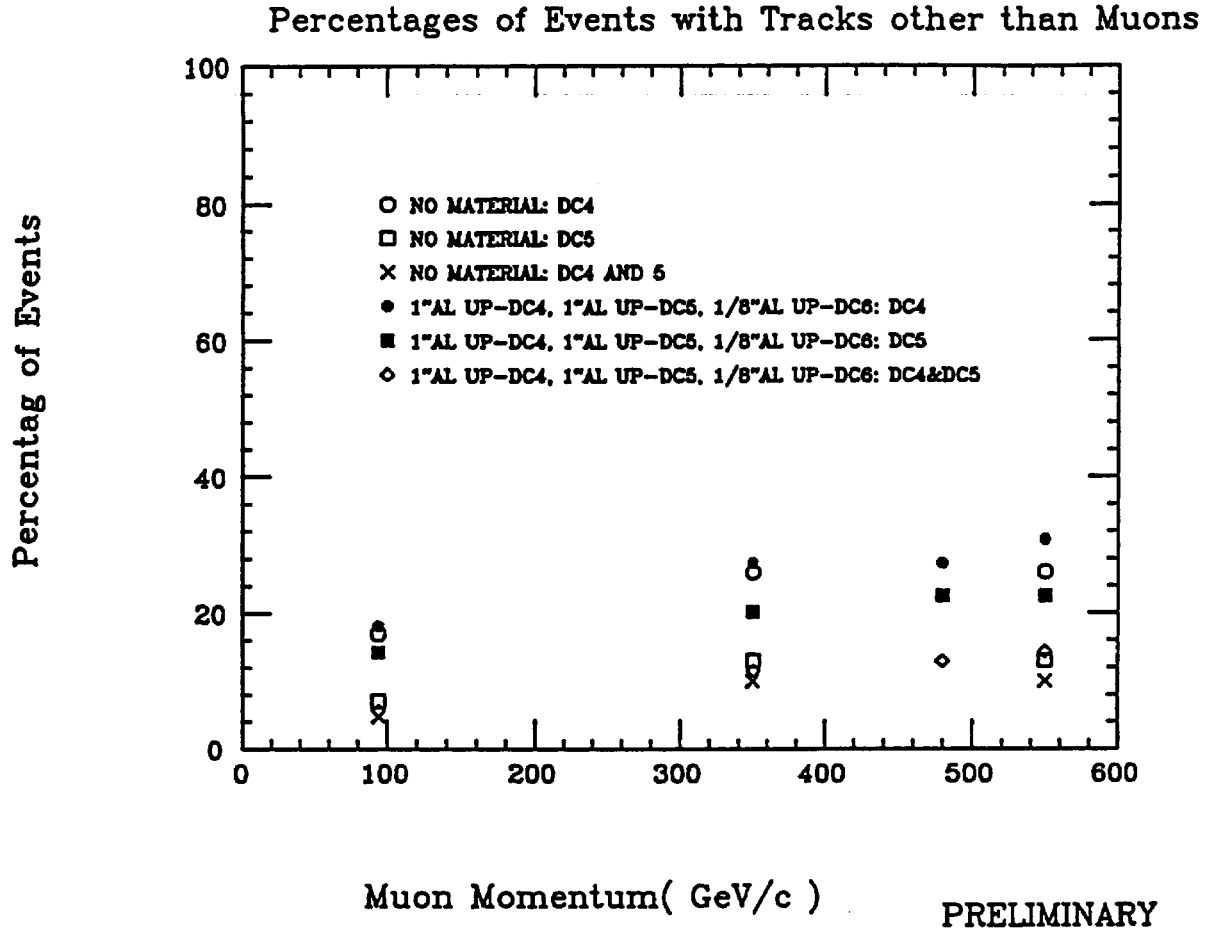

Fig. 3.3.1. The rate of events with extra local-tracks found in the downstream drift chambers to the events that have single tracks in DC2 and DC3 or one extra local-track in either DC2 or DC3. "DC4" indicates the events with extra local-tracks in DC4. "DC5" indicates the events with extra local-tracks in DC5. "DC4 and DC5" indicates the events with extra local-tracks in both DC4 and DC5.

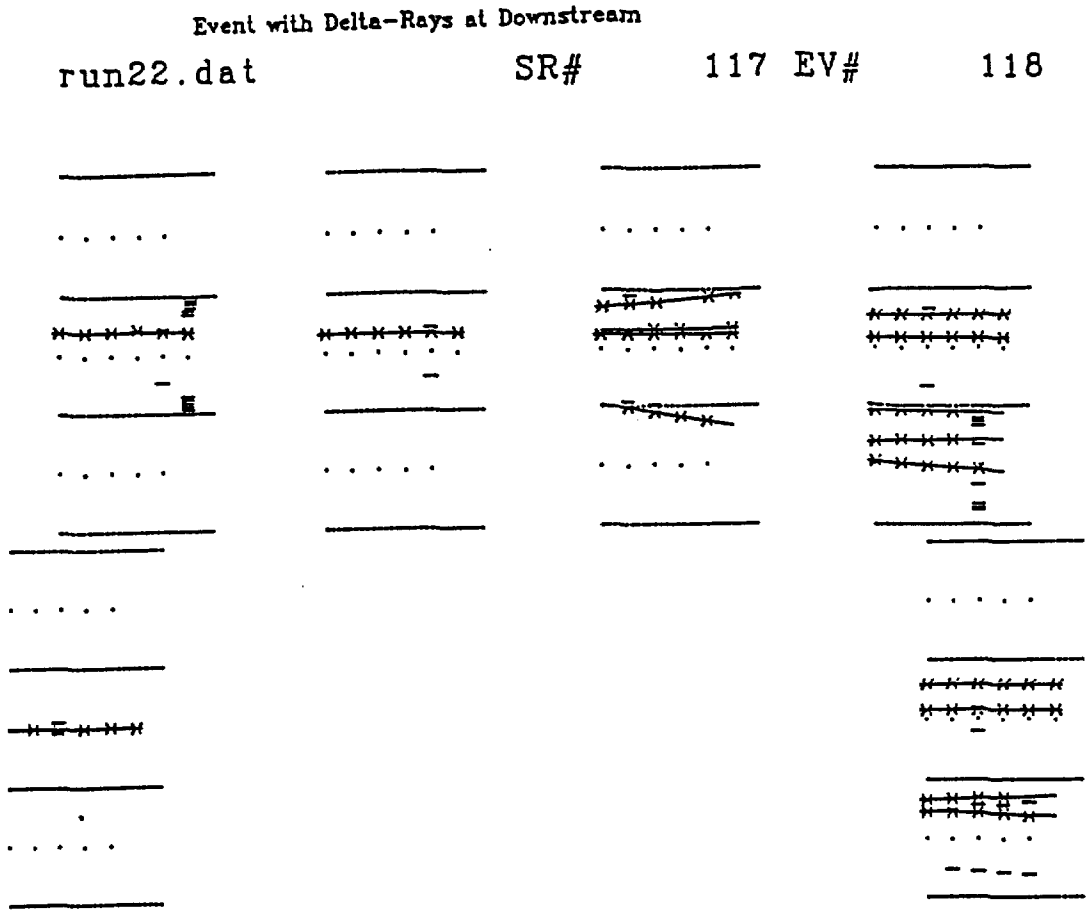

Fig. 3.3.2. A typical event. Scales of the display-windows are not proportional. Four chambers in the upper half are DC2, DC3, DC4 and DC5 from left to right. Two chambers in the lower half are DC1 and DC6 from left to right. In the vertical view, a muon entered the upper drift region of the middle cell of DC2, then it passed through DC3, DC4, DC5 and DC6. Right-left ghosts of the hits reconstructed as local-tracks were eliminated, but the ghosts of other hits were shown in this figure.

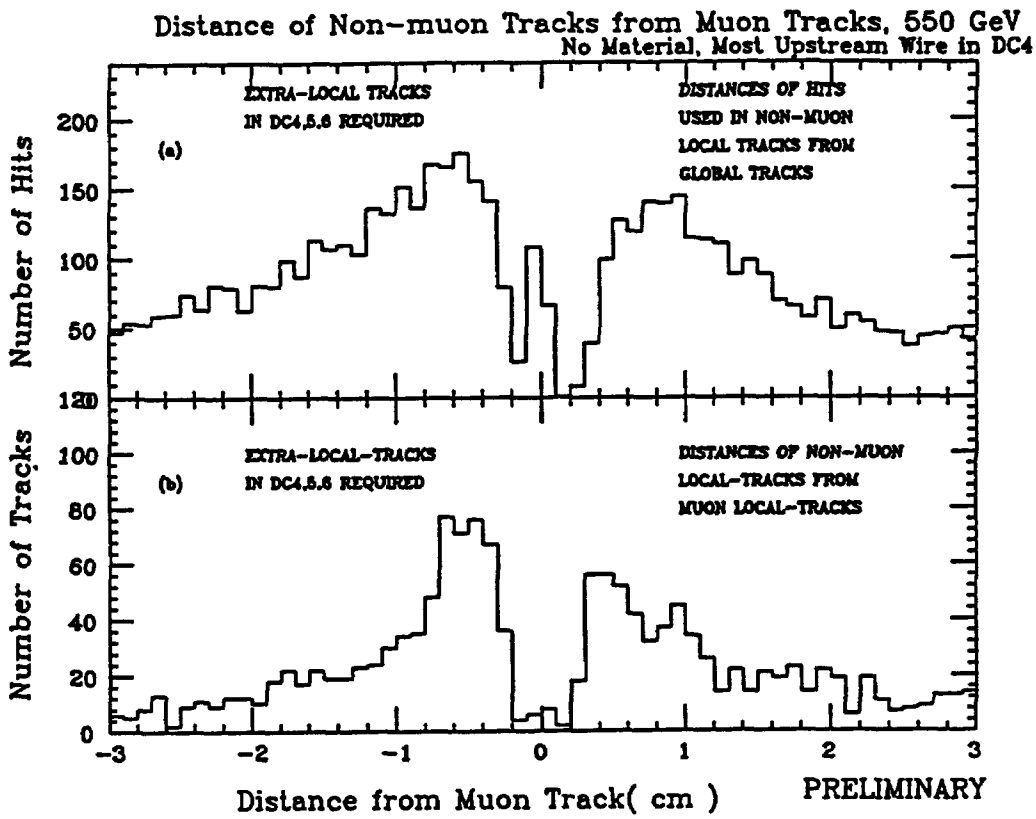

Fig. 3.3.3. (a) Distances of hits in the reconstructed delta-rays from the global muon-tracks. (b) Distances of local-tracks of reconstructed delta-rays from the global muon-tracks.

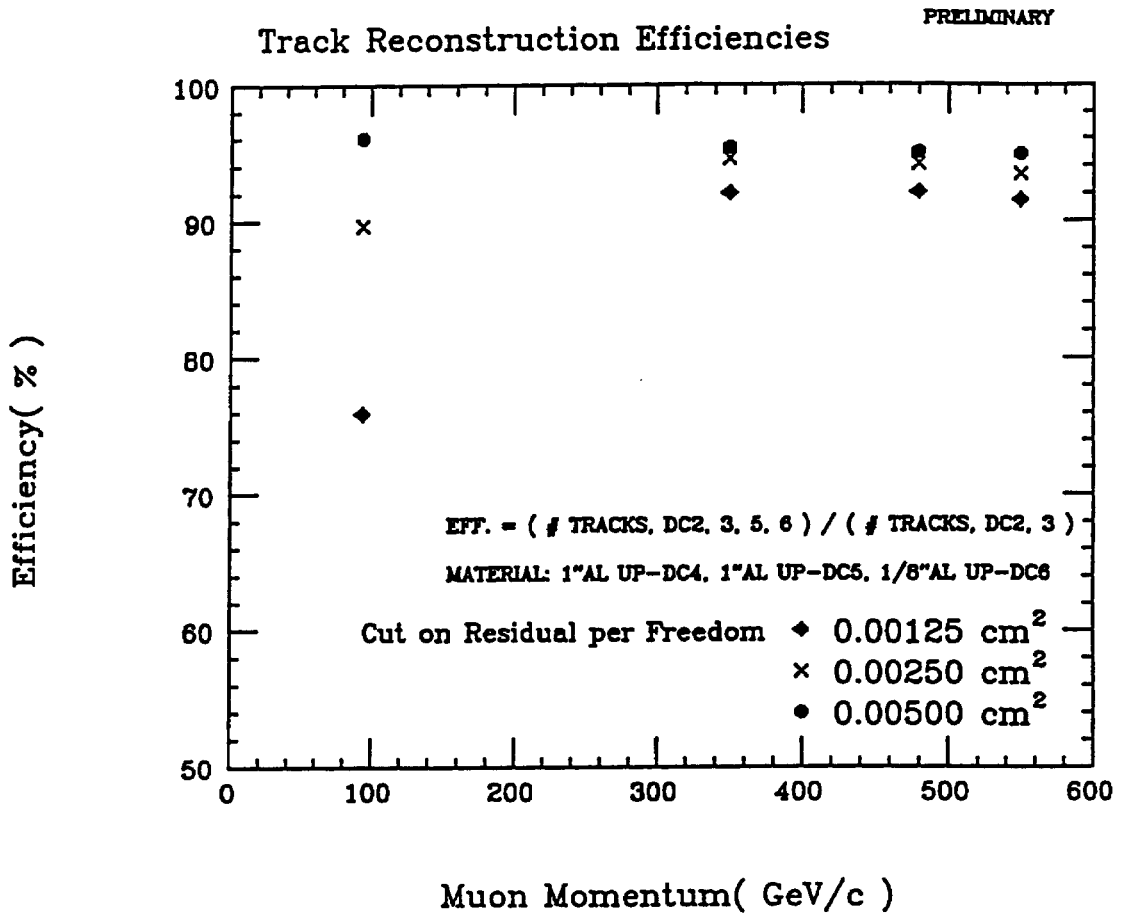

Fig. 3.3.4. Track-reconstruction efficiencies with respect to the incident muon-momentum for different cuts on the residual-squared per freedom in the global-track fits.

§4. Design Details

4.1 Cell design

The cell geometry and the parameters of electrodes have been described in section 2.1. In this section we describe in detail how those parameters have been determined, and present the intrinsic performance of the drift cell that we can expect. Further, we briefly discuss about the allowed tolerance of the mechanical structure and environmental conditions.

4.1.1 Gas choice

The choice of the drift gas is one of the most fundamental issues in the drift chamber design. We have chosen a mixture of Argon, CO_2 and Methane with a mixing ratio of 89:10:1, so-called HRS gas, as the first candidate. This mixture has good characteristics suitable for large drift chambers, and the stability in a long term operation has been proved by the experiences of many collider detectors, such as the central drift chambers of *HRS* at *PEP*, VENUS and AMY at TRISTAN, and the new main drift chamber of Mark II at PEP/SLC.

Nonflamability is the most serious requirement to the drift gas to be used for the SDC muon chamber, since the total gas volume is huge and since the detector is located underground. The mixture Ar/CO_2/Methane (89/10/1) is undoubtedly nonflammable.

The drift velocity of ionized electrons in a drift gas is known to scale as a function of the normalized electric field strength defined as

$$E_n = (\rho_0/\rho)E,$$

where ρ is the gas density and E is the field strength. The parameter ρ_0 is the gas density to which the result is normalized. The gas density is proportional to p/T, where p and T are the pressure and temperature of the gas, respectively. Therefore, the variation of the physical condition results in a variation of the normalized field strength in the form

$$\Delta E_n/E_n = \Delta T/T - \Delta p/p.$$

If we choose a linear drift gas, for which the drift velocity is proportional to E_n, a 1 % change of the pressure or the temperature results in a 1 % change of the drift time. This change corresponds to 400 μm of the measurement error for a 4 cm drift, which is not negligible compared to the required resolution. Since the SDC muon chamber system is enormously huge, we should consider that a pressure and temperature control to make them constant in space and time is practically impossible, and that the condition of the drift gas follows that of the environment. A saturation in the drift velocity is therefore desirable for the application to our design.

The measured drift velocity of the mixture Ar/CO_2/Methane (89/10/1) is pictured in Fig. 4.1.1. This mixture shows a saturation above the field strength of 800 V/cm. Although the saturation is not very good compared to Ar/Ethane (50/50), a well-known saturating gas, the influence of the change of the environmental condition can be substantially reduced. The ratio of the relative change of the drift velocity, $\Delta v/v$, to the relative change of the normalized field strength, $\Delta E_n/E_n$, is drawn in Fig. 4.1.1, as well. We can expect a reduction of more than a factor of 5 in a wide range of the field strength.

4.1.2 Parameters of the electrodes

The parameters of the electrodes, the thickness of wires and the voltages to be applied to, have been optimized so as to fit to the gas choice based on the jet cell structure. For an ideal jet chamber, the charge densities on the sense and potential wires and the cathode plane subject to the following relation:

$$\lambda_S + \lambda_P + 2w\sigma_C = 0,$$

where w is the width of each drift cell. The density on the sense wire, λ_S, is positive and the other two terms are negative by definition. The cathode charge density is determined by the nominal field strength E_D (>0) required, in the form $\sigma_C = -\varepsilon_0 E_D$. Thus the sense-wire charge can be written as

$$\lambda_S/2\pi\varepsilon_0 = (1 + R_P)wE_D/\pi.$$

The parameter R_P (>0) represents the relative contribution of the potential-wire charge and determines the focusing property of field lines onto the sense wire. A finite amount of negative charge on the potential wires, *i.e.* a positive R_P, reduces the electrostatic instability of the sense wires, as well.

We have chosen the nominal field strength to be 900 V/cm, around which the drift gas Ar/CO_2/Methane (89/10/1) shows sufficient saturation of the drift velocity as shown in Fig. 4.1.1. Since w = 1 cm in our cell design, this value leads us to a constraint that $\lambda_S/2\pi\varepsilon_0 > 286$ V. If we choose the R_P value to be around 0.3 in order to obtain a sufficient focusing property, the sense-wire charge $\lambda_S/2\pi\varepsilon_0$ must be around 370 V. According to such an estimate and to gas-gain measurements using tube chambers (see Appendix 1), we have chosen the sense-wire diameter to be 70 μm and a nominal value of $\lambda_S/2\pi\varepsilon_0$ to be 380 V. We expect a gas gain of about 10^5 under these conditions.

Now the charge densities on all electrodes have been determined, the voltages to be applied can be obtained by using an electrostatic equation of a conductor system if we specify the potential-wire diameter. The thinner the potential wires are, the better they are from a mechanical point of view because the total wire tension to be supported by the chamber structure may become smaller. However, there is an empirical constraint that the surface electric field should be smaller than 20 kV/cm in order to eliminate an aging effect to a reasonable level. Consequently, we have decided to use 140 μm-diameter wires. The surface field is about 12 kV/cm for this choice.

The voltages of the sense wires and the cathode plates, thus determined, are 2.07 kV and –3.04 kV, respectively, if we fix the potential wires to the ground voltage. This choice of the potential-wire voltage, in general, makes the absolute values of the high voltages to be used relatively smaller and allows us to make a cross talk between sense wires smaller.

The voltage to be applied to the guard wires has been determined by using a field calculation based on the actual cell geometry, so that the actual cell simulates an ideal jet-cell as much as possible. Although a good drift field uniformity should be the final goal of this optimization, it is hard to find a well-defined measure of a field uniformity. In spite of this, we adopted a balance of the charge densities between 3 sense wires in a cell as a measure. We thought that the field uniformity would be virtually realized if the uniformity between the sense wires was guaranteed.

The optimization was done for the simplest case, where the sense plane and the cathode planes are orthogonal to the ground planes. This case corresponds to the cells in θ-chambers located at θ = 90°. The charge densities of the 3 sense wires calculated are plotted in Fig. 4.1.2 as a funotion of the guard-wire voltage, V_G, where we tentatively defined the guard-wire diameter to be 200 μm. We can see that the 3 wires has an equal charge density for V_G = 2.33 kV. We apply this V_G value to all cells and examine the field quality in the following section. Also we can see that the sense-wire charge density is slightly larger than the design value, $\lambda_S/2\pi\varepsilon_0$ = 380 V, even at the optimum point. This difference corresponds to a small distortion of the electric field, which will be shown in the next section.

4.1.3 Expected performance

The parameters of the electrodes are summarized in Table 2.1. The field quality was examined using these parameter values. In the following, the results are shown for two extreme cases. One of them corresponds to a cell of θ-chambers in the barrel region at θ = 90°, for which the sense plane and the cathode planes are orthogonal to the ground planes; *i.e.* the tilting angle is equal to 0 (90° cell). The other is a cell having the tilting angle of 60°, *i.e.* θ = 30°, which corresponds to a cell of θ-chambers to be located near the edge of the barrel region (30° cell).

In the following calculations, planar electrodes, the cathode planes and the ground planes, are simulated with equally spaced wires having a circumference equal to the spacing. The relation between the charge density and the voltage, *i.e.* capacitance, can be accurately reproduced by using this

technique, if the distances of other electrodes to the plane are sufficiently larger than the spacing of the simulating wires. Thus the field behavior calculated is reliable if the region we examine is sufficiently far away from the plane. In other words, the behaviors near the planes are not realistic. The reliability of our calculation has been proved by the measurements using test chambers (Appendix 1).

Fig. 4.1.3 shows the equi-potential contours for the above two cases. Resultant drift paths of electrons are drawn in Figs. 4.1.4a and 4.1.4b. Ticks drawn along the paths represent equal drift-time contours taken every 100 nsec, where we used the drift velocity of the gas mixture of Ar/CO_2/Methane (89/10/1) shown in Fig. 4.1.1. A distortion of the electric field is visible even in the 90° cell; it is appreciable in the 30° cell. However, the effect is not serious in terms of the drift time to be measured.

Fig. 4.1.5 shows the time-to-distance relation simulated for tracks passing parallel to the sense plane. Note that the results for 3 sense wires in a cell is drawn in one picture. The most important quality required to the individual cell performance is the linearity of the drift time with respect to the track distance, because we propose a trigger scheme based on a mean-time measurement between a pair of half-cell staggered cells. Deviations of the expected drift time from a linear relation are shown in Fig. 4.1.6. The reference linear relation was determined by averaging the simulated results for the middle sense wire of the 90° cell within the drift distance range between 0.5 cm and 3.5 cm, which corresponds to a constant drift velocity of 4.96 cm/μsec.

As we can see in the figure, the deviations from the linear relation are always smaller than ± 2 nsec in the 90° cell except for a region very close to the sense wire, within a few mm. A negative value of Δt is a result of the negative correlation between the drift velocity and the field strength around the field strength of 1 kV/cm (see Fig. 4.1.1). A 2 nsec-deviation is fairly smaller than the resolution that can be expected from each measurement, ~ 5 nsec. Besides, in a real situation, a fluctuation of the ionization and gas amplification tends to shift the Δt values to the positive side, on the average,

in the region within a few mm from the sense wire. Namely the 90° cell can be thought as an ideal jet cell practically.

The deviation from the linear relation is at most 5 nsec for the 30° cell. Such a distortion is mainly due to the asymmetric arrangement of the cathode planes with respect to the sense plane. Though this amount of deviation is not negligible, it is still comparable with the measurement error expected. In the design of a trigger scheme, we have to take into consideration other uncertainties, such as a variation of the timing response of amplifiers, discriminators, cables *etc.* Such uncertainties would amount to nearly 10 nsec in total. Therefore, the distortion we observed in the above calculation will not be a serious problem in the trigger design. Besides, such a distortion can not be a problem in the final performance of the chamber since it can be corrected for in the course of offline analyses.

4.1.4 Wire materials and tension

As a starting point, we consider only conventional materials for the wires; Tungsten-Rhenium (3%) for the sense wires and Copper-Beryllium (2%) for the potential and guard wires. We pursue other materials if a serious problem arises or an obviously better choice is suggested. Our present choice of the materials and the tension to be applied is summarized in Table 2.1.

The maximum gravitational sag of wires can be approximated by the formula:

$$y_{max} = \frac{\sigma L^2}{8T},$$

where σ is the line density of the wire, L is the total length and T is the tension applied. Since we plan to add at least one intermediate wire support for long chambers, the span between the supporting points of wires is always 5 m or shorter. A tension of 400 g is about 1/2 of the tensile strength of 70 μm^{ϕ}-Tungsten wires and results in a maximum sag of approximately 600 μm for L = 5 m.

The tensions of the potential and guard wires were determined so that they give a gravitational sag equal to that of the sense wires. The tensions determined, 690 g for the potential wires and 1.4 kg for the guard wires, correspond to about 70 % of the tensile strength.

Electrostatic sag is not a problem for the sense and potential wires, since they are located at virtually balanced positions and the spacing is not very small. On the other hand, it may be a problem for the guard wires because they are placed at obviously unbalanced positions. However the tension we have chosen eliminates the electrostatic sag to less than 300 μm even for L = 5 m.

Electrostatic stability of wires may be a serious problem of large-size chambers. The instability can be parametrized as

$$\xi = \frac{dF/dx}{T}\left(\frac{L}{\pi}\right)^2$$

according to a first order approximation. The factor dF/dx represents the gradient of the force at the wire position, induced by the charges of the other electrodes. A wire has a non-trivial oscillation solution if ξ is 1 or larger. However, ξ should be fairly smaller than 1 since higher orders and non-linear effects, such as a change of the charge density caused by a wire displacement, are neglected here. In our case the parameter ξ is always less than 0.1 for all wires even for the longest wire span of 5 m.

Possible tension ambiguities due to a temperature change have been evaluated by comparing mechanical properties of the wires and chamber frame materials. The relative change of the tension can be approximated by

$$\frac{\Delta T}{T} = \frac{\Delta l_t(\text{frame}) - \Delta l_t(\text{wire})}{\Delta l_0},$$

where Δl_t denotes the expansion due to a temperature change, and Δl_0 is the expansion of the wire at a nominal tension. Δl_t is the product of the

coefficient of thermal expansion, the total length and the amount of the temperature change:

$$\Delta l_t = \varepsilon_t L \, \Delta t,$$

while Δl_0 can be written as

$$\Delta l_0 = \frac{TL}{ES},$$

where E is the modulus of elasticity of the wire material, and S is the cross section of the wire. Thus the relative tension change can be expressed as

$$\frac{\Delta T}{T} = \alpha_t \, \Delta t,$$

where

$$\alpha_t = \frac{[\, \varepsilon_t(\text{frame}) - \varepsilon_t(\text{wire}) \,]ES}{T}.$$

We assume that the frame is made of aluminum in the following estimation. The parameters of the materials are as follows:

material	ε_t (degC^{-1})	E (Pa)
Al	23×10^{-6}	7.1×10^{10}
W	4.5×10^{-6}	36×10^{10}
CuBe	18×10^{-6}	13×10^{10}.

As a result, the coefficient α_t is only 0.7 %/degC for the sense wires and 0.2 %/degC for the potential and guard wires. Even if a temperature change of 10 degC arises, these numbers correspond to only 40 μm and 10 μm changes of the maximum gravitational sag, respectively, even for the longest wire span of 5 m. Hence we can conclude that we may ignore the change of wire tension due to a possible variation of temperature.

4.1.5 Tolerances

A variation or a change of the physical conditions of the drift gas, pressure and temperature, deteriorates the measurement through resultant changes of the drift velocity and gas gain. As described in section 4.1.1, the drift velocity change is suppressed by more than a factor of 5 for the gas mixture

we have chosen. Even a ±2% change of the condition or a ±20 mbar change of the pressure or a ±6°C change of the temperature, results in a systematic measurement error of less than 160 μm for the maximum drift of 4 cm. This amount of change is tolerable in order to achieve an average resolution of 250 μm/superlayer.

As described in Appendix 1, the gas-gain (G) change to be caused by a change of the sense-wire charge (λ_S) and a change of the gas density (ρ) can be expressed as

$$\ln(1 + \Delta G/G) = \frac{\Delta\lambda_S/2\pi\varepsilon_0}{20.2\ \mathrm{V}} - 8.2\frac{\Delta\rho}{\rho},$$

for our choice of the sense-wire diameter and the gas mixture. Therefore, the above 2 % change of the condition results in a gas-gain change of approximately 16 %. Since usually the rise time of the signals is about 10 nsec and the signals will be discriminated at less than 1/10 of the typical pulse height, a change of the pulse height of about 20 % will correspond to only a 1 or 2 nsec shift of the drift time measurement; a 50 or 100 μm overall shift in the position measurement. Namely a 2 % change of the environmental condition is tolerable even concerning the gas gain.

We have evaluated the influence of mechanical errors for various cases, by including a reasonable amount of errors in the field calculation and the drift simulation. The most significant effect has been observed for the cathode plate displacement. Fig. 4.1.7 shows the results on the drift time change corresponding to a ±1 mm displacement of the right-side cathode perpendicular to the plane; *i.e.* the distance to the sense plane was varied. The change is always less than 3 nsec for this amount of displacement and tolerable compared to the expected resolution. In other words, the cathode planes have to be placed with an accuracy better than 1 mm. The gas-gain change due to this displacement is less than 10 % and is not significant.

On the other hand, an order of 1 mm displacement of the cathode inside the plane does not induce a significant deviation; the change is less than 1 nsec. Furthermore, the effect of a ±2 mm displacement of one of the ground

planes was also found to be smaller than 1 nsec in terms of the drift-time change.

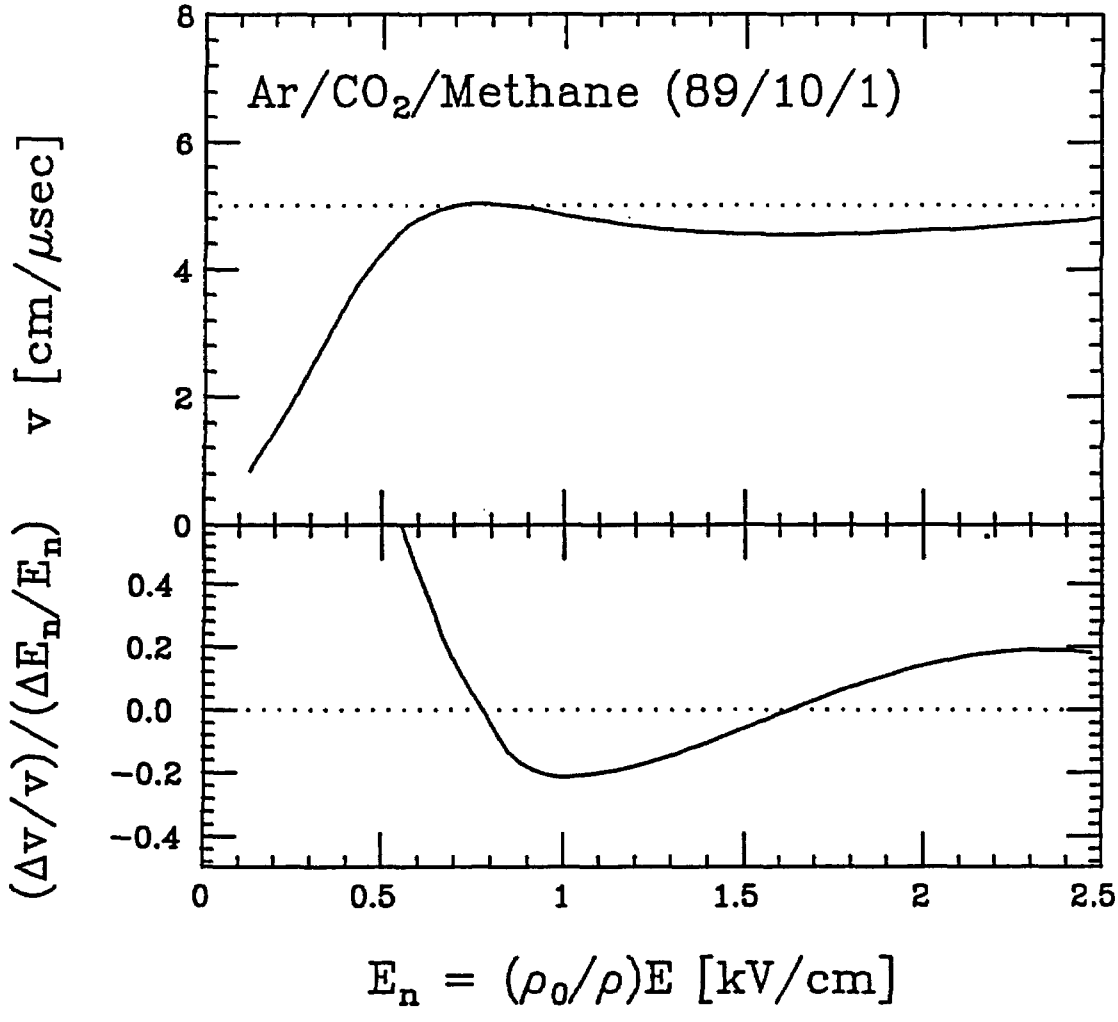

Fig. 4.1.1. The drift velocity of the gas mixture Ar/CO_2/Methane (89/10/1) measured by the VENUS-CDC group. Also shown is the ratio of the fractional change of the velocity ($\Delta v/v$) to the fractional change of the normalized electric field ($\Delta E_n/E_n$).

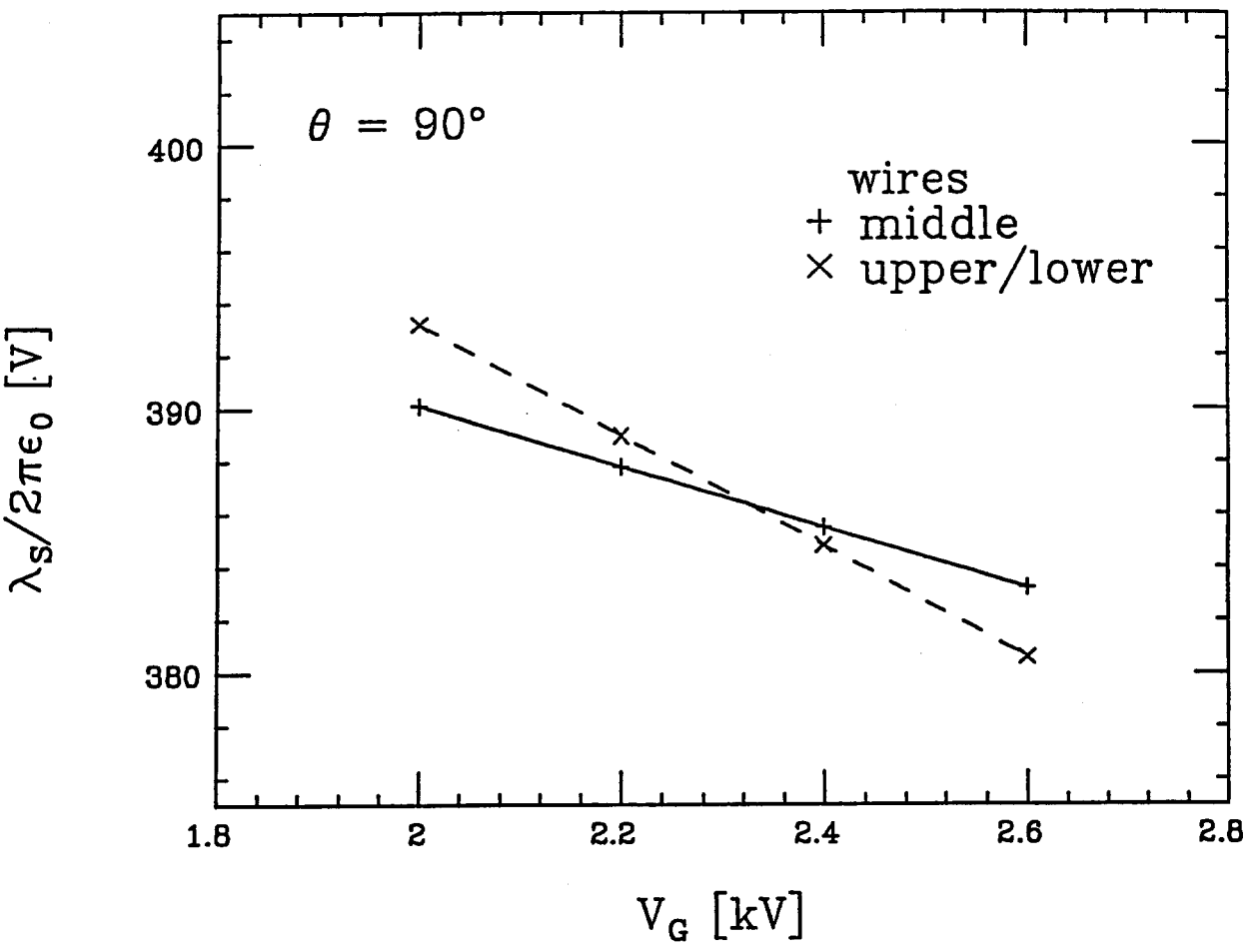

Fig. 4.1.2. The guard-wire voltage dependence of the charge on the sense wires in the 90° cell, obtained with a field calculation. The results for the middle wire is shown with a solid line and that for the outer wires with a dashed line.

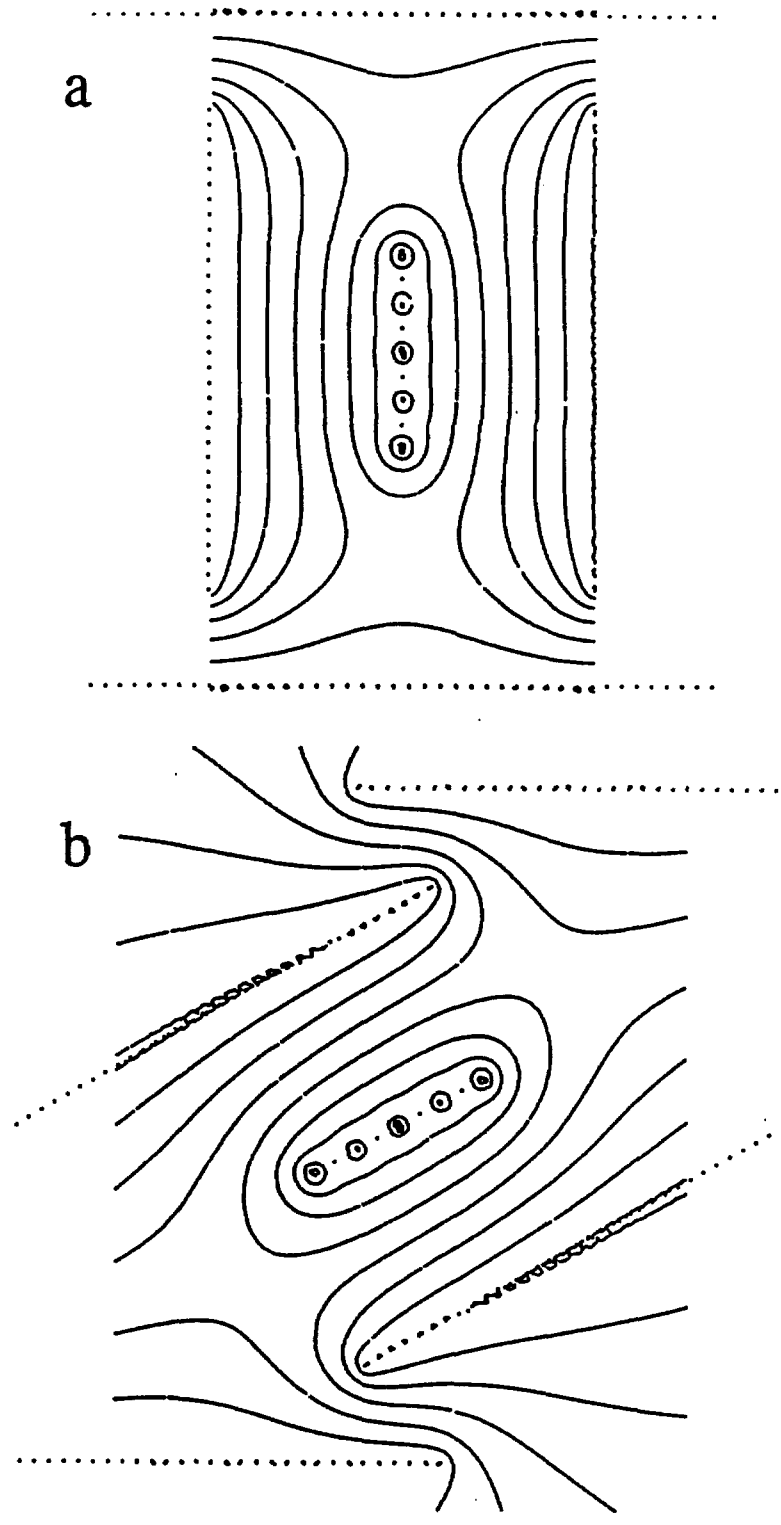

Fig. 4.1.3. The equi-potential contours for the 90° cell (a) and for the 30° cell (b).

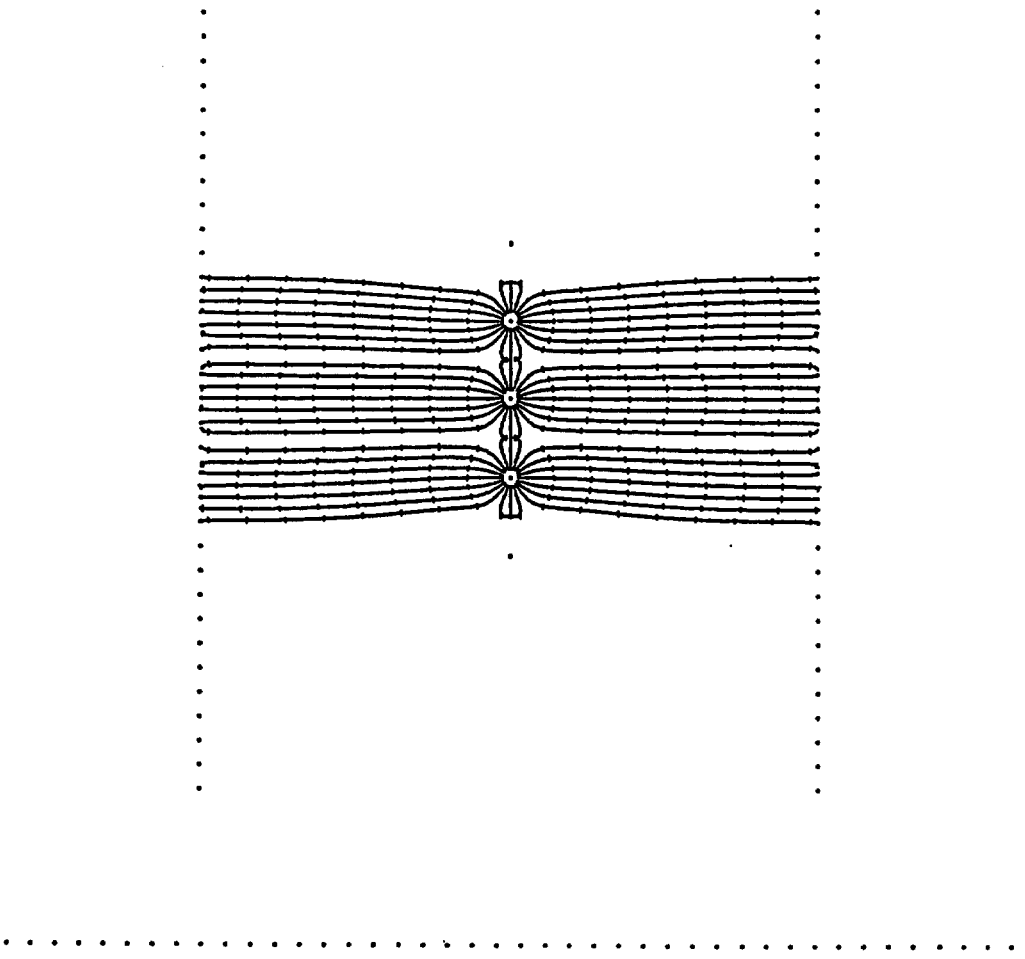

Fig. 4.1.4a. The drift paths of electrons for the 90° cell obtained by using a field calculation and a drift simulation based on the measured drift velocity shown in Fig. 4.1.1. The ticks drawn along the lines show the equal drift time contours taken every 100 nsec.

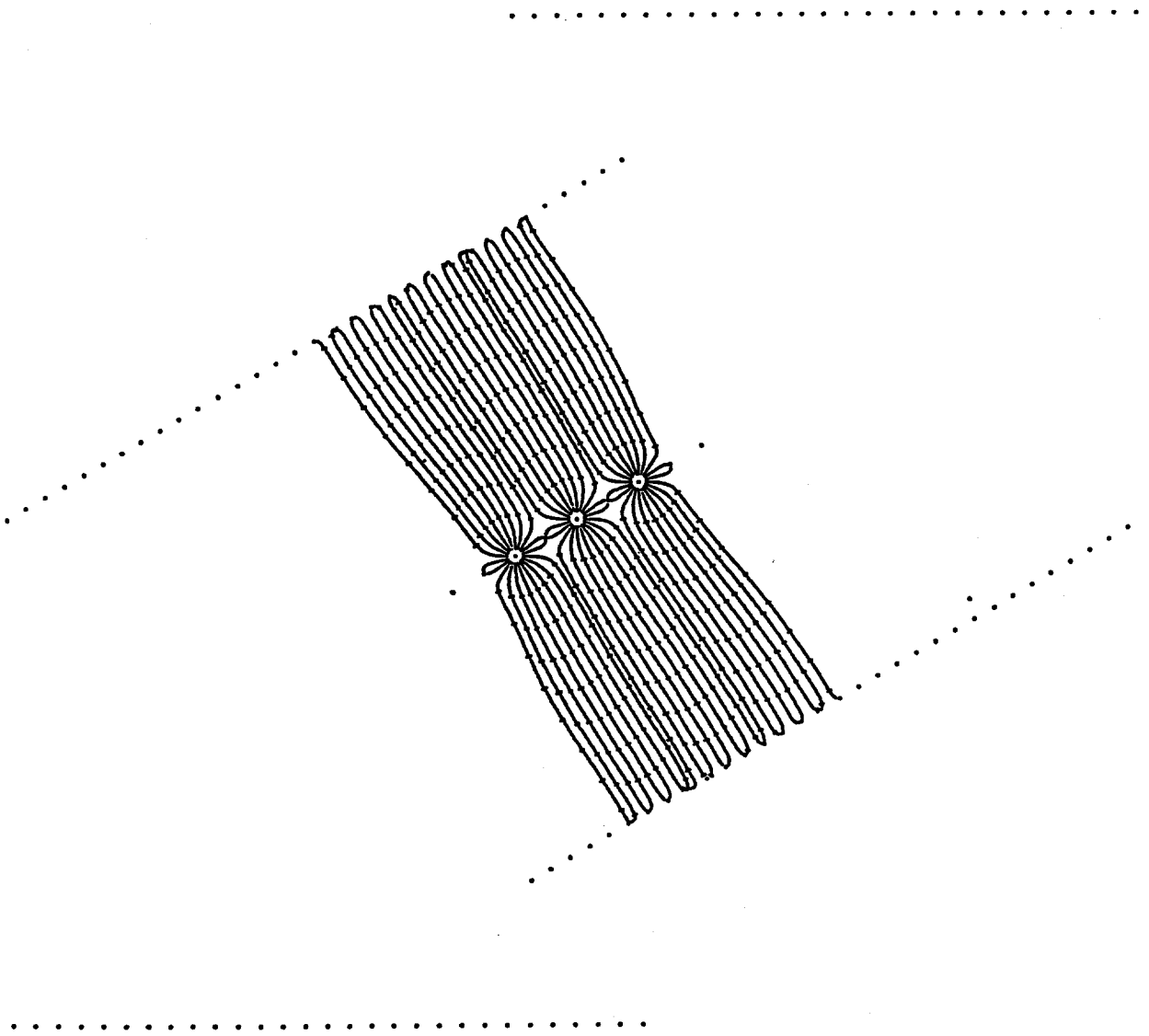

Fig. 4.1.4b. The same figure for the 30° cell.

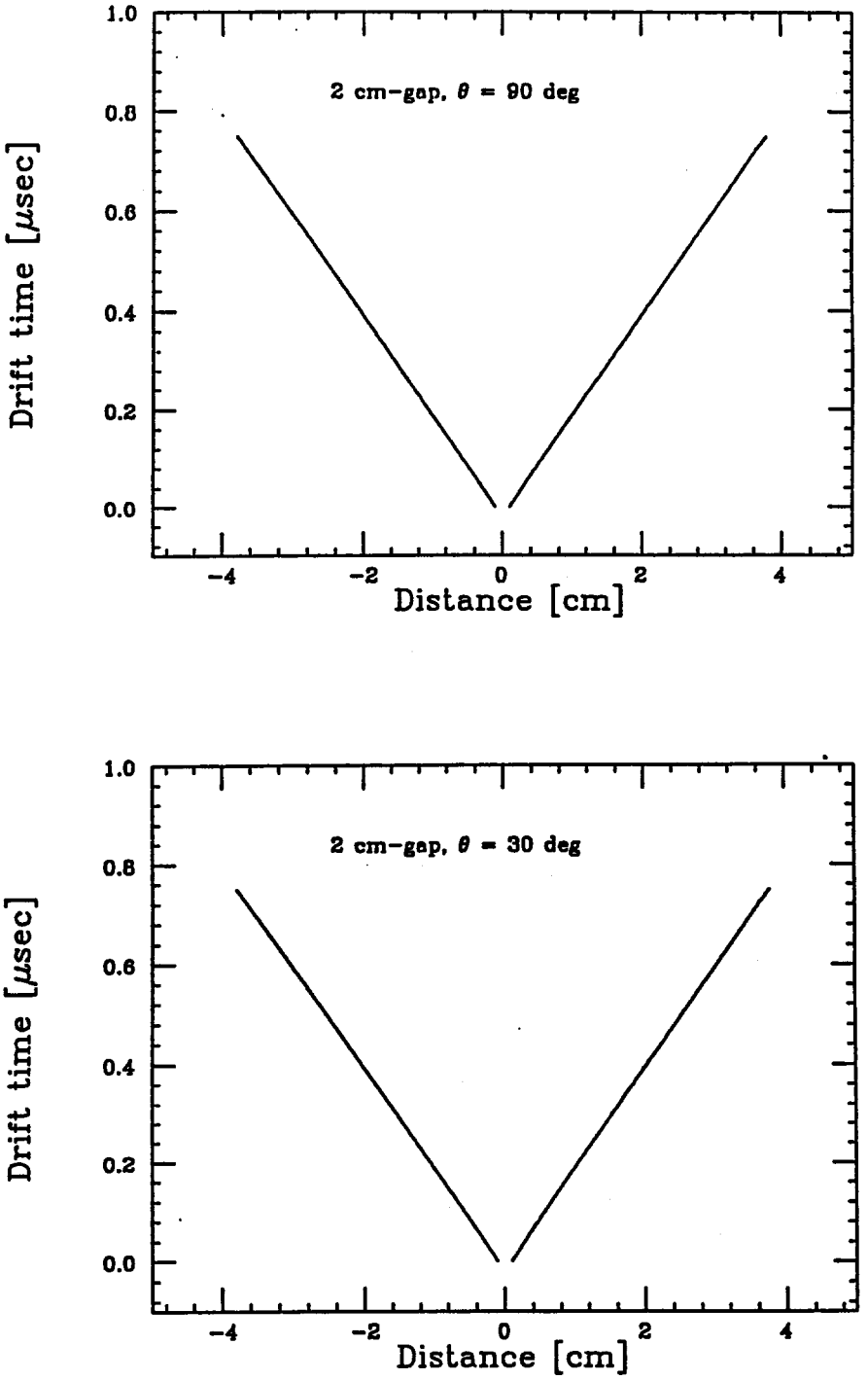

Fig. 4.1.5. The time-to-distance relations obtained as the results of the drift simulation. Results for 3 sense wires in a cell are drawn in each figure.

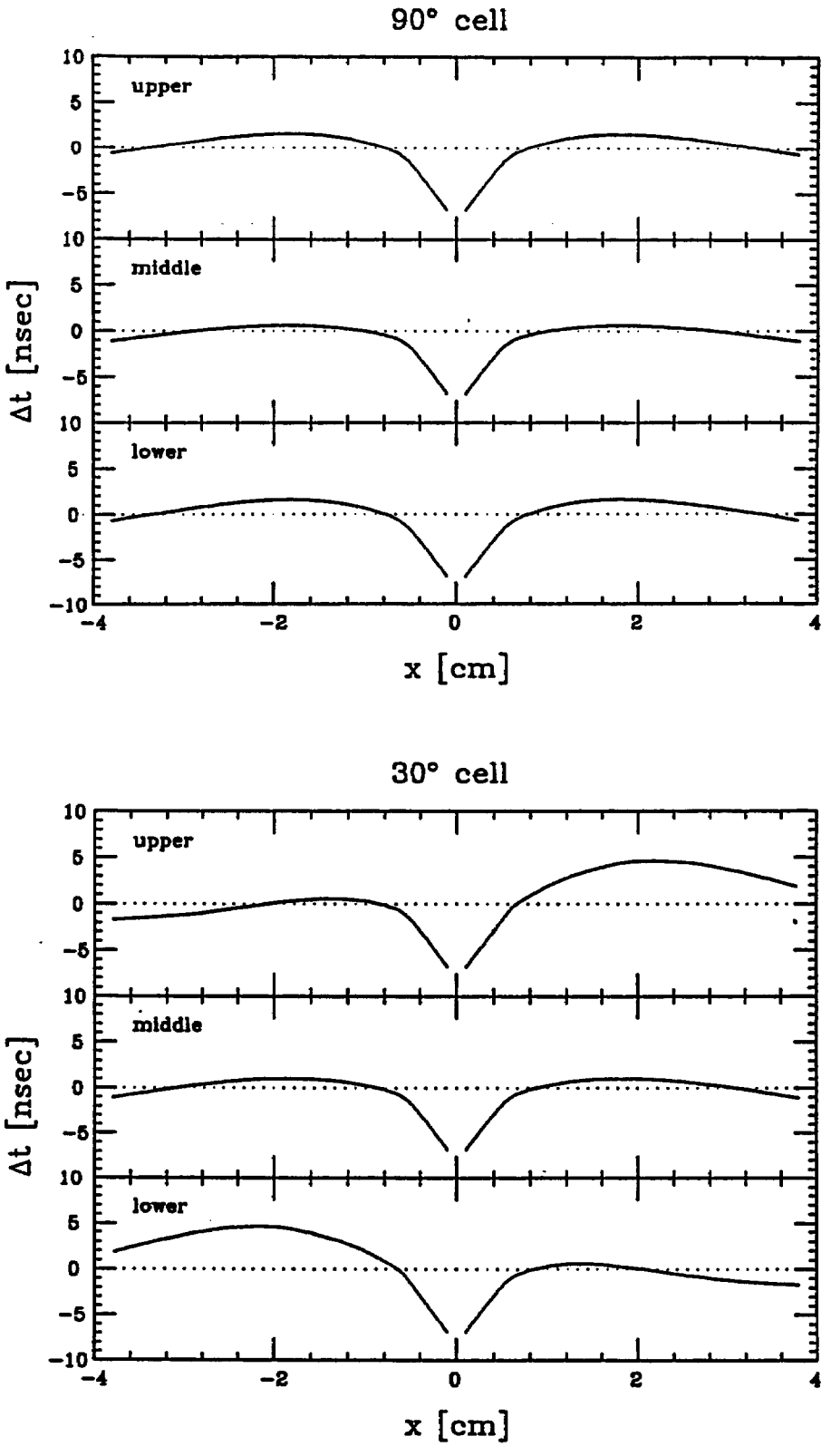

Fig. 4.1.6. The deviations of the simulated drift time from a linear relation. The reference linear relation was defined by averaging the simulated drift time for the middle sense wire in the 90° cell within the distance range between 0.5 and 3.5 cm.

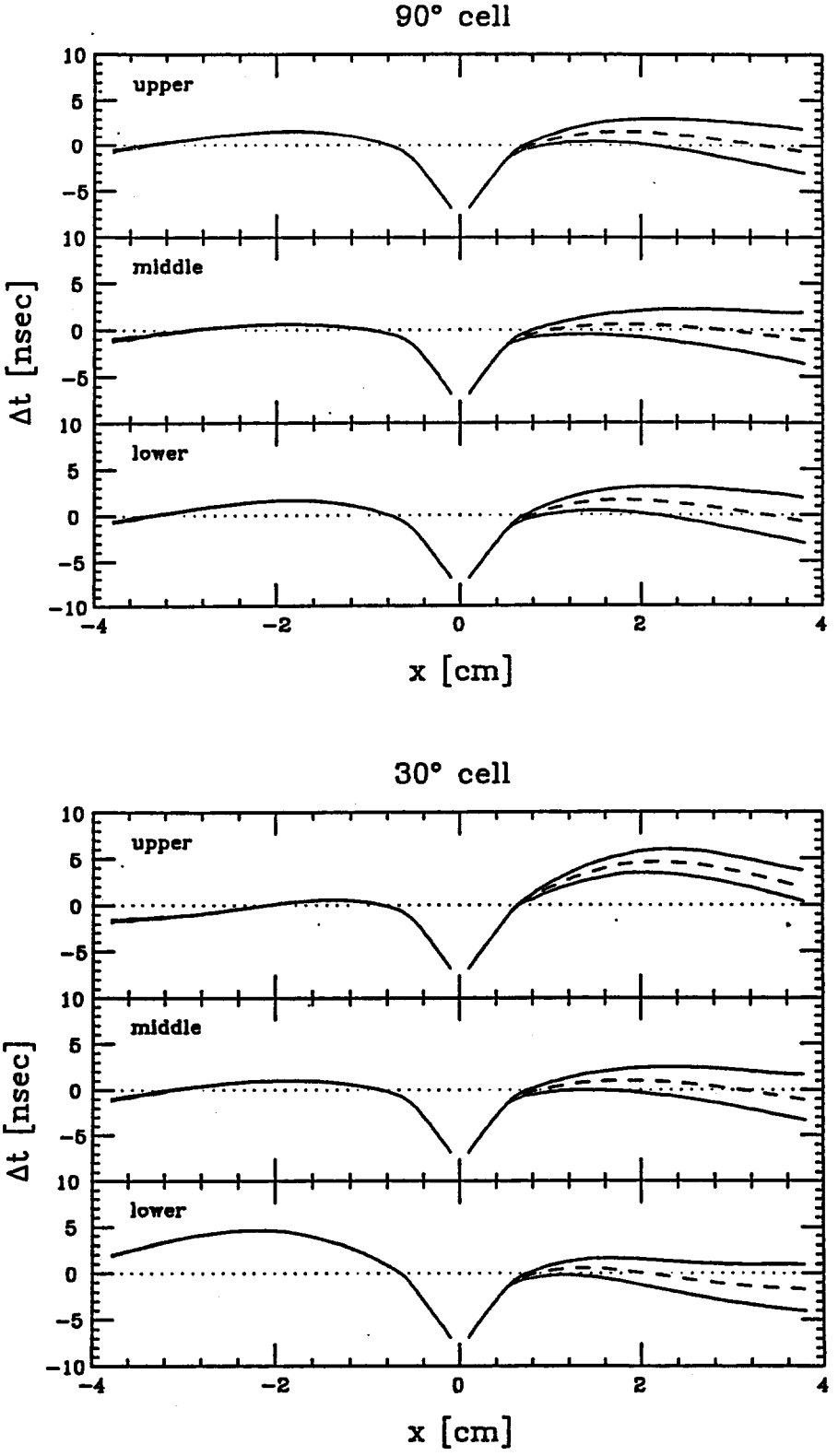

Fig. 4.1.7. The effect of a cathode-plane displacement. The distance between the sense plane and the right-side cathode plane was moved by ±1 mm. The dashed lines show the results for the ideal case having been shown in Fig. 4.1.6.

4.2 Chamber design

4.2.1 Module size and module boundary

The SDC muon system is indeed a large system. In fact, as shown in Fig.2.5, three superlayers in the barrel system have to cover the muon detection area of 4,700 m^2 in total. In order to cover this huge area efficiently and to satisfy the stringent requirements, particularly that for the chamber alignment as precise as about 100 μm, it is natural to make the size of a chamber module reasonably large. Then, a relatively small number of units is required to be mounted on the toroid with high precision alignment. Besides, as a module becomes larger, the module boundary which often causes a dead region becomes smaller. A larger size module also contributes to minimizing a number of readout channels, though it requires longer wires to be implemented. Thus, the size of the module is preferred to be maximum within the limits regarding fabrication, handling, and transportation.

In order to optimize the module width, the effect of the module boundary was carefully examined. For this examination, the module width was chosen to be rather wide, 3.58 m for theta modules in BW3, so that nine modules could cover each octant of BW3 whose half length was taken to be 16.1 m. Then the boundaries appeared at $|\eta|$ = 0.16, 0.46, 0.73, and 0.97, where the half cell staggered two layer arrangement became somewhat imperfect. The fraction of this boundary region became about 6 % of the whole barrel muon coverage measured in η. However, as shown in Fig. 4.2.1, at least one cell of either upper or lower layer covers the boundary, and also we can easily arrange the module boundaries so that the boundaries in BW2 and BW3 do not overlap each other at any η. As a result, at least one superlayer, either BW2 or BW3, can provide a healthy superlayer trigger at any region in the barrel. Thus, the module boundary is not a very critical problem for maintaining a good muon coverage both for off-line analyses and trigger purposes.

Considering also the optimum chamber layout in the superlayers based on the current SDC detector dimensions, a typical size of the largest module is chosen to be about 2.5 m (width) x 9 m (length) x 0.4 m (height). The

module structure should be suitable for realizing such large size modules with enough precision and rigidity. Even though the chamber size is chosen to be this large, a number of modules to be produced is 536 just for the barrel system. Therefore, the chamber must be designed so as to allow efficient mass production, in order to fabricate the large number of modules within our tight time schedule.

4.2.2 Module structure

The module we are proposing is essentially a rectangular flat box formed by thin frames made of extruded aluminum. However, as shown in Fig. 2.3, the inside of the box is partitioned with a middle plate to make a two-story structure. The two-story structure is intended to have the staggered two layers of jet cells in one box. By using a light weight but stiff plate, such as honeycomb panel, for the middle plate, the chamber frame can be made sufficiently rigid even if the frame is made of thin aluminum structure. Since the middle plate tightly connects the frame components, the module structure becomes very rigid even without top and bottom cover plates. This fact allow us to proceed the cathode plate assembly and wire stringing comfortably on the open frame without the top and bottom plates. Inside the box, needed is a center support frame which provides a mid support point to long wires in order to maintain the gravitational sag within an acceptable amount. This wire support frame also contributes to the enhancement of the rigidity of the chamber box.

Thus, the chamber module reinforced by the middle partition plates and the center support frame is indeed very rigid in spite of its relatively light weight with the thin aluminum structure. Actually, the results of the FEM analysis showed that the gravitational sag of the 9 m long module was 0.33 and 0.038 mm when it was supported at four corners and six points (4 corners and 2 points at both ends of the center support), respectively.

Incidentally, in the mounting scheme of the chambers on the toroid the chambers, at least those modules of 9 m in length, are considered to be supported at the six points, since the center support frame has to be aligned

precisely with respect to the end frames within about 0.1 mm to keep the wires as straight as possible. However, as also discussed in the next subsection, the chambers are so rigid that shorter ones (shorter than about 7 m) are estimated to sag only 0.12 mm at most with four corner supports. Therefore, they can be supported only at four corners.

(1) Frame components

The chamber frame consists of two end frames, two side frames and a center support frame for the intermediate wire support. These frames are all made of extruded aluminum. The frame components are bolted and glued each other to form a rectangular shape. They are also tightly braced by the middle plates so as to form a rigid frame structure without placing the top and bottom cover plates. The connection scheme of these frames and the middle plate and their cross sections are shown in Fig.4.2.2.

The end frame has a shape of a square C-shape in cross section to help resisting wire tension. It has elongated holes for feedthroughs with oriented angles such that every hole points the interaction point. Although a NC milling machine is required to make these holes in proper orientation which differs one by one depending upon the place of the hole. The precision of the hole itself is not required since the hole is sufficiently oversized than the feedthrough, which is positioned precisely (better than 50 μm) by positioning pins.

The side frame is the longest of all the components. It does not require an elaborated machining. The center support frame also has elongated holes similar to those of the end frame. However, the hole is a little smaller than that for the end frame, and it requires certain precision because the wire support made of plastic should be fit and held at the hole by friction. This arrangement are illustrated in Fig.4.2.3.

As shown in Fig.4.2.2, these three frame components have flanges on which the middle, top and bottom plates are placed. The middle plate flange is extended a little further so that the middle plate can be placed, after

completing the frame assembly, without interfering with the flanges for the top and bottom plates.

(2) Middle plate

The middle partition plate is a critical component to maintain the rigidity of the module box. It is preferred to be as light as possible for minimizing the gravitational sag of the chamber frame while keeping the sufficient rigidity. The low density of the plate is also preferable to minimize the material along a particle path. Since the cathode plates are placed on the middle plate, the sag of the plate itself should be smaller than 1 mm. The requirement to a flatness of the plate is also about 1 mm for the same reason.

A panel made of aluminum honeycomb core with thin aluminum sheets as skins is one good candidates. A production process for the honeycomb panel is well established and the flatness requirement can be achieved with a little care even for our very large size panel of 2.5 m x 4.5 m. The rigidity of the honeycomb panel is sufficient as discussed in the next section and Appendix 3. For a 4 cm thick panel (38 mm thick core with 1 mm thick aluminum skin sheets at both sides), the sag of the panel is merely 0.1 mm provided that the panel is rigidly connected to the frames. Even when the connection is very poor, the sag is about 0.4 mm at most. Needless to say the effective density is very small. The effective density of this 4 cm thick plate is only 0.18 gr/cm^3.

One possible drawback of the honeycomb plate may be cost. It is relatively expensive compared with other conventional materials. For this reason we have looked for alternative materials. An attractive alternative is a corrugated aluminum structure, shown in Fig.4.2.4. The panel seems to be very rigid and the effective density for the panel is 0.2 gr/cm^3 which is almost as light as the honeycomb plate. We are now preparing measurements of the rigidity and flatness for a sample panel. The corrugated aluminum plate is expected to be rather inexpensive.

(3) Top and bottom plates

After completing the assembly of the cathode structure and the wire stringing operation, the module is closed with top and bottom plates to be a gas-tight box. The requirement for the plates comes from withstanding the gas pressure difference of up to10 gr/cm^2 with a deformation of 3 mm or less to keep the effect to the chamber performance negligibly small. As the chamber width becomes wider, this requirement becomes more serious.

The same panel designed for the middle plate which is 38 mm thick aluminum honeycomb core skinned with 1 mm thick aluminum sheets can satisfy the above requirement. The FEM analysis discussed in the next subsection showed that the deformation of the 4 cm thick honeycomb plate due to the gas pressure of 10 gr/cm^2 was 1.3 mm, much smaller than our requirement.

The corrugated aluminum panel, as discussed in the previous subsection for the middle plate, may be a better choice since it seems to be more rigid and less expensive than the honeycomb panel of the same thickness.

(4) Weight of the module

Weight of the largest module (2.5 m wide x 9 m long x 0.4 m thick) is estimated. The thickness of the frame components are 16, 8 and 8 mm, respectively for the end, side and center support frames. The top and bottom and middle plates are assumed to be a 4 cm thick panel made of aluminum honeycomb core skinned with 1 mm thick aluminum sheets. As summarized in Table 4.2.1, the total weight of a module is about one ton which is considerably light for such a large size module.

Table 4.2.1 Summary of the module weight for the BW3 θ-chamber.

Component		weight (kg)	pieces/module
Frame	Side frame	98	2
	End frame	59	2
	Center support	32	1
	Middle plate	83	2
Frame total		512	
Top/bottom plate		83*	4
Top/bottom plate total		332*	
Cathode plate etc.		90	
total		940	

* We tentatively assume that the material is the same honeycomb plate as is used for the middle plate.

4.2.3 FEM analysis

A three dimensional finite element method analysis has been performed to investigate the rigidity of the module box under various conditions. The rigidity criteria we have required for the chamber module are as follows:

i) The central support and two end frames must be aligned within ±100 μm to keep sense wires sufficiently straight.

ii) When the top and bottom plates are removed, the sag is less than 5 mm with minimum four-corner supporting (hanging) points. This criterion is intended to make the module robust enough to allow easy handling and setting during fabrication and assembly processes.

iii) The end frame can hold the total wire tension without excessive deformation.

iv) The middle plate is flat within 1 mm in order to guarantee the location of the cathode plates with respect to the wires. This is also because the middle plate is the central element of the overall module structure.

v) The top and bottom cover plates are sufficiently rigid to hold the pressure difference between the chamber gas and the outside atmosphere for safety as well as for keeping the drift electric field unaffected. The criterion is that the plates hold the gas pressure difference of 10 gr/cm^2 with a deformation smaller than 3 mm.

In the FEM analysis, the thickness of the frames made of aluminum are 16, 8 and 8 mm for the end, side and center support frames, respectively. The middle, top and bottom plates are assumed to be aluminum honeycomb sandwich plates of 40 mm in thickness. In the calculation, the honeycomb composites are replaced with plates that have equivalent Young's modulus, Poisson ratio and density. The computer FEM result was compared to hand calculations by using a formula for simple cases and excellent agreement was obtained.

The effects of gravitational sag, wire tension and gas pressure have been investigated for the worst case of the largest module (2.5 m x 9 m x 0.4 m) in various conditions. There are mainly two cases for the module conditions,

CLOSED : the top and bottom plates mounted,
OPEN : the top and bottom plates taken off,

and two different cases of the module supports,

4-point support : supports at four bottom corners A,B,C,D,
6-point support : supports at four bottom corners A,B,C,D and at the bottom centers of the side frames E and F.

The CLOSED case corresponds to the completed module ready for chamber operation, while OPEN is the case during cathode plate assembly and wire stringing operation. In the cases of support conditions, the module is placed

horizontally and supported from the bottom. The external constraints at supporting points are

point A	:	no freedom of motion,
point B	:	one freedom along the edge of the module,
other points	:	two freedoms of horizontal motion,

with full rotational freedoms at all the points. The FEM results are shown in Figs. 4.2.5 and 4.2.6 for the CLOSED case with 4- and 6-point supports, respectively. The summary of the analysis is shown in Table 4.2.2, in which the maximum deformation (in μm) and the maximum stress (in kg/mm^2) are given.

In addition to the effects of the module weight, the effect due to wire tension was calculated to be only 14 μm at maximum in the end frame distortion for the worst case of the total tension of 400 kg per end frame at 90 deg.

An excess of internal gas pressure of 10 gr/cm^2 was applied to the module in the analysis. Fig. 4.2.7 illustrates the deformation. The maximum outward movement is 1.3 mm. This is well below our requirement.

In conclusion, the FEM analysis has demonstrated the excellent structural stiffness of the proposed chamber module. The maximum sag is less than 1 mm in the case of the largest chamber for the unfavorable condition (open, 4-point support and horizontal). In the operational mode (CLOSED), the 6-point support is required to meet the ±100 μm requirement in the worst case. Most of the chamber modules are, however, shorter and in different (better) orientations. Therefor, a relatively easy 4-point suspension can be adequate for mounting most of the chamber modules. The proposed structure shows sufficient stiffness against the gas pressure difference as well as the wire tension.

Table 4.2.2 Results of FEM analysis on the horizontally placed module.

	CLOSED		OPEN	
top/bottom plates	in place		taken off	
number of supporting points	4	6	4	6
max. deformation in side frames [μm]	344	32	904	61
max. stress in the side frames [kg/mm^2]	0.460	0.219	0.314	0.234
max. deformation in the middle honeycomb plate [μm]	375	96	912	118

4.2.4 Cathode plates

As shown schematically in Fig.2.4, the oriented jet cells, pointing toward the beam crossing region, are furnished in the chamber box. The cathode plates which are made of thin stiff plates establish the physical cell boundaries. Accordingly, the cells are physically and electrically well separated from each other. Even if some wires break, they are isolated within the cell and does not introduce farther troubles in the neighboring cells.

Whether we can come up with a convincing scheme for the cathode assembly or not is the central issue for succeeding this chamber design. A thin plate for the cathode is desirable to minimize the dead space caused by the finite thickness of the plate. On the other hand, a certain stiffness is required in order to keep the cathode in place by means of a realistic support scheme. It is advantageous for designing a realistic cathode assembly scheme that it can be done on the wide open structure, since the two-story structure is sufficiently rigid without the top and bottom plates.

As discussed in section 4.1.5, the accuracy required for positioning the cathode is rather moderate. They can be placed with a precision of about 1

mm. This sizable tolerance makes it possible to use a thin plate as the cathode. The cathode plates are fixed to the end frame and the center support and are also supported with narrow insulator strips which are placed perpendicularly to the cathode plates. The lower strip is fixed to the side frames and also to the middle plates while the upper one is attached to the side frames. Furthermore, the cathode plates and these strips are mutually connected with glue at notches to form a rigid matrix structure. Thus the matrix structure as a whole is supported by the middle plate and side frames. Incidentally, neither the top and bottom plates are connected to this cathode matrix. Although there may be many materials suitable for the cathode plates, we try a conventional 1 mm thick GFRP plate with copper clad as a first candidate for the R&D prototype chamber. The support strip used for the R&D prototype chamber is also a GFRP piece of 2 mm in thickness.

4.2.5 Wires and feedthroughs

Optimization of the wire parameters such as diameters, tension, and materials has been discussed in 4.1 and relevant parameters are summarized in Table 2.1. Since the parameters are all moderate, the technique required for the wire placement is rather straightforward.

All wires must be precisely positioned with respect to the chamber frame, particularly to the end frames and the center support, to achieve the required spatial resolution of 250 μm per superlayer. The wire tension also must be adjusted precisely to keep the wire sag within the tolerance. However, since the chamber frame is simple and rigid, the wire can be positioned by means of a conventional technique using brass pins and plastic feedthroughs placed in the NC milled holes at the end frame. The large chamber R&D (Appendix 2) suggested that a few 10 μm accuracy can be achieved with this technique.

Aligning the support point at the middle of the wire accurately seems to be more problematic. We will fabricate the chamber module precisely so that the center support can be aligned within 100 μm with respect to the end frames. Then the actual position of the support frame will be measured by

an optical system (discussed in the next subsection 4.2.6), which is similar to that used for the L3 muon chambers.

Since the high voltages applied to sense, potential and guard wires are comfortably low at about 2 kV, conventional plastic materials can be used for a feedthrough and a wire support. We have made several pieces of feedthroughs and wire supports using plastic for the R&D prototype module. Their drawings are shown in Figs. A2.7 and A2.8. They were made by machining in the present R&D project. For mass production, however, they can be made by an injection mold method. Details of the design will have to be modified to fit the molding technique.

The plastic wire support mounted on the center suuport is made small enough to pass through feedthrough holes on the end frame. This makes it possible to remove the plastic wire support in case of wire repairing without opening the cover plates. Besides, since a wire support can pass through a hole of the end frame, a set of wires can be set on the wire support outside the frame at the initial stage of the wire stringing operation. Then, the set of nine wires for a cell can be simultaneously pulled to be strung with help of a guide tape. Details of this operation are discussed in section 4.3.5.

4.2.6 Optical position monitor

To measure and monitor the position of the middle support with respect to the end frames, an optical system which consists of an LED, lens and CCD, illustrated in Fig.4.2.8, will be implemented inside the chamber. Utilizing this system, we can easily measure and monitor the misplacement of the center support and adjust it, if necessary, during the chamber mounting work with precision alignment.

4.2.7 Intermediate modules

The shapes of intermediate modules and their dimensions are shown in Fig. 4.2.9. The structure of the module is basically the same as that of the barrel module. The module is divided into two separate sublayers, each of which is further divided into cells by cathode plates. There are three sense wires in each cell, which are aligned to the interaction point for the theta chambers, IW2(θ) and IW3(θ). There is a center support in a module. The main difference is that it has a trapezoidal shape, except the middle modules in IW3(ϕ).

(1) Theta chambers

The IW2(θ) chamber is made of a single module of the parallel sides of 7.1 m and 5.1 m in length and 2.2 m in width. The IW3(θ) chamber is divided into 3 modules, each having a width of 2 m. The longest side of the module is 10.2 m. A concept of the end plate of the theta module is shown in Fig.4.2.10. Although the end plate and the direction of the wires are not perpendicular, feedthroughs must be attached on the end plate normal to the wire. Therefore, we have to make a flight of stairs on the plate. Since the size is not so large and since the slope is 22.5 deg, it is possible to make it as a single unit by using a standard computer controlled milling machine.

(2) Phi chambers

As for the phi chambers in IW3(ϕ), there are two types of modules. One is box shaped, and the other is almost triangular. Each sense wire is strung along the y-coordinate, while the row of the wires is parallel to the z-coordinate according to the definition in Fig. 4.2.9. Unlike the theta chambers, the cell is not aligned to point the interaction point for both types of modules. It is because we should avoid the extreme complexity of structures for the triangular phi chambers. We have to set feedthroughs on the hypothenuse. Since the slope is 67.5 degrees and since the height is 6 m, it is not possible to make it as a single unit. We separate the function of the hypothenuse plate into the mechanical part and the alignment part. A single plate with several windows serves as a mechanical structure. Plates on which feedthroughs are attached are separately machined and assembled on the mechanical plate. A concept of the hypothenuse plate is shown in Fig. 4.2.11.

Note that the error of machining along the plate is reduced by a factor of $\sin(22.5^0) = 0.38$ in the phi direction.

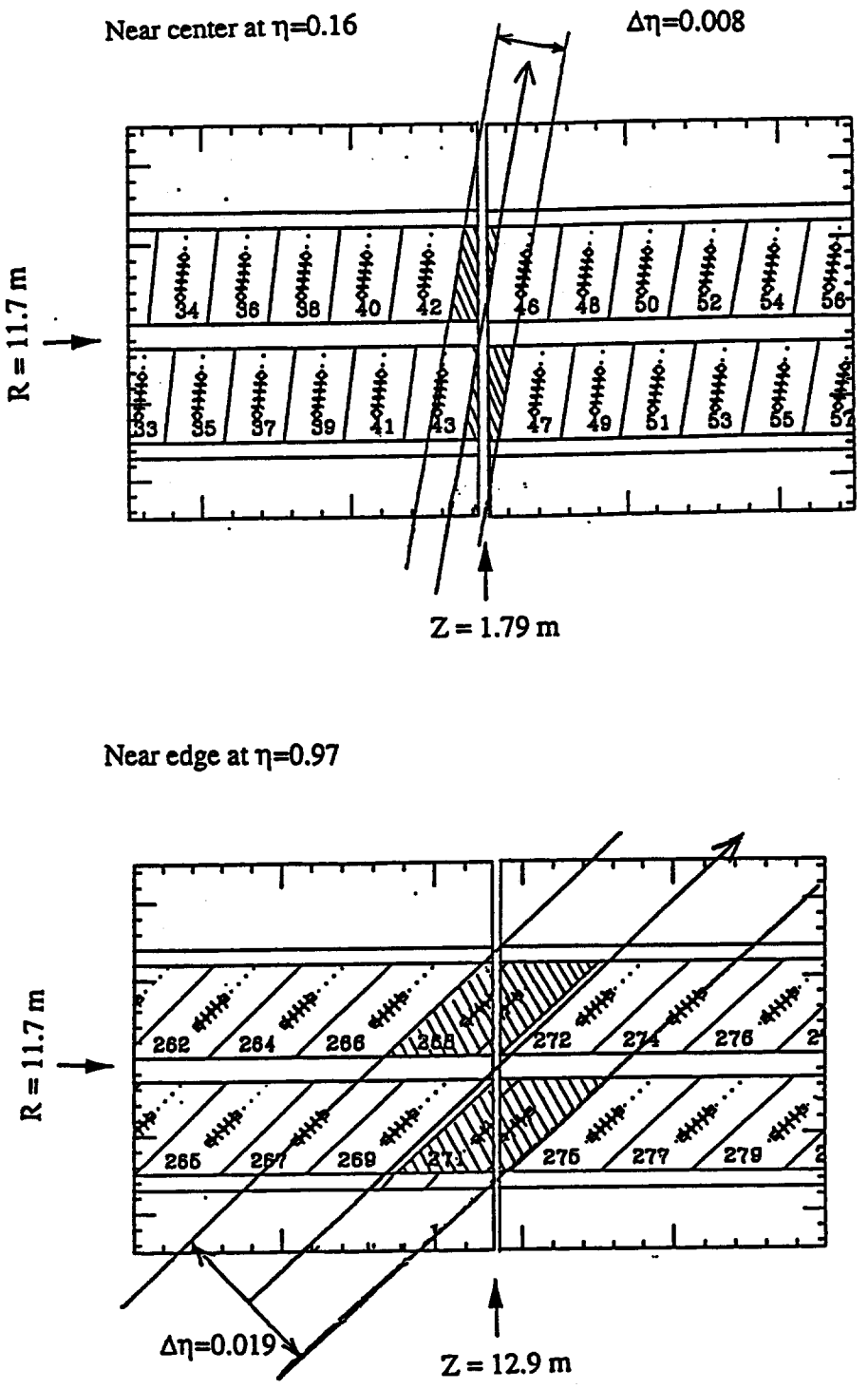

Fig. 4.2.1. Module boundaries of theta chambers in the BW3 superlayer.

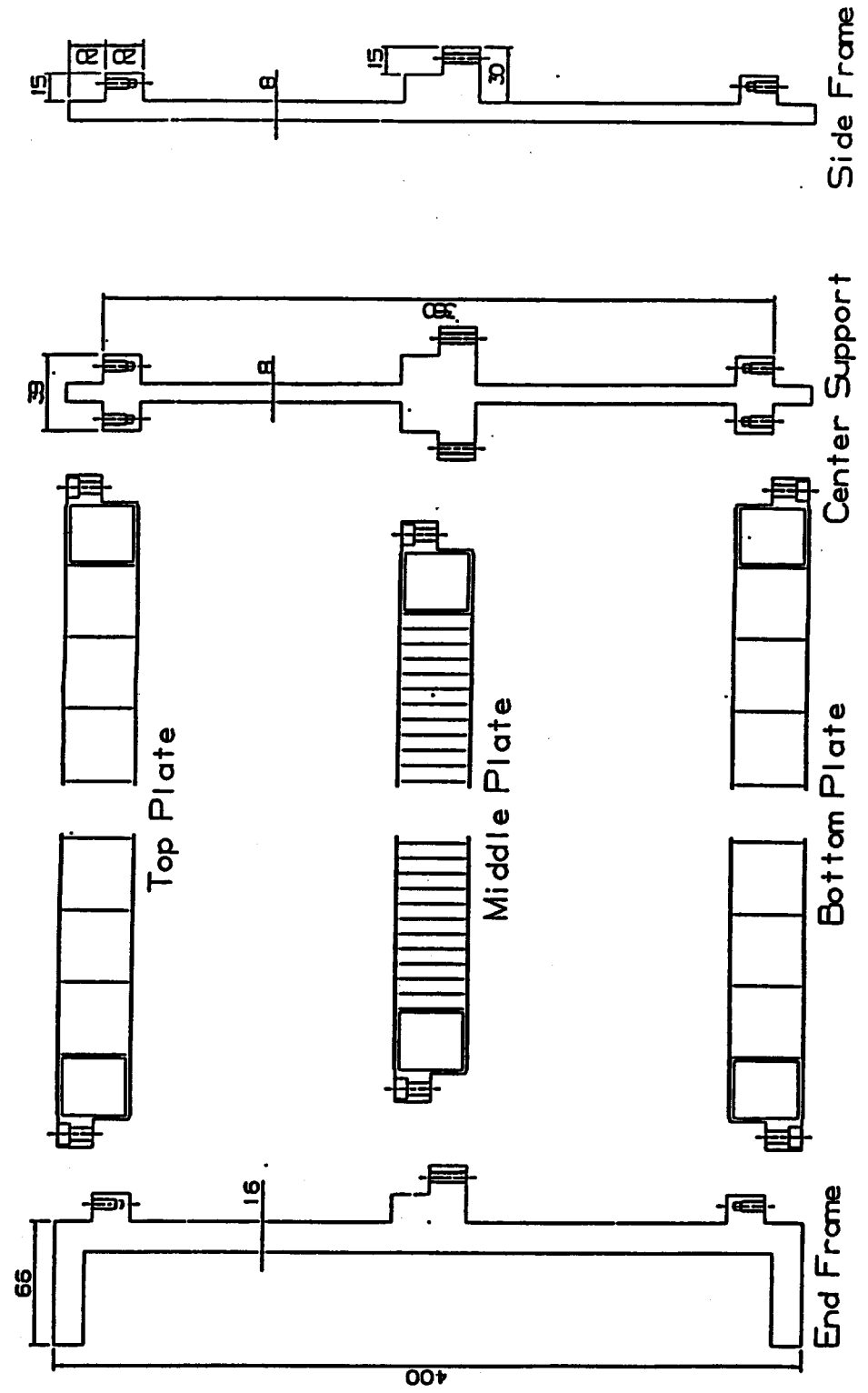

Fig. 4.2.2. Cross sections of the structural components and their connection scheme.

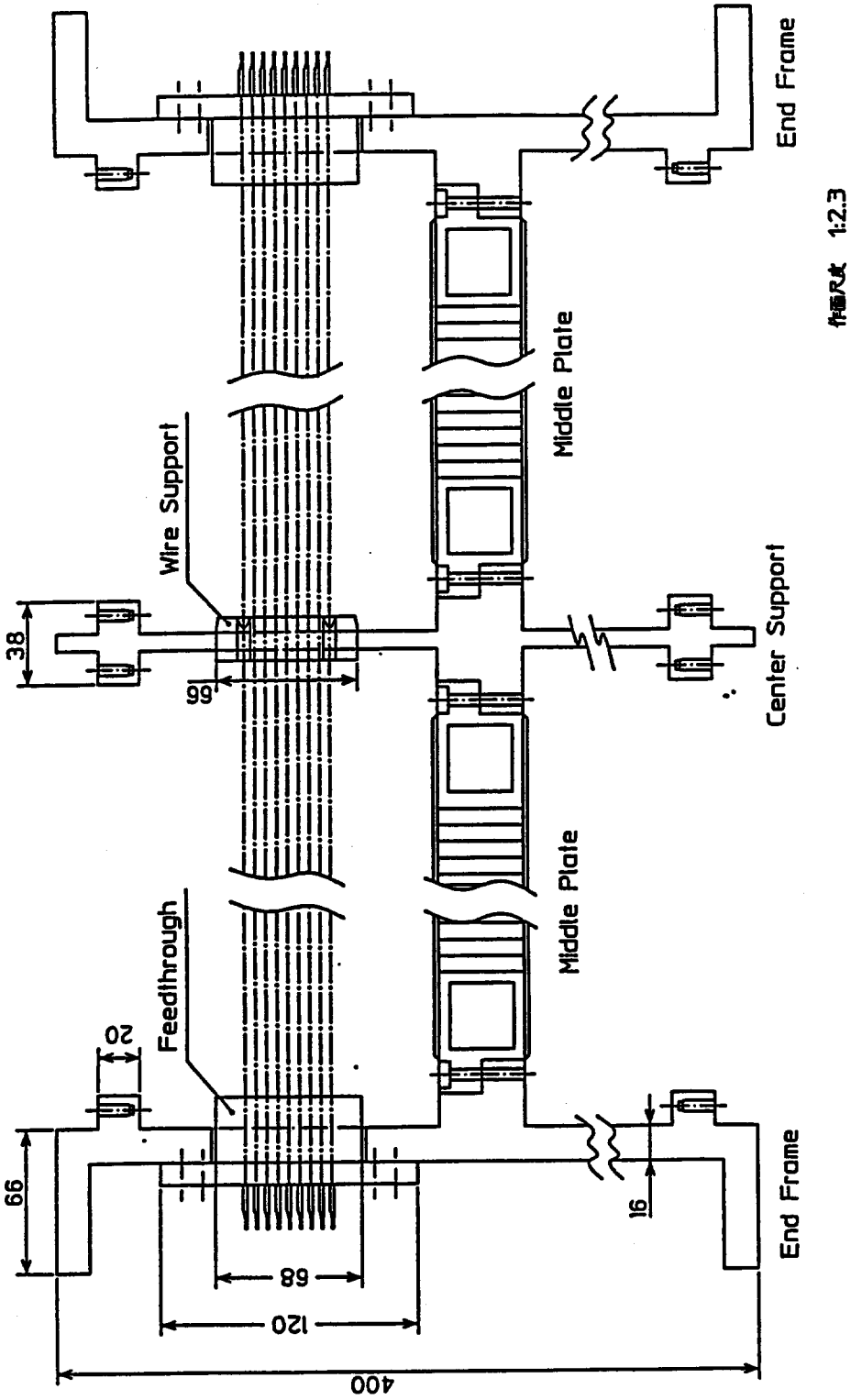

Fig.4.2.3. Feedthroughs and wire supports.

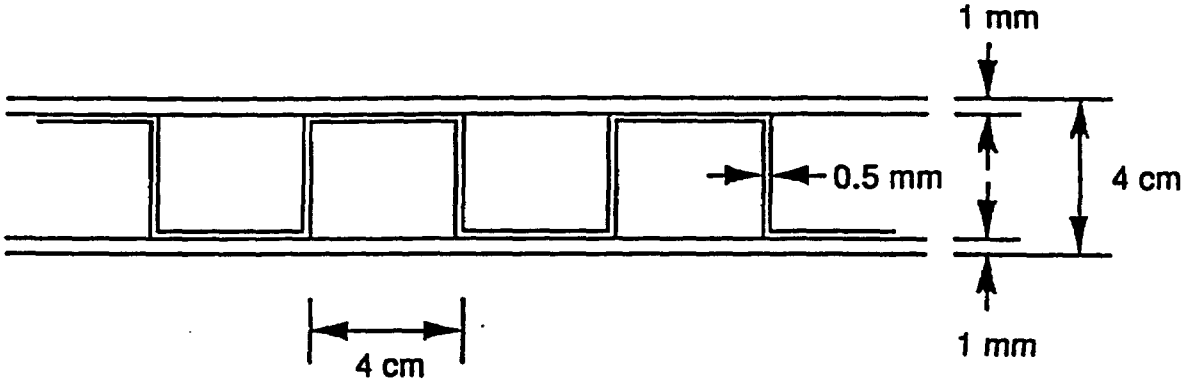

Corrugated aluminum with skins.

Fig. 4.2.4. Corrugated aluminum plates for the top and bottom plates.

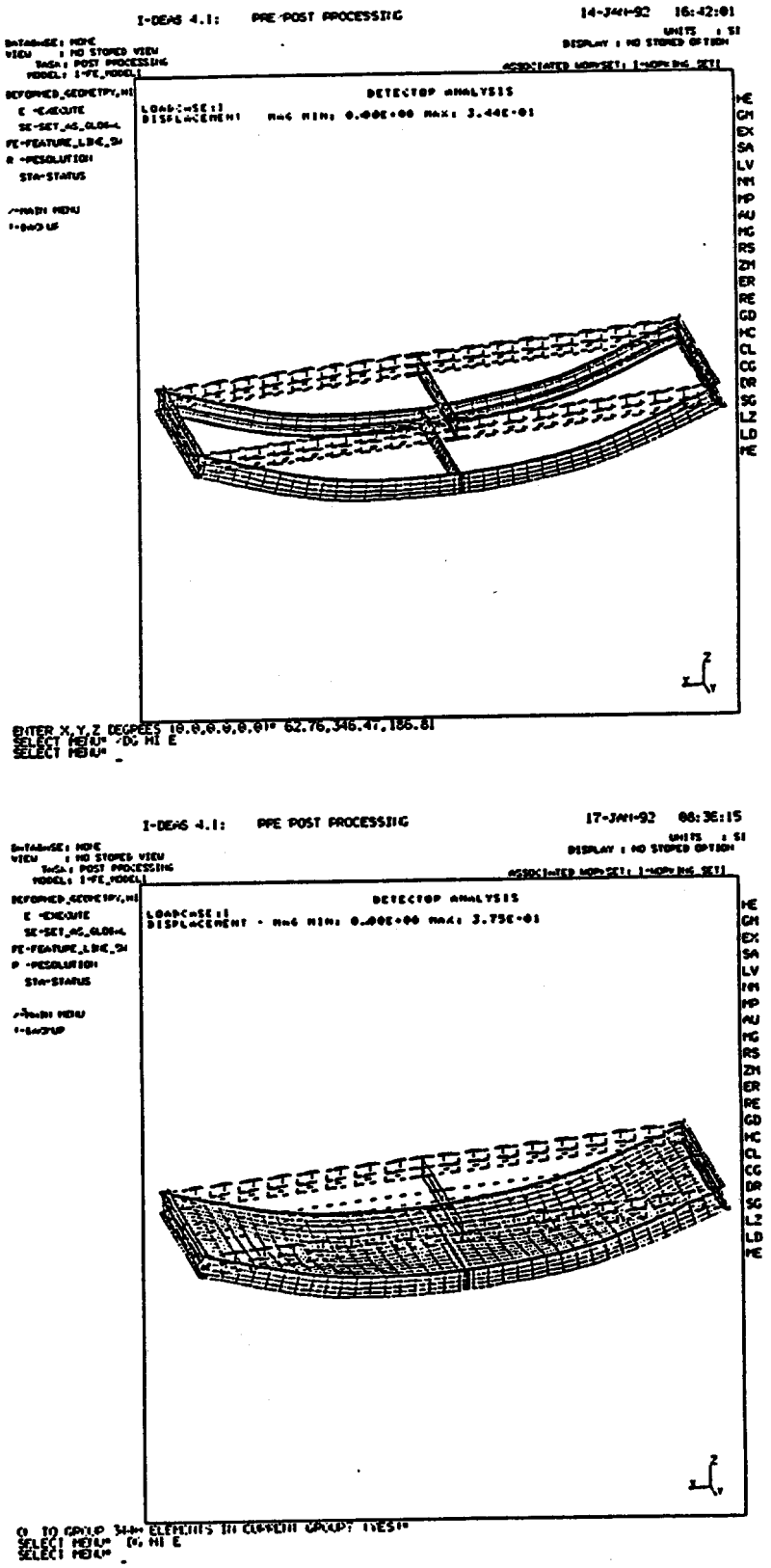

Fig. 4.2.5. Result of the FEM analysis for the case of 4-point support. The top figure shows deformation of the frames, while the bottom picture for the middle plates.

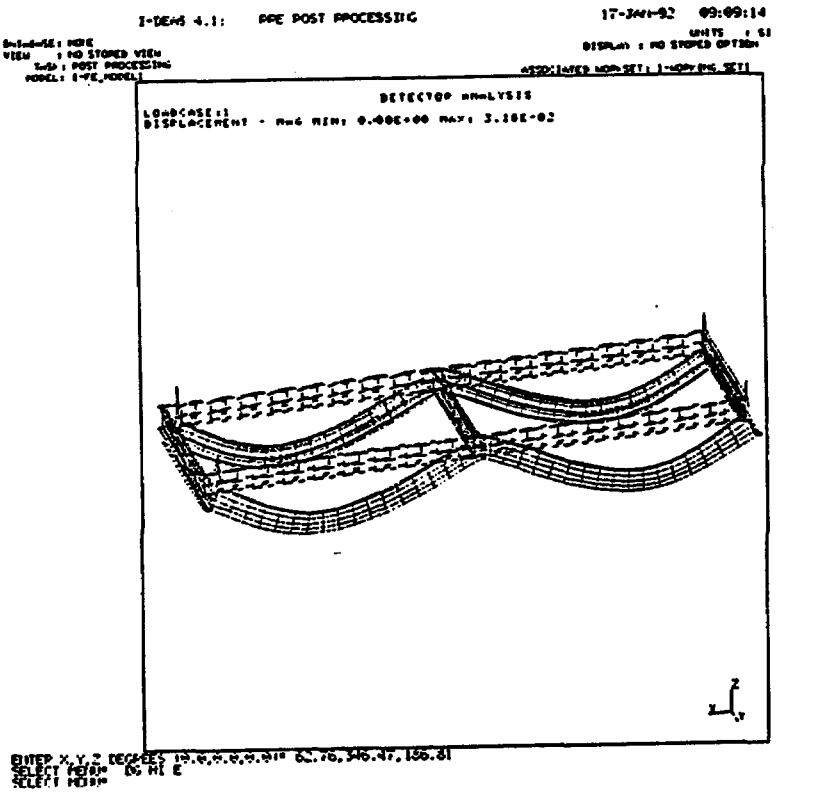

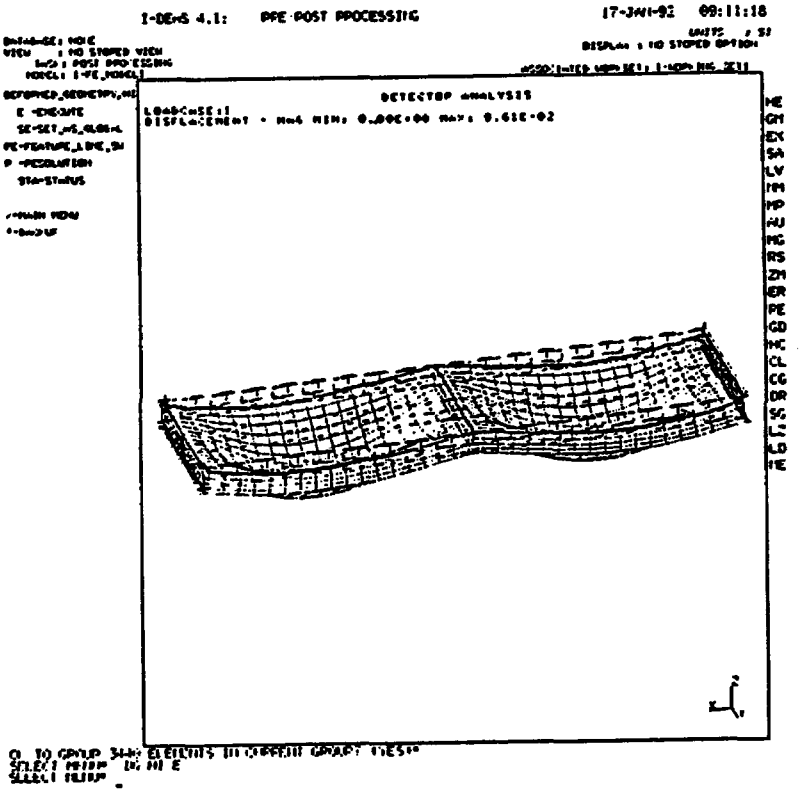

Fig.4.2.6. Same as Fig. 4.2.6 for the case of 6-point support.

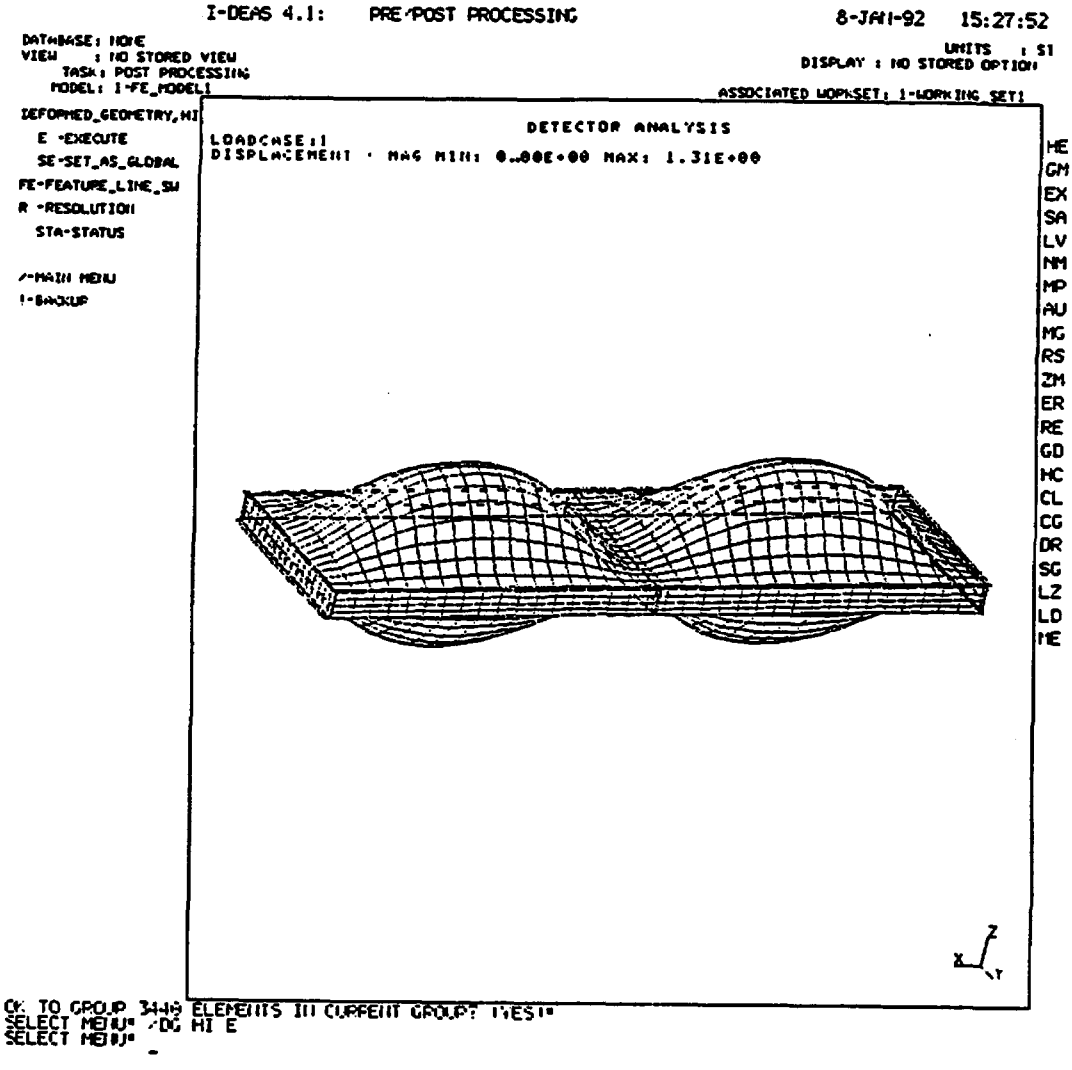

Fig. 4.2.7. The FEM analysis of the deformation of the chamber modules for the case of excess internal gas pressure of 10 gr/cm^2.

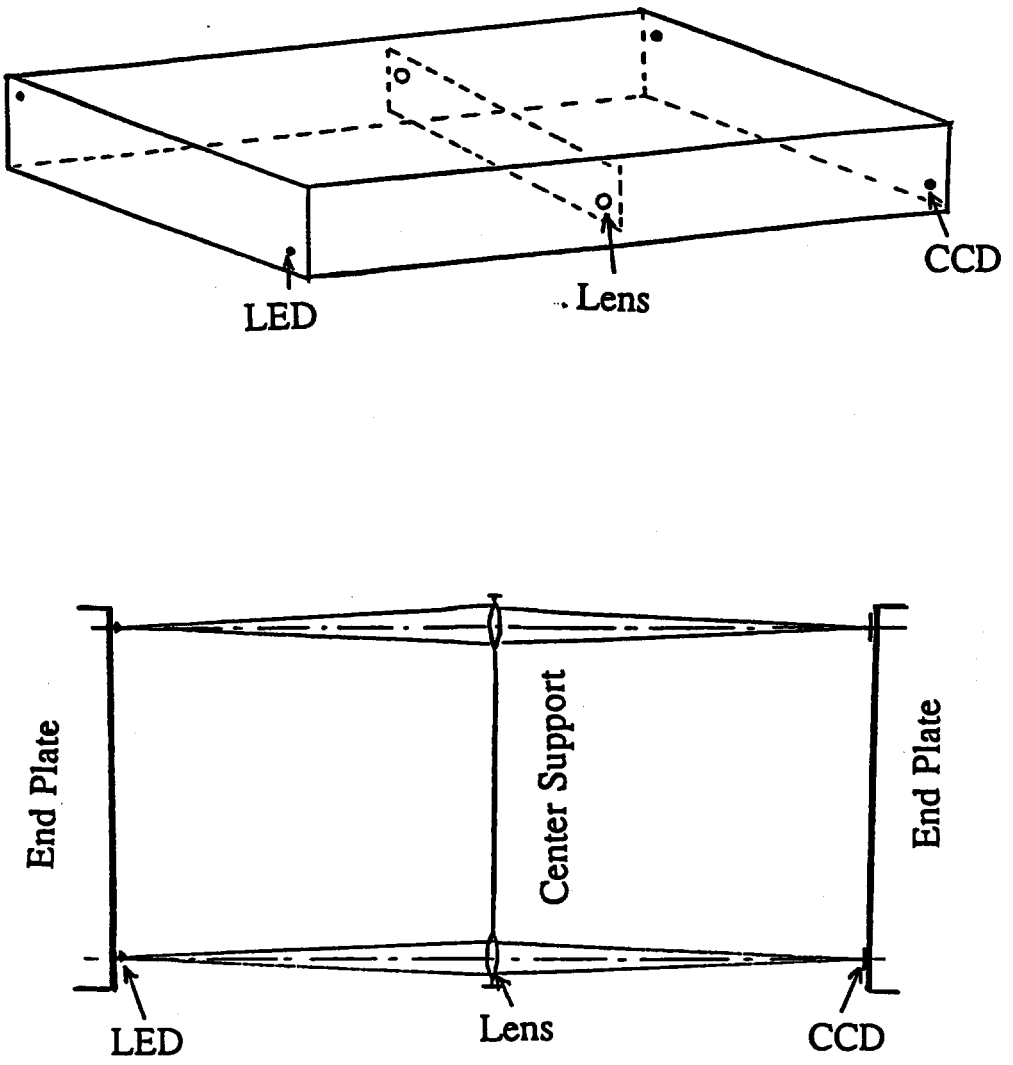

Fig. 4.2.8. Optical alignment system for the center support frame.

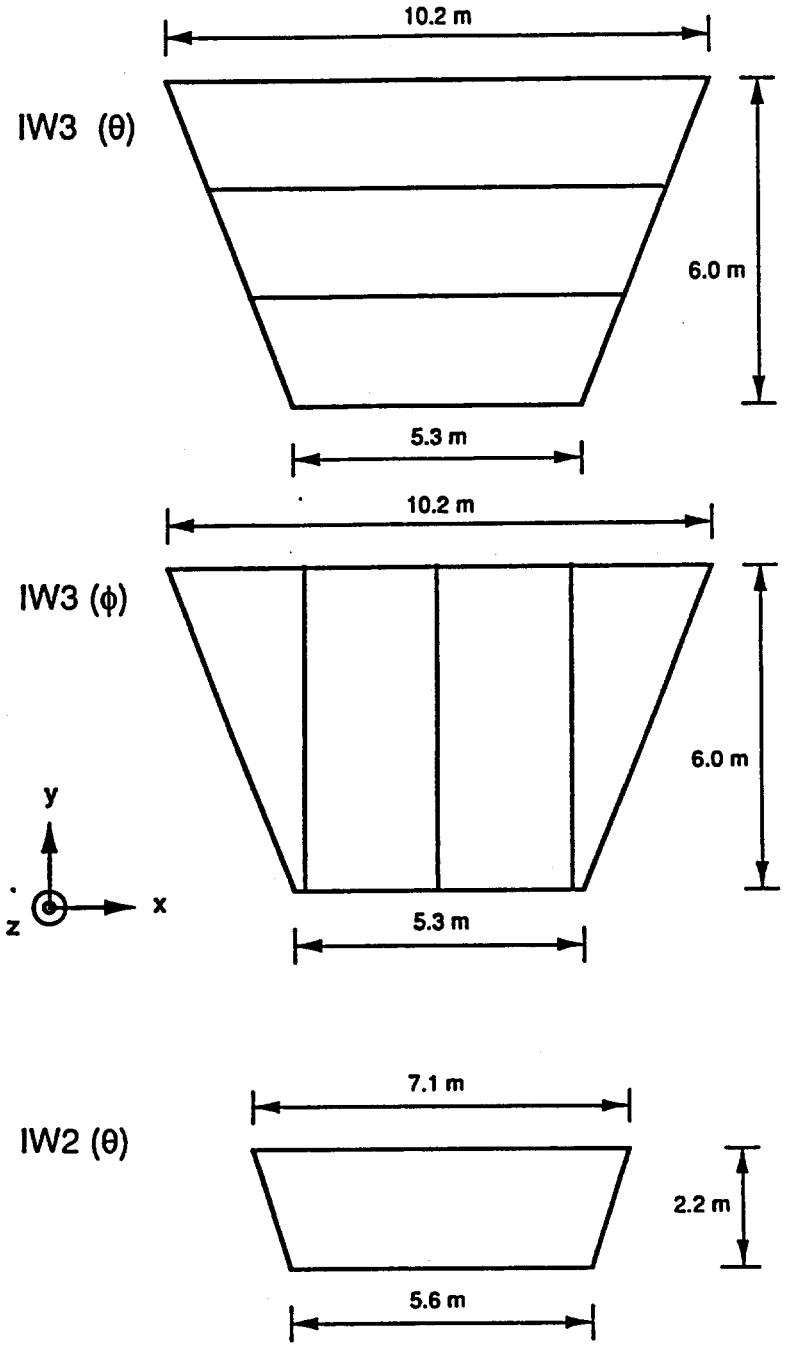

Fig. 4.2.9. Shapes of intermediate modules and their dimensions.

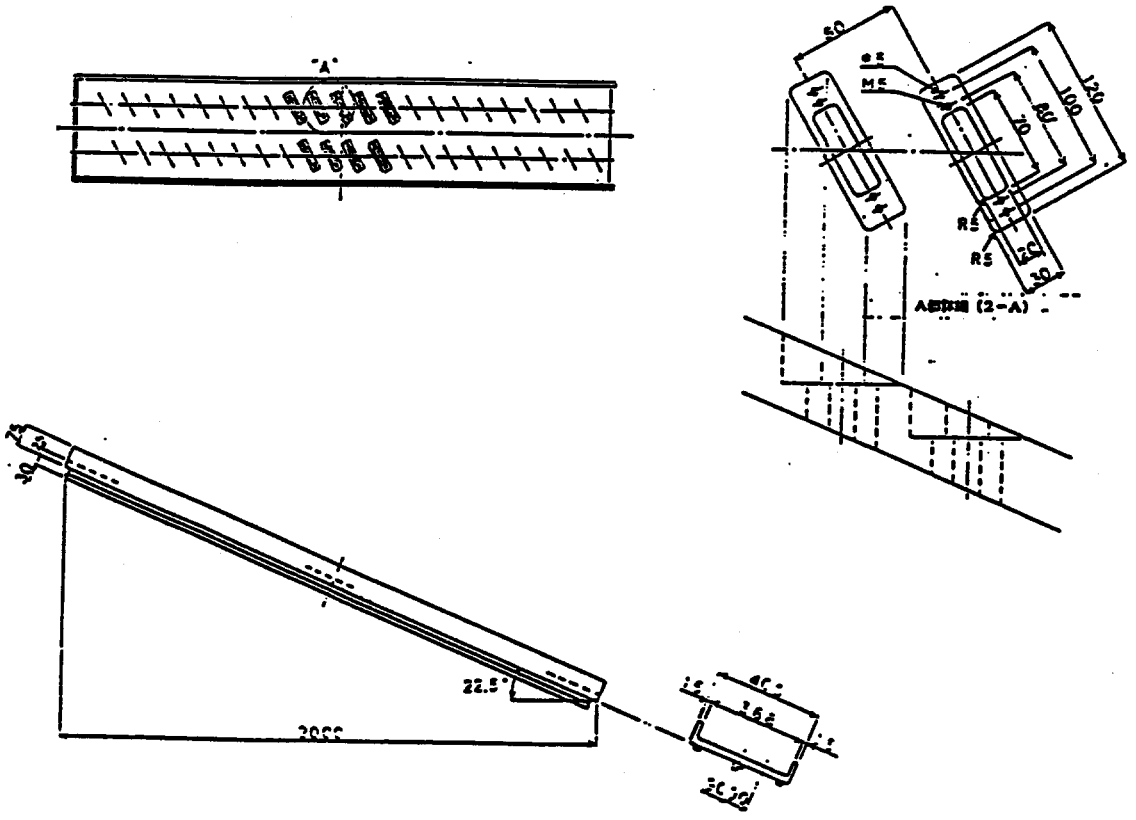

Fig. 4.2.10. A concept of an end plate of the theta module.

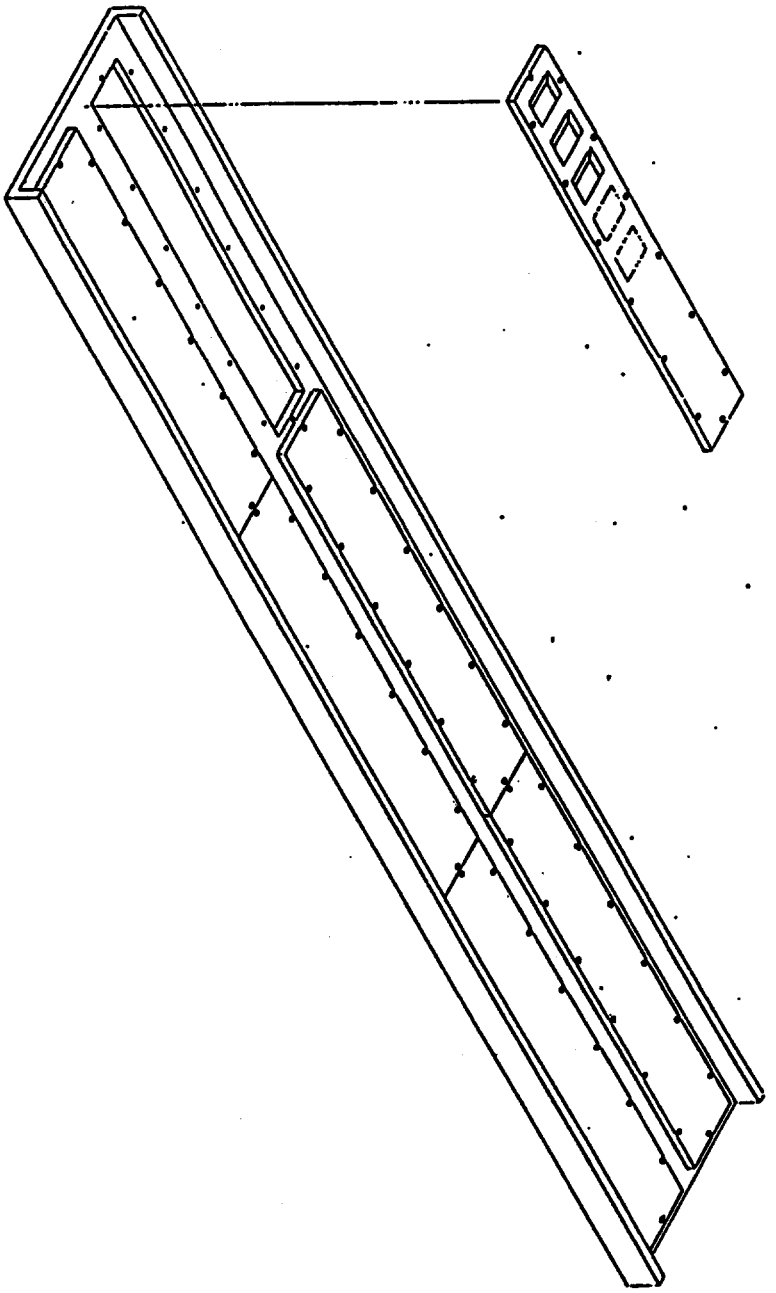

Fig. 4.2.11. A concept of a hypothenuse plate of BW3(ϕ).

4.3 Chamber production

4.3.1 Materials

As shown in Table 2.2, we have to fabricate 568 jet chamber modules for the barrel and intermediate muon system within the time period of about 3 years by the end of 1996. This means that about 200 modules must be completed in a year. This condition demands us a design of the jet chamber which fits to a mass-production line. From this view point we intended, as much as possible, to use mass-producible material, to machine pieces with enough precision so that too much fine adjustments are not required in the assembly processes, and to invent useful tools to avoid skilled technicians. The procedure is as follows.

We use four different types of aluminum extrusions for end frames, side frames, center supports and the frames of the top, bottom and middle plates (Fig. 4.2.2). The precision of these extrusions is expected to be better than 50μm in any dimension except the length. Except the center support, precision of the length is not necessarily great. Only the center support is machined with the precision of better than 50 μm in its length at the same time as the wire supporting holes are machined.

These extrusions must be cut to appropriate lengths and holes must be machined to provide precision before assembly. NC machines are programmed to make all the elongated and the feedthrough positioning holes point the interaction point. Several through holes must be made at both ends of the end frame for assembly of the side frames. Also a few through holes are needed at the center of the side frames for connection of the center support. All the extrusions that make the chamber frame, namely the end and side frames and the center support, need several tap holes on the flanges of the frame to bolt the top, bottom and middle plates to the frame. Some more tap holes are needed at the both ends of the side frames and the center support. All those holes are for 5mm screws and do not require high position accuracy. In addition to the above machining, the center support needs to be machined to remove parts of flanges at the both end so that it fits

with the side frames and to make reasonably smooth surface at the joint of flanges. This joint must be made gas tight with vacshiel glue (Fig. 4.3.1).

Top, bottom and middle plates are made of corrugated aluminum plates which are glued with two flat aluminum sheets on both sides. The plates are framed around all sides with aluminum extrusions as shown in Fig. 4.2.2. This plate needs to be machined to make through holes on the extrusions which are bolted to the flanges of the chamber frame.

It must be noted here that all the machining described above does not require any great accuracy except the small holes for the feedthrough positioning on the end frames and the center support and the length of the center support.

The cathode plates and their supporting strips are made of PC boards with notches so that they are assembled to make a parallel cross structure. All the cathode plates and supporting strips are fixed at both ends to the end and side frames and the center support with small insulators. In addition that, the supporting strips which come to the both sides of the middle plate are glued to the surfaces of the middle plate with similar small insulators. These fixing pieces of insulator could be of plastics and produced by a molding technique.

Two similar kinds of feedthroughs are prepared in a common way as those for other chambers, larger one for the end frame and small one for the center support. Gold plated tungsten and copper beryllium wires are obvious items to purchase.

4.3.2 Tools

In order to produce a large number of precision drift chambers of good quality, it is essential to build a mass production line with proper tools and to avoid processes which require large efforts of skilled labors.

In order to avoid tedious processes in the assembly to achieve required precision, we intend rather to use precision machining of materials and to build a solid machine for chamber assembly.

The assembly machine consists of four independent pieces, each having a flat surface to hold either end or side frame by vacuum sucking. The surface has positioning pins to precisely determine the position of the frame. Three of the four pieces have a motor driven moving mechanism in one direction with a stroke of about 5 cm.

A wire stringing machine has nine separate spool holders with resistive rotators and stoppers and a pulley system to guide wires to the nominal relative positions at the outlet. Here, two feedthroughs are held, a larger one inside and a smaller one outside, facing to an elongated holes on an end frame. Another pulley system is built where another large feedthrough is held at the inlet of the pulley system, facing to an elongated holes on the second end frame. At the outlet of this pulley system, the nine wires are lined up by separate pulleys so that proper weights are easily hanged by each wire. The positions of the feedthroughs are easily moved to the next elongated holes when a set of wires is strung.

In addition to the above machines, certainly we need many different kind of jigs to handle materials and chambers.

4.3.3 Chamber assembly

After machined to proper lengths and drilled to make proper through holes and tap holes, these materials are assembled in the following procedure to a chamber module (Fig. 4.3.2).

1) Set the four sets of the assembly machines on solid flat tables at the proper relative positions by precision survey.

2) With a crane and proper jigs, two side frames and two end frames are picked up and installed to each set of the assembly machine. They are tightly fixed to the flat surface of the assembly machine with the vacuum sucking system. The position of each frame is determined precisely with positioning pins.

3) In a similar way, a center support is picked up and one end is pasted with glue. Then it is placed at the center of the two side frames so that the glued end firmly presses the side frame which does not move. Bolt the center support and the side frame.

4) Move in the other side frame to the place where it firmly presses the center support. Then move in the two end frames until they touch the two side frames.

5) Survey the positions of the frames and the center support with preset survey equipments, specially positioning of the two end frames and the center support. With proper assembly machines and proper machining of the frames, we believe they can be lined up within an accuracy of 50 μm.

6) Retreat the two end frames and then one of the side frames by about a couple of centimeters. Put glue on all the ends of the side frames and the unglued end of the center support which is left unglued.

7) Repeat the same process as the process 4). Make sure that all wire supporting holes are properly lined up. Put a limited number of bolts as designed.

8) Pick up the middle plates and fix them to the chamber frames with glue and bolts one by one. Leave the box under the constraint of the assembly machines for overnight to cure the glue.

9) At the very first of the next morning, the whole assembly is moved out from the assembly place to another place for mounting the cathode plates.

4.3.4 Cathode mounting

1) Small fixing pieces are glued on the inner surfaces of both side frames at equal distances making two lines at the top and bottom of each side frame by using jigs and also on the surface of the middle plates. Continue the same procedure on the inner surfaces of the two end plates and on the both surfaces of the center support.

2) Slide down cathode supporting strips into the slots of the fixing pieces only at the bottom of the cell and drop glue in every slot of the fixing pieces.

3) Insert cathode plates into the slots of the fixing pieces on the end frame and the center support and into the pre-machined notches of the cathode supporting strips so that the two pre-machined notches on the cathode plates and on the supporting strips meet each other. Then drop glue in every slot and notch.

4) Install the top supporting strips in the similar way as 2) and 3). This completes the cathode mounting on one side of the jet chamber module.

5) With a crane and a lifting jig, turn over the module upside down. Repeat the processes 1) to 4) again on the new side.

6) Move the module to the wire stringing place.

4.3.5 Wire stringing

1) Set the chamber module on a rotating stage which holds the module at the frame part only and leave both top and bottom faces free for accesses. Hold the module with its 2 to 2.5 meter width vertically. Two teams of 2 to 3 people work for wire stringing from both sides on height adjustable catwalks.

2) Set two different types of feedthroughs at the outlet of the first pulley system, the larger one inside and the smaller one outside. Get nine wires through feedthroughs as the cell structure requires. Fix the nine wires on a guide tape which is laid through the elongated holes on the end frames and the center support(Fig. 4.3.3). Pull the guide tape to the other side of the module until enough amounts of wires come out of the other end of the module. Crimp the wires at the feedthroughs at the first end of the module.

3) Move the small feedthrough by hand, through the elongated hole on the end frame, to the center support and push it into the elongated hole on the center support. The feedthrough is precisely positioned in the hole by grooves inside the elongated hole and stay there by friction only (Fig. 4.3.4).

4) Move the large feedthrough into the elongated hole on the end frame and bolt it to the end frame. Crimp the wires at the feedthrough at the first end of the module.

5) At the second end of the module, remove wires from the guide tape one at a time and get them through the large feedthroughs which is held at the inlet of the second pulley system beforehand. Set the wires in the pulley system and hang appropriate weights at the end of wires.

6) Move the feedthrough into the elongated hole and bolt it to the end frame. Crimp the wires at the feedthrough of the second end of the module.

7) Repeat the processes 2) to 6) until all wires are strung in the module.

8) Check the electrical conductivity and insulation of wires.

9) Rotate the module to the horizontal position and get the top plates bolted on the module with gaskets in between.

10) Rotate the module by 180 deg and get the bottom plates in the same way as the process 9).

11) Move the module to the testing place and make a gas leak test.

12) Install preamp cards for cosmic ray and beam tests.

4.3.6 Global flow of the production

Flow of the chamber production is shown in Fig. 4.3.5. When the SDC collaboration finally chooses the jet chamber design for the barrel and

intermediate muon chambers, the KEK will renew the contract with the current engineering firm and strengthen the collaboration with them to a necessary level for the full production. Based on the experience of the prototype chamber production, we review the current design from the view point of the mass production and redesign the chambers in further details. During this process specifically and all the process afterwards, we like to establish better communication with the SSCL, through which and directly, too, we accept suggestions and helps from other muon subgroup members.

The Japanese group orders to various material suppliers almost all the materials which need for the whole muon jet chambers. After all necessary machining, these materials are shipped to two or three assembly places both in Japan and US. The second place of assembly is naturally the SSCL. If any other institutions wish to take the responsibility, we could help to set up another center of chamber production.

The Japanese group also designs necessary tools with the help by experts from the collaborating groups and places orders of these tools with outside tool makers. Depending upon the number of the chamber production centers and their responsibilities, a necessary number of sets of each tool are produced and shipped to appropriate places.

Those chambers produced at the production centers are tested with cosmic rays and/or beams. Some fraction of modules can be transported to other collaborating institutes for these tests. After completion of the test, all the modules are brought into the SSCL for installation into supermodules. Again chambers are tested with cosmic rays as a system of a whole supermodule before being brought down into the hall.

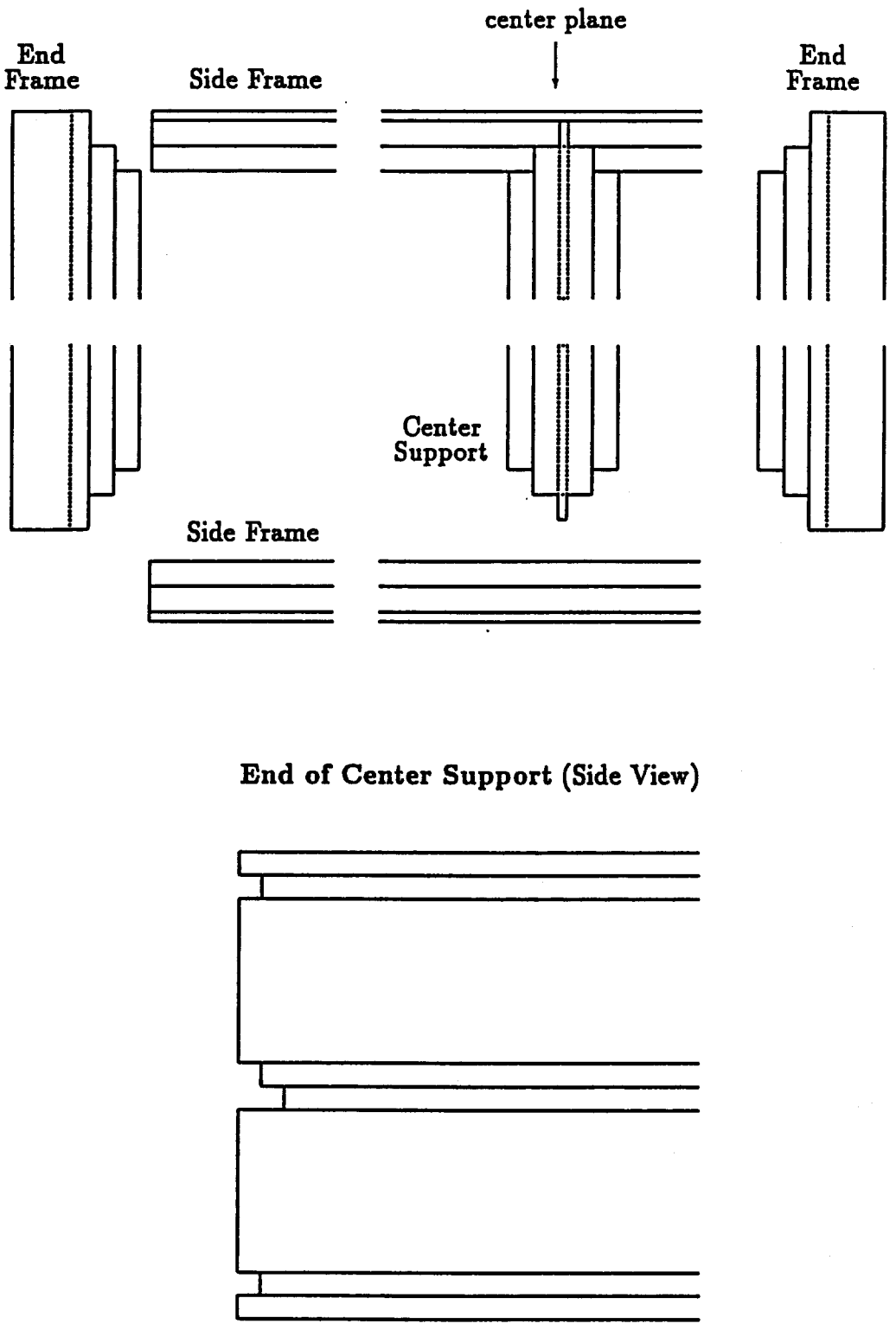

Fig. 4.3.1. Frame assembly of the chamber module.

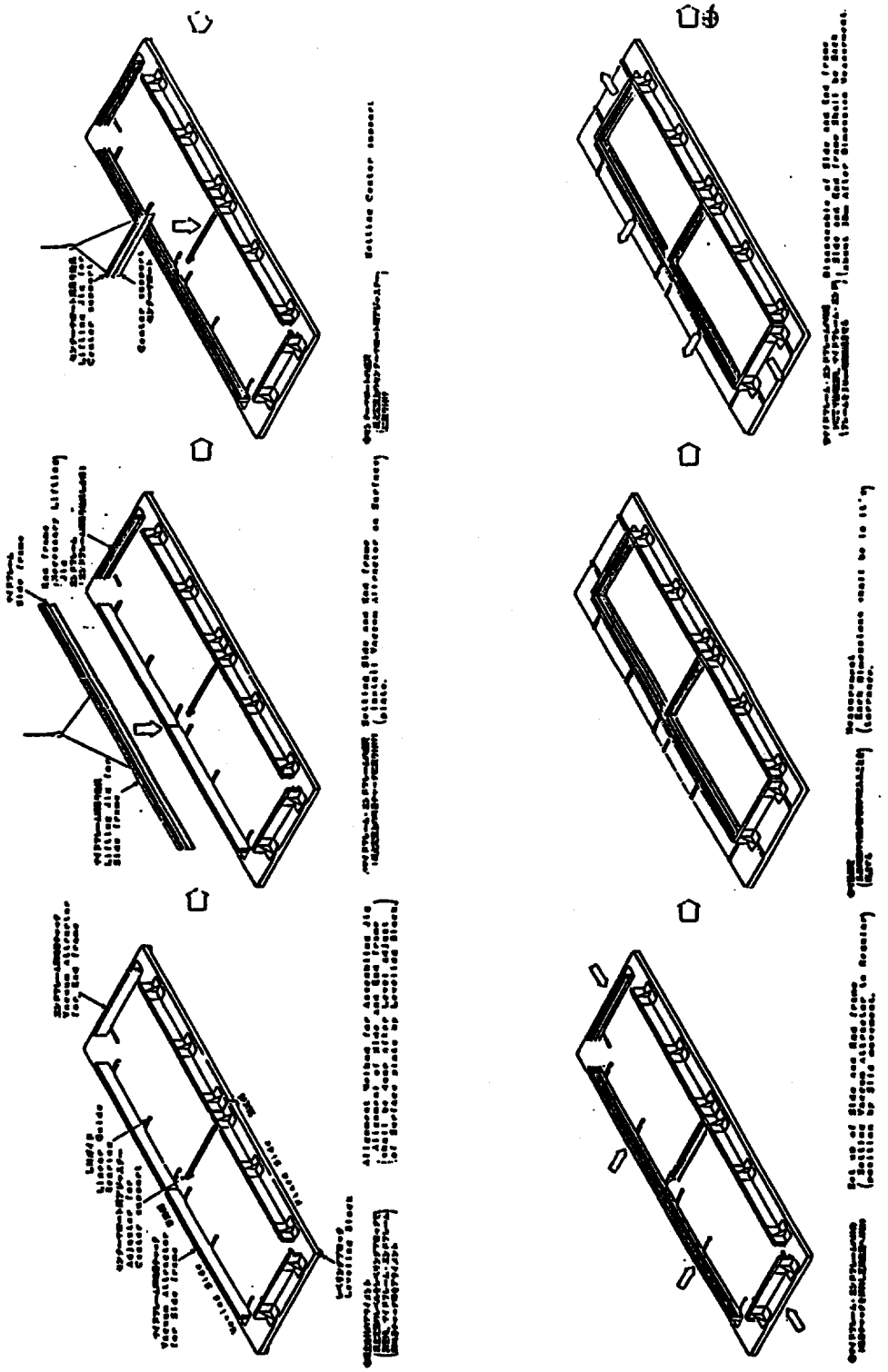

Fig. 4.3.2 Chamber assembly process. Chambers are assembled with a frame locating machine which holds frames and locates them with enough precision. [continue to next page]

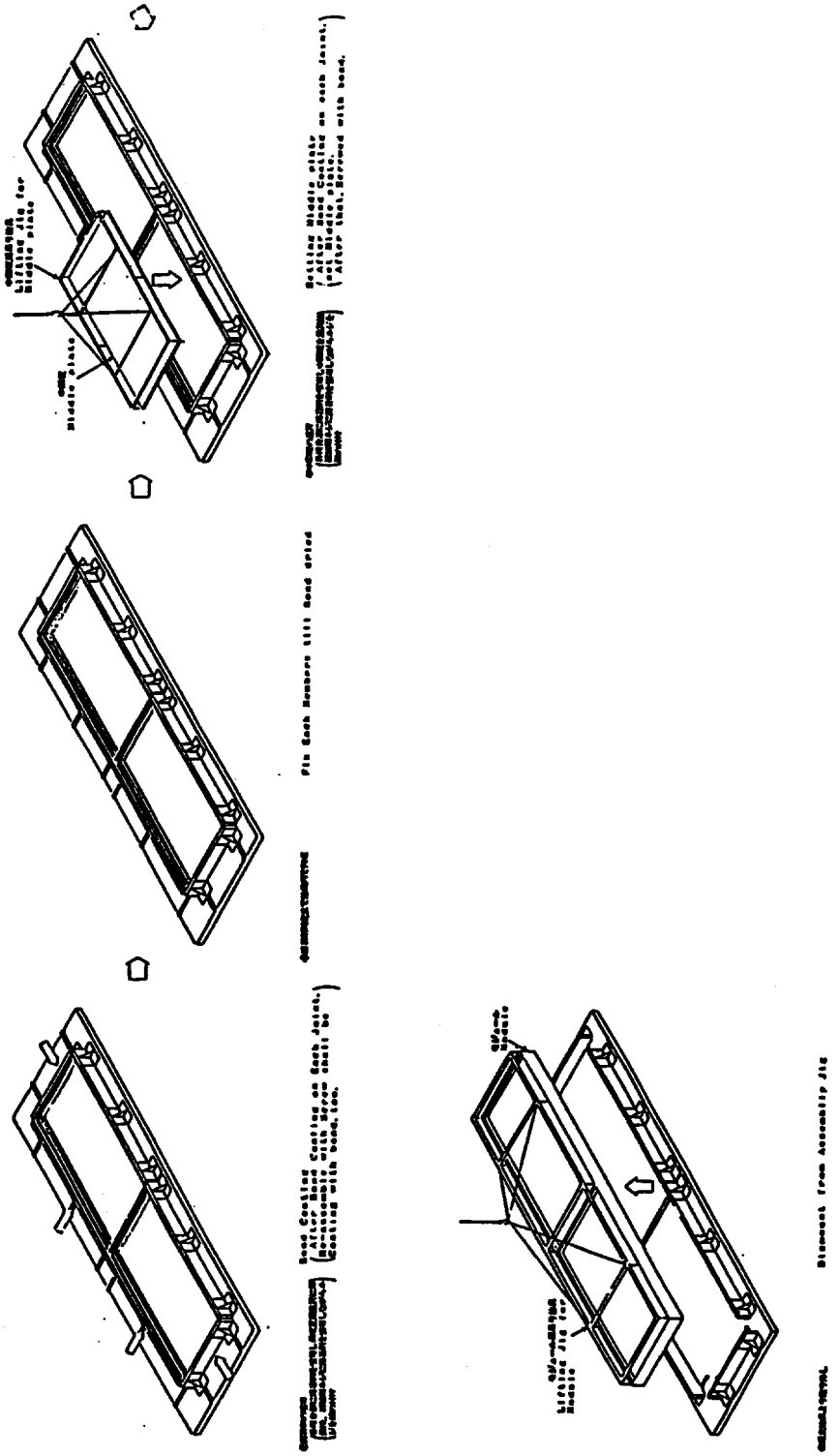

Fig. 4.3.2 [continued from the previous page]

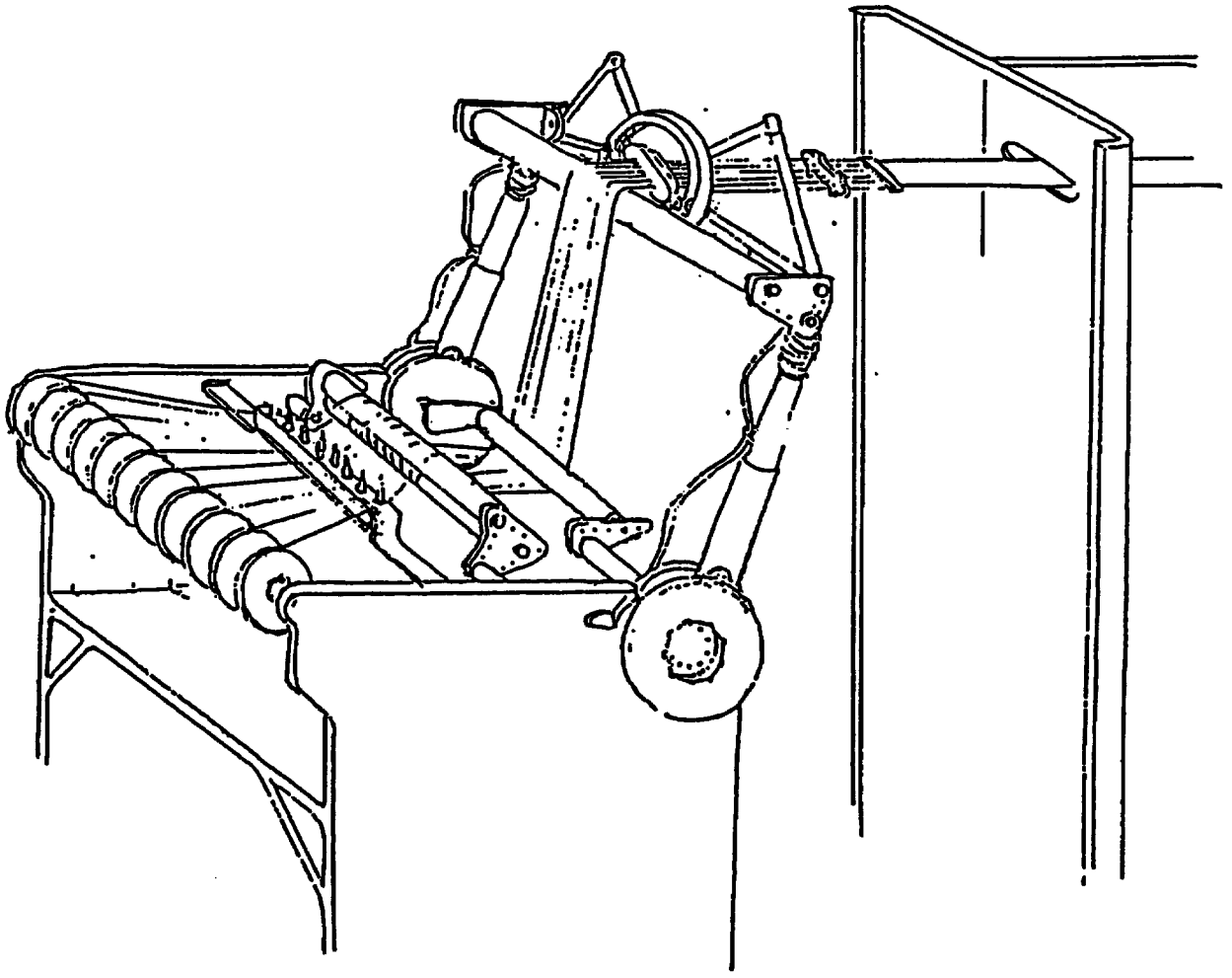

Fig. 4.3.3 Wire stringing : A set of nine wines is supplied from the spools and fixed to a guide tape through the two feedthroughs held at the entrance hole of the module. The side frame is not shown for a better visibility.

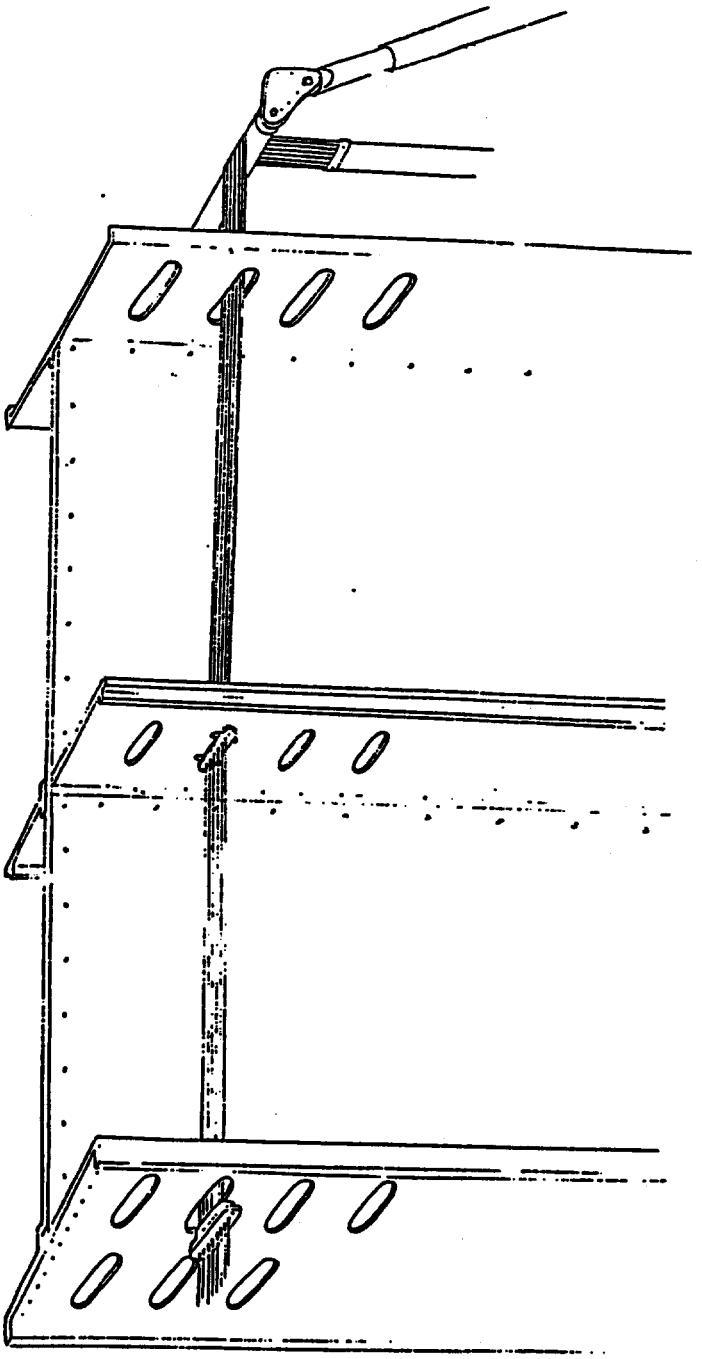

Fig. 4.3.4 Wire stringing : After the wires are pulled out of the exit hole, a feedthrough is moved to the center support and fixed. The side frame is not shown for a better visibility.

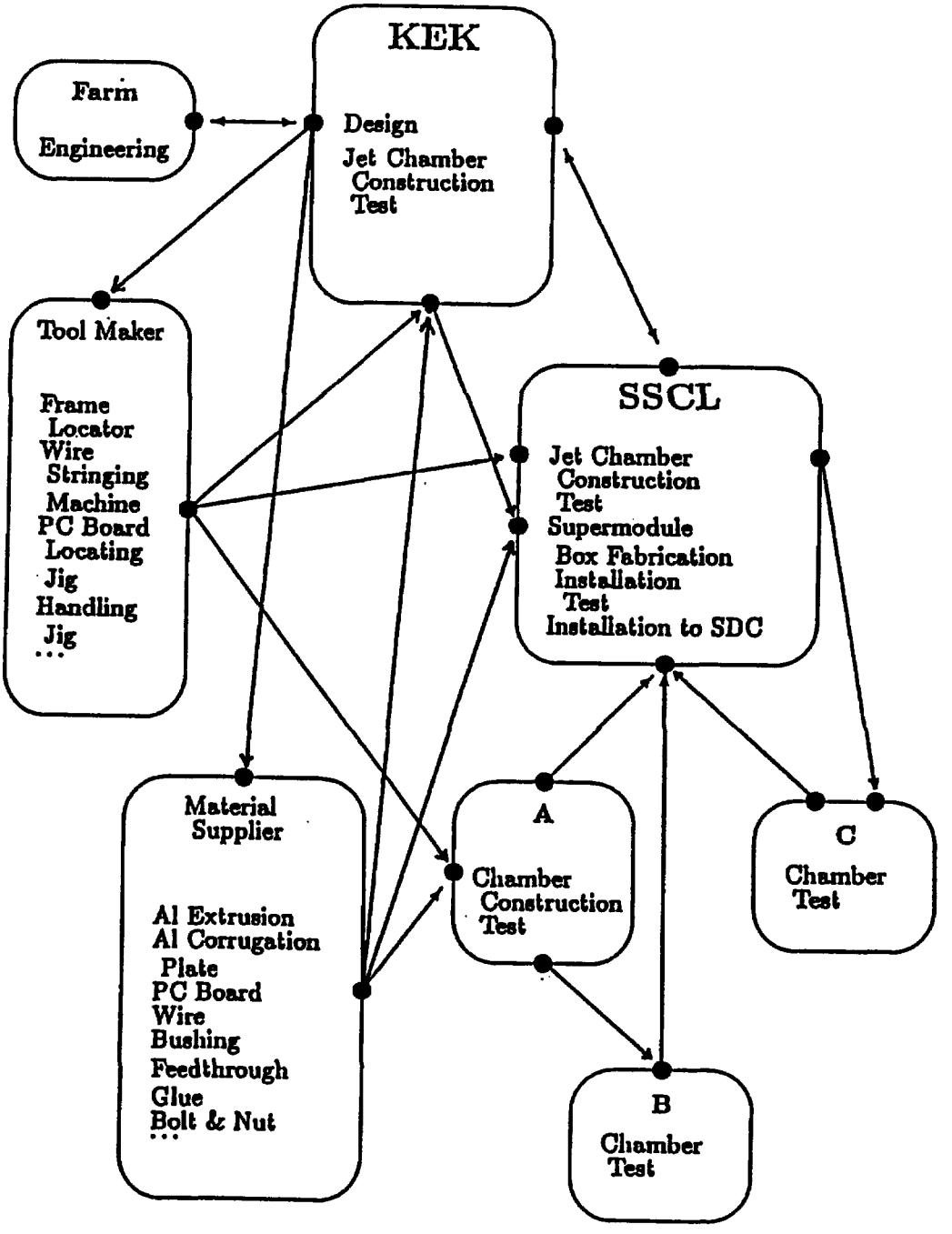

Fig. 4.3.5 Flows of the jet chamber production and relations among institutions.

4.4 Supermodule

4.4.1 Supermodule structure

As depicted in Fig. 4.4.1, the outer chamber system of each octant (BW2 and BW3) consists of four supermodules and the inner chamber system (BW1) consists of three supermodules. An outer supermodule has three theta chamber modules in both BW2 and BW3, and four phi chamber modules and three stereo chamber modules in BW3 and BW2, respectively. An inner supermodule has three theta chambers and two phi chambers.

Since an individual jet chamber module is rigid enough and since its sag is negligible when it is held at six points, we are not directly combining several modules to form a supermodule. Instead we prepare a stiff box made of steel plates of about 1 cm in thickness, structured as a well crib with walls between chamber modules (Fig. 4.4.2). In the outer supermodule each compartment has two rails to roll in and out a chamber module like a drawer. Rail holders are bolted to the chamber module at four corners and at the joints between the center support and the side frames (Fig. 4.4.3) Out of the six rail holders, three at one side have a slide mechanism to absorb errors in the distance between the two rails. Therefore, only the other side determines the chamber wire position. Needless to say a part of the rail holder is made of insulating material like a kind of engineering plastics to isolate the drift chamber electrically.

The inner supermodule has not enough room to afford the rail system in a compartment in the current design (see section 4.4.2). Therefore, individual modules are brought into compartments with thin needle bearing pads and fixed directly to the inner surfaces of the supermodule box at the same six points as the outer supermodule (Fig. 4.4.4). Again the small plates fixed to the chamber module are made of electrically insulating material. Those supermodules are installed on the rail systems which are built beforehand and run parallel to the beam axis on both surfaces of the toroid.

As of writing, a finite element analysis is being prepared and any result is not yet available.

4.4.2 Options

Although no numerical calculation has been done yet, we are studying the following possibilities.

We have gained reasonable feeling that 2 cm thick corrugated sandwich plates made of 0.6 mm thick aluminum sheets can hold chamber gas pressure of 10 gram/cm^2 which we set as the maximum gas pressure difference between the inside and outside of the jet chamber operated at 50 meter below the ground. Since these plates are also rigid enough for the middle plates, we are considering to reduce the module thickness from 40 cm to 34 cm just by replacing 4 cm thick top, bottom and middle honeycomb plates with 2 cm thick corrugated sandwich plates (Fig. 4.4.5).

The current module design is a simple square box and creates a rather large insensitive area at the boundary of octants. If this turns out to be serious, this problem can be much reduced by introducing small complexity. We can prepare two different types of the end and side frames as shown in Fig. 4.4.6. This option introduces some more complexity in jigs, machining and assembly which increases production time and cost.

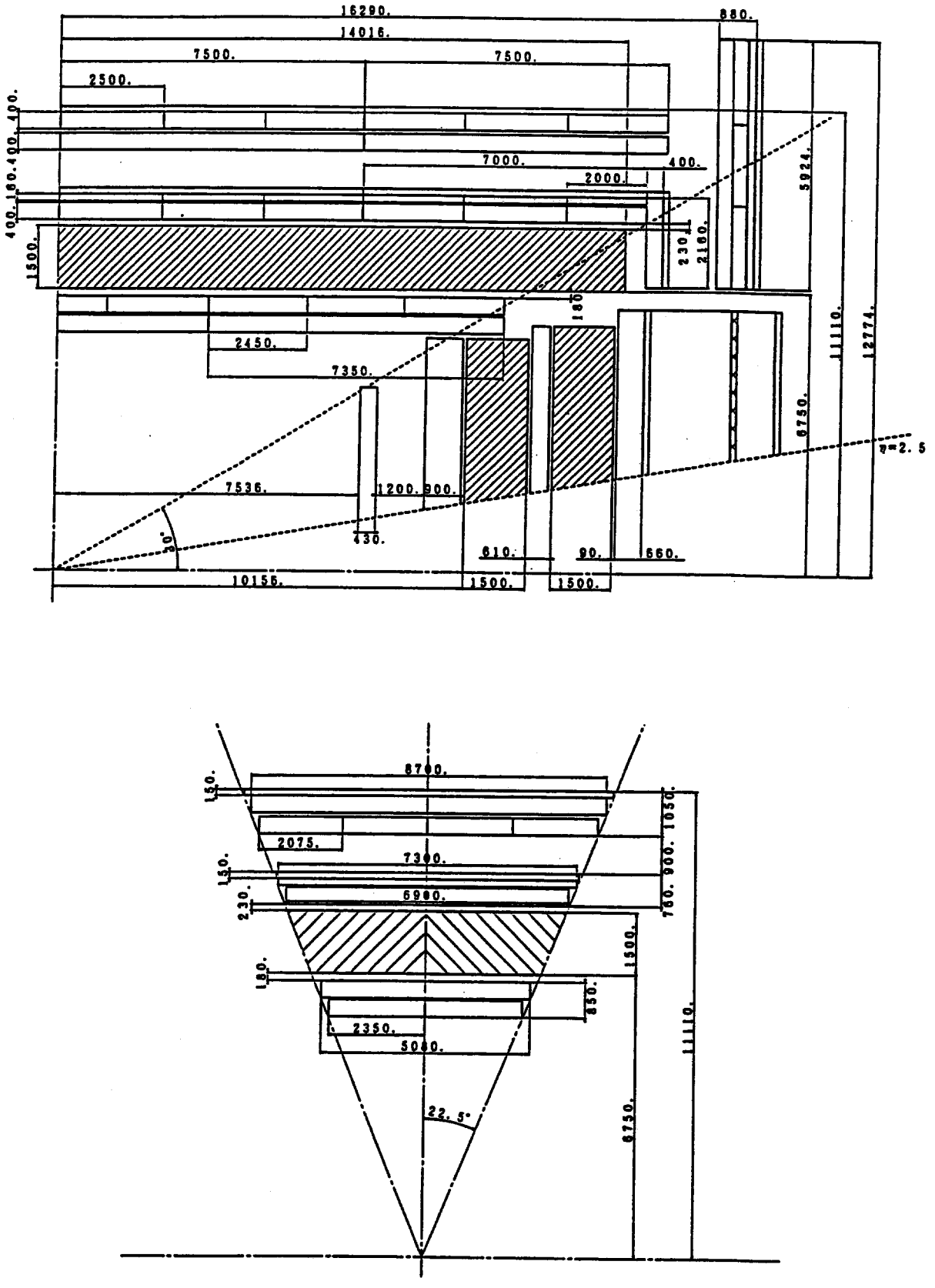

Fig. 4.4.1. The jet chamber module and its supermodule arrangements.

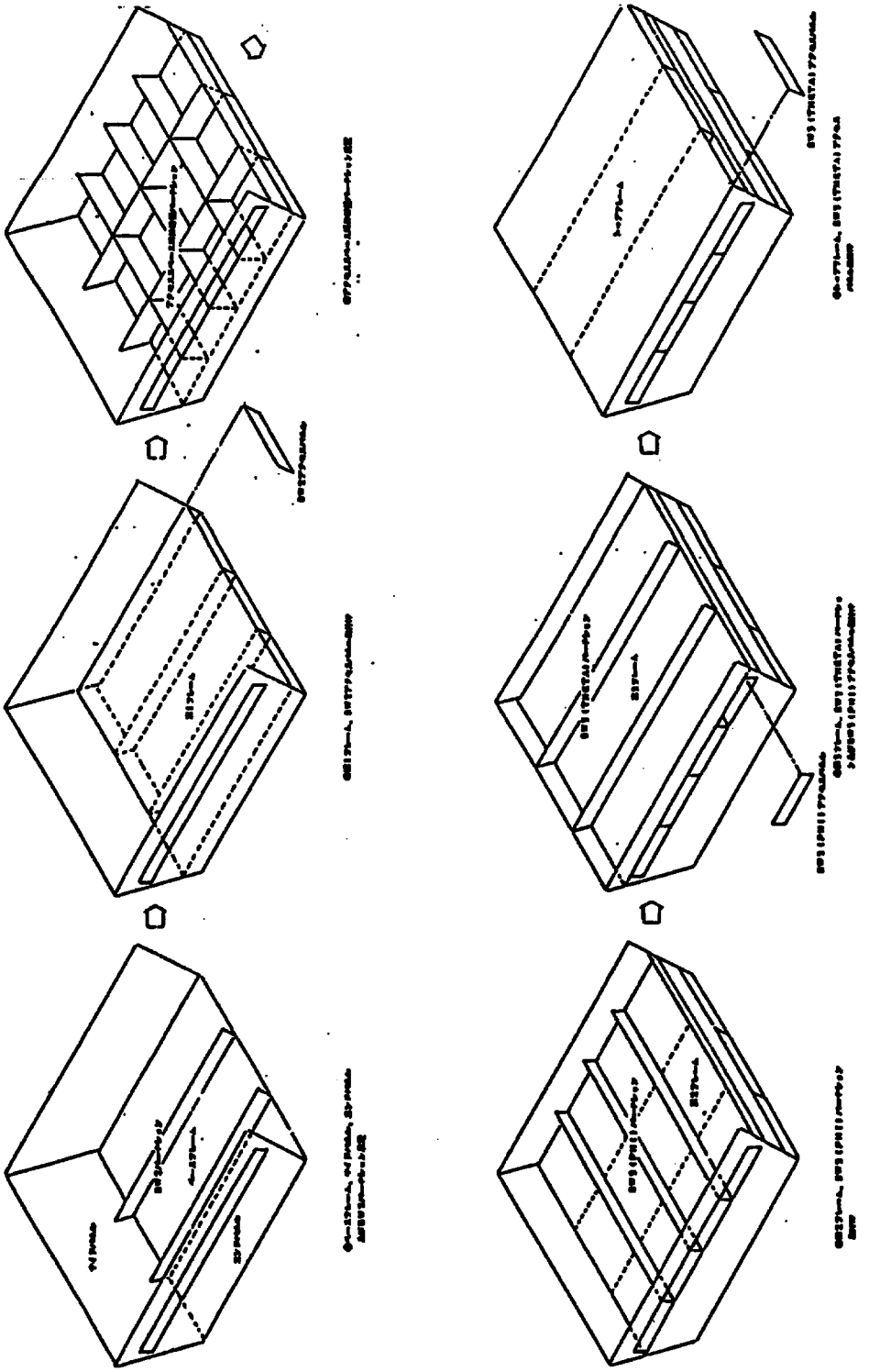

Fig. 4.4.2a. 1) Conceptual illustration of the outer supermodule box production for the jet chamber design.

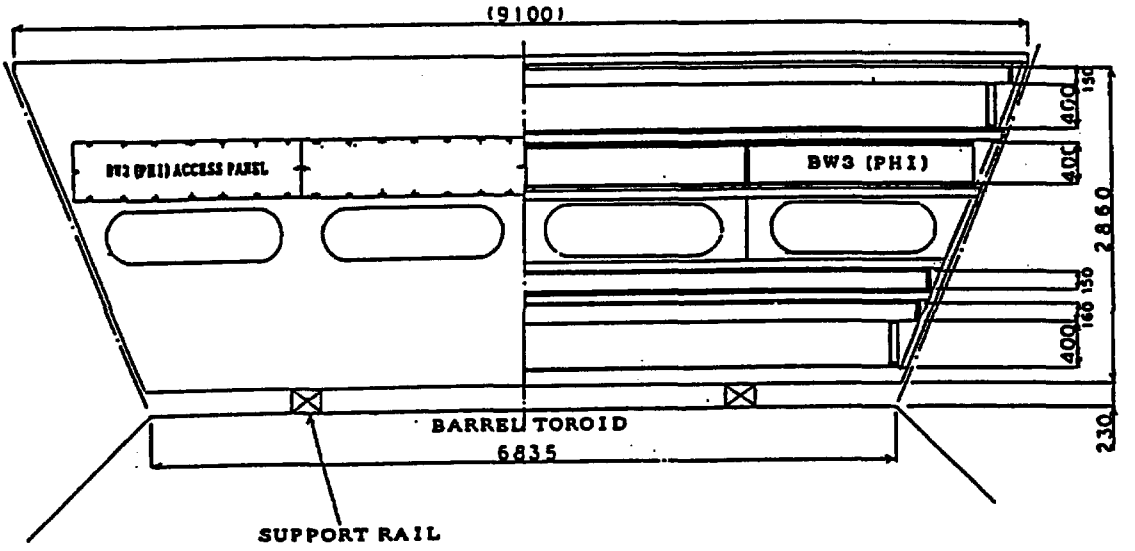

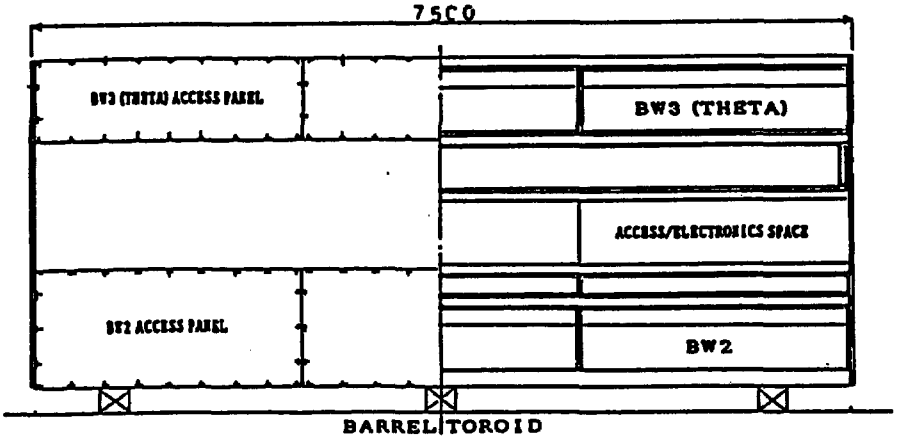

Fig. 4.4.2b. 2) Scaled drawing of the outer supermodule box.

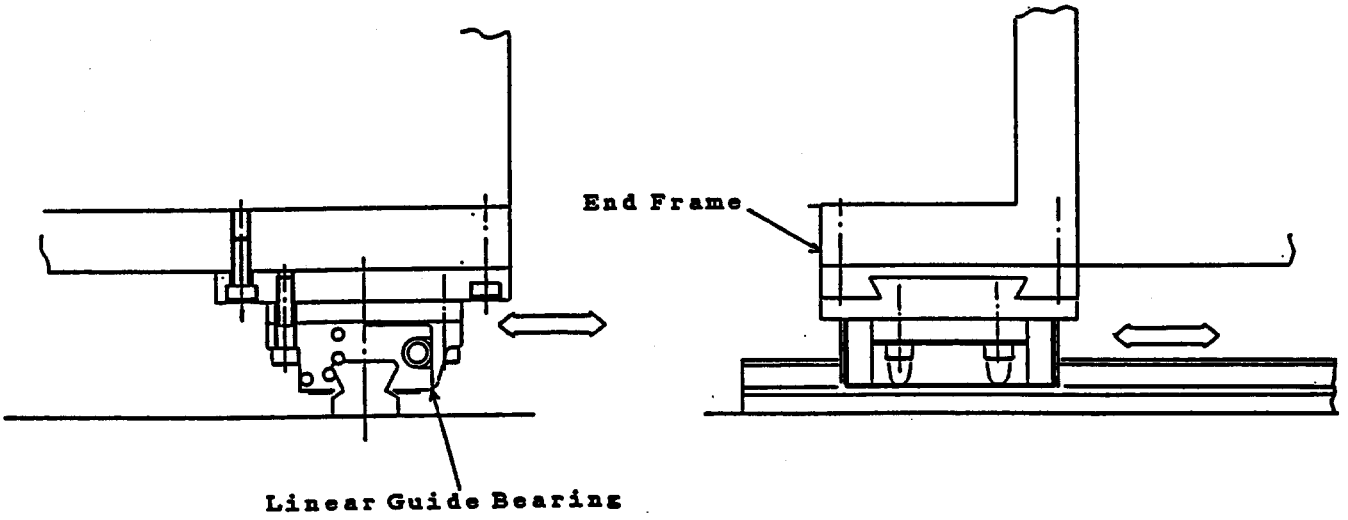

Fig. 4.4.3a. Rail support concept of jet chambers in the supermodule box.

1) Rail holder which can slide perpendicular to the rail to absorb the errors in the distance between the two rails at the time of the chamber installation.

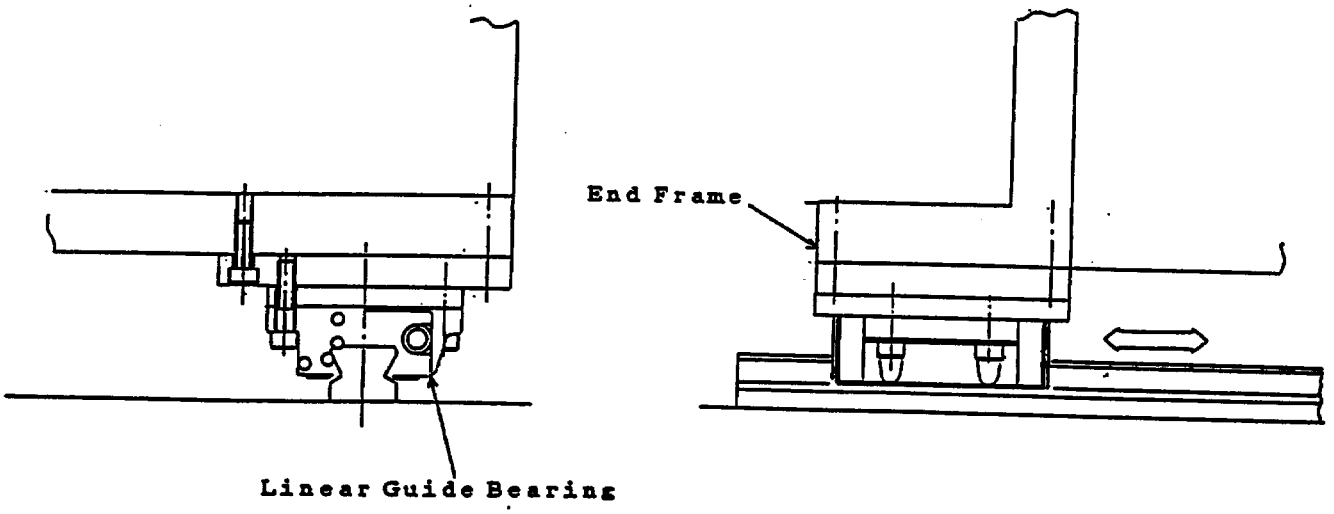

Fig. 4.4.3b. Rail support concept of jet chambers in the supermodule box.
2) Rail holder which does not have a slide mechanism.

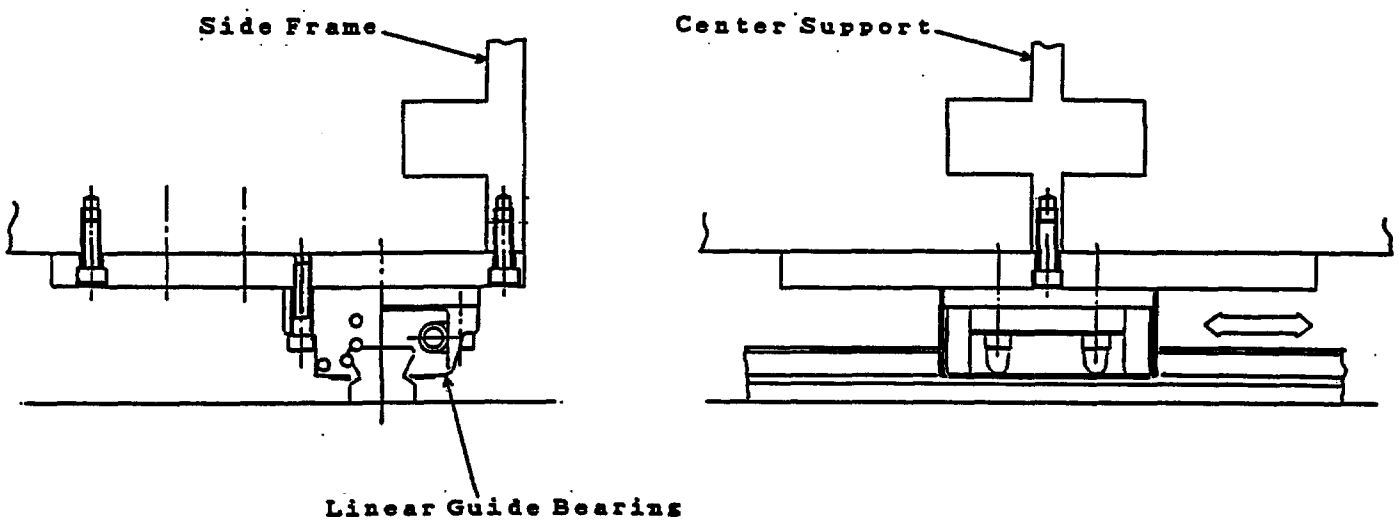

Fig. 4.4.3c. Rail support concept of jet chambers in the supermodule box.

3) Rail holder at the joint between the side frame and the center support.

BW1 Super Module Support

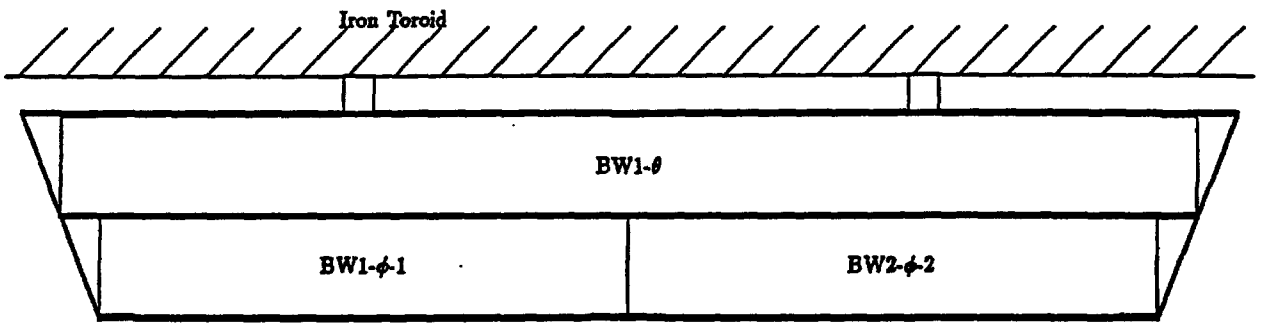

Fig. 4.4.4a. 1) Inner supermodule held from the rails on the inner surface of the toroid.

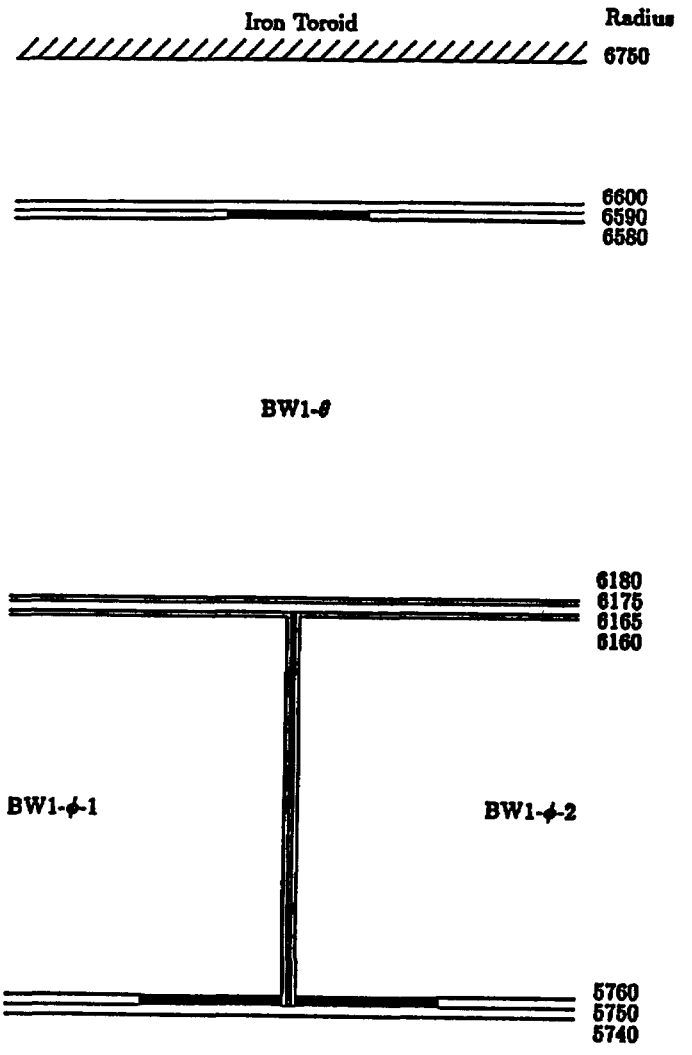

Fig. 4.4.4b. 2) Details around the module boundary and support position. Solid rectangular pieces are the fixing pads.

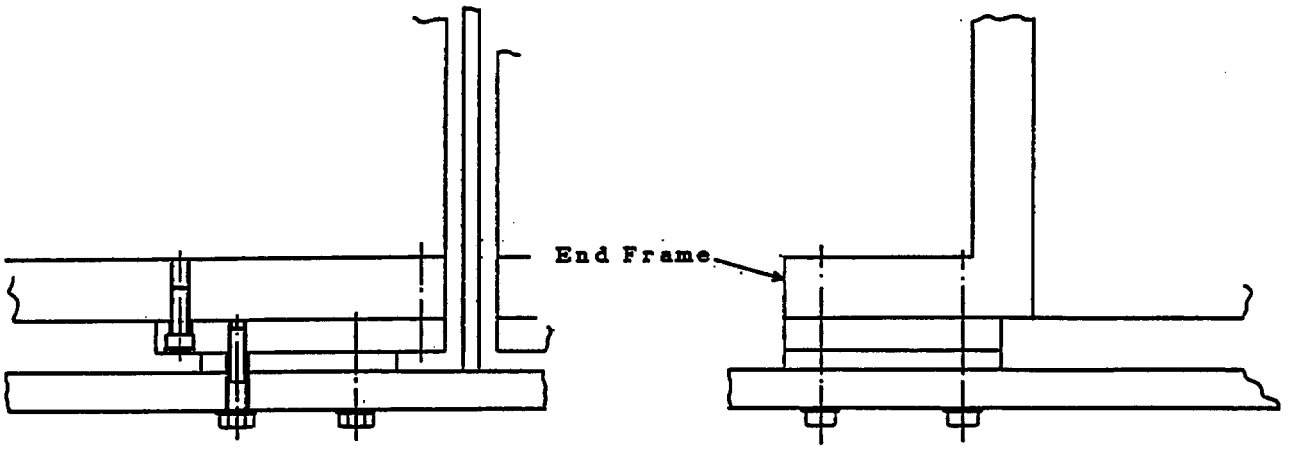

Fig. 4.4.4c. 3) Details of the fixing scheme.

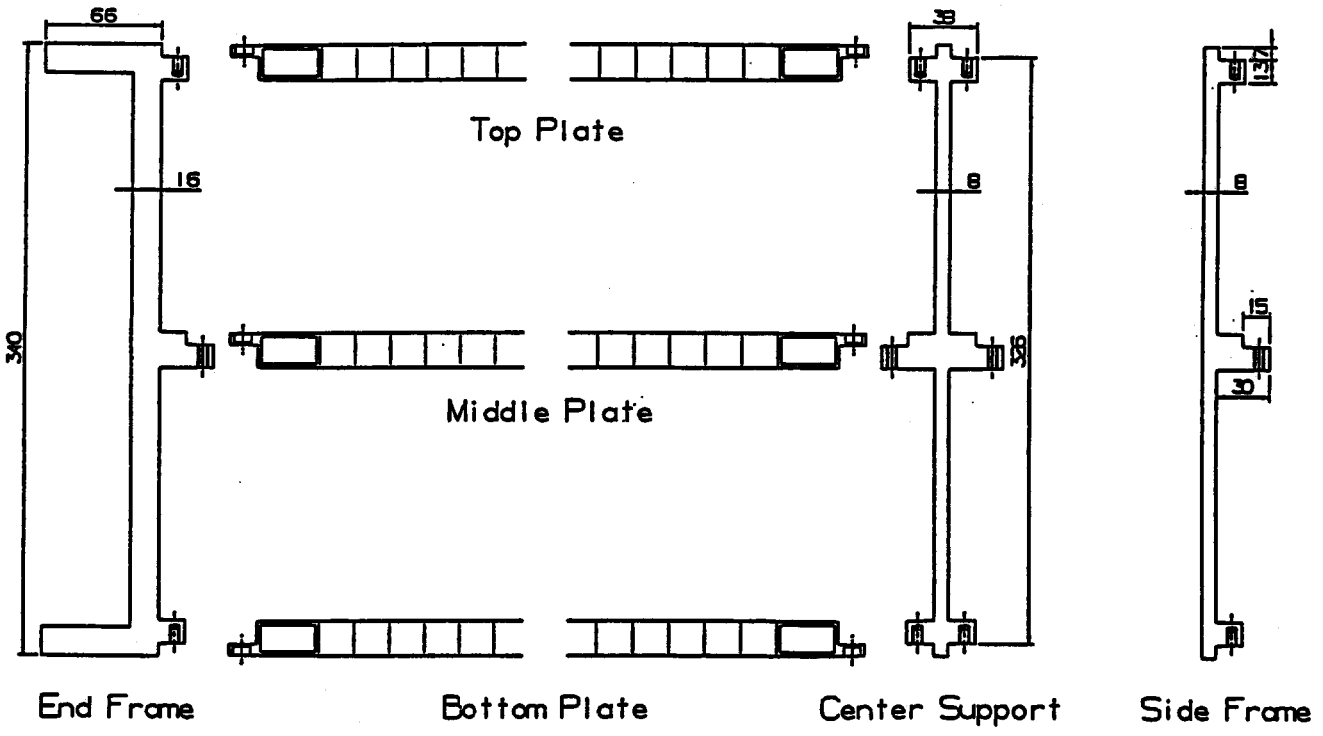

Fig. 4.4.5. An optional design of a 34 cm thick jet chamber.

Optional Frames

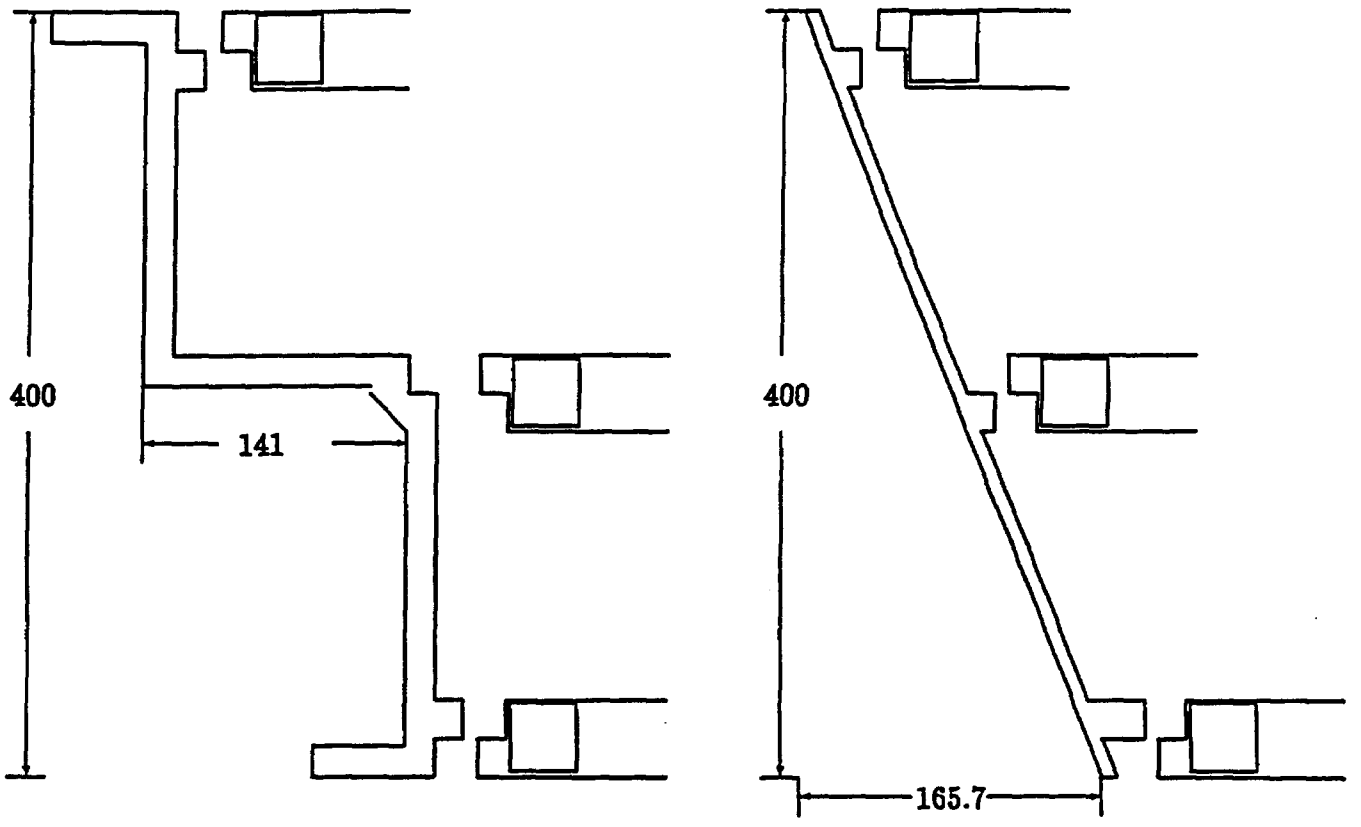

End Frame for θ-Chamber

Side Frame for ϕ-Chamber

Fig. 4.4.6. Optional end and side frames to reduce the dead area at the boundary of the octants.

4.5 Installation and alignment

Since the supermodule boxes are too large for the transportation on road, they have to be assembled at the SSCL site at least at the final stage. When the muon chambers are brought in the laboratory and are inspected, they are installed into the supermodule box as described in the supermodule section. Although both the supermodule box and the chamber modules are designed so that the modules fit in the relative position with required accuracy, the alignment is inspected by using the built-in laser alignment system for wire positions within the module and the optical survey equipments for the inter-module position. The inter-module relation may eventually be measured with the UV laser running through windows on the top, bottom and middle plates of a module and ionizing the chamber gas when the muon system becomes operational [4.5.1]. While they are still on the surface, the supermodule is held in many different directions to simulate the installation on to the toroid surface and the same measurements as those described above are performed.

Completed supermodules are brought down the underground hall and installed on to the toroid by using a crane and chain blocks to make a fine adjustment of the supermodule angle and direction. In order to minimize these fine adjustments, we will design and build a lifting jig which can cope with the different octants. For the installation of the BW1 supermodule, we need to build extensions of the rails inside the toroid. We first set the supermodule on the extension rails in the same way as the outer supermodule and slide it into the toroid structure. Since the jet chamber is much lighter in weight compared to tube chambers, the installation of the supermodule might be much easier and less expensive.

Although we design a rigid enough supermodule box and rely on the rigidity and the survey data performed on the surface, we are going to survey the chamber system in place with an optical survey system we are still designing. Eventually the relative wire positions within an octant may be measured with the UV laser system described above, this time, through the iron and BW1 chambers. For this purpose we need many holes of about 1 cm in diameter in the iron toroid.

For the operation of the muon chamber installation, we need to continuously occupy a 15 ton crane, preferably with double hooks.

Reference

[4.5.1] F.Hartjes, J.Konijn, and Y.Peng, Nucl. Instr. and Meth. **A269** (1988) 544.

4.6 Electronics

4.6.1 Overview

Primary functions of the front end electronics of the muon chamber are a drift-time measurement and a trigger signal production for the level 1 and 2 trigger systems. These functions are similar to those required in the straw chamber [4.6.1]. Thus it may be natural to use common parts for both muon chambers and straw chambers. However, there exist several differences between the two systems which we must taken into consideration:

- Muon electronics is distributed in a very wide area ,
- Muon electronics needs little care for the radiation damage,
- Most of the readout electronics for muon chambers can be easily accessed when the beam is off,
- Conventional cooling technique can be used in the muon electronics,
- Limitation for the power consumption is not so severe in the muon electronics,
- Packaging density of the muon electronics is not so severe compared with that of the straw.

The judgment for the common parts for both muon and straw electronics must be done through careful considerations of cost, development efforts, maintenance, etc.

Although the electronics of muon chambers looks simpler than those of the calorimeter or the central tracker, it does not mean that developments of new electronics is not required. There are many demanding requirements in the electronics for the SDC muon system:

- Number of channels is very large (~100,000 ch),
- The readout system must be synchronous to the beam crossing cycle (16 ns),
- Front end electronics must keep the drift-time information locally until the 1st level trigger (~3 μs) and 2nd level trigger (~100 μs) decision is completed,

- The muon electronics must provide sufficient information to the L1/L2 trigger system.

These require developments of many kinds of high-speed custom LSIs.

In the straw chamber readout, the Time Memory Cell (TMC) chip [4.6.2] will be used for time-to-digital conversion and for first level buffering. A prototype TMC chip has been developed at KEK and already demonstrated a good timing resolution ($\sigma \sim 0.53$ ns), a high density (4 channels of 1 μs storage in a chip) and a low power consumption (~7mW/ch). Thus we propose a muon readout electronics system which uses TMC as a central component.

As for the trigger logic, we are studying two approaches: one option is based on a relatively simple electronics and the other aims a maximum flexibility by using digital electronics. Below we describe mainly the first option, while the other approach is described in Appendix 4.

4.6.2 Readout electronics

Fig. 4.6.1 shows a block diagram of the readout electronics that we propose. High voltages and test pulses are supplied from one end of the muon chamber, and wire signals are read out at the other end. Separation of the readout path from other cables minimizes the unnecessary coupling to the input channels. Since the access to the ends of the chamber is very restricted after installation, we should minimize the number of components in that position and make them as reliable as possible. We attach only a preamplifier to the chamber end as an active component. Although it may be possible to pull out the chamber raw signals to outside the detector without amplification, it looks quite risky due to possible electrical noises in the SSC environment. We use differential signals for the transmission from the preamplifier to a front-end crate through shielded twisted pair cables.

In the Front End Board (FEB), isolation transformers are used to disconnect ground loops. A differential receiver/shaper/discriminator chip (Post Amp) receives the chamber signal and converts it to a timing pulse.

The TMC converts the timing of the input pulses to digital values and stores them in its memory. When the level 1 trigger arrives, the data stored are transferred to the level 2 buffer (L2B) with synchronous to the beam crossing. Fig. 4.6.2 illustrates the data transfer scheme between TMC and L2B. The L2B consists of a buffer memory, readout sequencers and a data compression logic. The L1 read sequencer generates a read sync signal for TMC when it receives the level 1 trigger. The L2B has a register keeping the number of columns to be read (N) which is usually the number corresponding to the maximum drift time. The L1 read sequencer sets a trigger bit at the first column of the data when the readout starts. This marks the trigger point. If another trigger is received while reading an event, another mark of the trigger is written in the trigger bit, and the number of channels to be read is reset to N. Specifications of the chips for the muon readout are listed in Table 4.6.1.

Table 4.6.1. Specifications of the chips used in the muon readout.

Chip	Specifications
Pre Amp	Bipolar device. Differential outputs. 4 ch/chip or 6 ch/chip
Post Amp	Bipolar device. Differential inputs. Shaper amp and discriminator. 4 ch/chip.
TMC	CMOS device. Time-to-Digital conversion and level 1 buffer. 2ns/bit resolution. 4 μsec buffer. 4 ch/chip.
L2B	CMOS device. Readout sequencer, level 2 buffer memory, and data compression logic. 4 ch/chip.

The Data Collection Board (DCB) collects data from FEB's in each crate after receiving the level 2 trigger signal. Assuming a chamber hit rate of 1% and a data size of 4 bytes for each hit, the data transfer rate on the backplane amounts to ~600 kB/sec for the case of a L2 trigger rate of 10 kHz and 14 FEB's in the crate. This amount of data transfer rate can be easily attained with an existing technology. After collecting the data from FEB's, the data are transferred to the event builder through an optical fiber. The DCB also has a network interface for monitoring and debugging purpose.

There are a Signal Distribution Board (SDB) and a Trigger Summary Board (TSB) in each muon local crate. SDB distributes control signals, such as L1/L2 Trigger and System Clock, to other board through the backplane or a front panel connection. TSB is described in the next section.

The jet chamber we propose has 3 sense wires in each drift cell, while the number of channels in a chip is convenient to be a multiple of 2. Thus we will use three chips of 4-ch or two chips of 6-ch preamplifiers in the Amp Card, which receives signals from 4 jet cells. An example of the mounting of the Amp Cards (4-ch version) is shown in Fig. 4.6.3. The front end board has 96 channels of inputs, and it receives signals from eight Amp Cards. We assume the TMC and the L2B chips have 4 channel inputs per chip, and 24 chips of these are implemented on a board. The FEB also contains trigger logics as described below.

Table 4.6.2 summarizes the primary parameters for the barrel and intermediate muon chambers and associated electronics. We need 72 Local Crates in total for the barrel muon chamber system; that is, 9 crates per octant. All the local crates for the barrel section are placed on the space between BW2 and BW3 at both ends of the octant. A conceptual view of the local crate mounting is shown in Fig. 4.6.4.

4.6.3 Trigger electronics

The trigger sequence for the level 1 trigger of the muon chamber, described in section 2.2, can be divided to 2 successive steps: the cell trigger and the layer trigger. The former is a process inside each jet cell to eliminate spurious hits. The momenta of tracks are analyzed in the latter step by means of a mean-timer method. The circuits for the cell and layer triggers are included in the Front End Board (FEB) as shown in Fig. 4.6.1. The block diagram of the Cell/Layer Trigger Logic is shown in Fig. 4.6.5. Each FEB includes 4 Cell /Layer Trigger chips and each chip has 27 input channels. Three of the inputs are used to connect the information from an adjacent cell.

Table 4.6.2. Primary parameters for the barrel and intermediate muon electronics.

Layer	Wire	Channel	Super-module	Ave.No. Ch/SM	Amp Card 12ch/card	FEB 96ch/board	Local Crate	Ave. No. FEB/Crate
BW1(ϕ)	6	8200	24	341.7	684	86	12	7.2
BW1(θ)	6	10100	24	420.8	842	106	12	8.8
BW2(θ)	6	13400	32	418.8	1117	140		
BW2(s)	2	6100	32	190.6	509	64	16	12.8
BW3(ϕ)	6	19300	32	603.1	1609	202	16	12.6
BW3(θ)	6	14800	32	462.5	1234	155	16	9.7
sub total	32	71900	176	–	5995	752	72	–
IW2(θ)	6	2300	16	143.8	192	24		
IW3(θ)	6	6100	16	381.3	509	64		
IW3(ϕ)	6	12100	16	756.3	1009	127		
IW3(s)	2	2500	16	833.3	208	27	32	7.6
sub total	20	23000	64	–	1918	242	32	–
Total	52	94900	240	–	7913	994	104	

The block diagram of the Cell/Layer Trigger chip is shown in Fig. 4.6.6. The outputs from the Layer Trigger logic are ORed and sent to the level 1 trigger circuit. In this design the Cell/Layer Trigger chip includes two sets of Layer Trigger logics in order to maintain two different p_t thresholds. An output logic counts the number of tracks accepted by one of the two sets, while whole information from the other set is transferred to a level 2 trigger processing.

The Cell Trigger logic finds a track of p_t more than ~10GeV/c by making a "two out of three" coincidence. An example of the logic is shown in Fig. 4.6.7, where input signals are first clipped to have a fixed pulse width, and then they are fed into a "two out of three" coincidence circuit. The output timing is determined by the second hit in this design.

A schematic diagram of the Layer Trigger logic is shown in Fig. 4.6.8. The circuit is basically a pair of shift registers which have a length corresponding to the maximum drift time. The Cell Trigger outputs from a pair of staggered cells are fed via opposite ends of the shift registers and run in opposite directions. The gates of the shift registers at a same column are connected to an AND gate. The AND gates are strobed by the signals from scintillation counters delayed through another shift register circuit, the total length of which approximately corresponds to the maximum drift time. The delay circuit must be programmable, *i.e.* the amount of delay and the length of the signal train are adjustable, in order to make the momentum threshold variable. The output from the AND gate array has information of the track position. This information is encoded to 6-bit data and transferred to a level 2 processing.

The signals needed for the level 1 trigger are transferred to a Trigger Summary Board (TSC) through a special backplane or a front connection. The other signals for a level 2 trigger are buffered in a level 2 trigger buffer and sent to the TSC after receiving a level 1 trigger signal. The TSC further processes the trigger signals and sends the results to the surface trigger crate through optical fibers.

References

[4.6.1] Y.Arai, H. Ikeda, and Y. Watase, *Conceptual Design of Straw Tube Readout with TMC*, Version 1.0, Aug. 21, 1991. SDC-91-63.

[4.6.2] Y. Arai, T. Matsumura and K. Endo, *A CMOS Four-Channel x 1K Time Memory LSI with 1 ns/b Resolution*, to be published in IEEE Journal of Solid-State Circuits, Vol. 27, No.3, March 1992.

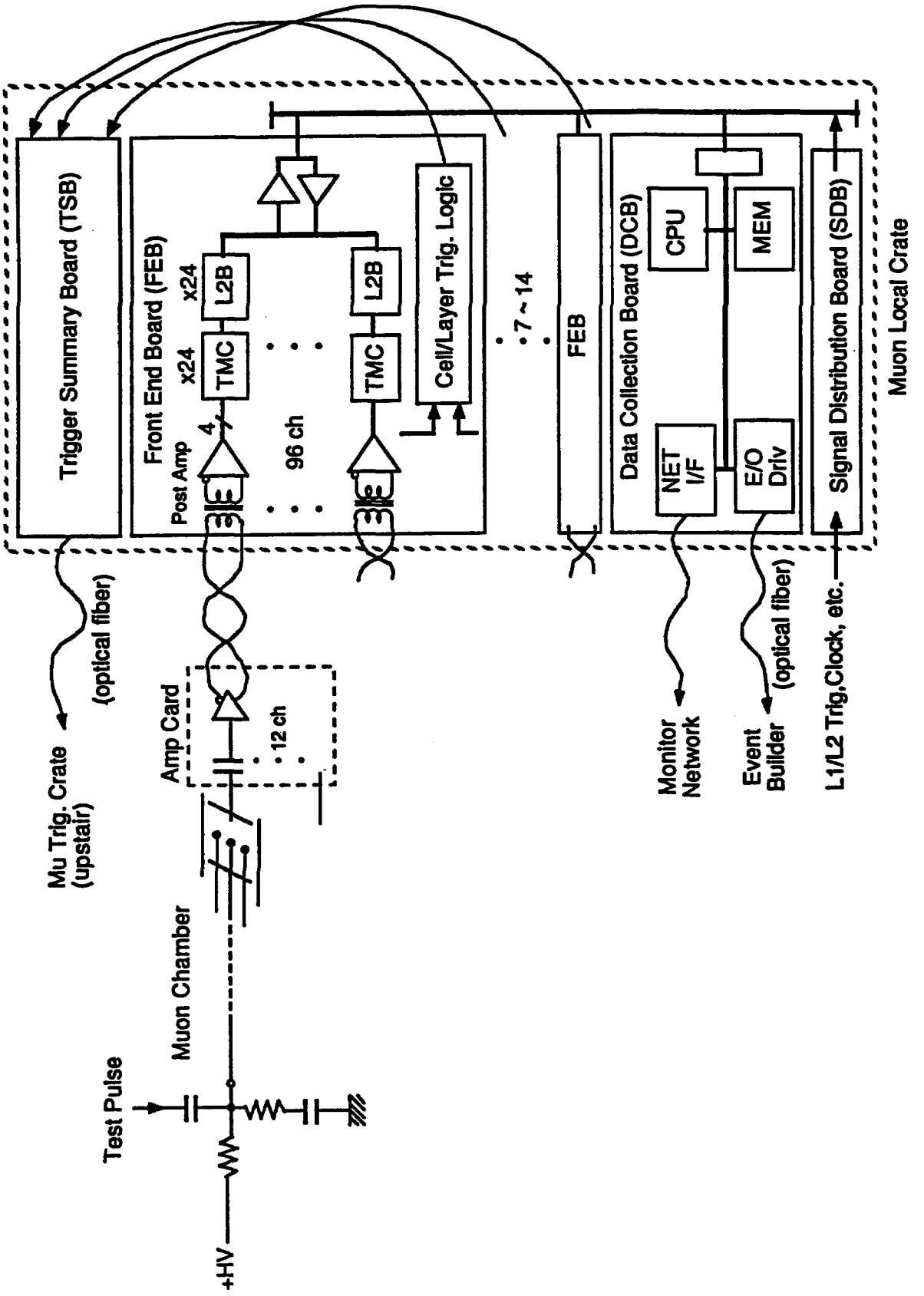

Fig. 4.6.1 Front End Electronics for Muon Chamber

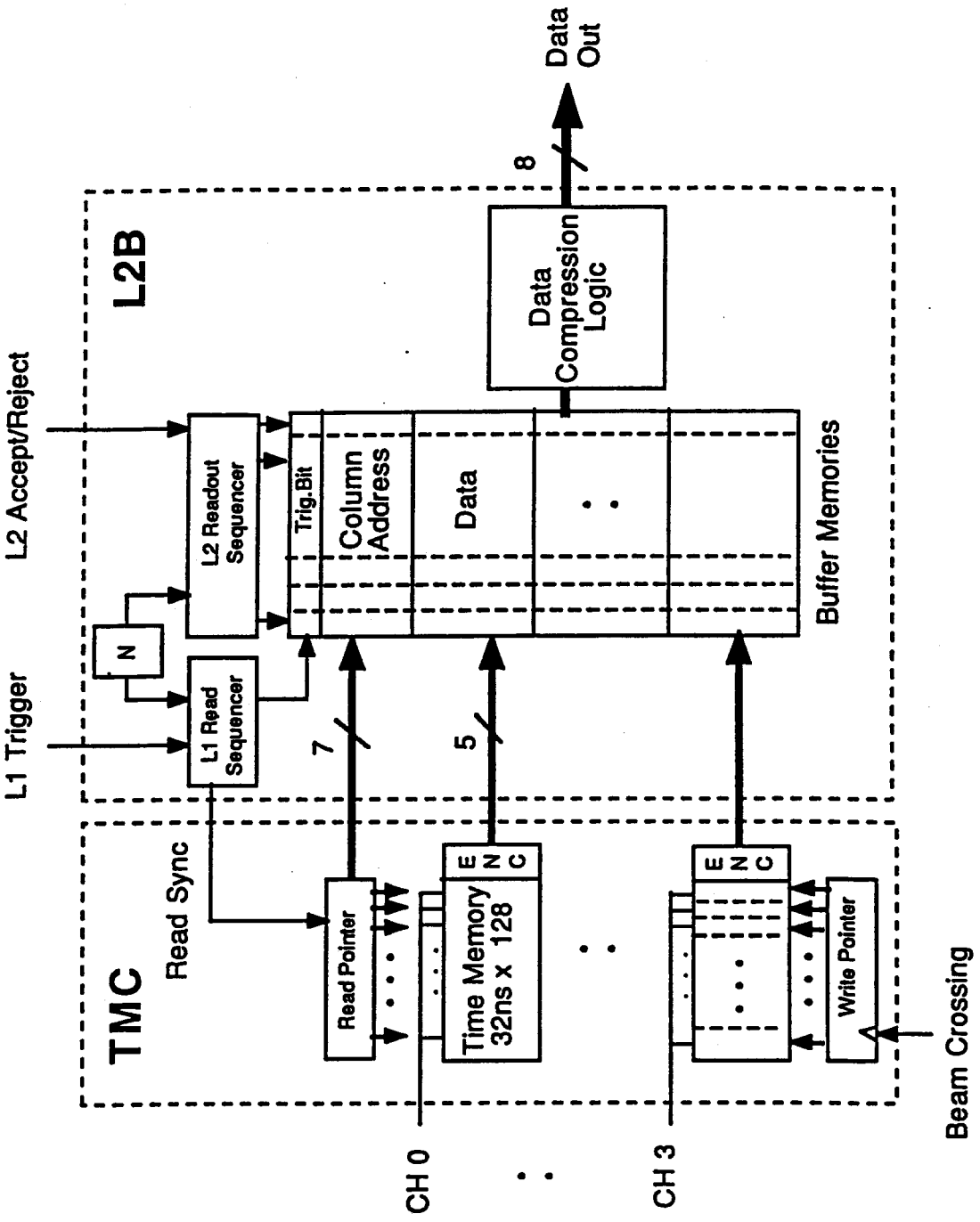

Fig. 4.6.2 TMC and L2B Readout Scheme.

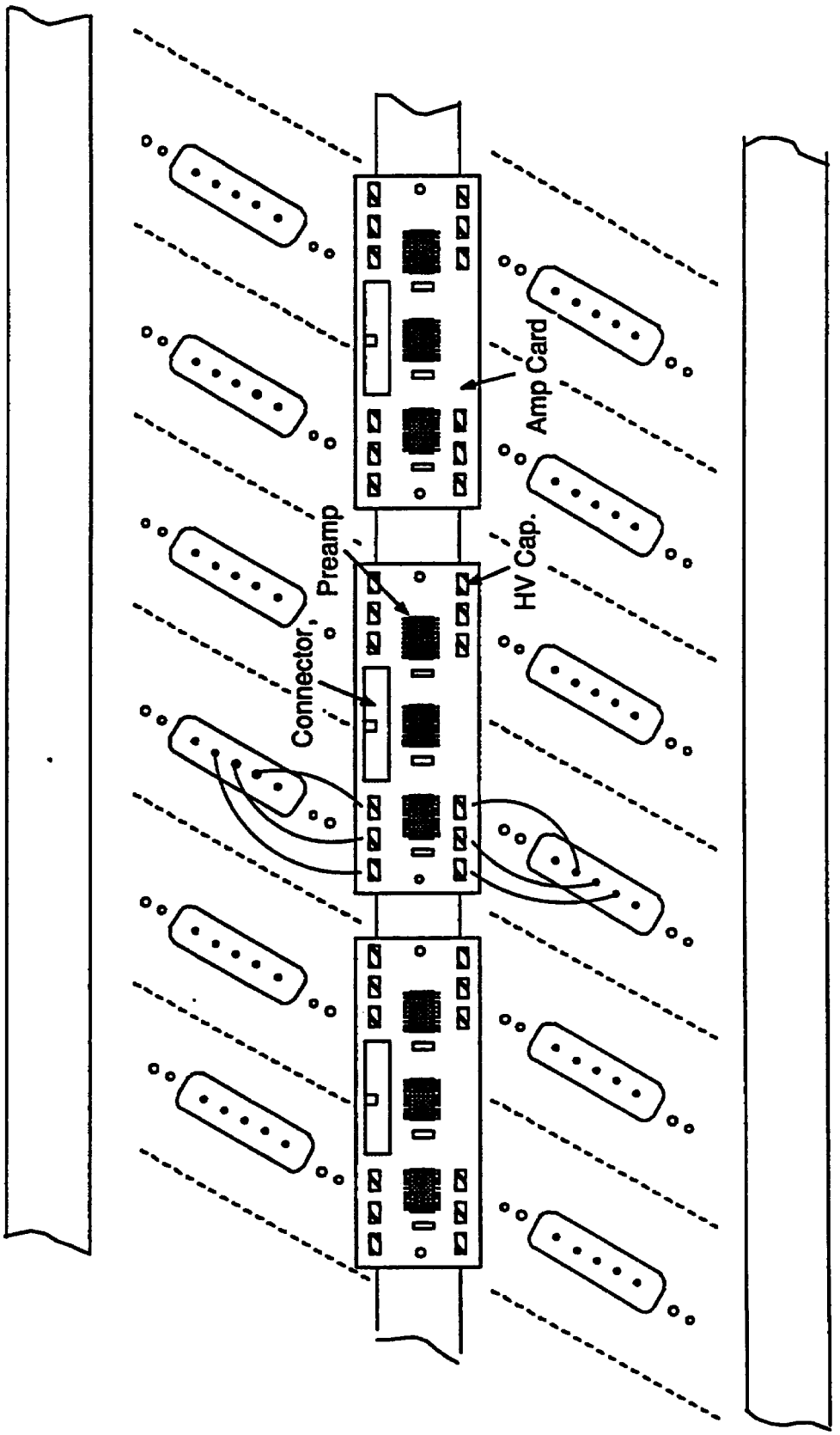

Fig. 4.6.3 Amp Card Mounting Scheme.

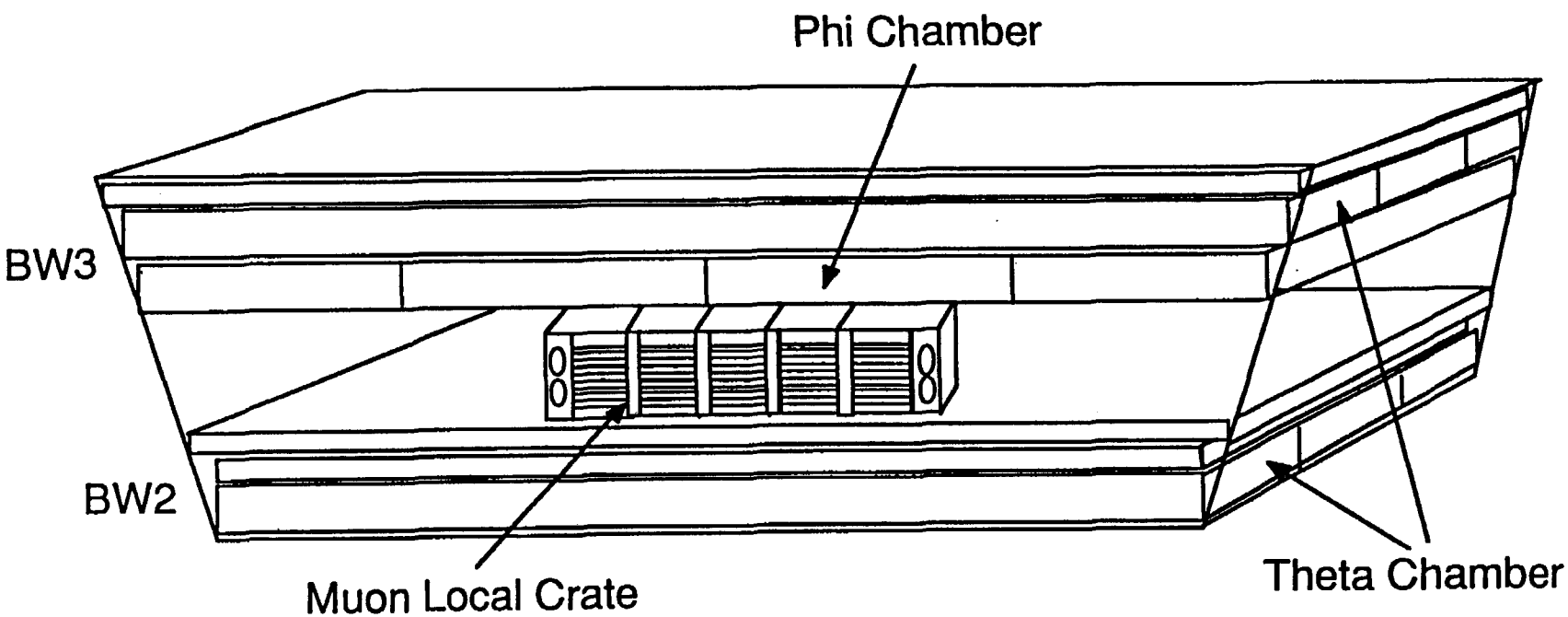

Fig.4.6.4 Local Crate Mounting Sheme in the Super Tower.

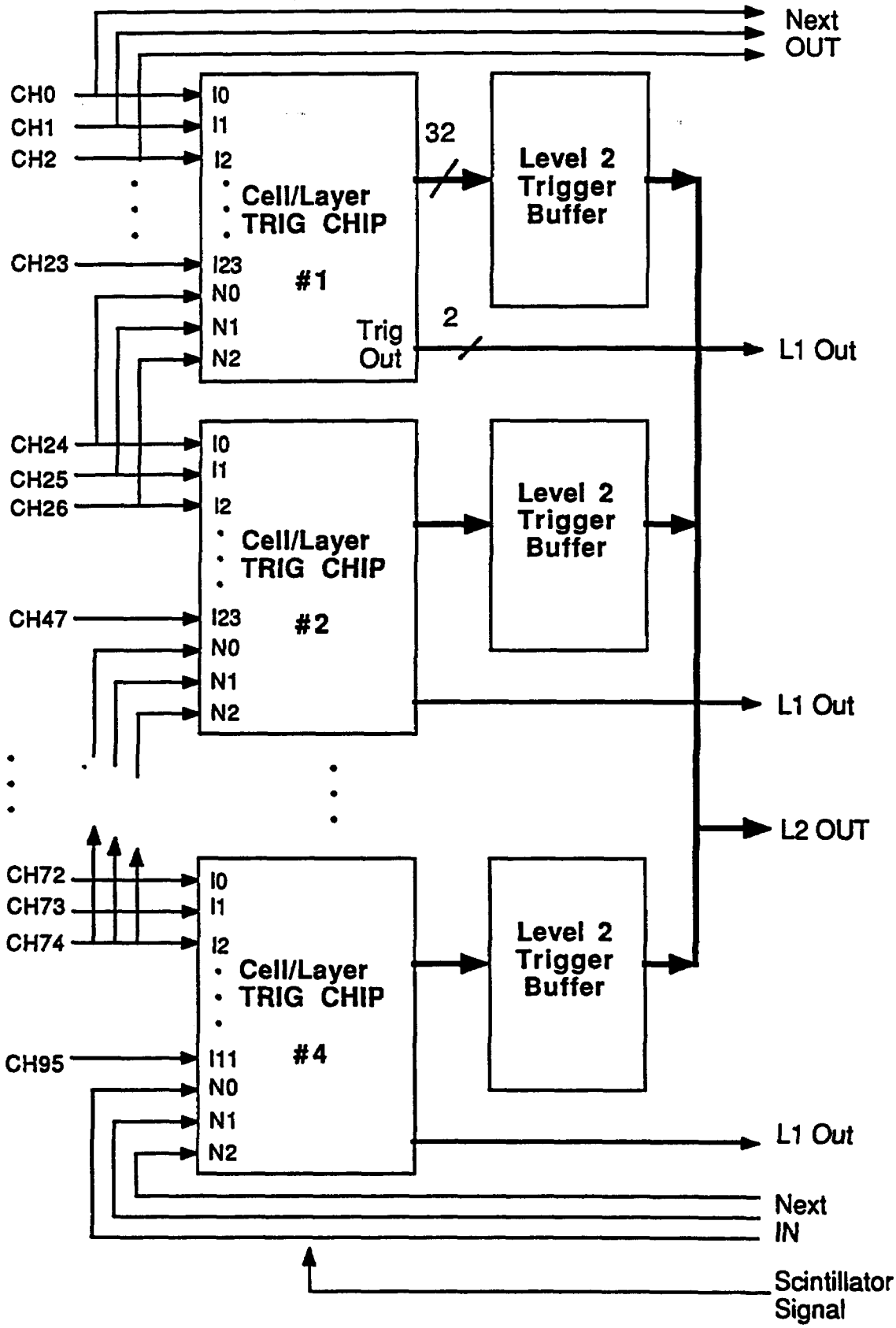

Fig. 4.6.5 Cell/Layer Trigger Logic.

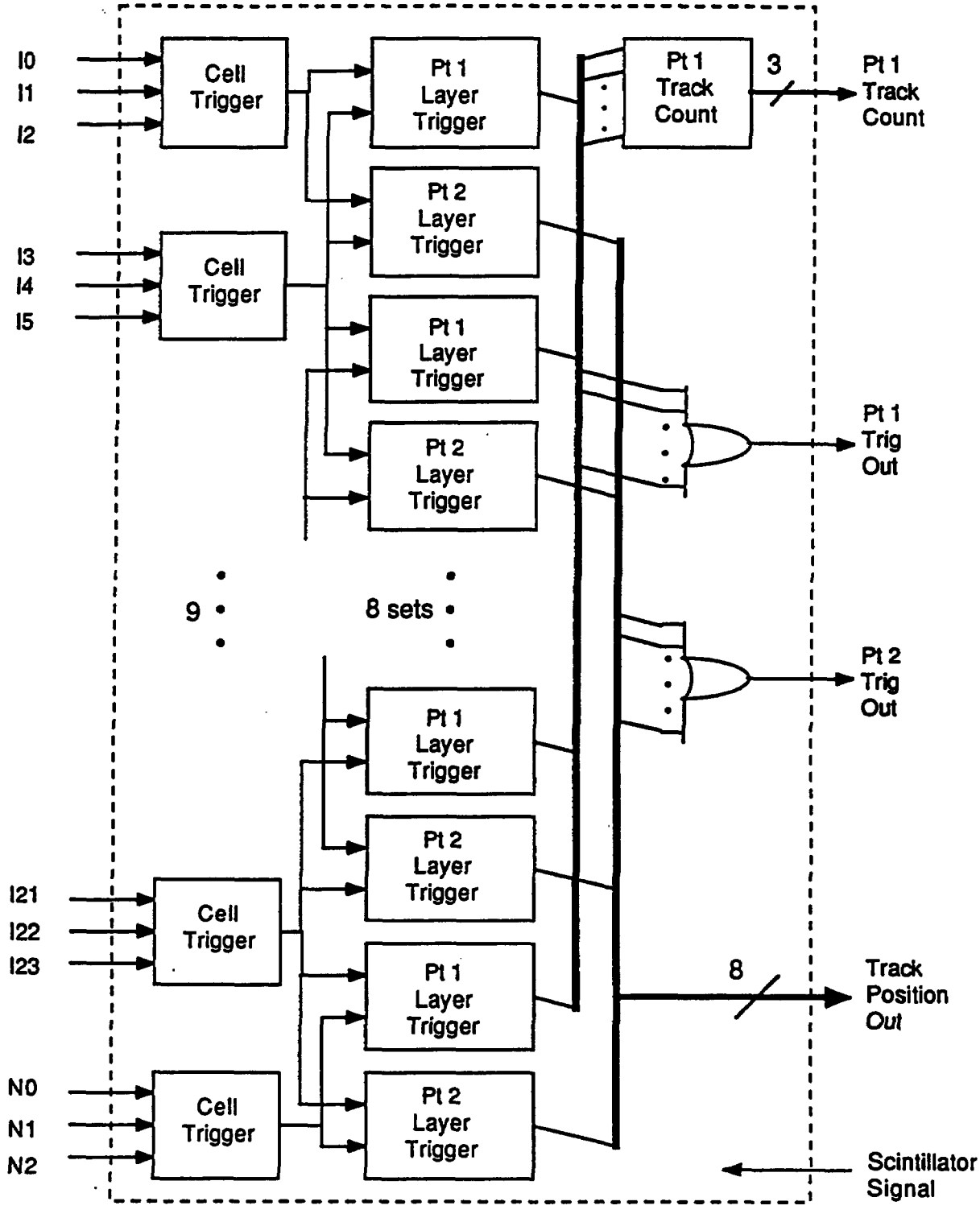

Fig.4.6.6 Cell/Layer TRIG Chip.

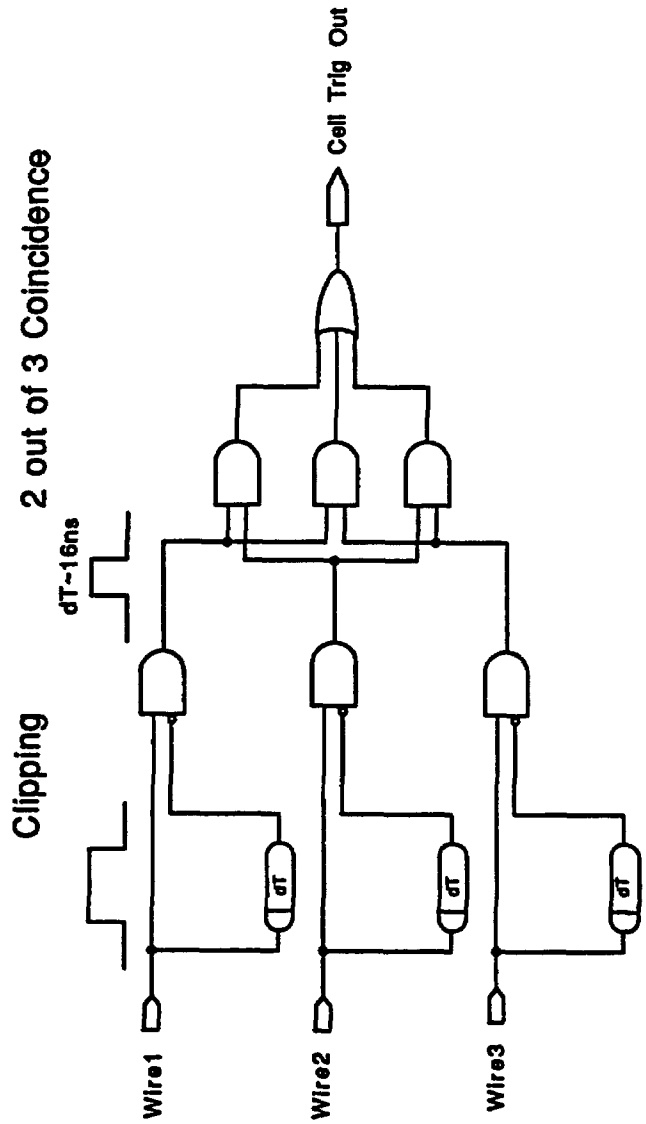

Fig. 4.6.7 Cell Trigger Logic

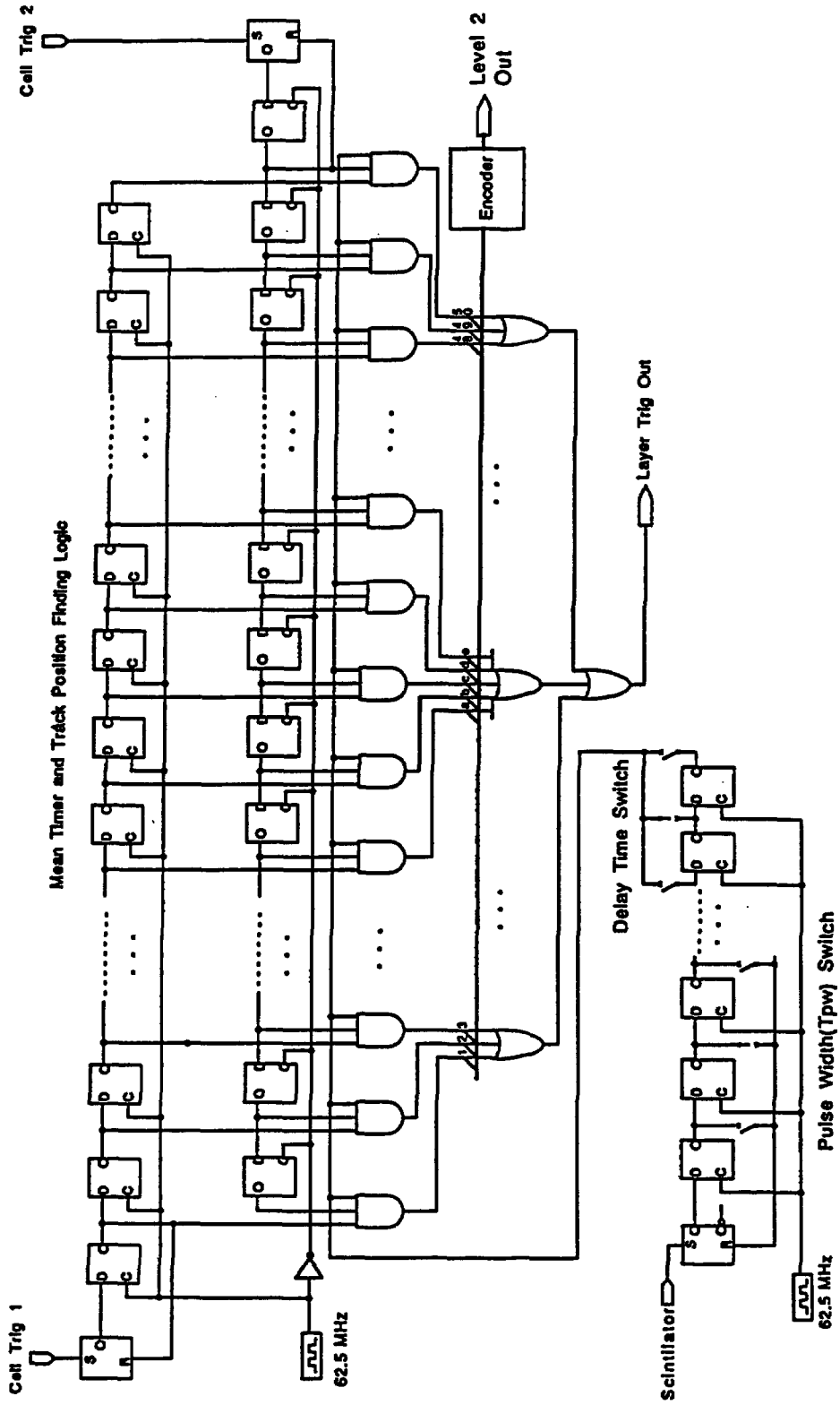

Fig. 4.6.8 Layer Trigger Logic

§5. Schedule and Cost

5.1 Schedule

After the decision in February 92 on the chamber type, we review the current design in details and redesign the chamber and its production jigs and machines so that it best fits the geological conditions and the capabilities of the participating groups. This will complete before the summer 92. Before the completion of the redesign, when we finish the essential part of the study, we start producing materials and machines. We complete the first production prototype by the end of Japanese fiscal year 92 (March 93) including cosmic ray tests. After redesigning and preparation for setting up other construction center(s), full production will start around summer 93 and last until March 96. During this period completed chamber modules are shipped to the SSCL in several batches and installed into super modules. The first super module of BW1 is installed into the toroid structure summer 96. Whole installation including the survey and alignment in the underground hall will take about half a year.

The followings are our current estimation of the time needed for a single module production.

1) Frame assembly completed with the middle plates one module occupies the assembly machine for one day due to overnight curing of glue	1 day
2) Cathode installation one side in one day due to over night curing of glue before turning or removing from the place	2 days
3) Inspection	1 day
4) Wire stringing may be reduced by about half if two crews can efficiently work from both sides simultaneously	4 days
5) Inspection	1 day
6) Top/Bottom plates	1 day

7) Gas leak and performance test 5 days

Needles to say, this does not mean that we produce only one chamber in 15 working days (3 weeks). Each operation can accept one after one. However if we prepare only one set of machines and jigs, the wire stringing operation could be the bottle neck of the total production line. Certainly we need to design most efficient lines of production and to establish multiple production centers. At the moment we feel that 100 modules per year at one production center is a reasonable design goal. This is translated that we need 3 production centers to produce 568 jet chamber modules in 2 and a half years.

5.2 Cost

According to the WBS in 'SDC Muon Chamber Cost Comparisons; 11/8/91 ', cost for the material dominated the over-all cost of the jet chamber system. The honeycomb plates for middle plates and both the top and bottom plates dominated the cost for the material.

So far, we bought two pieces of 4 cm thick honeycomb panel of 3 m x 4 m for the middle plates of the R&D prototype. The company charged us 1,200,000 yen which is about $8,600 with an exchange rate of 140 yen/dollar, so the unit cost became $358/m^2. The price used in the WBS was $247 which seems to be a bit conservative. In fact the company told us that the price might go down significantly, say 1/2, if we order several hundreds pieces of plates of this size.

As discussed in section 4.2.2.(2) and also stated in Appendix 2, the corrugated aluminum technique will be used for fabricating those plates. Then the price for them may come down significantly. One Japanese company is suggesting that the production cost of a corrugated plate of 0.3 m x 1 m is 590 yen ($4.2) including the material cost provided that a sheets of 0.6 mm thick aluminum is formed to be a 38 mm thick corrugation. If we use a 1 mm thick aluminum sheet for the skins, the unit cost for the material to fabricate the 4 cm thick panel is about 5,700 yen ($40.7)/m^2. Thus, the material cost for the corrugation is actually very cheep. Although it is not clear at this moment that the cost for glueing the skins on the corrugation core and putting appropriate frames around the core to make the proper

panel for top/bottom plates, the final cost may be significantly cheaper than the honeycomb panel.

Another item that is contributing the material cost significantly is a GFRP plate for the cathode. The unit cost used in the WBS was $17.93/m for us, while the one used for the oval chamber was $4.27/m. Those two numbers does not seem to be consistent. Anyway, cost minded optimization for the cathode including the choice of the material should be worked out seriously.

§6. Conclusions and Outlooks

We proposed the system of jet-type drift chambers for the barrel and intermediate muon detectors of SDC in this report. Below is the summary of the proposed system;

type of cell (θ, ϕ)	tilted jet-type drift chamber, staggered
drift distance	40 mm max
chamber gas	Ar/CO_2/Methane (89/10/1), 1 atm.
wires	3 sense, 4 potential, 2 guard wires
cathode	plane
high voltage	+2.07 kV (s), +2.33 kV (p), -3.04 kV (c)
maximum drift time	800 nsec
ionization length /meas.	1 cm
local spatial resolution	better than 250 μm / measurement
two track separation	< 5 mm
type of stereo cell	8 cm × 8 cm drift tube chamber, staggered
chamber size (θ, ϕ)	2.5×9×0.4 m^3 max
chamber weight (θ, ϕ)	940 kg max
barrel chambers	264 (θ), 176 (ϕ), 96 (s)
intermediate chambers	64 (θ), 64 (ϕ), 48 (s)
readout channels	71.9 K (barrel), 23 K (intermediate)
preamplifiers	12 ch. amp cards on chambers
time measurement	TMC (δ_t=1ns) with buffers of 4μs depth
level 1 trigger	2-out-of-3 coincidence in a cell and mean timers for layer coincidence
L1 rate at 20 GeV/c	1.8 kHz (prompt dominates)
50 GeV/c	0.16 kHz
position resolution	200 μm/ superlayer
$\Delta p_t/p_t$ at 50 GeV/c	17 % (η=0), 14% (η=1.0)
$\Delta p_t/p_t$ at 500 GeV/c	33% (η=0), 23% (η=1.0)
reconstruction efficiency	> 95% at any station (>90GeV/c)

We believe that the proposed design described has the following advantages:

Mechanical structure :

- the basic unit is a simple box structure
- the intermediate wire support keeps wire sag within a tolerable level
- simple frame structure realizes light weight for its size minimizing gravitational sag
- the chamber module has the excellent structural stiffness
- module size and weight is appropriate for assembly, transportation and installation
- light weight and stiff structural stiffness make support mechanism with accurate alignment realistic
- gas piping is straight forward
- gas seal is simple and certain
- structure withstands gas pressure difference of max 10 g/cm^2
- wire position is determined by NC machined end frames
- open box structure is stiff enough for wire stringing operation
- materials needed are readily available
- chamber module and support structure are mechanically independent allowing parallel production and easy installation
- 4-point (or 6-point at most) suspension of chamber module is adequate

Drift chambers :

- jet cell structure is simple having one wire plane and simple cathode planes with no strip patterns
- jet cell is tilted to point the interaction region with no appreciable drift-field changes
- the field is sufficiently uniform providing constant drift velocity and linear x-t relation
- the spatial resolution of drift chamber is excellent for its size
- resolution of double track separation is about 5 mm and has been proven by beam test data
- multi-hit capability to distinguish high momentum muon tracks from accompanying electromagnetic debris

Chamber gas :

- the chamber is operated with well known nonflammable gas
- the chamber is operated close to saturating drift velocity providing stable long-term operation and immunity to environmental changes
- the gas gain is approximately 10^5 with relatively low high-voltages

Triggering :

- two layers in one chamber module are half-cell staggered so that simple and powerful trigger can be formed utilizing a drift time sum between a pair of staggered cells
- staggered cell structure provides definite one-to-one correspondence in each superlayer so that trigger system is systematic and simple
- basic trigger pulse formed by 2-out-of-3 three logic in a cell provides high efficiency, suppression of spurious hits and 1-st order cut of low energy particles or off-angle tracks (cosmic rays)
- the same trigger circuit is used in ϕ-chambers to select tracks that originates from the I.P. and to effectively eliminate cosmic rays
- the output of trigger mean timer is strobed by fixed-delayed signals from trigger scintillation counters
- the adjustable width of the strobe signal determines the tolerance of the angle measurement providing 2-nd cut with variable p_t
- outputs from mean timer circuits have position information that can be used in higher level triggers

Readout electronics :

- the maximum drift time of 800 ns fulfills the SDC DAQ requirement
- the drift time is digitized and stored by a compact chip TMC, the proof of principle of which has been demonstrated by a 4-ch prototype

Pattern recognition :

- each drift cell has track identification capability and provides a track vector for easy track connection to other layers
- double layer of half-cell staggered chamber allows independent confirmation of track existence

It is also our belief that nobody knows what will happen in the exciting TeV region physics that can be opened up by SSC. Whatever happens, new discoveries or no discovery, the luminosity must be upgraded eventually at SSC to continue pursuing more physics in depth and in energy. The SDC detector must be ready for future high luminosity operation. Under such conditions, the muon detection capability in the transverse momentum region of over 100 GeV/c must be maintained to be of best possible quality, not only for providing triggers and information redundant to the SDC inner tracker, but also for providing self-sufficient information such as charge determination without relying upon the inner tracker, the functionality of which might become limited in the high luminosity operation. The physics associated with muons of a few hundred GeV/c, such as heavy Higgs, new W'/Z', WW scattering and new technicolor resonances, most of which require high luminosity operation, will certainly become important once the initial phase of SSC physics is over.

Acknowledgment

The authors wish to thank the team of engineers from the Toshiba Corporation for their engineering cooperation, and the KEK machine shop under the supervision of Prof. S.Koizumi for their valuable supports. They are grateful for the beam test data from the Fermilab experiment T816 lead by Prof. H.Lubatti, University of Washington. The authors also acknowledge the support and encouragement by Prof. S.Iwata, head of the KEK Physics Department.

Appendix 1. Test results of small R&D chambers

1. Gas gain measurement using tube chambers

(1) Thin-tube chambers

Gas gain is one of the most fundamental properties that determine the basic parameters of drift chambers, such as the sense wire thickness or the cell size. Besides, a knowledge of its dependence on the operating condition is essential to optimize the practical performance of chambers. We measured the gas gain of the gas mixture that we have chosen for the SDC muon chamber, Ar/CO_2/Methane (89/10/1), using thin-tube chambers.

The layout of the chamber is schematically illustrated in Fig. A1.1. The chamber module is an array of 8 thin aluminum-tubes having an inner diameter of 15.4 mm and a length of 20 cm. The tubes are arranged in three layers because this chamber was originally designed to test the tracking performance of various gas mixtures. Both ends of the tubes are inserted into circular grooves precisely machined on 2 cm-thick aluminum endplates. The grooves are made so that the inner diameter fits to that of the tubes. The grooves are filled with an epoxy glue for gas sealing and painted with a conductive paint to ensure an electrical contact between the tubes and the endplates.

Wires are strung between plastic feedthroughs inserted into holes drilled in the endplates, and soldered to brass pins inserted into the feed-throughs. Because all machinings were done with a precision better than 50 μm, we expect the positioning accuracy of the wires and the tubes is better than 100 μm. Gas is supplied and exhausted through gas manifolds drilled in the endplates. The gas volumes of the tubes and the manifolds are connected with small drilled holes.

(2) Setup for the gas gain measurement

The gas gain was measured by irradiating the chamber with 5.9 keV-X rays from a ^{55}Fe source through a 3 mm-diameter window made at the center of

the tubes in the uppermost layer. The window was covered with an aluminized Mylar sheet and a Kapton tape in order to minimize the electrostatic effect.

The setup of the measurement system is illustrated in Fig. A1.2. The signal was amplified with a preamplifier having been designed and fabricated for the use of VENUS-CDC. A detail of this amplifier is described in the next section. Because the output polarity of the preamplifier is positive, the amplified signals were converted to negative pulses by using a pulse transformer. The signals converted were integrated and the total charge was measured with LeCroy's *qVt*. A capacitor was inserted to the input line in order to eliminate the pedestal of *qVt*. The *qVt* was operated in the internal-trigger mode with a gate width of 200 nsec. Calibration pulses were fed to the chamber through a 10 pF capacitor via the end opposite to the readout side.

The pressure of the gas was subject to that of the atmosphere. A slightly positive pressure with respect to the atmosphere, ~ 10 mm H_2O, was kept by a bubbler and a weight of the gas in the exhaust line. The absolute pressure and the pressure difference with respect to the atmosphere were monitored on the exhaust line just upstream of the bubbler. The temperature was quite constant through the measurement, within 0.5 deg C, because the test bench was located on the floor of an experimental hall of TRISTAN, which is about 15 m below the ground level and air-conditioned.

Because the setup was unchanged and the same preamplifier channel was used through the measurements, we expect no systematic uncertainty depending on the variation of the measurement electronics. Fig. A1.3 shows a typical signal shape and a charge spectrum measured. A peak corresponding to the 5.9 keV-X rays is clearly seen, together with an associating escape-peak of argon.

(3) Wire thickness dependence

First, the measurement was done for various thicknesses of sense wires: 30, 50, 70 and 100 μm in diameter, in order to optimize that of the sense wires

to be used in the SDC muon chamber that we propose. The results obtained are shown in Fig. A1.4. The absolute value of the gas gain is very hard to obtain because of a finite band-width of the readout electronics and of a limited time interval for charge integration. Hence we present the results in terms of the relative gain with respect to that for a typical operation condition of VENUS-CDC, which corresponds to a charge density $\lambda_S/2\pi\varepsilon_0$ of 270 V for a 30 μm sense wire and the gain of approximately 10^5. It should be noted that very large signals corresponding to a limited streamer mode were seen for the conditions above the dashed line in Fig. A1.4.

We evaluate the charge density in terms of $\lambda/2\pi\varepsilon_0$, where λ is the charge density in an ordinary definition, because this definition is convenient for field calculations. Note that $\lambda/2\pi\varepsilon_0$ has a dimension of voltage and that the surface field of a wire can be obtained by dividing $\lambda/2\pi\varepsilon_0$ with the wire radius. In the case of tube chambers the sense wire charge $\lambda_S/2\pi\varepsilon_0$ can be calculated from the high voltage value, using the following relation:

$$\frac{\lambda_S}{2\pi\varepsilon_0} = \frac{V_S}{\ln(c/a)}, \qquad (1)$$

where V_S is the voltage applied to the sense wire, and c and a are the inner radius of the tube wall and the radius of the sense wire, respectively.

As is described in section 2-1-3, the sense wire charge around 370 V is optimum for our jet-type drift chamber in order to obtain a nominal drift field of 900 V/cm. The results shown in A1.1.4 tells us that a sense wire diameter around 70 μm is an optimum choice for such a constraint.

(4) Gas density dependence

Once the gas mixture and the sense wire diameter are fixed, the gas gain can be described as a function of the sense wire charge and the gas density. We carried out the gas gain measurement under several conditions of the gas pressure, in order to understand the dependence on the gas density. The measurement took several days because we had to wait for a significant

change of the atmospheric pressure, which the pressure of the chamber gas follows.

The setup is the same as that having been described in the above, and the measurement was done only for the 70 μm-sense wire that we have chosen for our muon chamber. The temperature was constant within 0.5 deg.C throughout the measurement. The results for three pressure values are shown in Fig. A1.5 in terms of the observed signal charge. We found that those results are well reproduced by the following empirical function:

$$\ln Q_{obs}(\mathrm{pC}) = \frac{\lambda_S/2\pi\varepsilon_0}{20.2\ \mathrm{V}} - 8.2\,\frac{\rho}{\rho_0} - 10.6, \qquad (2)$$

where ρ is the gas density for which the chamber is operated, and ρ_0 is the density at the standard condition: the pressure of 1.033 kg/cm^2 and the temperature of 25°C. The relation corresponding to the three test conditions are drawn with solid lines in the figure.

The above relation can be converted to a relation between the gas gain change and the changes of the sense wire charge and the gas density:

$$\ln(\,1 + \Delta G/G\,) = \frac{\Delta\lambda_S/2\pi\varepsilon_0}{20.2\ \mathrm{V}} - 8.2\,\frac{\Delta\rho}{\rho_0}. \qquad (3)$$

This expression is useful to evaluate the possible effects of mechanical errors and variation of environmental conditions.

2. Tests using short test chambers

(1) Short Test Chambers

Two types of short, 50 cm-long, test chambers were built to test the reliability of our field calculation. Each chamber contains one drift cell; the cell contained in Type I chamber simulates a θ-chamber cell at $\theta = 90°$, while Type II simulates a cell at $\theta = 30°$. The cross sections of the chambers are schematically illustrated in Fig. A1.6. The geometry and the wire

diameters are exactly the same as we have described in section 1-1, except that the gaps between the cathode and the ground planes are 1 cm instead of 2 cm.

The two chambers have essentially the same mechanical structure. The chamber frame, consisting of two endplates and two side walls, are made of 2 cm-thick aluminum plates. They are glued and bolted to each other to form a rigid chamber structure. The upper and lower walls are made of 2 mm-thick aluminum plates. The lower wall is glued and bolted to the frame structure, while the upper wall is bolted to the frame with a rubber gasket inserted in order to allow an access into the chamber.

Wires are strung between plastic feed-throughs inserted into holes drilled in the endplates. Cathodes are made of 1 mm-thick glass-epoxy printed boards. The board is tightly glued on a support board made of 10 mm-thick glass-epoxy, in order to ensure a flat surface of the cathodes. Both ends of the support boards are inserted into grooves carved on the inner surface of the endplates and positioned by fitting the edges to the grooves. Further, the support boards are tensioned with bolts inserted through the endplates. All the components of the chamber were machined with a precision better than 50 μm. Thus the above structure guarantees a precise positioning of the electrodes with an accuracy better than 100 μm. We made these test chambers as precisely as possible, because we intended to examine the intrinsic performance of the chambers based on our cell design in an ideal condition.

(2) Gas gain measurement

The gas gain of the sense wires is a good measure to test the field quality. According to Eq. (3) only a 1 % deviation of the sense wire charge, corresponding to $\Delta\lambda_S/2\pi\varepsilon_0 = 4$ V, results in as much as a 20 % change of the gas gain. The measurements were done for both Type I and Type II chambers, using the same setup described in the last section. The chambers were irradiated with a ^{55}Fe source through 1 cm-diameter windows made on the upper wall. The windows were covered with Mylar tapes for gas sealing.

The voltages applied to the electrodes were the same as we have presented in section 2-1-3, except for the guard wire voltage.

Because we used the same readout electronics and, what is more, the same bottle of gas that we used in the measurements described in the last section, we can make a prediction on the gas gain to be observed without any ambiguity, in principle, if the field calculation is reliable. The results obtained are plotted in Fig. A1.7 in terms of the observed signal charge as a function of the guard wire voltage, and compared with the predictions shown with solid and dashed lines. The dependence on the guard wire voltage is well reproduced in both Type I and Type II chambers.

The absolute value is also in a good agreement with the prediction in Type I, while a 15 % systematic shift of the absolute value can be seen in the Type II results. We observed a similar amount of gain reduction in a tube chamber connected to the gas outlet of the Type II chamber. Therefore, the gain reduction that we can see in the Type II chamber is probably due to a degradation of the gas purity, maybe due to an outgas or a leakage. By the way, the 15 % deviation of the gas gain corresponds to only a 0.9 % error in the sense wire charge, even if the deviation is a result of a field calculation error. Namely, the reliability of the field calculation has been proved with an accuracy better than 1 % in terms of the sense wire charge.

(3) Setup for the cosmic-ray test

Cosmic-ray tests were also carried out for both Type I and Type II chambers in order to test some basic characteristics as a tracker. The setup is illustrated in Fig. A1.8. Cosmic-ray tracks were triggered with a coincidence between two scintillation counters, having an area of 9×10 cm^2 each, placed just above and below the test chamber. The signal from the upper counter was used for the start signal of TDCs.

The amplifiers and the discriminators, including the cable in between, are the spare parts of VENUS-CDC. The system is described in the following, slightly in detail, because this is one of the good examples for the readout system of the SDC muon chamber. The amplifier board is mounted on the

endplate of the chamber. The board, 6×8 cm^2, contains 16 channels of HV-blocking capacitors (3kV, 330pF) and monolithic amplifiers (Fujitsu MB43468), while only 3 channels were used in the test. The amplifier is basically a current feedback amplifier having a gain of –20 mV/μA. For impulse inputs the rise time is typically 6 nsec and the fall time is 15 nsec (10 to 90 %). Four channels of the amplifiers are included in a 14 pin-flat package. The power dissipation is only 24 mW/channel. This amplifier has shown a very good reliability in the experience of VENUS-CDC. No failure has been observed for more than 7000 channels through a 5-year operation at TRISTAN.

Signals amplified are transferred through a 30 m-long twisted pair cable to the discriminator board. Each pair of the cables is individually shielded with aluminum foil, and 19 pairs are forming a bundle. The shield of the cables is connected to the ground only at the preamplifier board. On the discriminator board, the signals are received with pulse transformers (100 μH) and further amplified by, nominally, a factor of 10. The amplified signals are discriminated with LeCroy's MVL 407. The above scheme of the signal transfer is very powerful to eliminate the noise pickup, because the transformer has a good common-mode rejection capability in a wide range of frequency. The rejection factor is 100 or more up to several 10 MHz.

Although it is not a problem in our case because the band width of the post amplifier is not very wide, only up to a few 10 MHz, we have to remind that this scheme does not always show a good characteristic. The rejection factor, at least for the transformer we used, steeply decreases in a several 10 MHz region, and the common-mode response shows a resonance structure around 100 MHz. This property is due to a small interwinding capacitance of the transformer. Therefore a matching between a transformer and an amplifier has to be carefully considered in an application to very fast signals.

In the case of VENUS-CDC, ECL outputs of the discriminator are directly fed to a FASTBUS TDC system, while they were converted to NIM signals and fed to a CAMAC TDC through 200 nsec-cable delays in the setup of this test. The CAMAC TDC we used has a dynamic range of 12 bits and a full scale of 2 μsec. The least count therefore corresponds to 0.5 nsec. The

TDC was roughly calibrated using cable delays, and there still remains a few % uncertainty in the overall time scale. The data digitized were readout and stored by a personal computer. The digital part of the setup, including the discriminator board, was placed nearly 10 m away from the test chamber, in order to eliminate a noise pickup at the chamber to an acceptable level. The personal computer and the cable between the personal computer and the CAMAC crate were the most severe sources of the pickup noise.

The high voltages that we applied in the test are the same as we determined in section 2-1-3, except for the guard wire voltage. Since the gap between the cathode and ground planes is narrower than the geometry used in section 2-1-3, we have to use a different value in order to make the gas gain of three sense wires be equal to each other. The optimization was done only for the 90° cell, which corresponds to the Type I chamber. From the results of field calculation, which we have already shown in Fig. A1.7, we determined the guard wire voltage to be 2.17 kV. The same voltage was also applied to the Type II chamber.

The discriminator threshold was fixed to 25 mV through the tests. Because the ^{55}Fe X-ray signal is about 1.5 V at the input of the discriminator, we expect a pulse height of several 100 mV for cosmic-ray tracks. Thus the threshold level is expected to be lower than 1/10 of a typical pulse height of the signals.

(4) Results from the cosmic-ray test

Fig. A1.9 shows the measured drift time distributions. The shapes of the distributions do not show the efficiency of the chambers, but represent the geometrical acceptances of the setup. We can see that the maximum drift time is approximately 800 nsec and there is no apparent difference between the wires and the chamber types. The efficiency of each wire is shown in Fig. A1.10 as a function of the drift time. Almost a full efficiency was obtained in the whole drift time range for both chambers. In this estimation the sample of events for which the efficiency was examined was defined by a coincidence of the signals in the other two wires. A small inefficiency observed would be mainly a fake made by a noise pickup, because the

inefficiency is smaller for the outer wires than the middle wire and we observed that the outer wires were noisier than the middle wire.

The resolution was examined by using a three-wire method. The variable Δt_3 was defined as

$$\Delta t_3 = t_2 - (t_1 + t_3)/2, \qquad (4)$$

where t_i denotes the drift time of i th wire; *i.e.* t_2 is for the middle wire. If the three wires are exactly identical, the timing resolution of each wire, σ_t, can be obtained using the following relation:

$$\sigma_t = \sqrt{2/3}\, \sigma_3, \qquad (5)$$

where σ_3 is the r.m.s. of Δt_3. The distribution of Δt_3 is shown in Fig. A1.11 for both test chambers. The r.m.s. of the distribution obtained by a fitting is 6.00±0.11 nsec and 6.21±0.08 nsec for Type I and Type II, respectively. These results correspond to the timing resolution σ_t of 4.90±0.09 nsec and 5.07±0.07 nsec. Further, if we assume a constant drift velocity of 5 cm/μsec, we can convert these timing resolutions to the spatial resolutions of 245±5 μm and 254±4 μm, respectively.

The same study was done by dividing the sample into 4 drift time regions. Fig. A1.12 shows the resultant Δt_3 distributions and the fitting results. The fitting results converted to the spatial resolution per wire are presented in Fig. A1.13. A resolution around 250 μm is achieved in the whole drift time region for both Type I and Type II chambers.

There are many factors that we have ignored and may have deteriorated the resolution. For example, the cosmic-ray tracks we used in the test are expected to be dominated by the tracks having momenta around 1 GeV/c. The multiple scattering of those tracks in the chamber gas corresponds to approximately 80 μm of the position uncertainty. Therefore, the resolution that we can finally achieve will be better than the present results. We note that the results obtained in the above test are far better than the resolution required, which is 250 μm/superlayer.

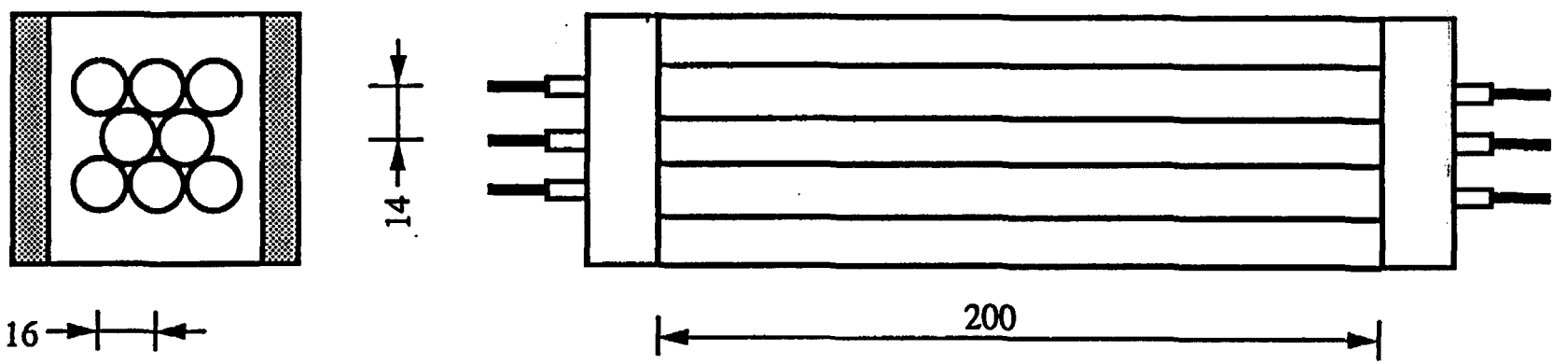

Fig. A1.1. The layout of the thin-tube chambers used for the gas gain measurement.

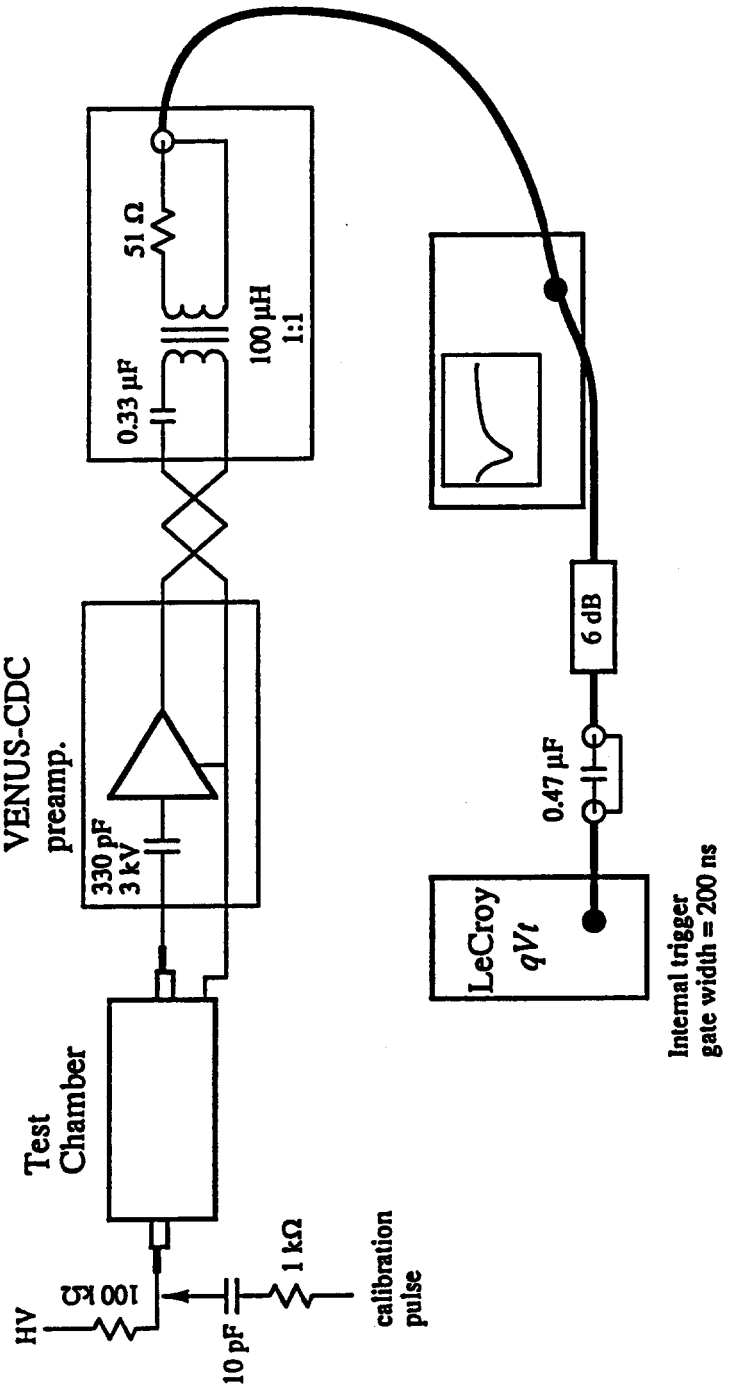

Fig. A1.2. The setup for the gas gain measurement.

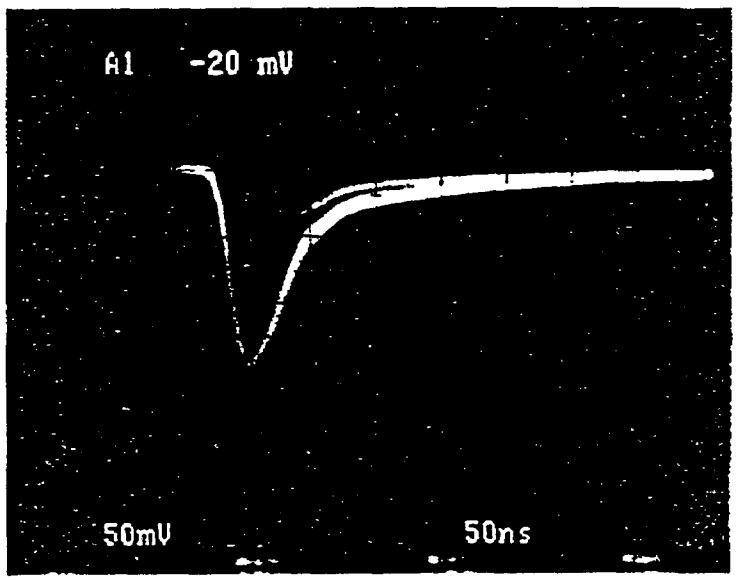

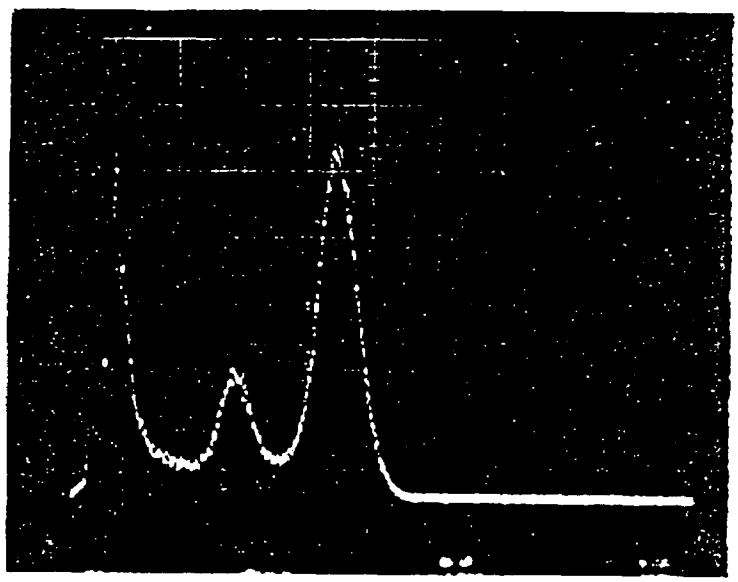

Fig. A1.3. A typical signal shape and corresponding charge spectrum for ^{55}Fe-X rays.

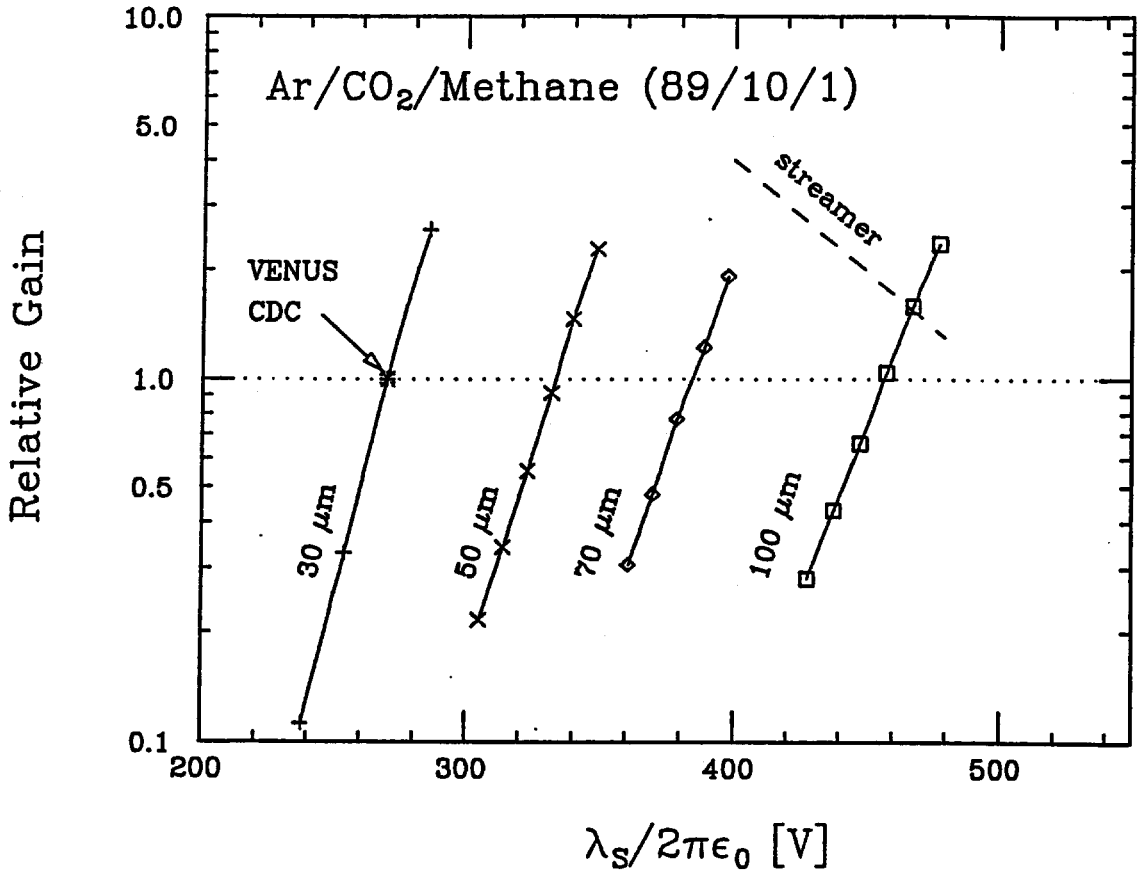

Fig. A1.4. The gas gain obtained for sense wires of various diameters. The results are normalized to that for a typical operation condition of VENUS-CDC, and plotted as a function of the charge density on the sense wire.

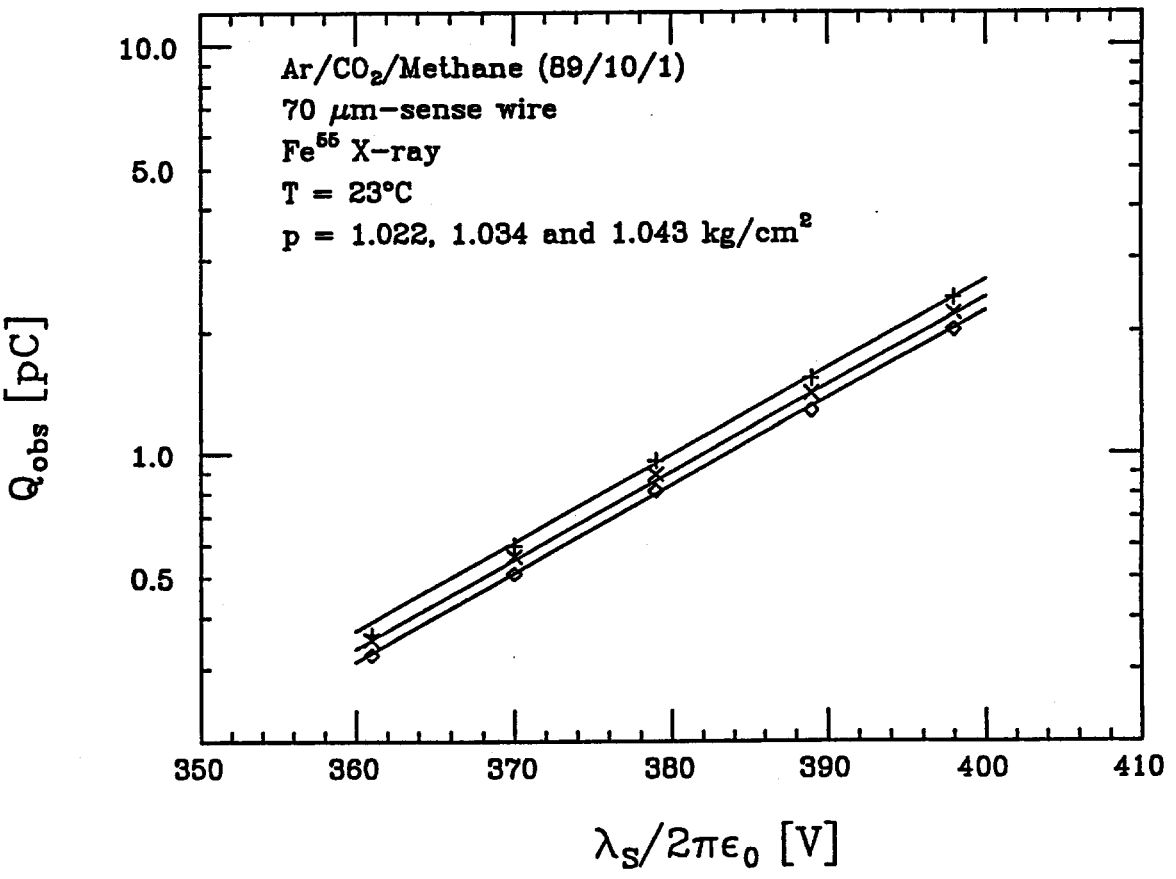

Fig. A1.5. The results of the gas gain measurements performed in three different gas pressures. The solid lines show the empirical relation, described in the text, corresponding to those three conditions of the gas.

Type I

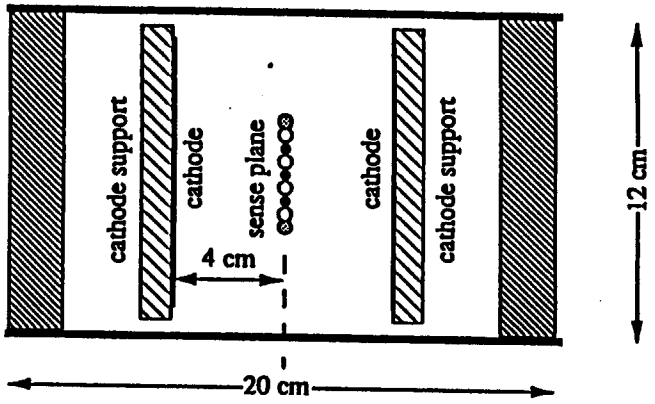

Type II

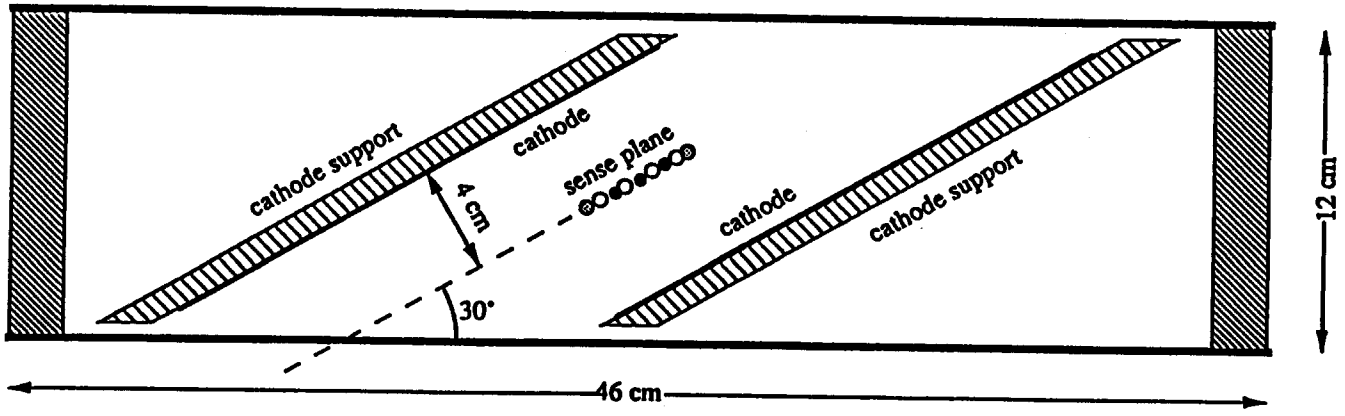

Fig. A1.6. The cross sections of the short test chambers.

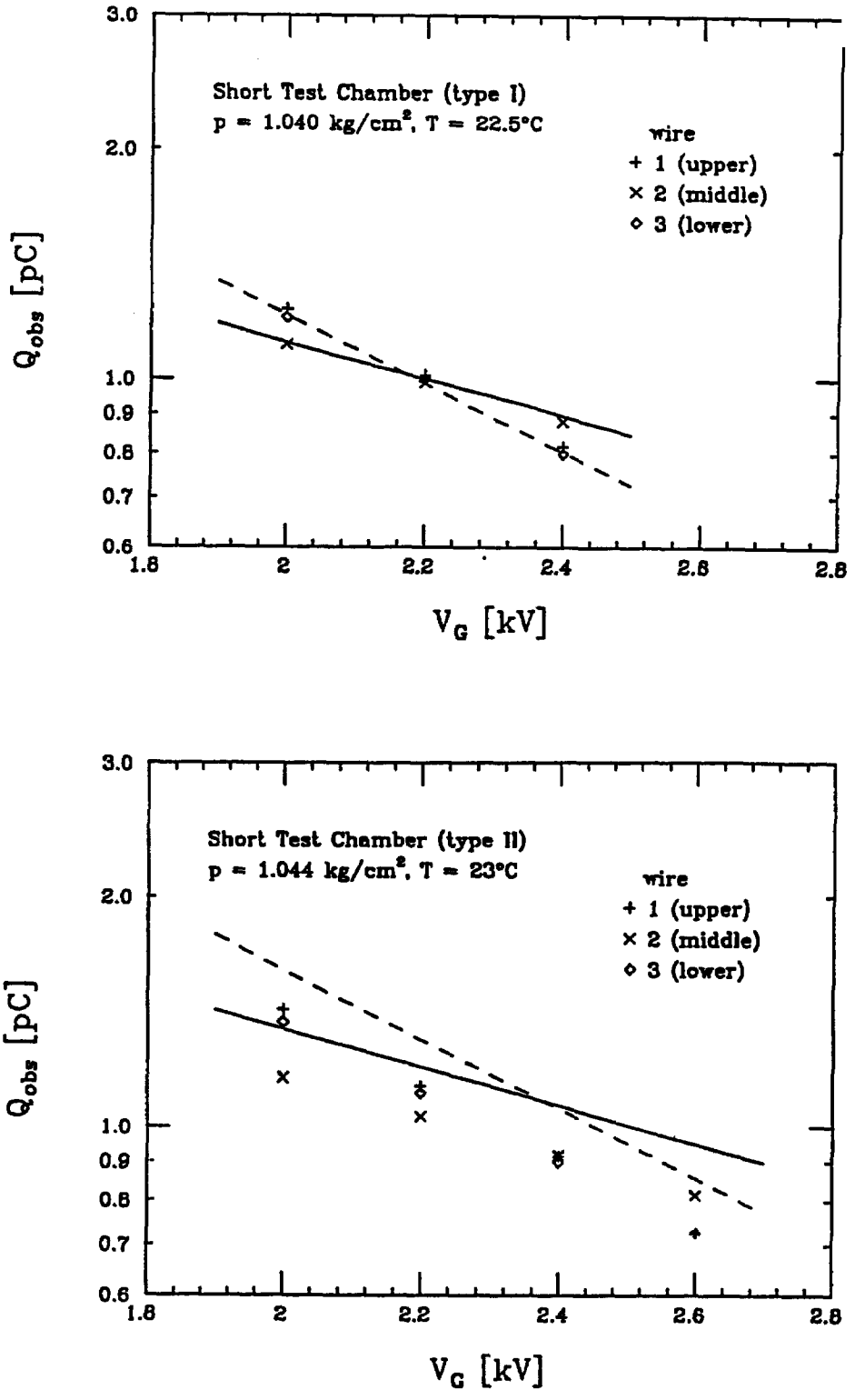

Fig. A1.7. The gas gain of the short test chambers. The results are shown in terms of the observed signal charge for ^{55}Fe-X rays and as a function of the guard wire voltage. The solid line shows the prediction for the middle wire, and the dashed line for the upper and lower wires.

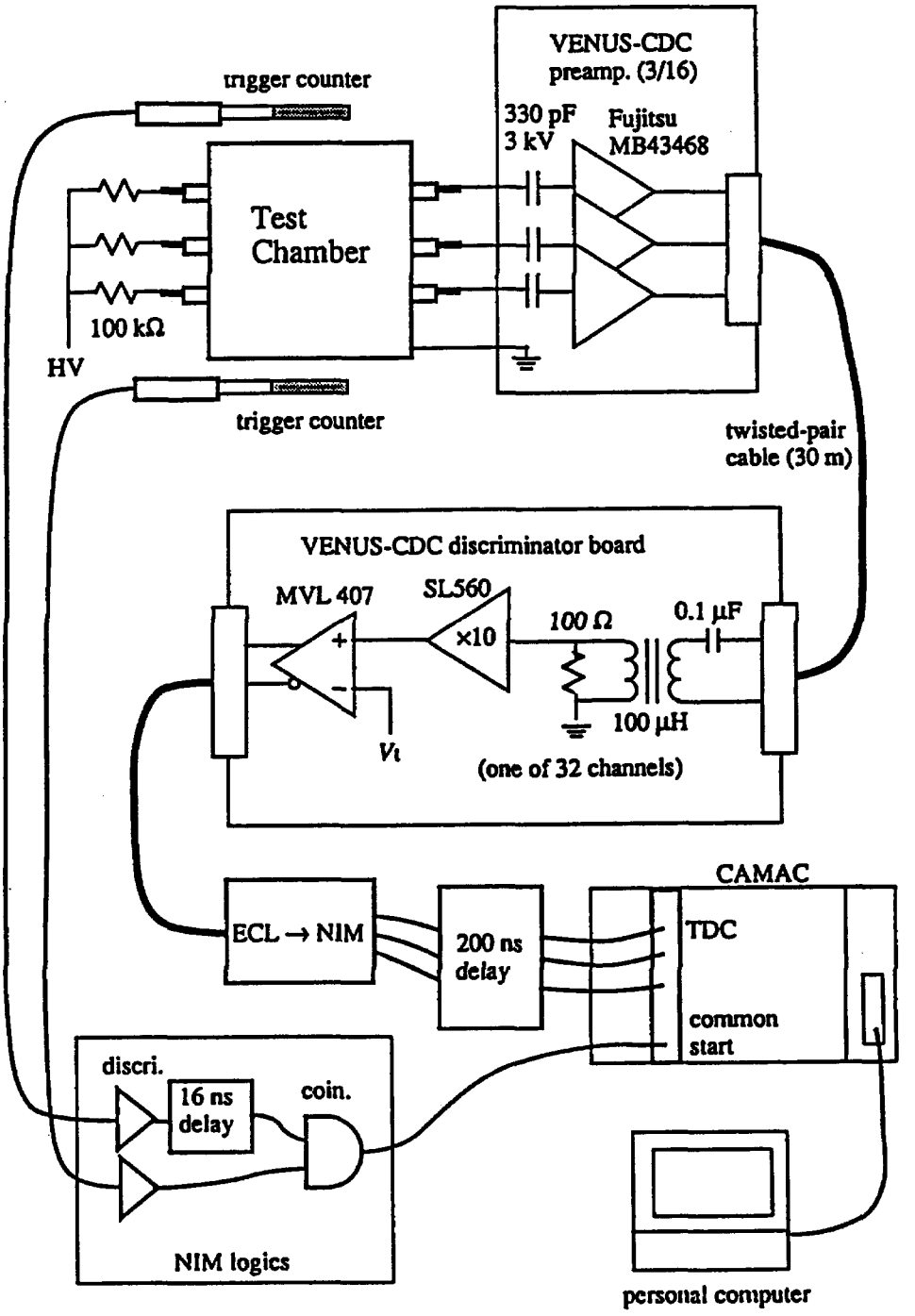

Fig. A1.8. The setup for the cosmic-ray test of the short test chambers.

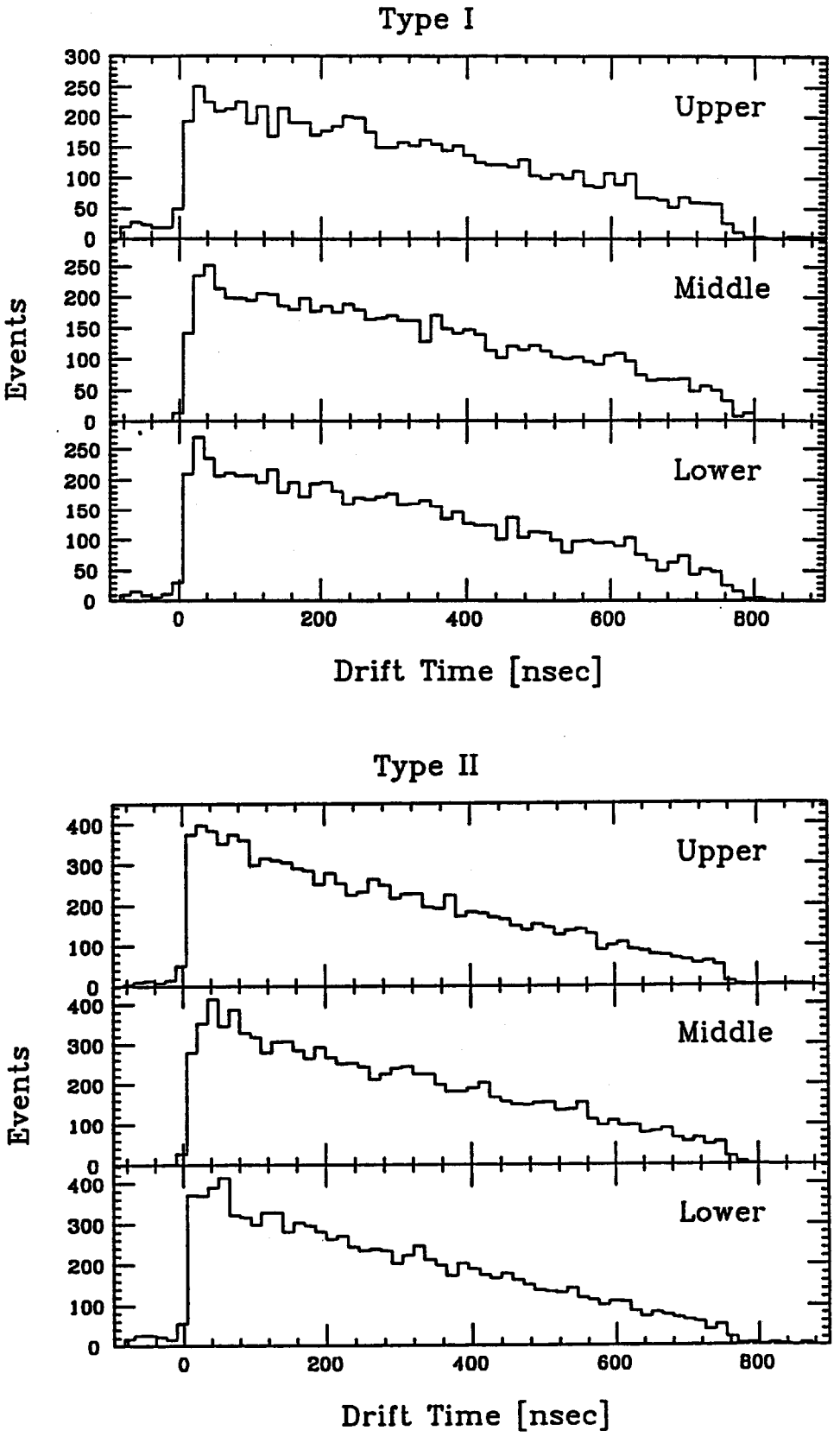

Fig. A1.9. The drift time distributions obtained in the cosmic-ray test.

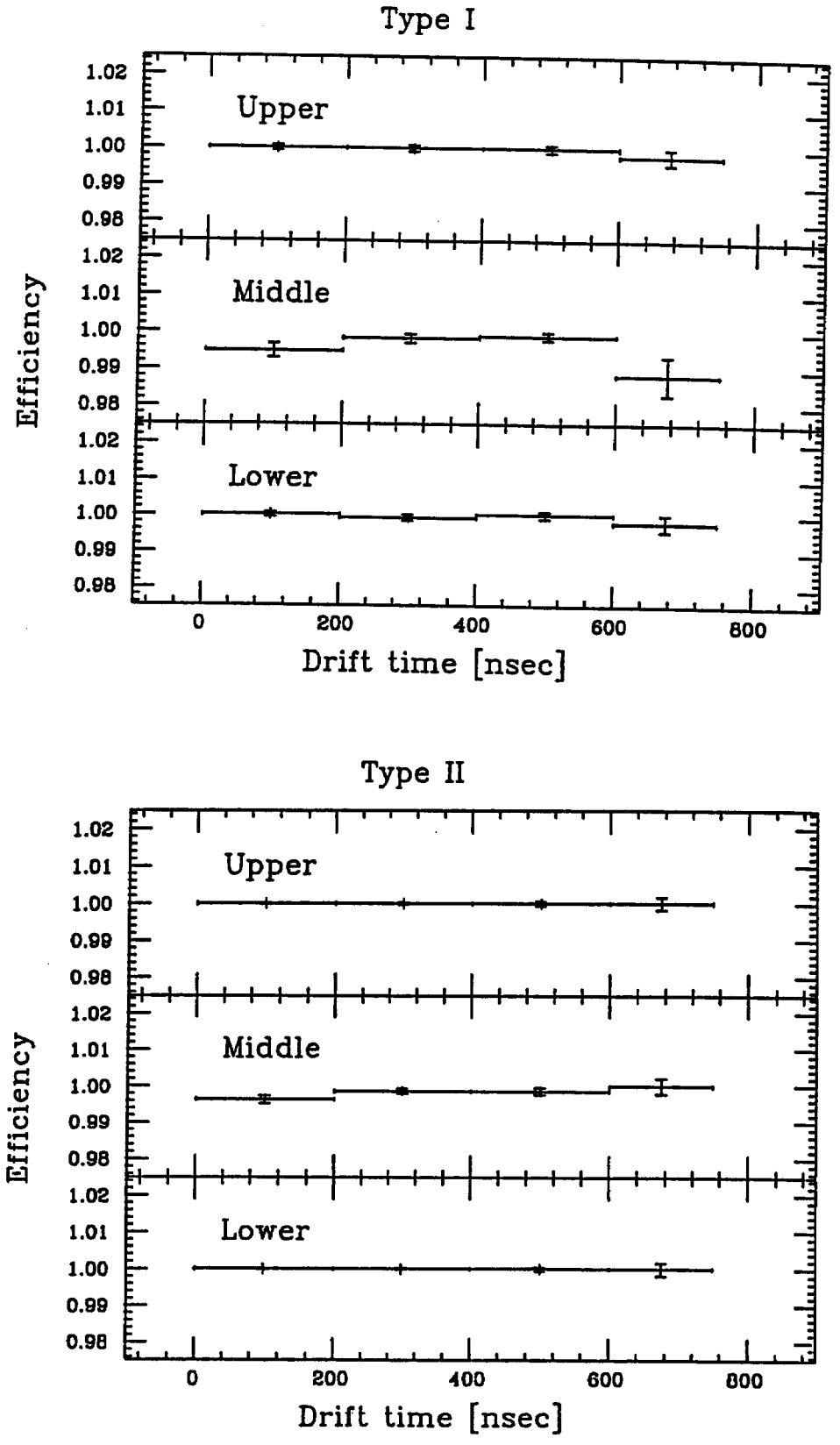

Fig. A1.10. The efficiency measured for cosmic-ray tracks.

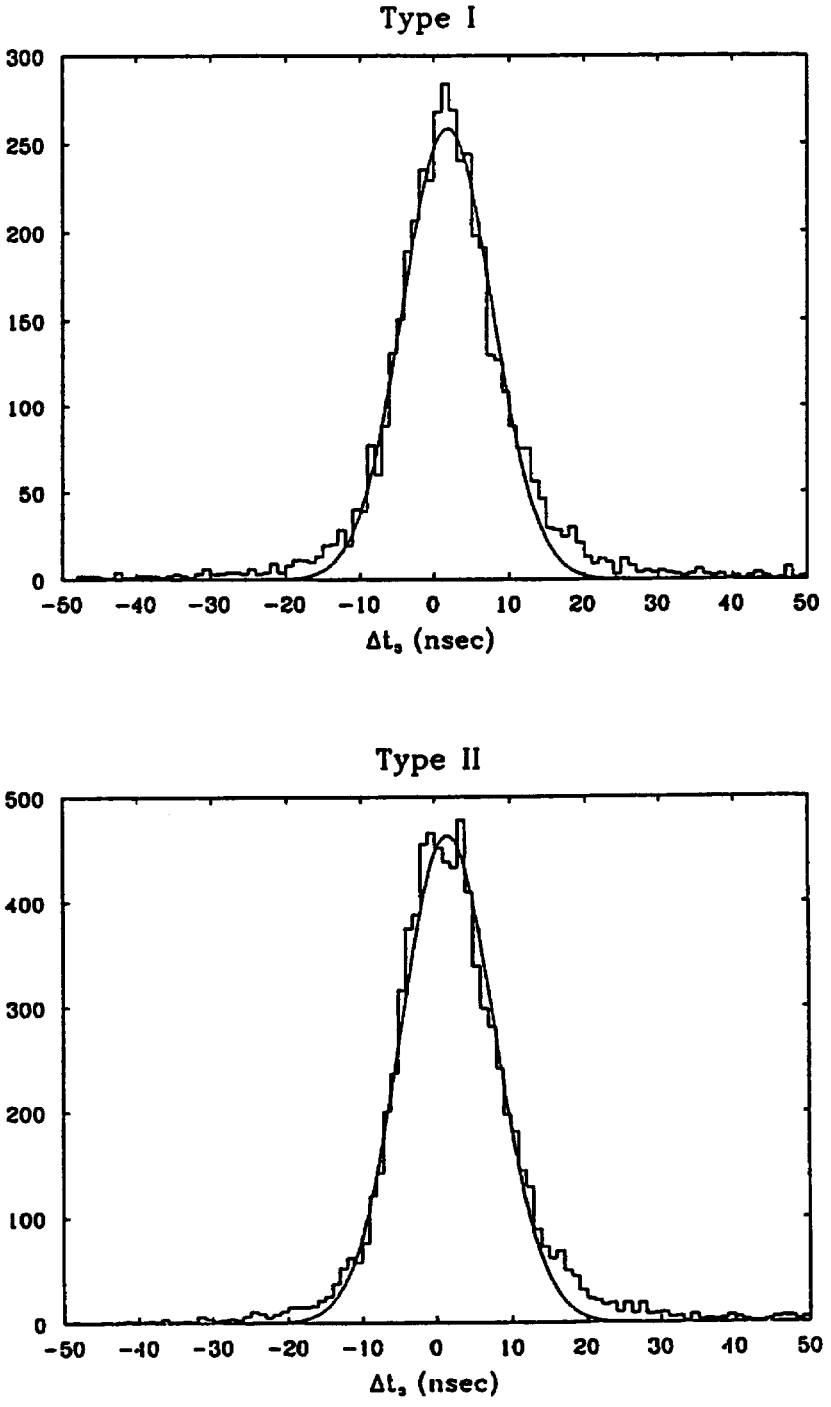

Fig. A1.11. The Δt_3 distributions obtained in the cosmic-ray test.

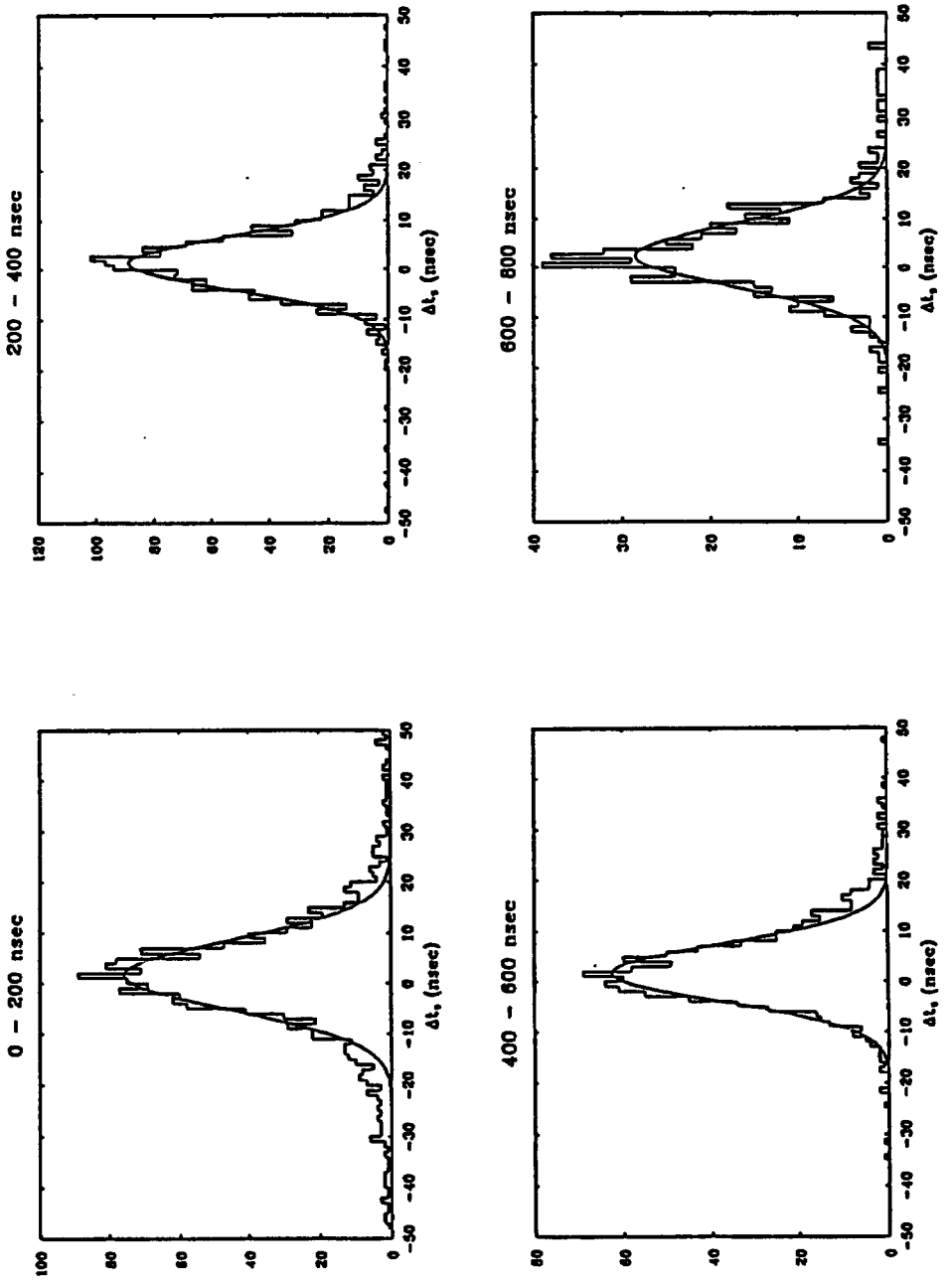

Fig. A1.12a. The Δt_3 distributions in drift-time bins (Type I).

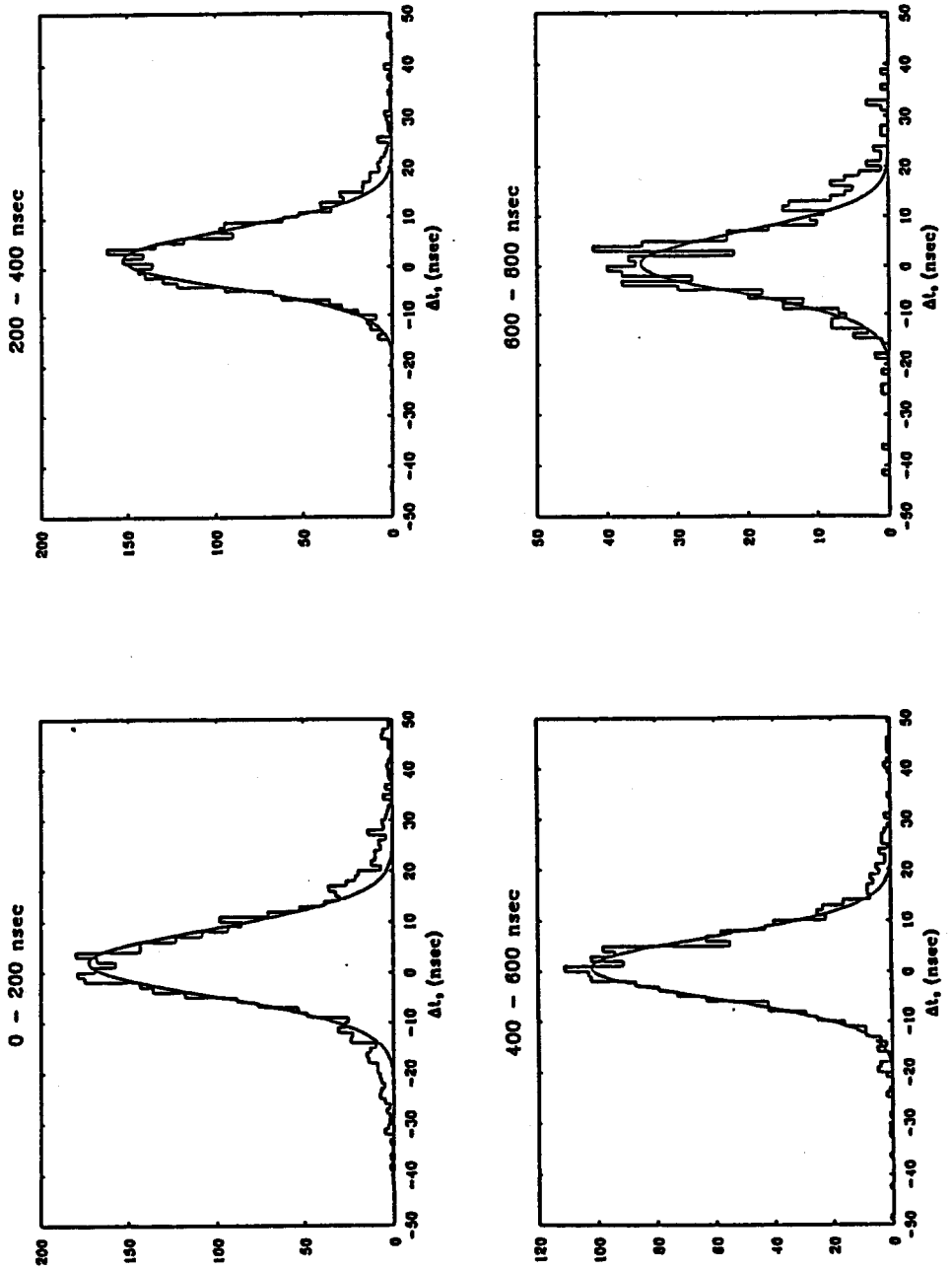

Fig. A1.12b. The Δt_3 distributions in drift-time bins (Type II).

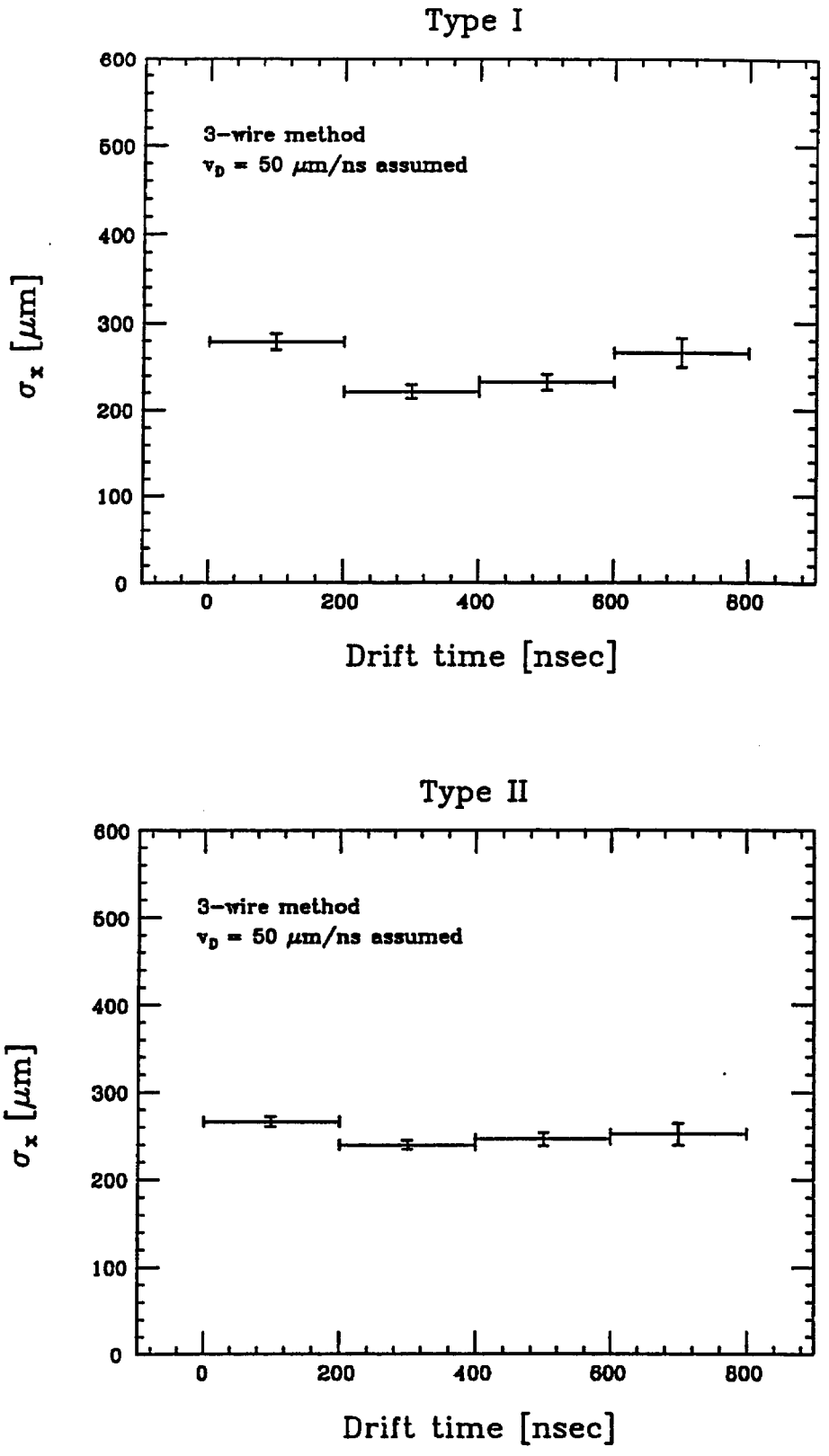

Fig. A1.13. The spatial resolution per wire obtained in the cosmic-ray test. A constant drift velocity of 5 cm/μm is assumed.

Appendix 2. Engineering R&Ds on large jet chambers

1. Introduction

A large size jet chamber R&D project is under way at KEK, Japan. The primary intention of the project is to investigate the feasibility of realizing such a large size jet chamber suitable for the SDC muon system in a realistic manner. Rigidity of the chamber should be proven to be sufficient for easy handling, transportation and precision mounting on the detector. It should be also demonstrated that the high precision chamber can be constructed by means of a reasonably simple fabrication procedure which must be appropriate for producing a large number of large size chambers within our tight schedule and limited resources.

Another important issue to succeed the project is to find out the optimum way of assembling the projective cell structure in the chamber frame. In particular, how to fix the oriented cathode plates reliably inside the frame is a key item to make this jet chamber design in reality.

2. Prototype chamber design

The frame size of the prototype chamber was chosen to be 3 m wide x 8 m long x 0.42 m thick as depicted in Fig. A2.1. The scheme to connect the frame components, schematically shown in Fig. A2.2, is somewhat different from the production chamber design. This is because the extrusion technique is too expensive to produce a single R&D prototype chamber. Honeycomb plates of 42 mm in thickness were used for the middle plate. The details are shown in Fig. A2.3, together with the connection scheme to the side frame. The length of 8 m was limited by the size of honeycomb plates since commercial honeycomb readily available was 4 m by 4 m maximum in size.

The number of cells assembled in the chamber is minimized mainly for an economical reason. In the present R&D work, three sets of cell groups with orientation angles of 90, 60 and 30 deg. are designed to be assembled.

Those arrangements are shown in Figs.A2.4 and A2.5 for the end plate and the center support, respectively. Each group has 6 cells to form the staggered two layer arrangement so that we can proceed the study of the chamber performance in the practical cell arrangement.

3. Chamber fabrication

3.1 Frame components

As pointed out in the previous section, the assembly scheme of the frame is slightly different from the production chamber, since the fabrication techniques for the frame components are different. The frames have a groove in which the middle plates are inlaid and connected with bolts. The groove was made by welding L-shaped angles on the frame.

The holes for fixing feedthroughs and wire supports are NC milled on the end frames and the center support, respectively. Those holes are shown in Figs. A2.4 and A2.5 for the end plate and support frame, respectively. The precision of the NC milling was better than 50 μm.

During the frame assembly, the center support was adjusted to be aligned with respect to the end plates using a cross wire target precisely positioned on each of them. The lateral position of the center support with respect to the end frames is measured to be aligned within 100 μm using a theodolite.

3.2 Cathode assembly

The cathode plates we use in the prototype is conventional 1 mm thick GFRP plates with copper clad on both sides. Details of the support scheme are shown in Fig. A2.6. The cathode plates are supported with narrow insulator strips. The lower one are fixed to the side frames and also to the middle plates while the upper one is only supported by the side frames. Those cathode plates and strips are tightly connected with glued notches to form a rigid matrix structure. The support strip is also a GFRP piece of 15 mm in width and 2 mm in thickness.

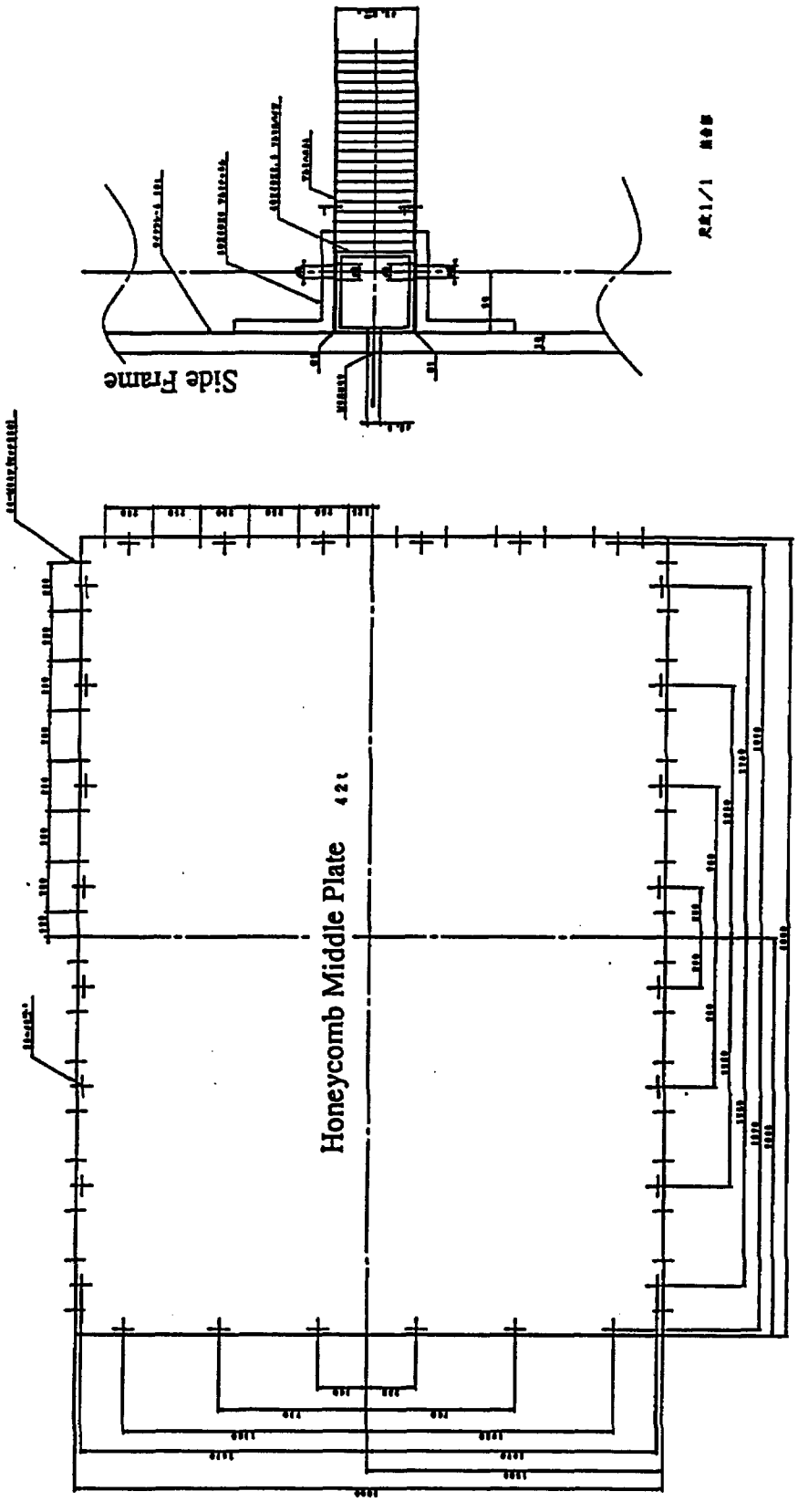

Fig. A2.3. Honeycomb middle plate and connection to the side frame for the R&D prototype.

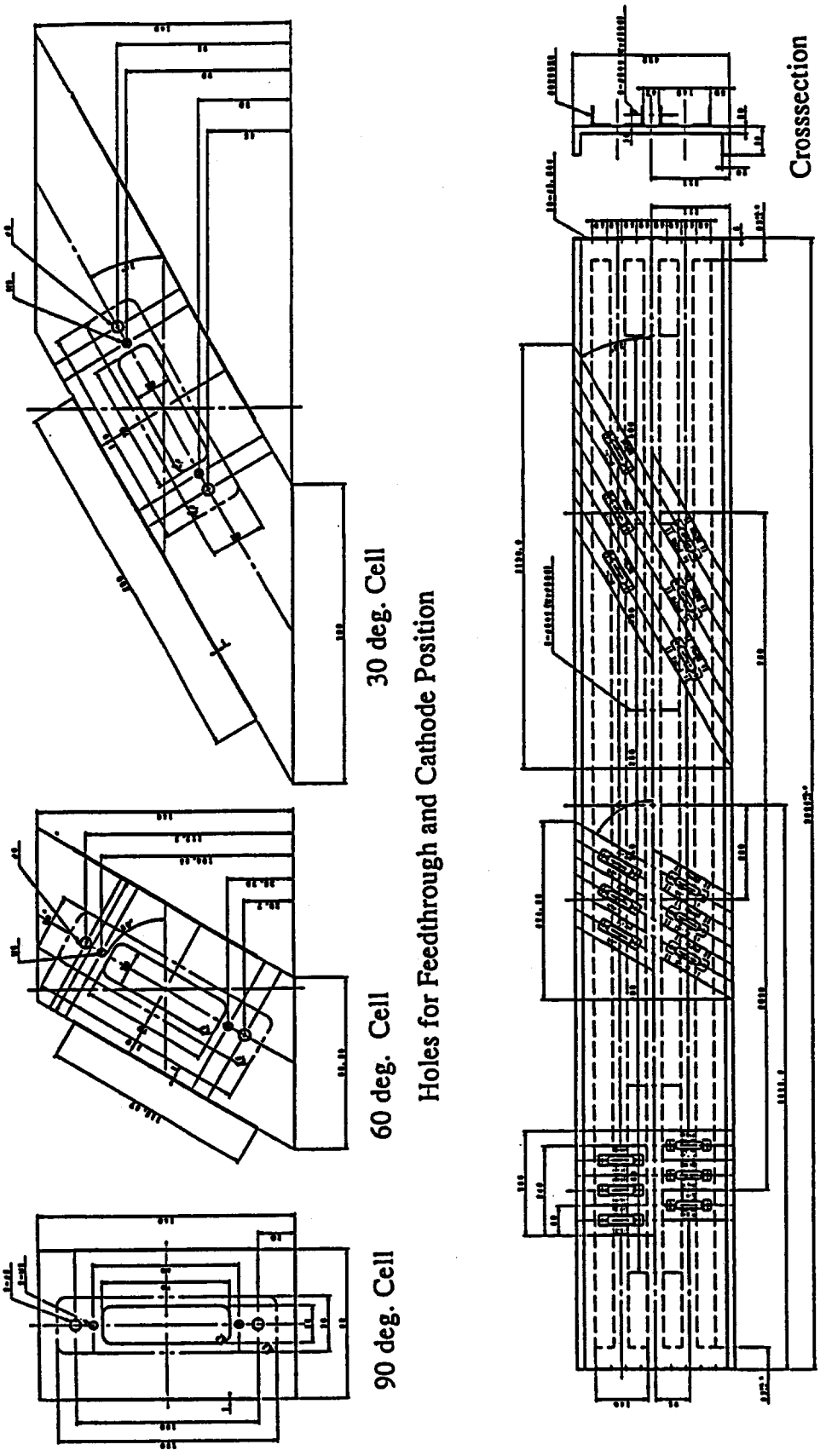

Fig. A2.4. End Plate for the R&D prototype.

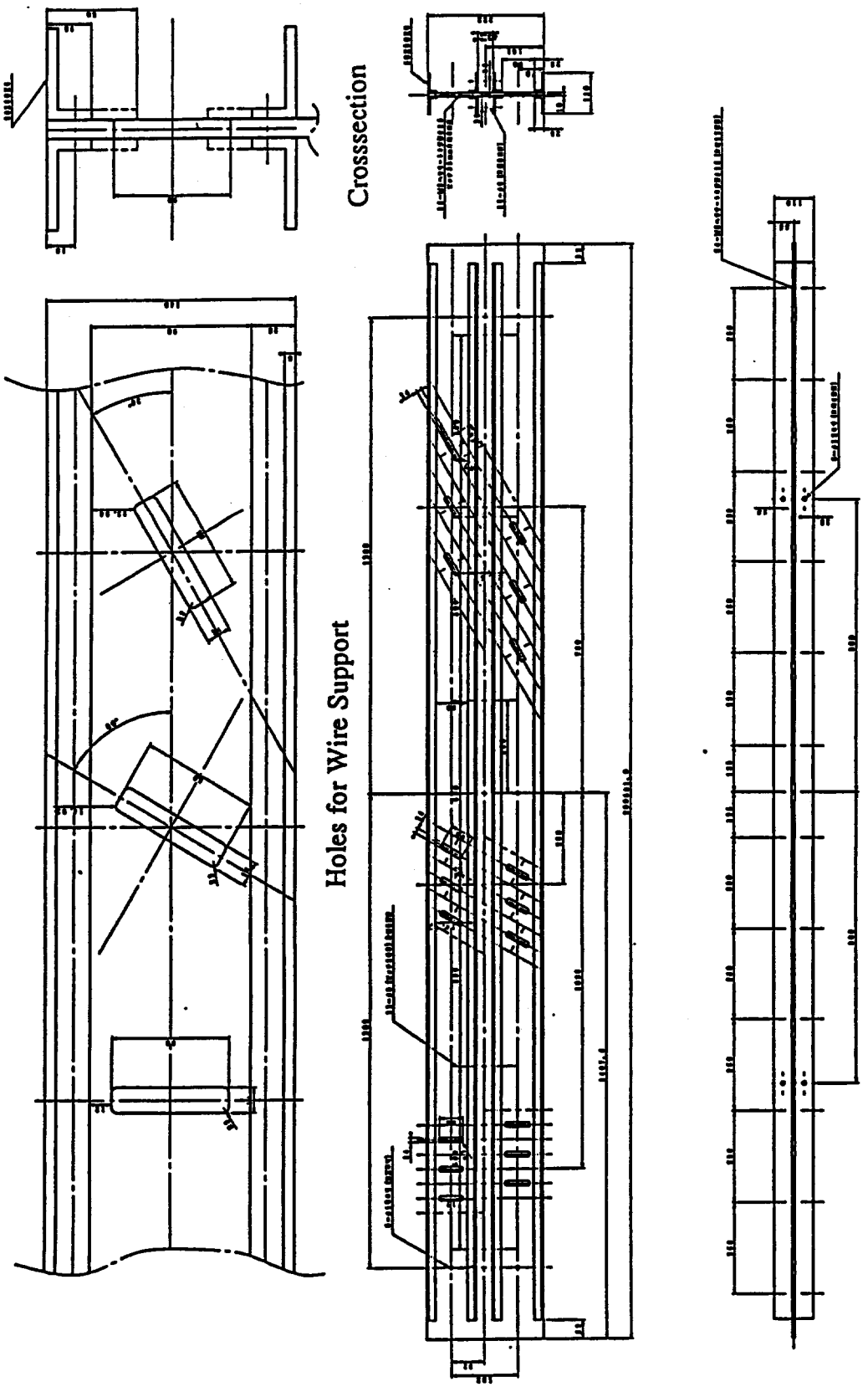

Fig. A2.5. Center Support Frame for the R&D prototype.

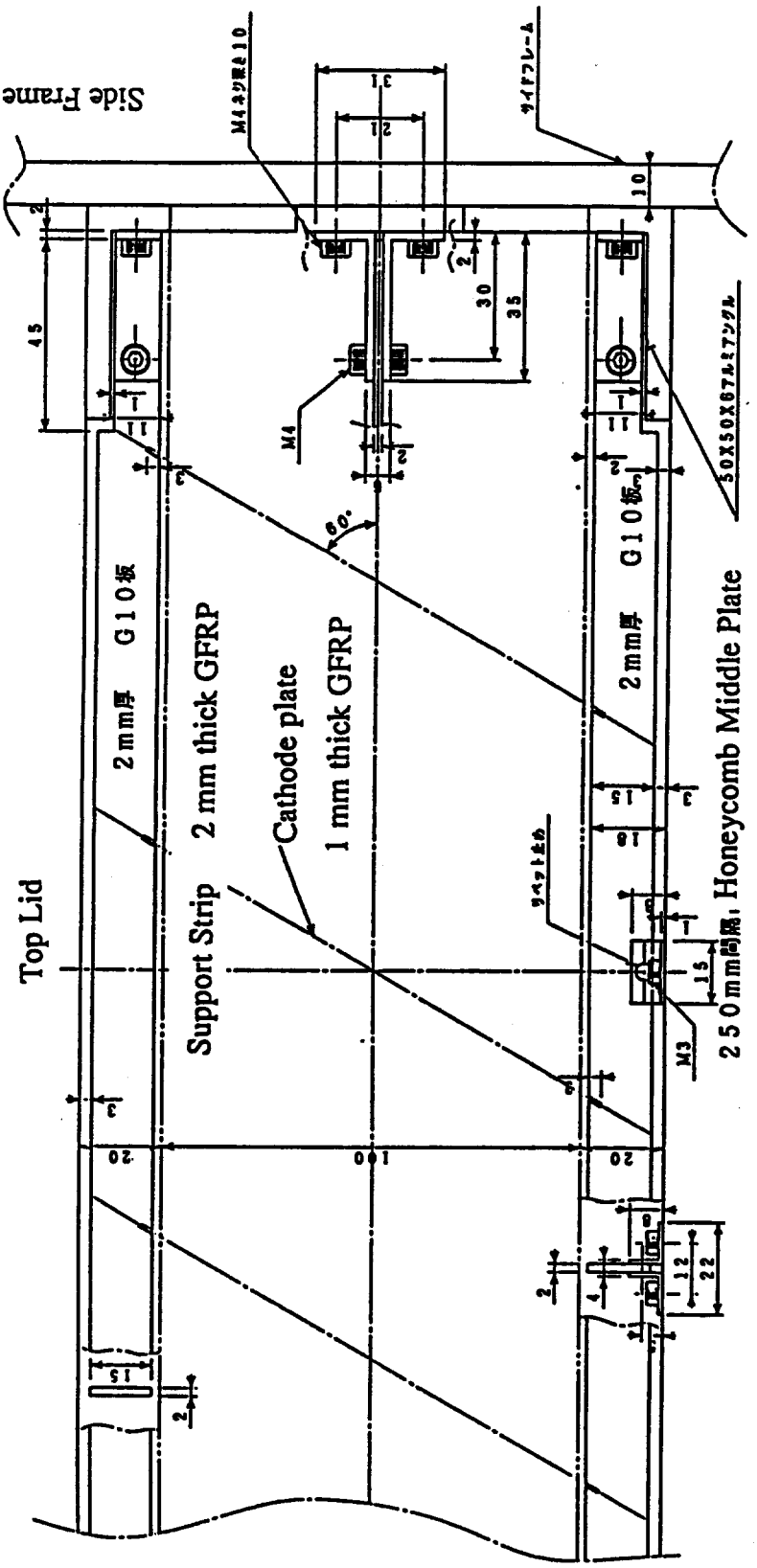

Fig. A2.6. Cathode Assembly Scheme for the R&D prototype.

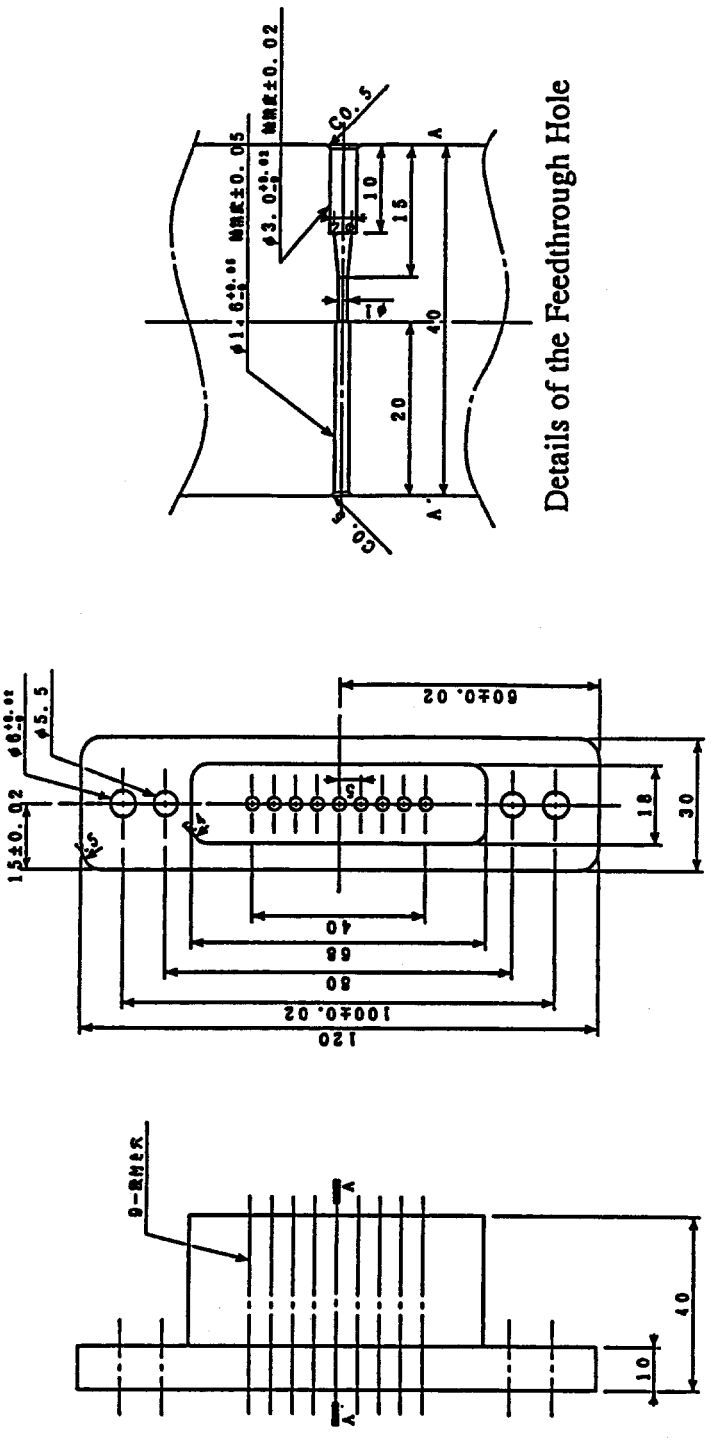

Fig. A2.7. Feedthrough for the R&D prototype.

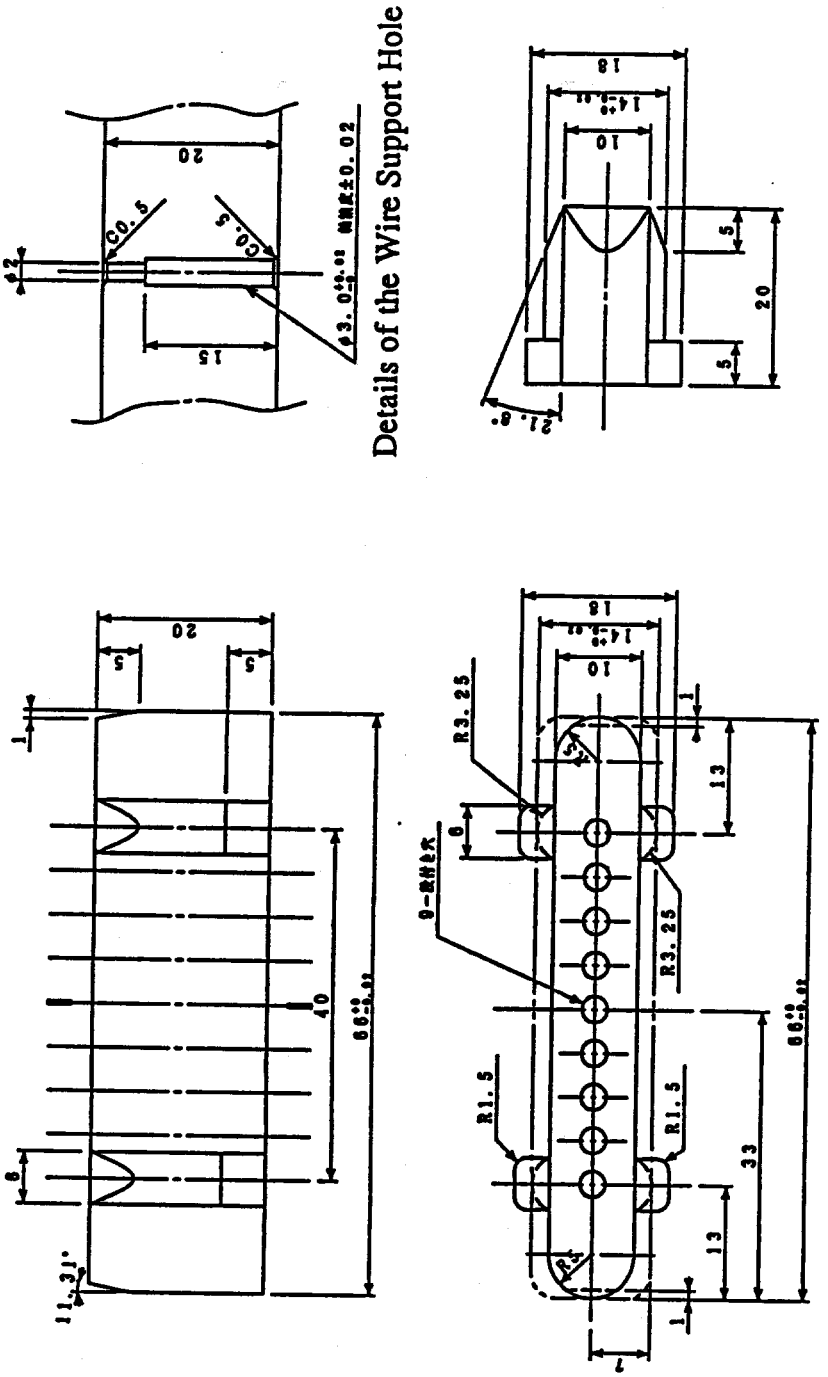

Fig. A2.8. Wire Support for the R&D prototype.

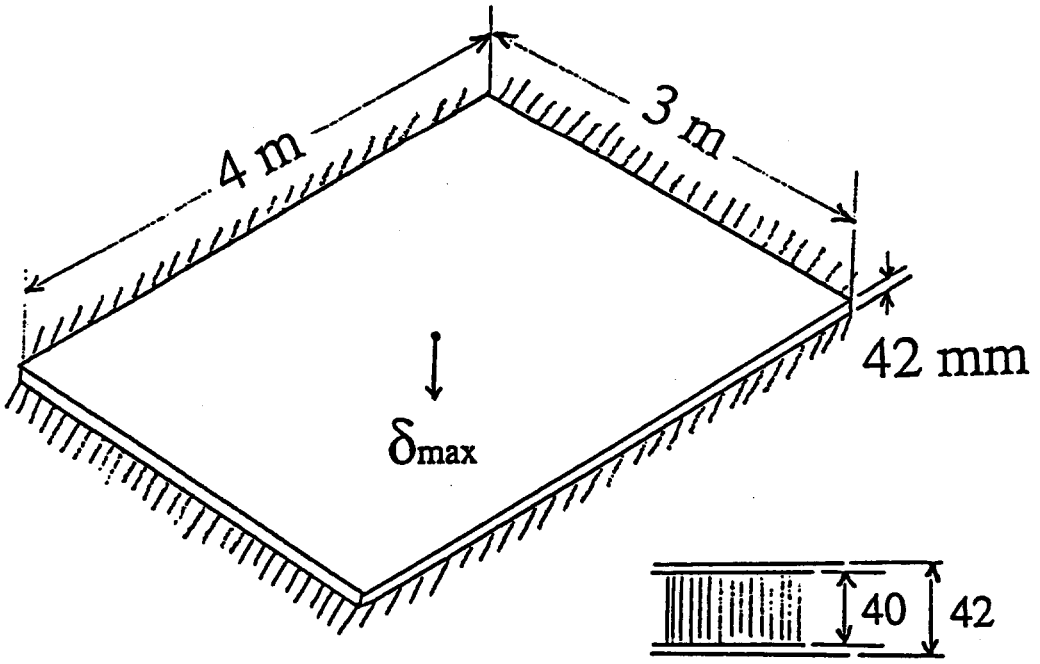

Fig. A2.9. Support condition of the honeycomb plate for the manual calculations.

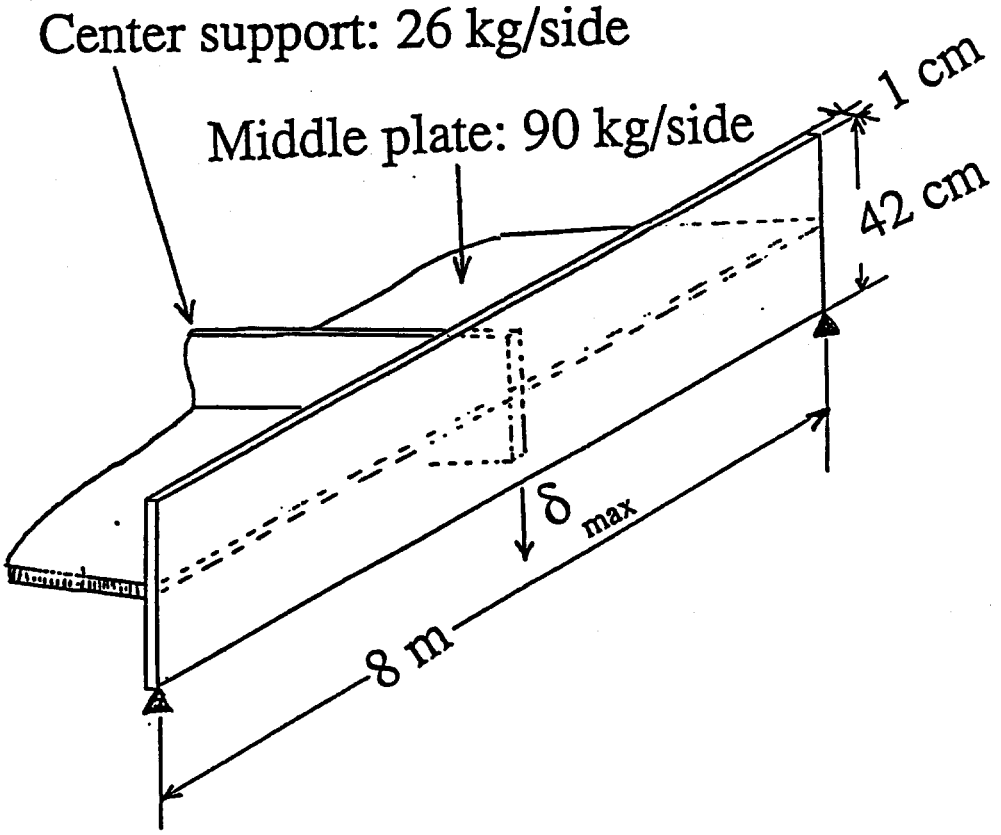

Fig. A.2.10. Simplified model of the chamber frame for the manual calculations

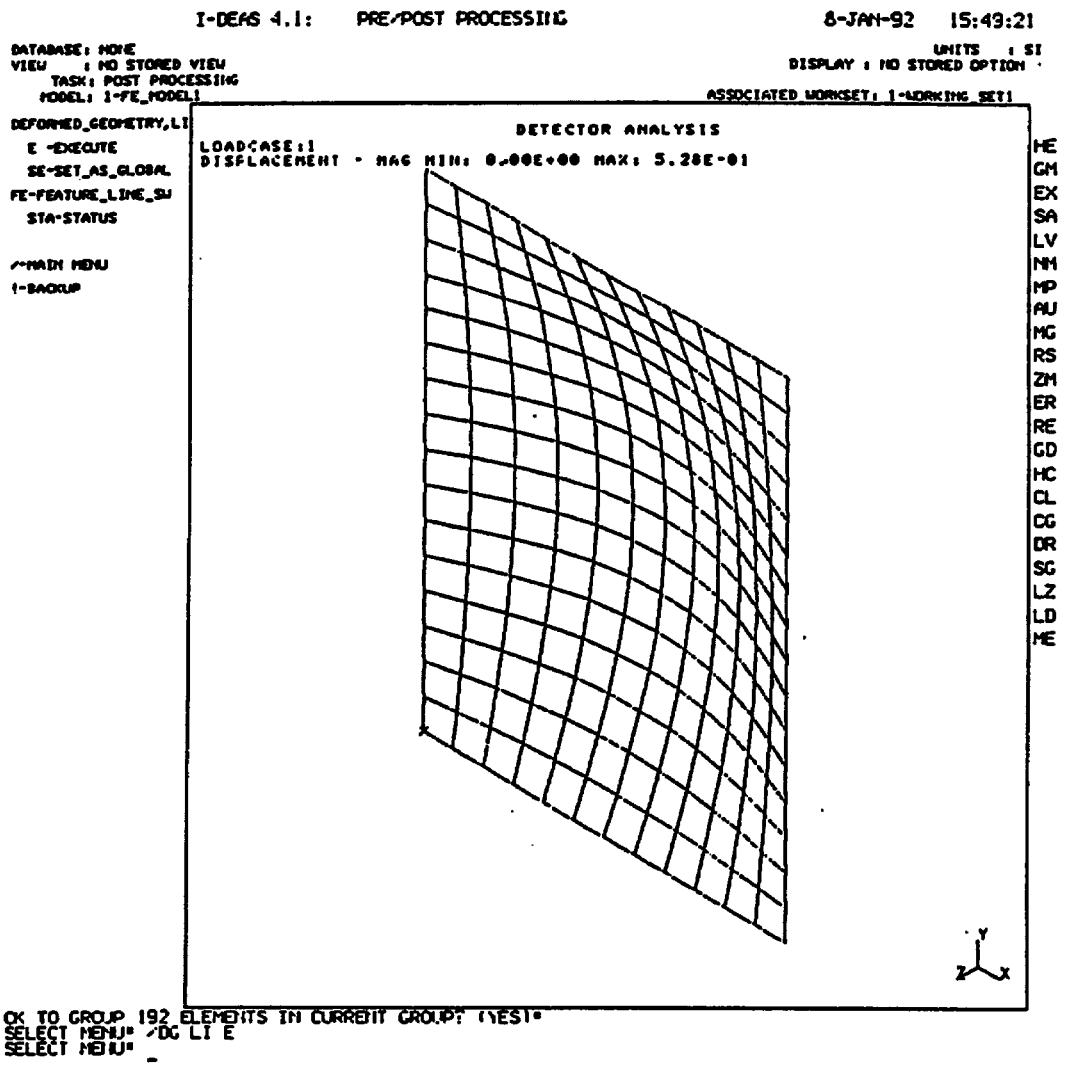

Fig. A.2.11. Results of the FEM analysis. Gravitational sag of the honeycomb plate which is simply supported at four side.

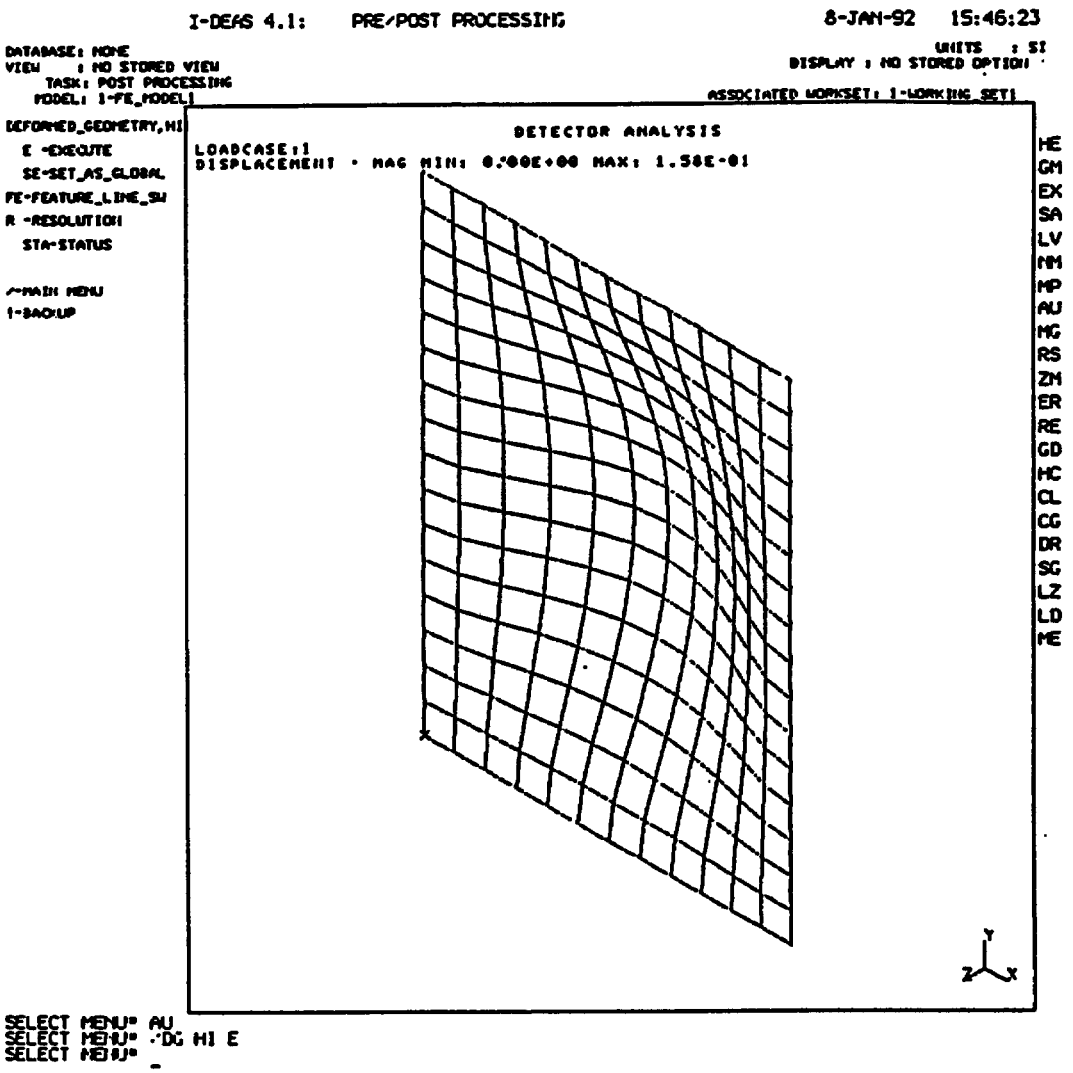

Fig. A.2.12. Results of the FEM analysis. Gravitational sag of the honeycomb plate when the plate is rigidly supported at four side.

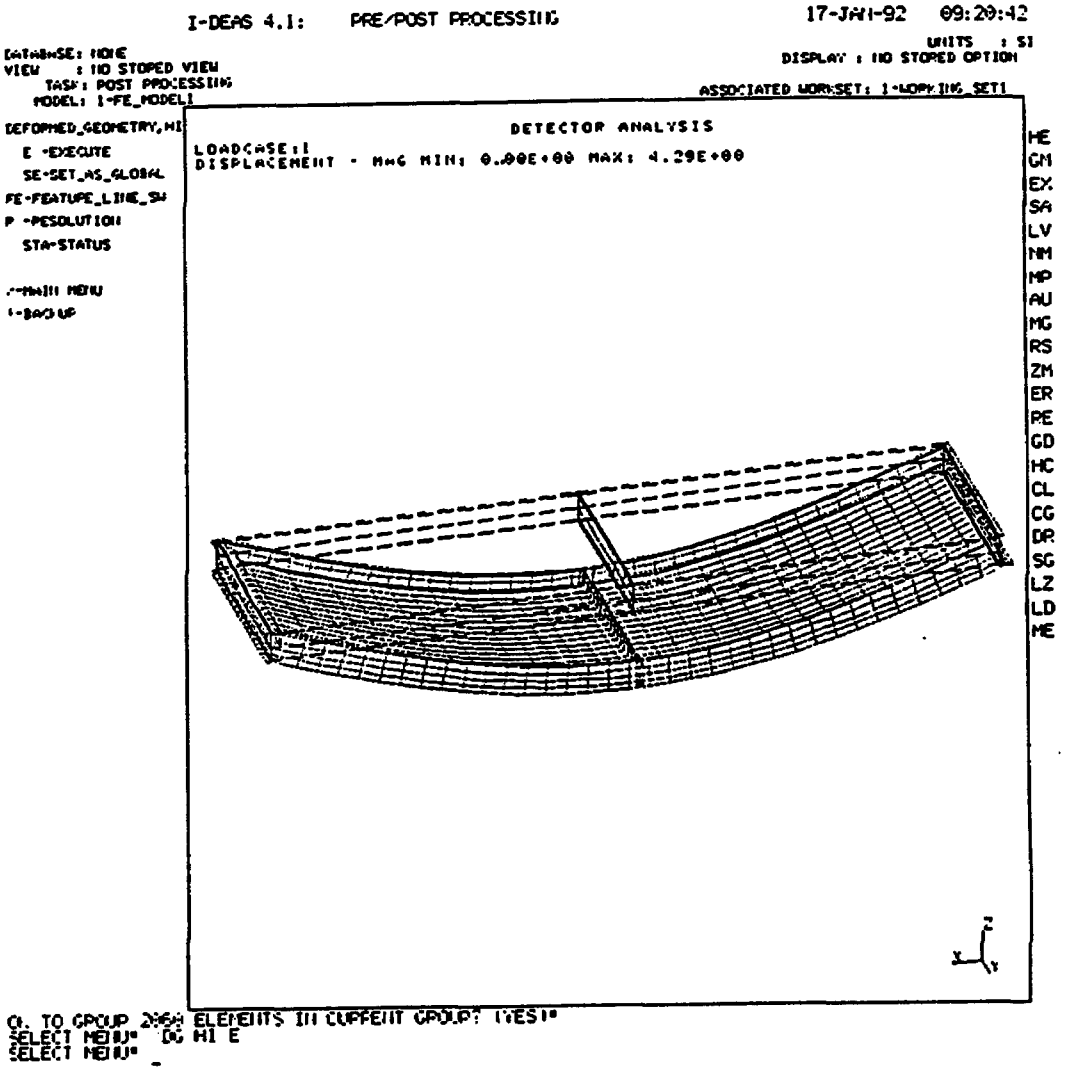

Fig. A.2.13 Results of the FEM analysis. Gravitational sag of the prototype module (2.5 m x 9 m x 0.4 m). Middle plates are simply put on the flange of the frame

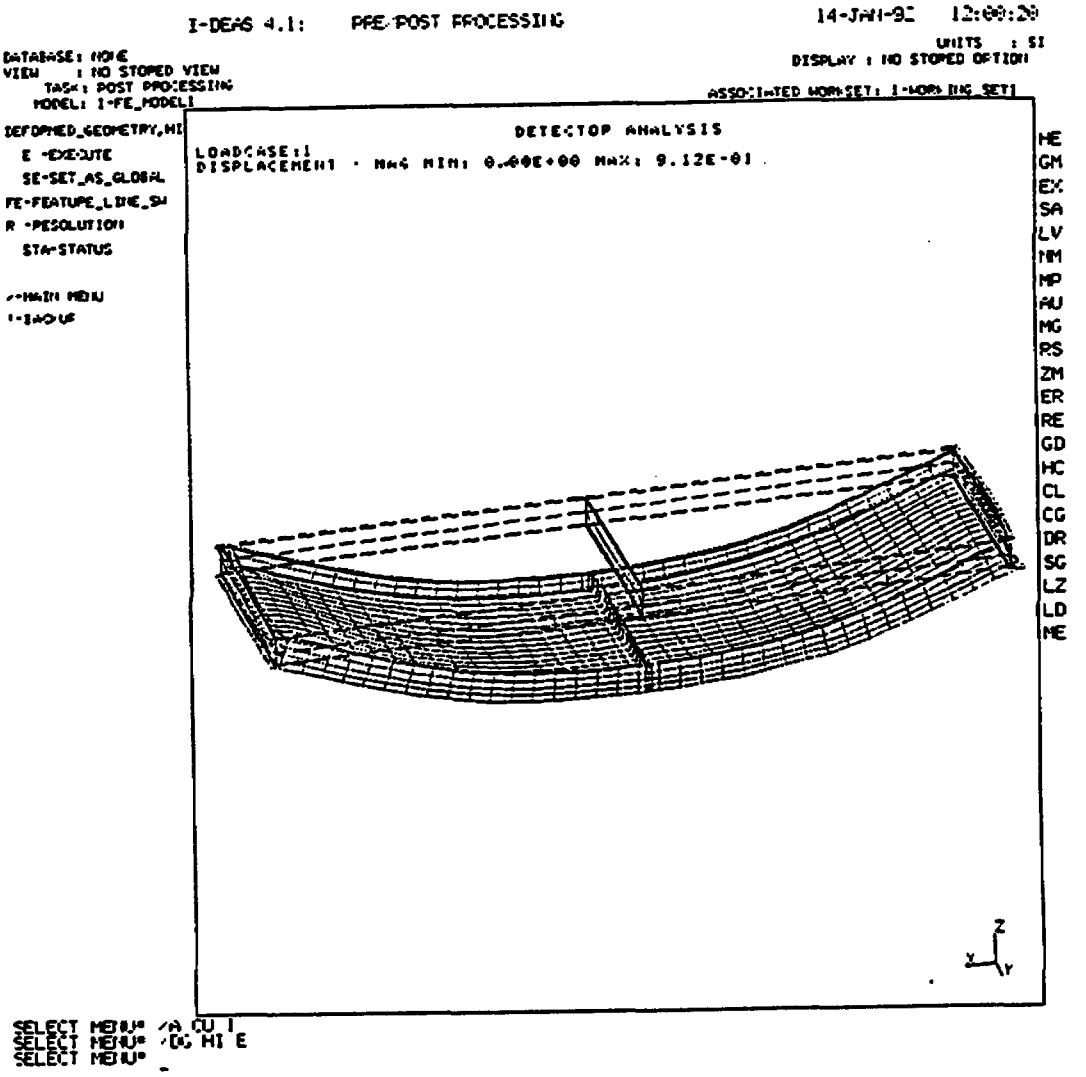

Fig. A.2.14 Results of the FEM analysis. Gravitational sag of the prototype module (2.5 m x 9 m x 0.4 m). Middle plates are rigidly connected to the frame.

Appendix 3. Test beam results from T816

********** Important notice **********

This note is entirely based on the beam test data (Fermilab T816 : the SDC detector muon subsystem beam tests) collected by the muon collaboration of the SSC detector subsystem R&D. The collaboration is lead by Prof. H.Lubatti, University of Washington. T816 members are :
D. Green, P. Martin, J. Morfin (Fermilab), R. Downing, S. Errede, A. Gauthier, M. Haney, I. Karliner, T. Liss, T. O'Halloran, P. Sheldon, V. Simiatis, J. Thaler, J. Wiss (U. of Illinois), S. Kunori, A. Skuja (U. of Maryland), A. Sill (U. of Rochester), T. Okusawa, T. Takahashi, Y. Teramoto, T. Yoshida (Osaka City U.), T. Kafka, A. Mann, R. Milburn, A. Napier (Tufts U.), R. Davission, G. Liang, H. Lubatti, R. Wilkes, T. Zhao (U. of Washington), D. Carlsmith (U. of Wisconsin), which are cited from the MOU of T816, and K. Johns (U. of Arizona), Y. Asano (U. of Tsukuba), M. Christoph (U. of Colorado), T. Fukui (SSCL), W.Dougherty, U.Nauenberg (U. of Washington).

The results in this note, obtained by one of the T816 collaborators, Y. Teramoto, are too preliminary to be submitted to the general approval of the T816 group. We think, however, that it is beneficial and meaningful to present the results here informally, since they are extremely useful for the discussion on the design of SDC muon chambers. We like to express our gratitude in advance to the T816 collaboration, especially to H. Lubatti, T. Zhao, D. Davission, S. Errede, M. Christoph, W. Dougherty, T. Fukui, K. Johns, S. Kunori, A. Napier, and U. Nauenberg.

****

3.1 Introduction

Very preliminary results on the muon beam test (T816) are described in two parts: a brief description of the general results and the results related to the properties of the proposed jet-chambers.

T816 is located at the downstream of the muon experiment, E665, in the muon laboratory at Fermilab. The purposes of T816 are (1) to measure the

effect of materials to the creation and absorption of delta-rays and, (2) to provide a test bench for the prototypes of the muon chambers for SSC. The experimental setup consists of six drift chambers (DC1 - DC6), five scintillation counters for triggers, a 50cm-thick iron block and a 14cm-thick iron toroid magnet at the upstream of DC4 as shown in Fig. A3.1. Each drift chamber consists of three 2·3/4"-cells. Each cell has six sense wires, of which all six are read in the middle cell, but only five wires are read in the other cells. Windows of each chamber are made of Mylar sheets plated with aluminum to ensure the minimum disturbances to the measurements of the effect of test materials. The positions of those chambers along the beam direction are 19.05 cm (DC2), 118.11 cm (DC3), 217.17 cm (DC4), 316.23 cm (DC5) and 335.28 cm (DC6), measured from the most upstream chamber (DC1). All drift chambers except DC1 are arranged to measure the vertical positions of tracks. DC1 is arranged to measure the horizontal positions. Beam positions are defined by a 1" scintillation counter as shown in Fig. A3.2. The data were taken with various incident muon-beam momenta of 94 GeV/c, 350 GeV/c, 480 GeV/c and 550 GeV/c for various kinds and thickness of materials placed between the drift chambers in the downstream of the iron block. The analysis was done for the data in two conditions: (1) no extra material other than the iron block and the toroid ("no material condition"), (2) single 1" aluminum plates at the upstream of both DC4 and DC5, and a single 1/8" aluminum plate in between DC5 and DC6, other than the iron block and the toroid ("extra-material condition").

3.2 General Results

A typical event for a 550-GeV/c-muon incident with a shower of delta-rays coming from the iron block and/or toroid in the upstream of DC4 is shown in Fig. A3.3. This event illustrates the capabilities of jet-chambers to reconstruct multi-tracks.

Fig. A3.4 shows the muon-momentum dependence of the rate of events that have extra "local-tracks" other than muons found by the pattern recognition program in the drift chambers at the downstream of the iron block. We call the tracks reconstructed inside each chamber "local-tracks". We call the tracks reconstructed using local-tracks in more-than-one

chambers "global-tracks". The rates of events with extra local-tracks (δ-rays) increase with muon momenta especially in the momentum region of 94 GeV/c to 350 GeV/c. Percentages of such events in DC5 are 15 % for 94 GeV/c and 24 % for 550 GeV/c, in the "extra-material condition". In this preliminary analysis, the definition of δ-rays is not established yet. By scanning the events by eyes, we found about 20 more events with δ-rays than the ones found by the pattern recognition program. The program only searches local-tracks of delta-rays that traveled three wires or more. We can find shorter tracks by eye scan.

The rates of events that have at least one extra local-tracks within a certain distance, x, from the muon tracks, $P(x)$, are shown in Fig. A3.5 for 550 GeV/c. Inefficiency of detecting muon signals in a simple 8 cm-tube due to the disturbances by delta-rays, η, is calculated by

$$\eta = \frac{1}{8} \int_0^{4\,\mathrm{cm}} P(2x) \cdot dx$$

Rough estimates of η are 6% for 94 GeV/c and 10% for 550 GeV/c. The wavy structures in the distributions are due to the failures of resolving right-left ambiguities by the pattern recognition program.

Vertex positions of local-tracks along the beam direction are shown in Fig. A3.6 for the "no material condition" and Fig. A3.7 for the "extra-material condition". The large peak at the upstream of DC4 in Fig. A3.6 shows that the delta-rays were coming from the iron block. The broad bumps in the distributions of DC5 and DC6 at the upstream of DC5 and DC6 show that some of the tracks in DC5 and DC6 were coming from the iron block. In Fig. A3.7, the sharp peaks in front of DC5 and DC6 show that the delta-rays were produced by the aluminum plates. Spreads of the distributions are mainly due to the failures of reconstruction of local-tracks by the pattern recognition program. Systematic shifts of the broad bumps at the upstream of DC5 and DC6 from the position of the iron block in the "no material condition" are not known yet.

3.3 Results specific to the proposed jet-chambers

As shown in Table A3.1., the similarity of geometries of the T816 jet-chambers to the proposed jet-chambers make possible for us to derive the expected performance of the proposed jet-chambers for high energy muons from the date obtained by T816 jet chambers.

The capability of two-track separation may depend on the front-end electronics and the chamber gas as well as the cell-geometries, but its limit is set mostly by the cell-geometries which determine the optics of drift-electrons. We studied the spatial resolution, the pulse-widths, spurious hits, *distributions of hits with respect to the global-tracks as well as the efficiency* of track-reconstruction for different muon-beam momenta in the T816 jet-chambers.

Table A3.1. T816 jet-chambers and the proposed jet-chambers

	T816 jet-chamber	proposed jet-chamber
cell size	6.985 cm	8.0 cm
anode-anode spacing	0.9525 cm	1.0 cm
anode wire staggering	± 0.0254 cm	(no stagger)
number of wires in one cell	6	3
number of cells per chamber	1	2 with a half cell stagger
chamber gas	$Ar/C_2H_6 = 50/50$	$Ar/CO_2/CH_4 = 89/10/1$

3.1. Spatial resolution

Deviations of hit-positions in one wire from the expected positions by the least-squares fits of local-tracks in DC4 is shown in Fig. A3.8. The root-mean square of the distribution is 110 μm, which corresponds to 100 μm for the spatial resolution of one wire. Deviations of the positions of local-tracks in the most downstream chambers (DC6) with respect to the expected positions from the global-tracks reconstructed by using the upstream chambers (DC2, DC3, DC4 and DC5) are shown in Fig. A3.9. We only used three wires in each chamber to get this distribution, in order to simulate a half super-layer of the proposed jet-chamber. The root-mean square of this

distribution is 75 μm corresponding to 60 μm for the spatial resolution of one half-super-layer.

To derive these distributions, we assumed the constant drift velocity, 52 μm/nsec throughout the cells, and we used all the tracks found in the 550 GeV/c data taken with "no material condition". The irradiation of the beam was approximately uniform in the drift regions of 0.5 ~ 2.3 cm in DC4 and 0.2 ~ 2.0 cm in DC6 as seen in Fig. A3.2. It is noted that, since the spatial resolution depends on the chamber gas as well as other parameters, the spatial resolutions of the proposed jet-chambers may differ from these results.

3.2 Two-track separation

(1) Spurious hits

Fig. A3.10(a) shows the distribution of the pulse width for single-hit events. These hits are mostly by high energy muons. Fig. A3.10(c) shows the similar distribution for the hits accepted in the global-track fitting without the constraint on the number of hits on the wire. Both distributions have the average width of 4 mm (80 nsec). The cause of periodic glitches seen in these distributions is not known yet. The pulse width distribution for the multi-hits on that wire is shown in Fig. A3.10(b). It shows two peaks at 0.7 mm (14 nsec) as well as at 4 mm. We know the second peak is due to muons. The peak at short width corresponds to about 10% of all the hits in data. Our studies below indicate that the narrow pulses of about 14 nsec in width are likely to be by "spurious" hits occurring only after the main muon signals.

We looked at the distributions of the pulses arrived at the sense wire just before and just after the muon pulses. The muon hits were identified by the inclusion in the global-track fitting. Fig. A3.11 shows distributions of the distance, pulse width and inter-pulse gap separately for pulses before and after the muon signals. The existence of a large peak at short pulse width of 0.7 mm is apparent in pulses after the muon pulse but not so much before.

The distribution of the distance between the trailing edge of one pulse and the leading edge of the next pulse, "inter-pulse gap", is also shown in Fig. A3.10(d). One sees a clear peak in a small gap followed by a flat gap component. We looked at distributions of hit distance and pulse width separately for the pulses with inter-pulse gaps less than 2 mm and greater than 2 mm in Fig. A3.12. The hit-distance distribution for shorter inter-pulse gaps (A3.12b) has a peak at 3.8 mm , but none for that of longer inter-pulse gaps (A3.12a). In Fig. A3.12(d) one also sees at peak at short pulse width for the short inter-pulse gap case.

As a conclusion, the narrow pulse of about 14 nsec in width is "spurious" associated with muon pulses occurring only after the muon signals with very small inter-gap widths of less than 2 mm or with small hit-distances of 3~4 mm from muons. Its frequency is about 10 %. This spurious "after" pulses observed may be due to overshoots in circuits or cross talks, or may be real pulses caused in the drift chamber.

(2) Two-track separation

To derive the resolution of two-track separation, we analyzed the delta-ray tracks close to muons. The ability of two-track separation is degraded by the existence of spurious hits mentioned above. The analysis to reject those spurious hits could be done by setting the cuts on pulse-widths of the signals and/or inter-pulse gaps, but we haven't done this yet. The following are the results without rejecting spurious hits.

Fig. A3.13 shows a distribution of hits in one wire with respect to the expected positions from the global-tracks fitted by using the local-tracks in DC2, DC3, DC4 and DC5. The bump at 3 ~ 4 mm in the positive side is due to the spurious hits. Thus the positive side cannot be used to study two-track separation. Now, delta-rays associated with muon tracks are expected to make a gradually decreasing tail in the negative side of the distribution, because the frequencies of delta-rays should have the maximum at the muon tracks. However, Fig. A3.13(b) shows no such clear tail in the negative side. Instead the number of hits actually decrease within 5 ~ 6 mm from the muon-tracks. This is probably due to the various cuts applied in the

reconstruction of local-tracks and the cut on the residual-squared per freedom, 0.001 cm^2, in the process of fitting the global-tracks. The existence of delta-rays which arrive very closely prior to the muon-hits will kill the muon-hits and make apparently deviated hits, and it causes the pattern recognition program to reject such tracks. This speculation has not been proven yet. The depletion of hits near the muon peak on the positive side, on the other hand, is caused by muon-hits.

Fig. A3.14(a) shows the distribution of the hit distances used in the extra local-tracks in DC4. The distance is measured from the prediction of the global-tracks. Events used are required to have extra local-tracks in all chambers in the downstream of the iron block as well as the existence of local-tracks in DC5 and DC6 that matched each other. This selection was done in order to enhance the events with high energy delta-rays coming from the iron block. Fig. A3.15(b) shows the distribution of the distances between the local-tracks in DC4 which were not used in the global-tracks (δ-rays) and the local-tracks which were used in the global-tracks (muons). The event selection is the same as for Fig. A3.14(a). Both distributions show the depletion on both sides of the muon-tracks within the distances of 5 ~ 6 mm. These numbers are consistent with a simple calculation by adding (1) normal pulse-width (4 mm), (2) inter-pulse gaps between the normal pulses and their spurious hits (1 mm), and (3) pulse width of spurious hits (1 mm).

It is concluded, very preliminary though, that the capability of the two-track separations is measured to be approximately 6 mm. Since the two-track separation largely depends on the behavior of the pattern recognition program for close tracks as well as the delicate behaviors of the chambers, we may get the better resolution by tuning up the pattern recognition program. The spread of drift electrons due to the different drift-path is expected to be 5 mm/$\sqrt{2}$ ~ 3 mm. This gives a theoretical lower limit of the two-track separability in this cell geometry.

3.3 Track reconstruction efficiency

Since the purposes of the muon chambers in the SDC detector are not to reconstruct delta rays, but to reconstruct the muon tracks without affected by

delta rays, we estimated the robustness of the jet chambers to delta rays by measuring the track reconstruction efficiency in the simulated environment of T816. Fig. A3.15 shows the momentum dependence of the track-reconstruction efficiency for various cuts on the residual-squared in the global-track fit. The efficiency is defined by the ratio of the number of events that have global-tracks throughout DC2, DC3, DC5 and DC6 to the number of events that have global-tracks found in DC2 and DC3. The global-tracks were searched for the combinations of local-tracks as well as their mirror images in DC5 and DC6. We included the mirror images to minimize the inefficiency caused by the failures of solving right-left ambiguities by the local pattern recognition program. Superlayers of the proposed jet chambers are made of cell pairs with one-half-cell staggered. This configuration is expected to allow the pattern recognition program to solve the right-left ambiguities easier than the case in T816.

Data used in the analysis were taken with the "extra-material condition" for the momenta of 94, 350, 480 and 550 GeV/c. The residual-squared per freedom is defined as the square of the residuals in the least-squares fit of the positions of local tracks in DC2, DC3, DC5 and DC6. Positions of local tracks are defined as the fitted positions of local tracks at the most upstream wire of the chamber. Fits were done by straight lines assuming that there is no magnetic field. The residual-squared per freedom of 0.00125 cm^2 corresponds to the equal local track resolution (or super-layer-resolution) of 250 μm. The efficiency of track reconstruction is approximately independent of the momentum above 350 GeV/c as shown in the figure. For tight cuts the efficiency, however, drops at 94 GeV/c. The distributions of the residual-squared per freedom are shown in Fig. A3.16. The one for 94 GeV/c is broader than those with higher momenta. The broadening is consistent with the spread expected by multiple scattering in the 36 radiation lengths of the iron block plus toroid. It corresponds to the angular spread of 0.9 mrad, causing the position spread of about 1.5 mm in DC5 and DC6. Therefore, the effect of the scattering to the residual-squared per freedom is $(0.15/3)^2/2$ = 0.00125 cm^2, explaining the observed broadening effect.

The measured efficiency with the 0.00500 cm^2 cut, for which the effects of multiple scattering are small, is approximately independent of the

momenta and it is 95-96 %. Therefore, if one applies the residual-squared cuts adjusted for the momentum measured by the inner trackers of the SDC detector, the track reconstruction efficiency can be kept at this level for all muons. It is noted that the efficiency depends on the quality of the pattern recognition program. It is possible that a better pattern recognition program can make this efficiency even higher.

4. Summary

A very preliminary analysis was done on the T816 data. The rate of events with δ-rays increases with the incident muon-momentum from 15 % at 94 GeV/c to 23 % at 550 GeV/c in the chamber approximately 1 m downstream of the iron block with 1" aluminum at the upstream of the chamber. This arrangement simulates the environment of the SDC muon chambers. The performance of the T816 jet chamber was studied to estimate the expected behavior of the proposed jet chamber. A typical event with a shower of delta rays illustrates clearly the capability of jet chambers to reconstruct multi-tracks. The measured spatial resolution of a single wire is 100 μm. The measured spatial resolution of a half-super-layer is 60 μm. Muon hits are accompanied immediately after by a narrow spurious hit at a rate of 10 %. The two-track separation was studied in various ways. The resolution of two-track separation is estimated to be 6 mm with the current pattern recognition program. The efficiency of global track reconstruction in the downstream of the iron block is an order of 95 % in the muon momentum range from 94 GeV/c to 550 GeV/c.

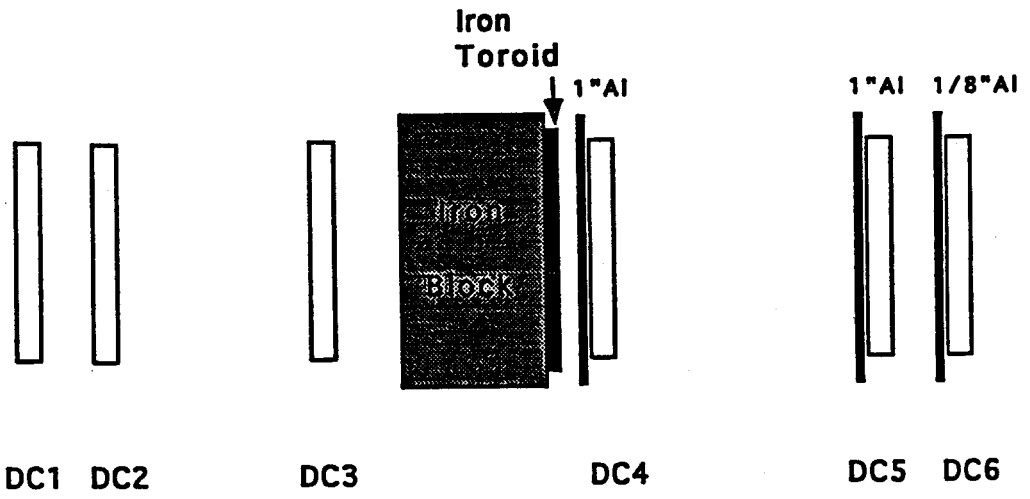

Fig. A3.1. A schematics of the experimental setup. This shows the test materials for the "extra-material condition". Muon beams are coming from left.

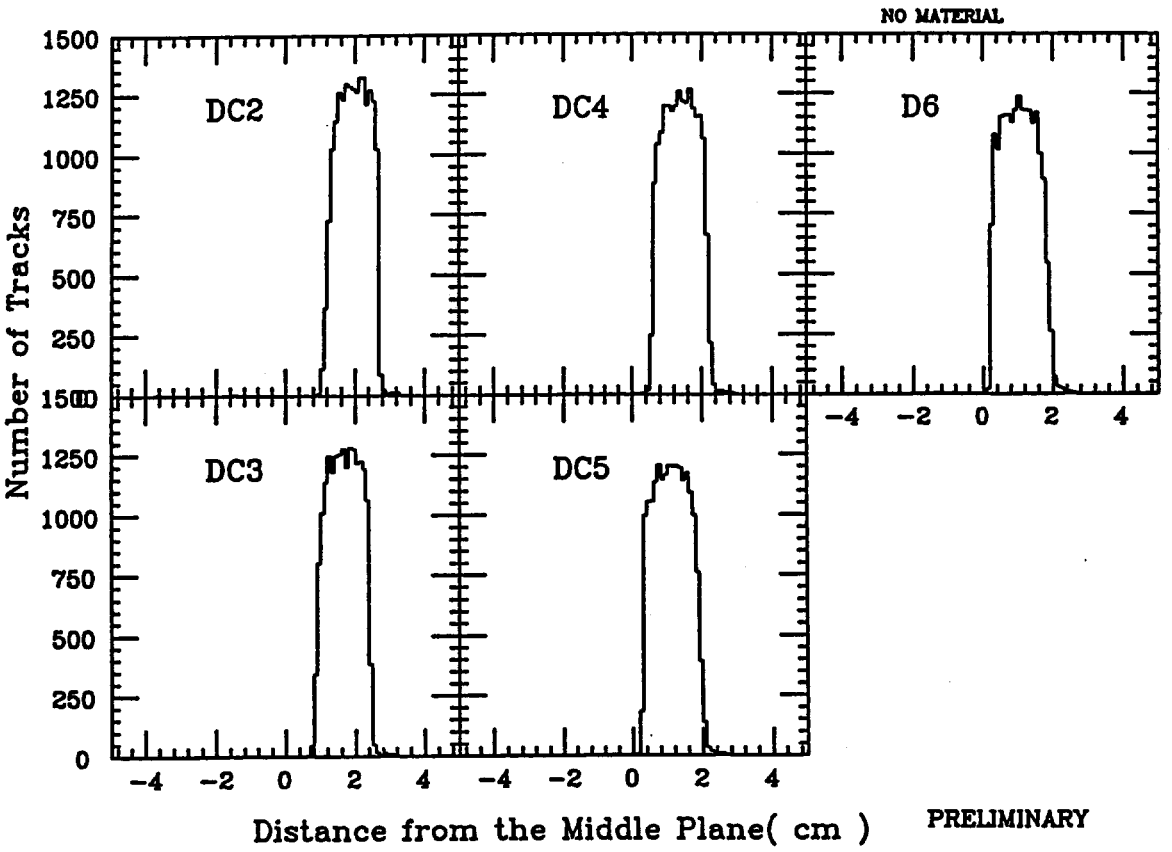

Fig. A3.2. The beam profile in the 550 GeV/c data.

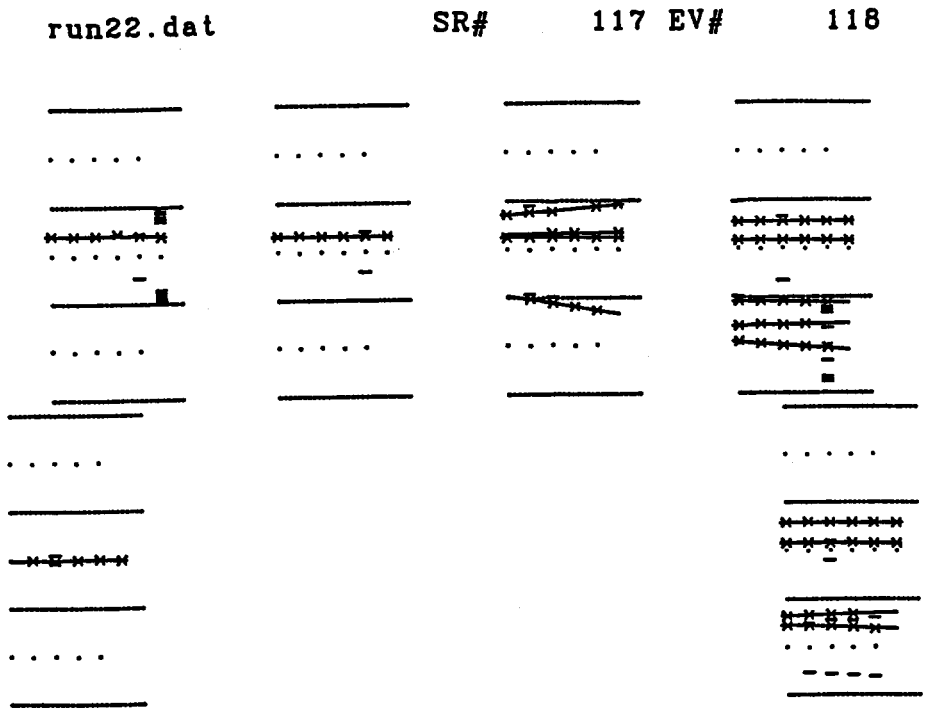

Fig. A3.3. A typical event. Scales of the display-windows are not proportional. Four chambers in the upper half are DC2, DC3, DC4 and DC5 from left to right. Two chambers in the lower half are DC1 and DC6 from left to right. In the vertical view, a muon entered the upper drift region of the middle cell of DC2, then it passed through DC3, DC4, DC5 and DC6. The average incident angle of the beam was 3.0 mrad tilted to the downward direction from the normal incident with a 0.6 mrad r.m.s. spread. Right-left ghosts of the hits reconstructed as local-tracks were eliminated, but the ghosts of other hits were shown in this figure.

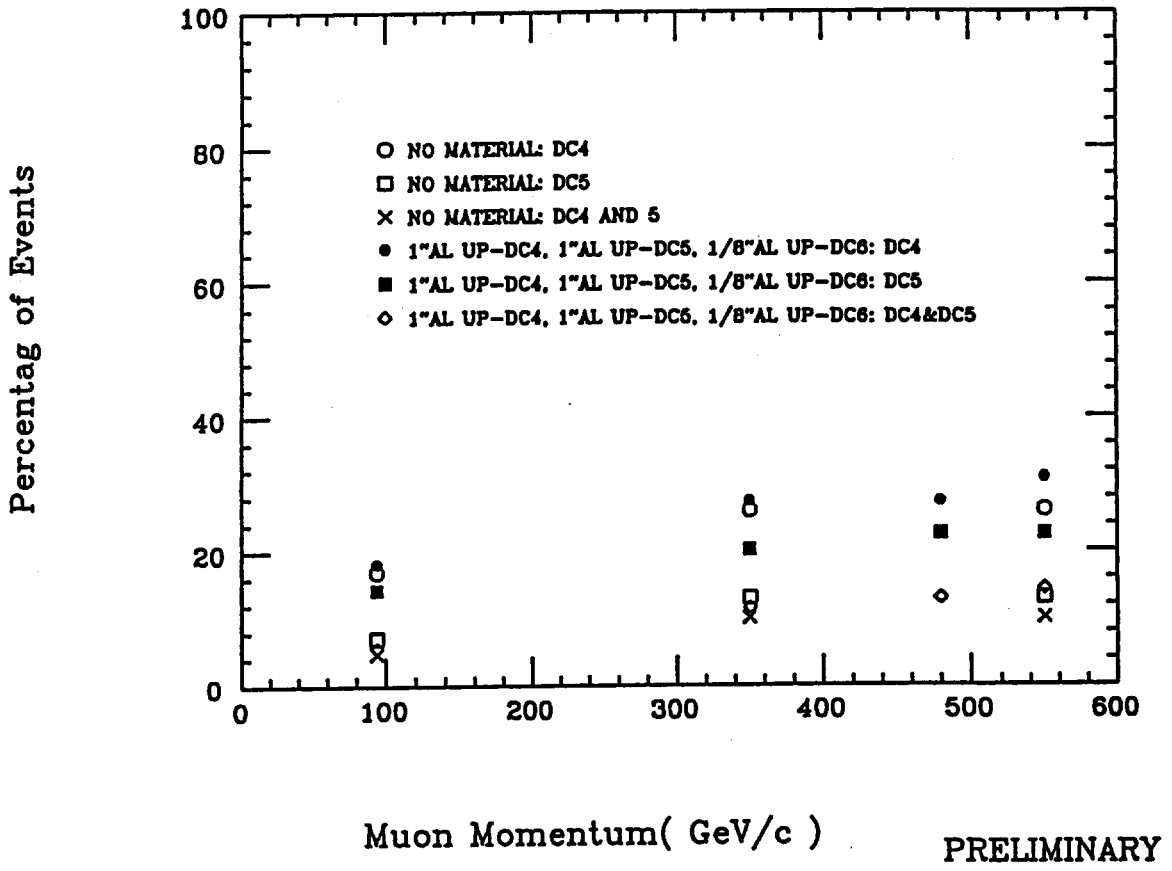

Fig. A3.4. The rate of events with extra local-tracks found in the downstream drift chambers to the events that have single tracks in DC2 and DC3 or one extra local-track in either DC2 or DC3. "DC4" indicates the events with extra local-tracks in DC4. "DC5" indicates the events with extra local-tracks in DC5. "DC4 and DC5" indicates the events with extra local-tracks in both DC4 and DC5.

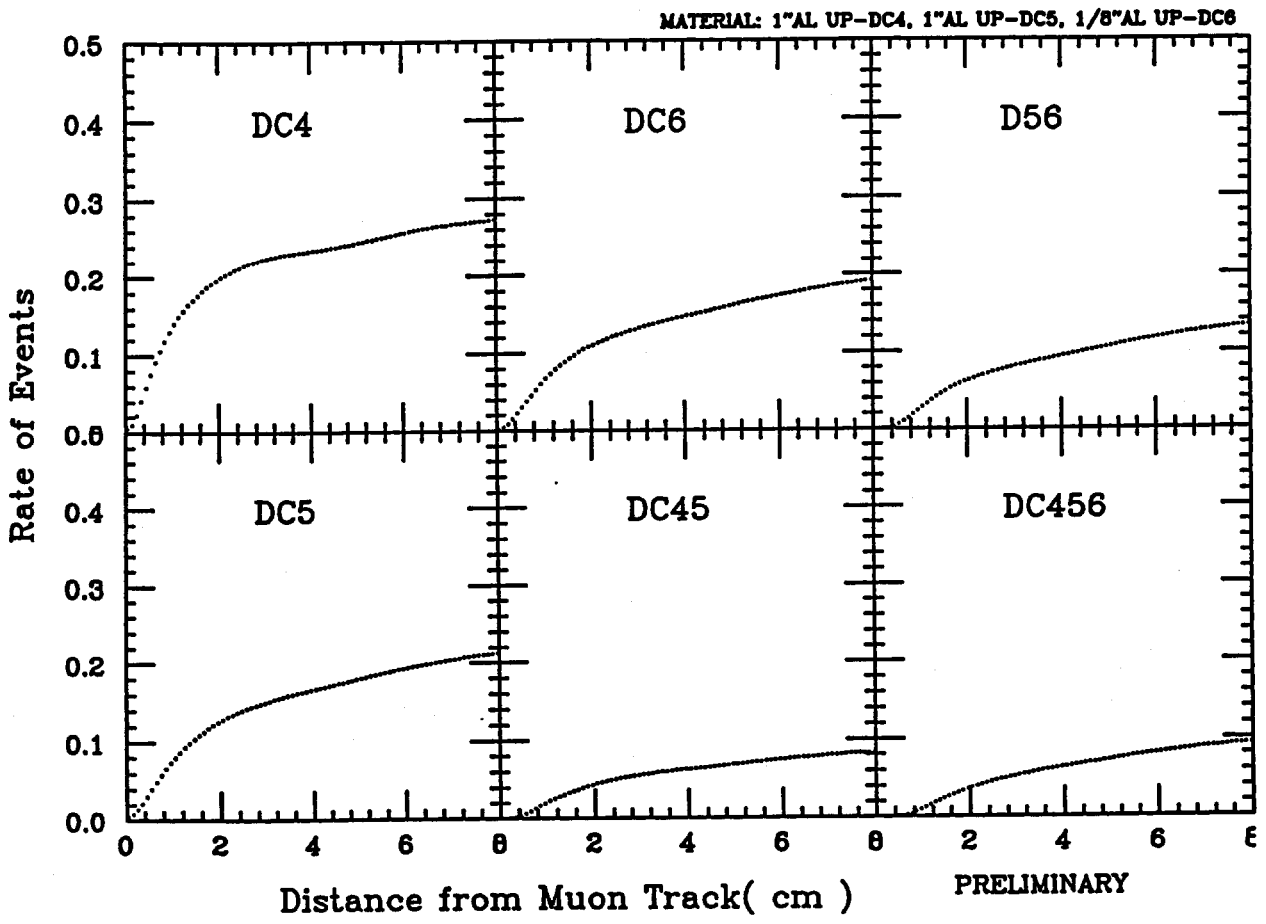

Fig. A3.5. The distribution of $P(x)$ for 550 GeV/c muons for the "extra material condition". "DC4" indicates the cases that at least one local-track within the distance, x cm, in DC4. "DC5" and "DC6" are defined similarly. "DC45" means that at least one local-track within the distance, x cm, in both DC4 and DC5. "DC56" and "DC456" are also defined similarly.

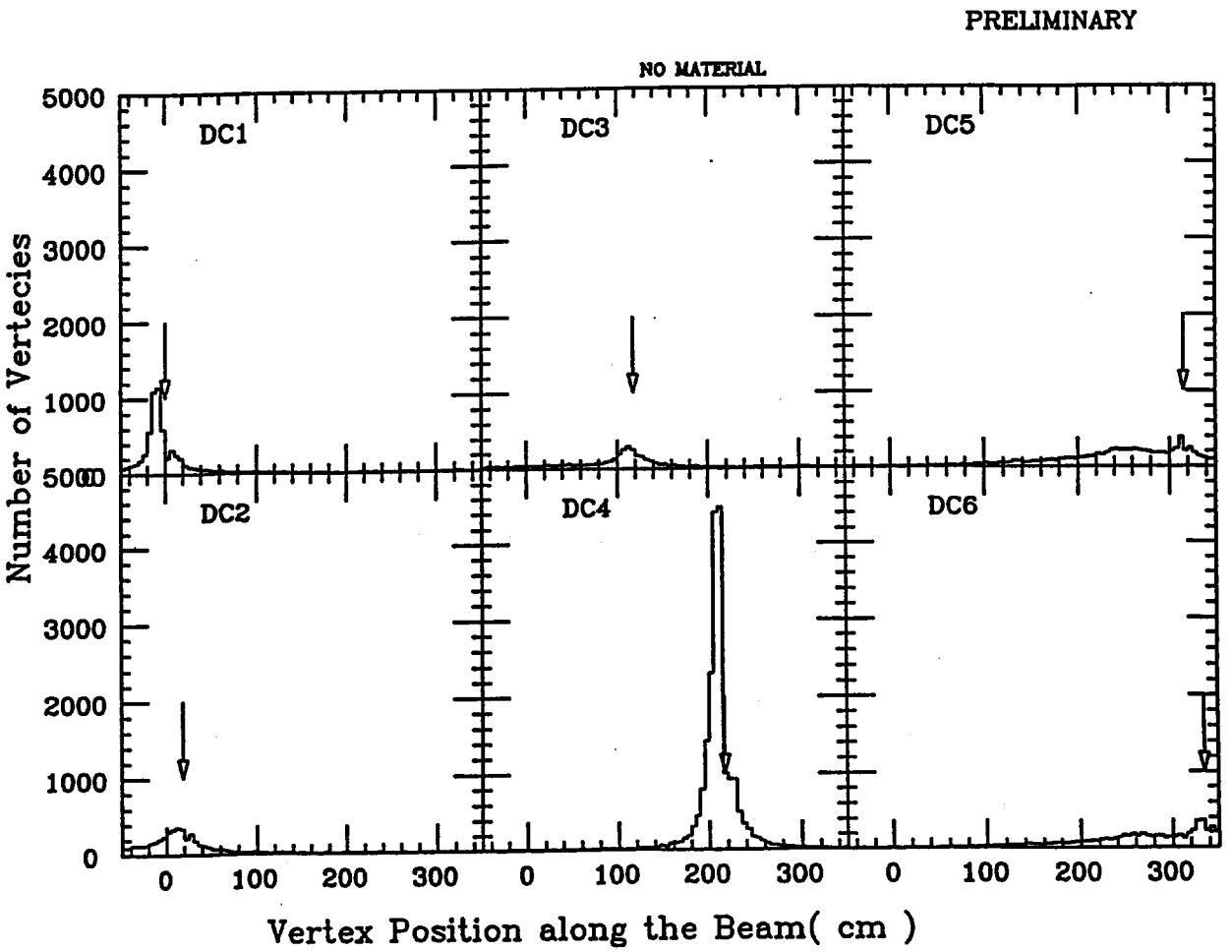

Fig. A3.6. Vertex positions of local-tracks along the beam direction in the 550 GeV/c data for the "no material condition". The position of each chamber is shown by an arrow.

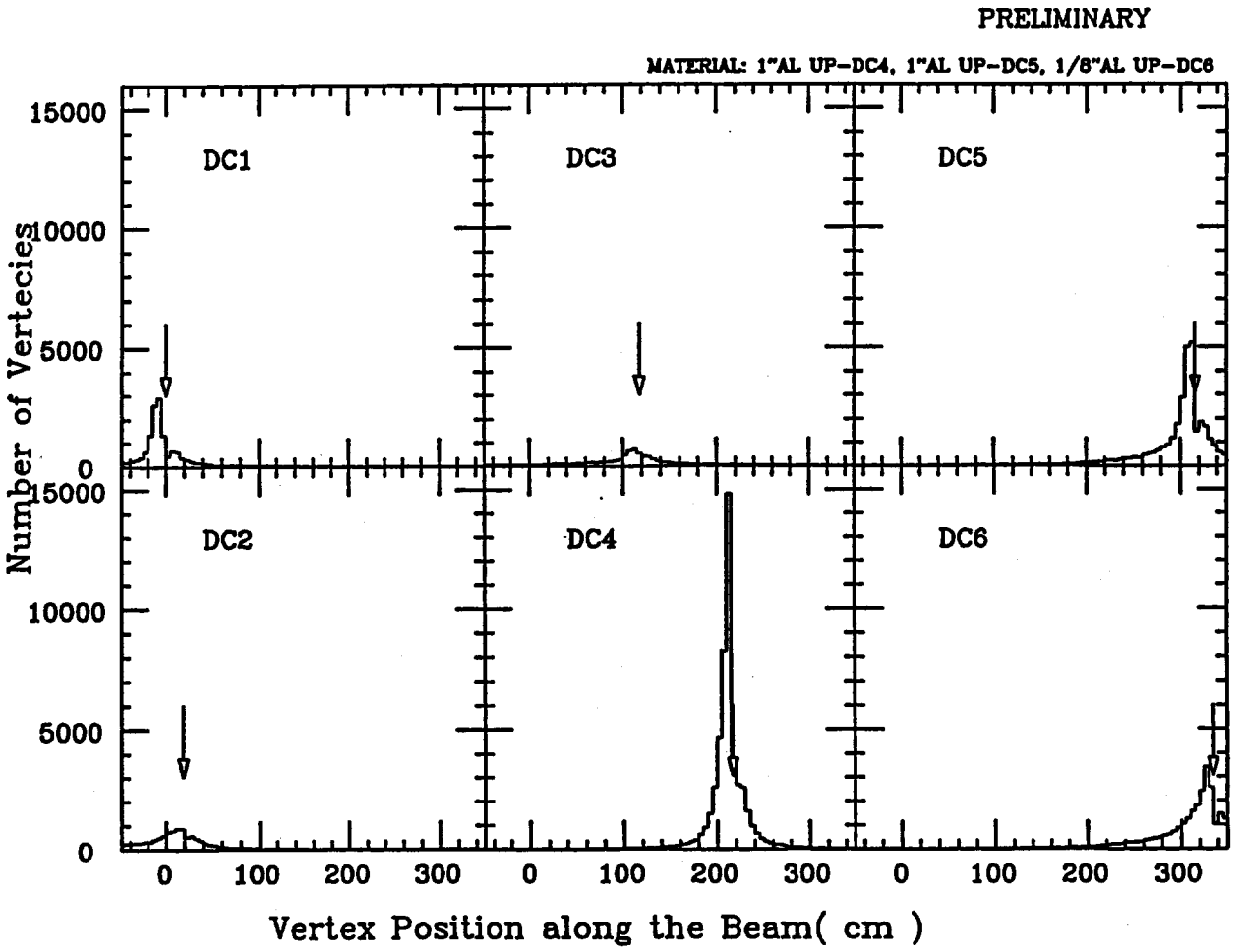

Fig. A3.7. Similar distribution as Fig. A3.8 for the "extra-material condition".

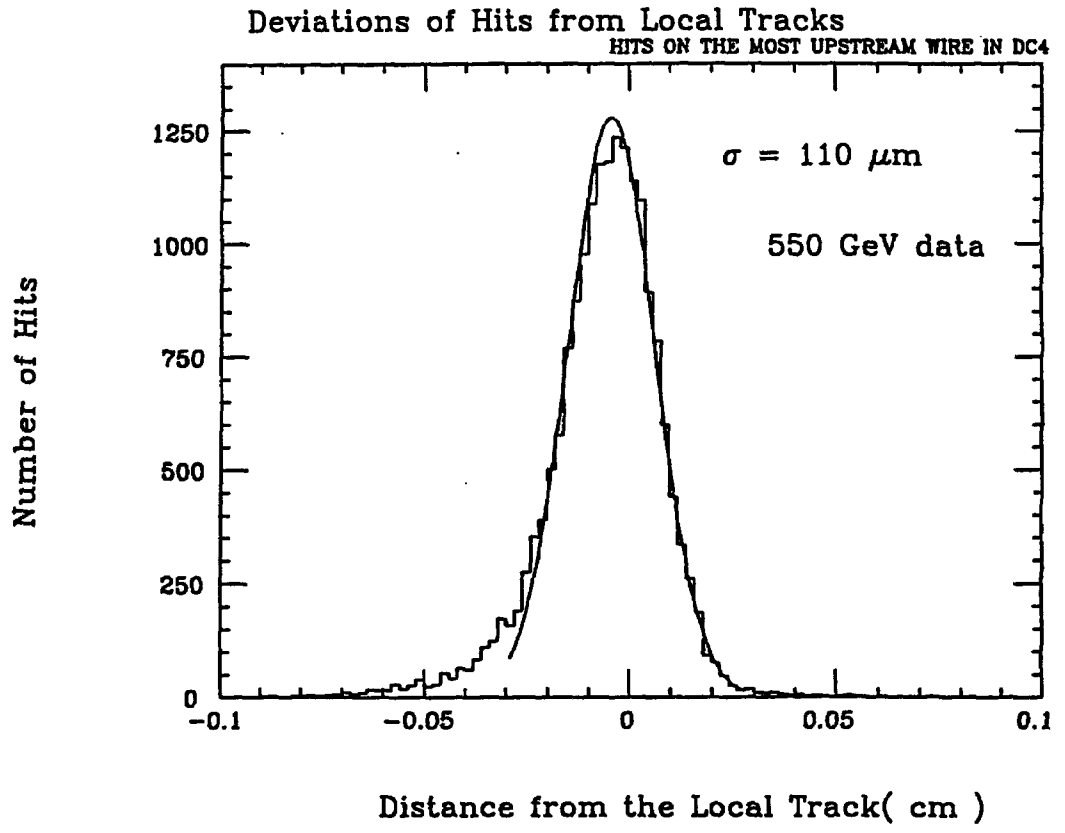

Fig. A3.8. Deviations of the positions of hits with respect to the expected positions by local-tracks in DC4.

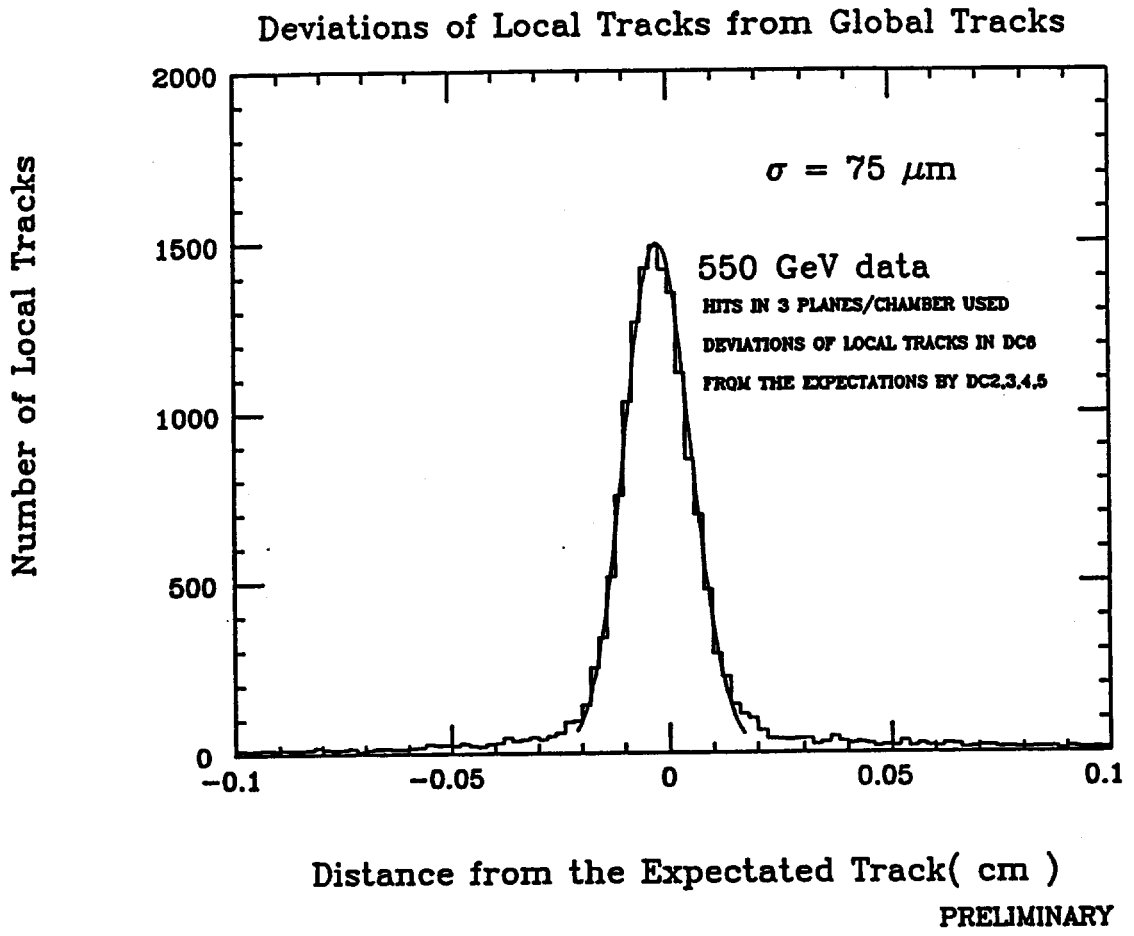

Fig. A3.9. Deviations of the positions of local-tracks in DC6 with respect to the expected positions by the global-tracks reconstructed by using DC2, DC3, DC4 and DC5. Only three wires in each cell were used to simulate half-super-layers of the proposed jet-chambers.

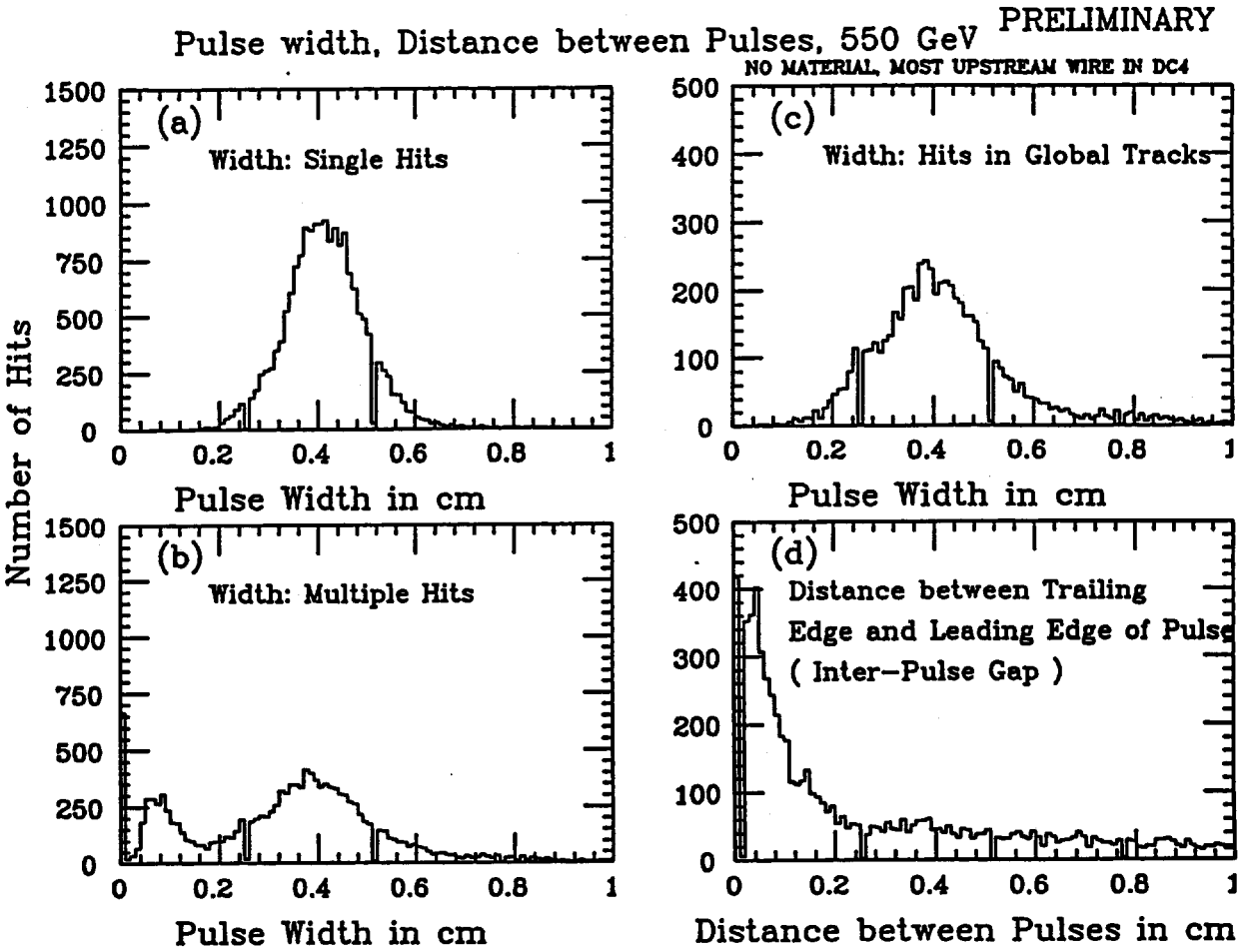

Fig. A3.10. Pulse-width distributions and the distribution of pulse-gaps. (a) The pulse-width for single-hits on the wire. (b) The pulse-width for multiple-hits on the wire. (c) The pulse-width of the hits in the local-tracks that passed the global-track fits. (d) Distances between the trailing edges of the pulses and the leading edges of the next pulses. We call this as "inter-pulse gaps".

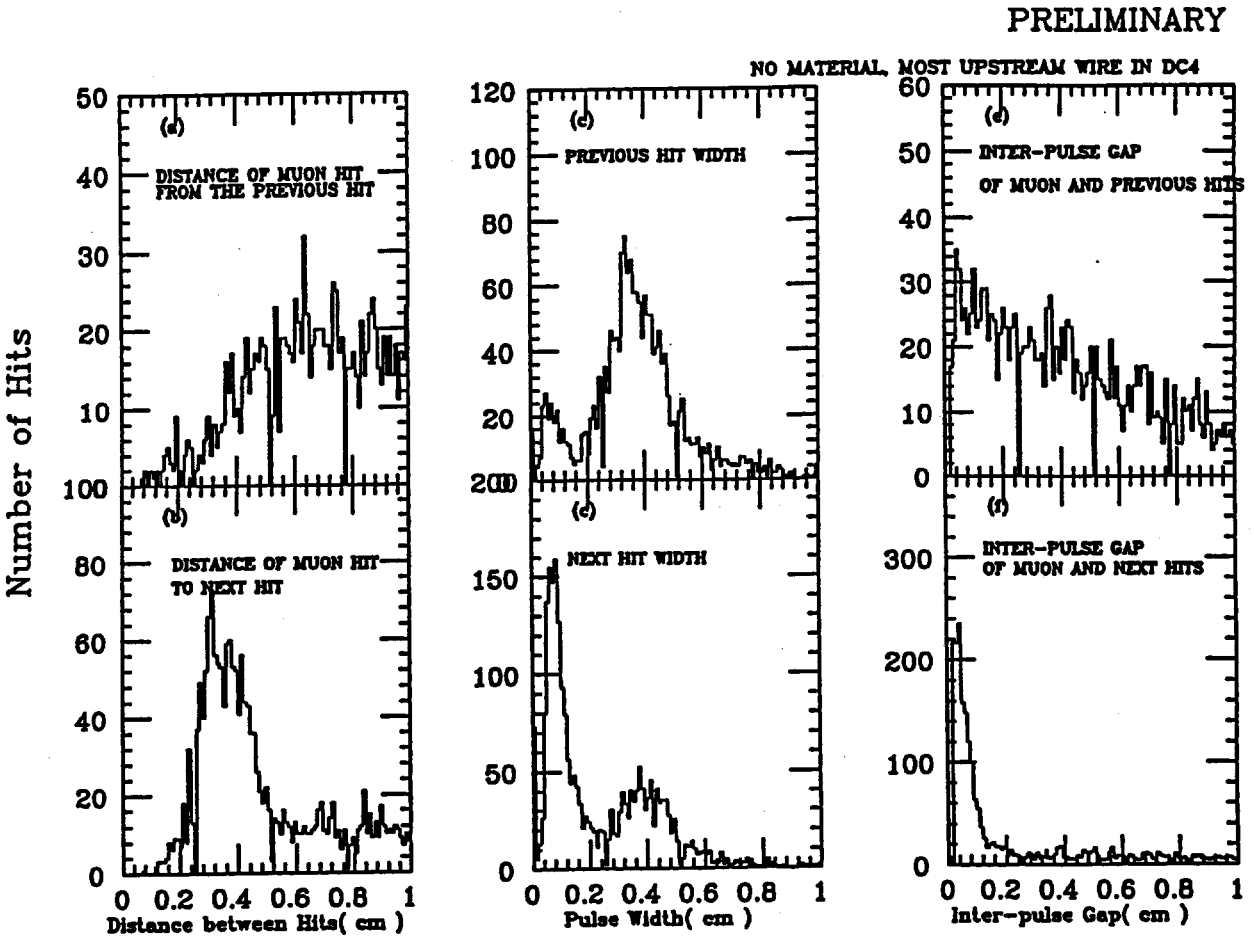

Fig. A3.11. (a) Distances between the muon-hits and the hits one before the muon-hits. (b) Distances between the muon-hits and the hits one after the muon-hits. (c) Widths of the hits just one before the muon-hits. (d) Widths of the hits just one after the muon-hits. (e) "Inter-pulse gaps" of muon-hits and the hits one before the muon-hit. (f) "Inter-pulse gaps" of muon-hits and the hits one after the muon-hits.

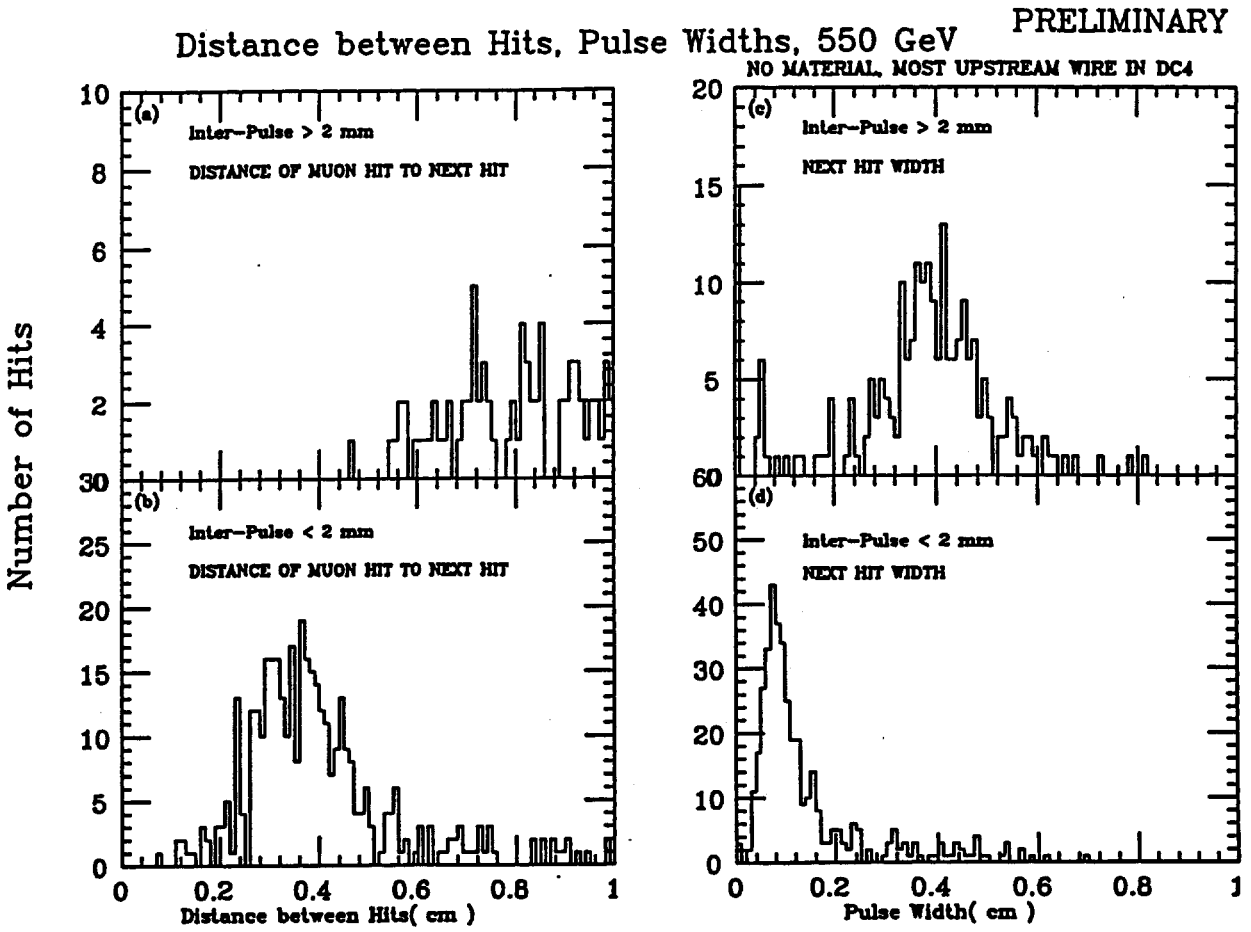

Fig. A3.12. Pulse-widths of the hits one after the muon hits and the distances between muon-hits and the hits one after the muon-hits for small and large "inter-pulse gaps". (a) Distances of hits for "inter-pulse gaps" > 2 mm cases. (b) Distances of hits for "inter-pulse gaps" > 2 mm cases. (c) Pulse-width for "inter-pulse gaps" > 2 mm cases. (d) Pulse-width for "inter-pulse gaps" > 2 mm cases.

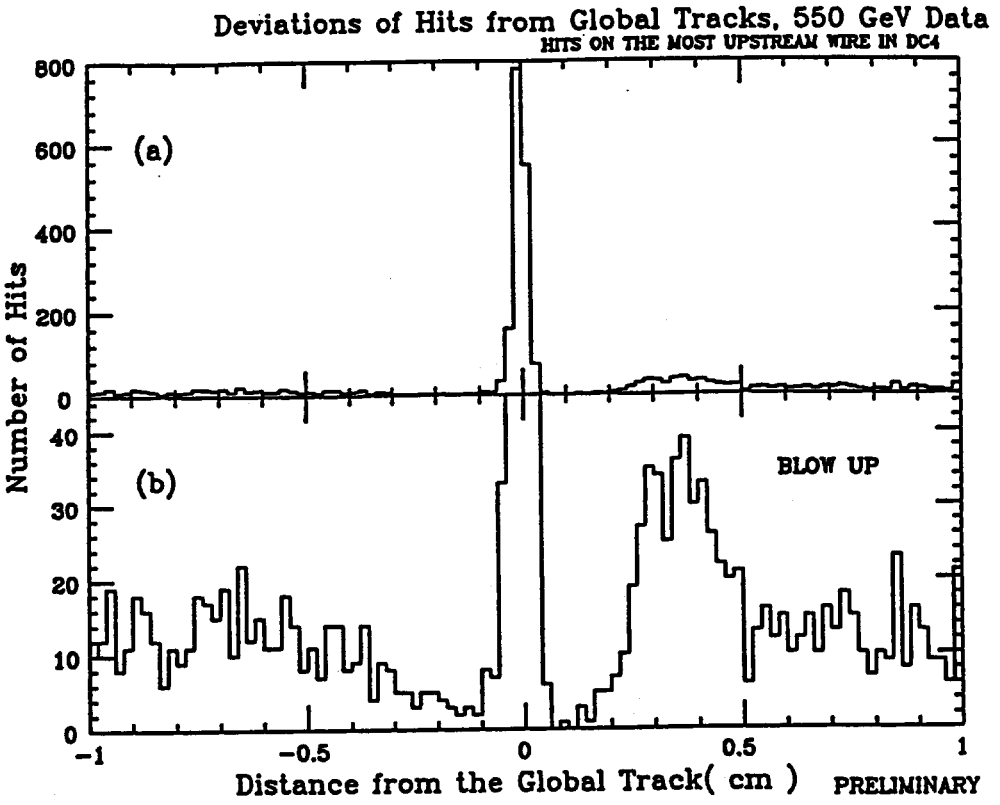

Fig. A3.13. (a) Deviations of hit-positions from the global-tracks. (b) Blow-up of (a).

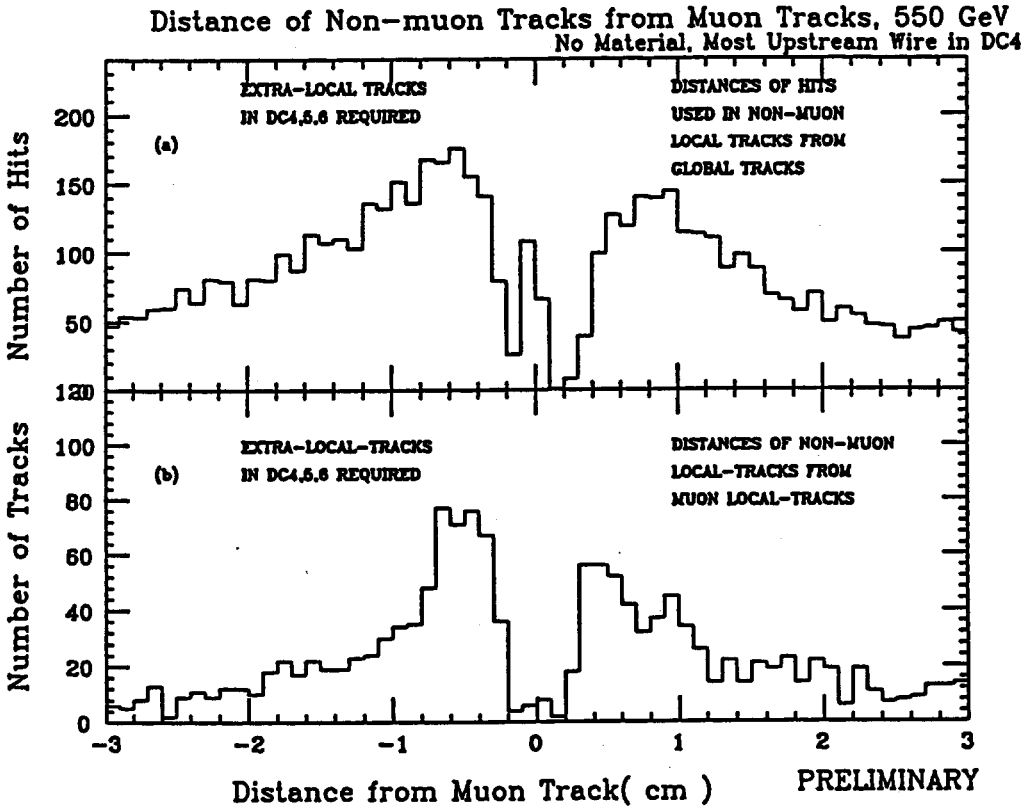

Fig. A3.14. (a) Distance of hits in DC4 in the reconstructed delta-rays from the global muon tracks. (b) Distance of local tracks of reconstructed delta rays from the global muon tracks.

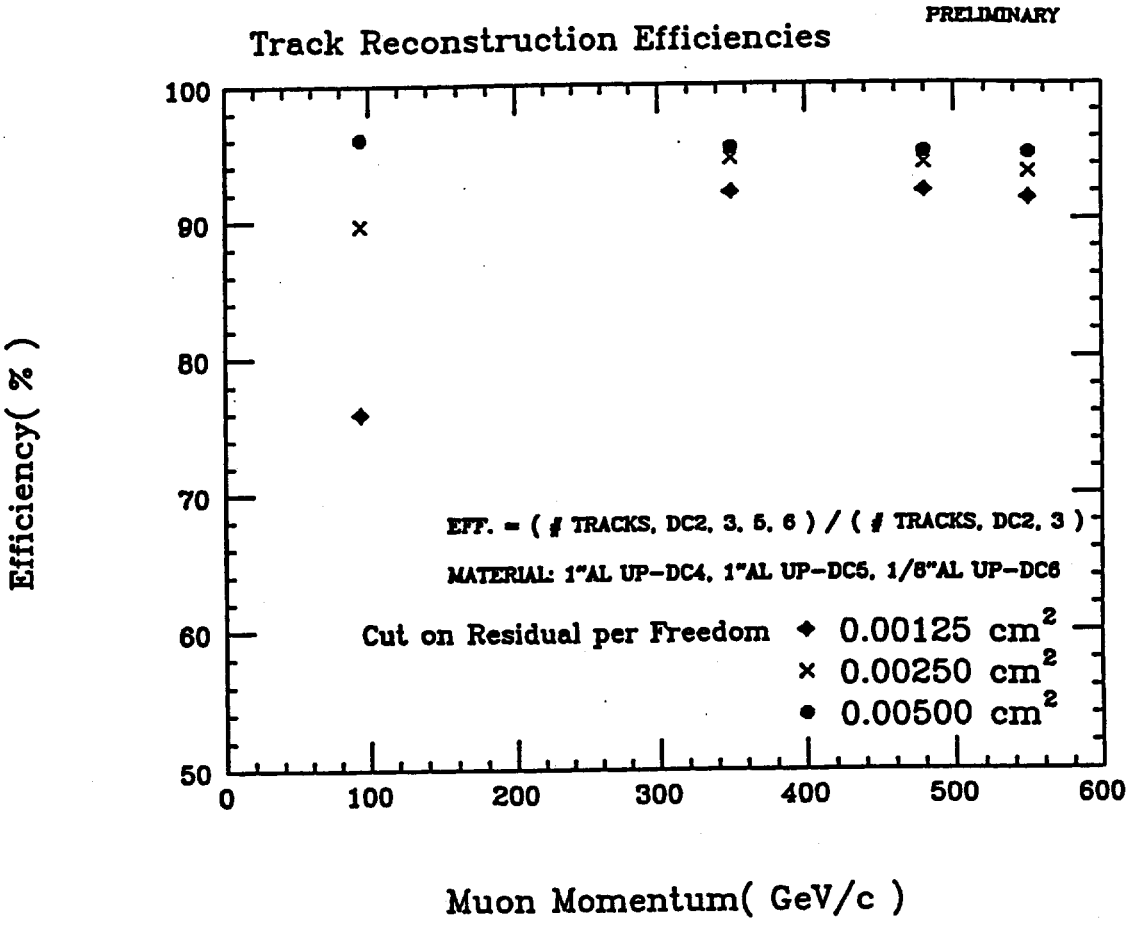

Fig. A3.15. Track reconstruction efficiencies with respect to the incident muon momentum for different cuts on the residual squared per freedom in the global-track fits. The date is for extra-material case.

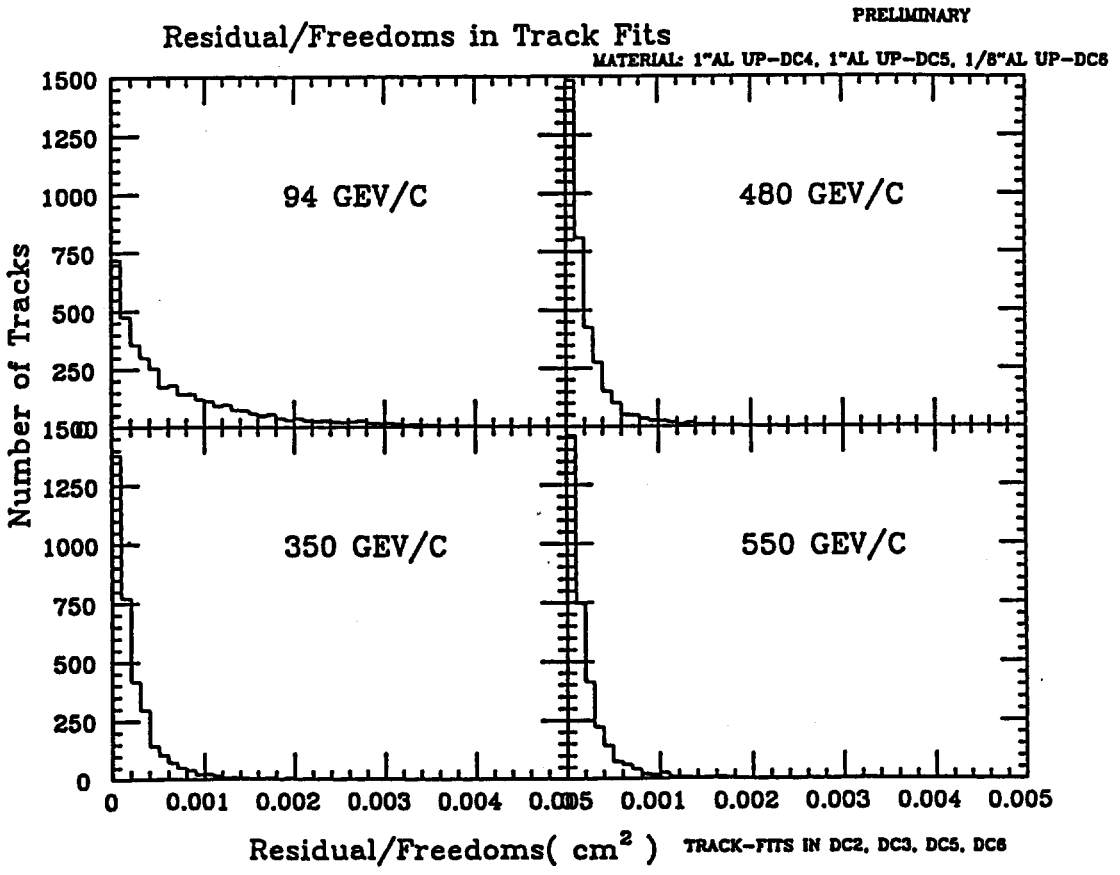

Fig. A3.16. Residual-squared per freedom in the global-track fits for various muon momenta.

Appendix 4. Alternative muon trigger option

1. Trigger strategy

This appendix describes an alternative option of the level-1 and 2 muon trigger. The trigger formation is entirely based on digital processing, contrary to the semi-analog method described previously. The principle of this option is

Level 1 : to find track segments in each superlayer

Level 2 : to connect information from superlayers and to improve the resolution of P_t trigger.

The level-1 trigger processing is based on signals from discriminator outputs.and is independent of the TMC time digitizers. The level-2 trigger is processed using output of level-1 trigger as well as output from TMCs.

2. Implementation

The structure of the muon trigger system is shown in Fig. A4.1. Initial trigger processing is done locally in the crates that are attached to the underground SDC detector. The output of trigger signals from each crate are transmitted to the surface via an optical fiber for final level-1 processing and for level-2 trigger formation.

As schematically shown in Fig. A4.2, each SD card mounted on the back of a muon crate receives 48 channels of analog signals from muon chambers. A pair of the SD cards supplies 96 descriminated signals to one TMC Board and one L1 Trigger Board. These boards are arranged in the muon crate as illustrated in Fig. A4.3. The backplane of the muon crate transmits the L1 trigger signals as well as L2 trigger information to a Trigger Processor Module.

3. Level-1 trigger

The level-1 local trigger will be formed through five consecutive operations :

(1) Track Segment Finder (TSF) to find tracks in a cell,

(2) Track Segment Match (TSM) to find matched tracks in

staggered superlayer cells,

(3) Track Segment Counter (TSC) to count the number of tracks,

(4) Track Segment Summation (TSS) to sum up muon tracks,

(5) Track Segment Encoder (TSE).

Operations (1) through (3) are done in a muon trigger board, while those for (4) and (5) are executed on a trigger processor mounted in each crate. A conceptual layout of the trigger board and the crate processor board are shown in Figs. A4.4 and A4.5 respectively.

3.1 Track Segment Finder (L1TSF)

The circuit receives 3 sense wire signals from a jet cell. It is possible to set the minimum time resolution at 2ns, 4ns, 8ns or 16ns. The circuit details depend on this minimum time resolution. Selection of the time resolution will be done based on the cost and complexity of the actual chips used. Two examples of TSF are shown in Figs. A4.6 and A4.7 for the cases of 16ns and 4ns. In principle, the chamber hits, after clipping, are stored in the shift registers with a depth of 3 clock cycles. Outputs of the shift registers are sent to MLU (memory lookup units) to examine the hit patterns every clock cycle against the pre-loaded patterns of acceptance. The output of MLU consists of

CSP : Cell Track Segment Presence	1 bit
CSL : Cell Track Segment Location	2 bits
CSG : Cell Track Segment Gradient	4 bits max
CSQ : Cell Track Segment Quality	4 bits max

The time sequence of this process is as follows;

clock cycle	
1	signal clipping
2	shift 1
3	shift 2
4	shift 3
5	segment finding by MLU
6	segment encoding.

It is estimated that about 20 input/output pins are required for each cell. Thus 4 cells (12 sense signals) can be handled in one TSF ASIC chip. Shift register outputs will be used for L2 trigger.

3.2 Track Segment Match Finder (L1TSM)

This circuit makes a connection between staggered jet cells with mean timer method using TSF outputs. At the same time, the circuit make a coincidence with a signal from scintillation counters. The conceptual block diagram is shown in Fig. A4.8.

The CSP(cell track segment presence) signals from L1TSF circuits of staggered cells A and B are matched by means of a mean-timer logic. The clock of the mean timer is 16ns so that its depth is 50 units corresponding to 800ns, maximum drift time of the jet chamber. After making appropriate coincidence with delayed timing signals from corresponding scintillation counters, other L1 quality bits such as CSG, CSQ generated by the TSF circuits are filtered through synchronization circuits. Then these bits will be sent to an MLU logic in order to select or eliminate the track candidates. At the same time, the hit position is encoded to 5 bits for the use of higher level triggers.

The clock cycles used for TSM is

drift time wait	50 cycles
track segment match detection	1 cycle
track segment encoding	1 cycle.

The output from TSM is

LSP: Layer Track Segment Presence	1 bit
LSL: Layer Track Segment Location	6 + 2 bits
LPT: Layer Track Segment Pt	4 bits
LSQ: Layer Track Segment Quality	4 bits.

Out of these output results, LSP and LPT will be transmitted further to the surface for global L1 trigger. It is estimated that one ASIC chip is needed for each pair of staggered cells, and therefore 32 chips must be mounted on one trigger board (see Fig. A4.4).

3.3 Track Segment Counter (L1TSC)

TSC sums up the number of candidate tracks found in each module. Then the total number of tracks found in a muon crate is obtained in the trigger processor module. In addition, it is possible to sum up the track numbers for

every octant. These numbers of tracks are separately calculated for each bin of P_t (4 bits). Necessary clock cycles are

decode in terms of Pt	1 clock cycle
track segment counting	2 clock cycles.

The output is called SCS (segment count set) consisting of 32 bits. This is because we have 16 different P_t categories (4 bits including sign) and 2 bits are allocated for each P_t range in order to represent the number of tracks as

0: no tracks,	1: one track,
2: two tracks,	3: more than 2 tracks.

It is estimated that one ASIC chip per board is probably possible since 5 pins from each TSM chip times 32 TMS chips makes 160 input pins for a TSC.

3.4 Crate Summary Board

This module is mounted at the 17th slot of a muon crate. It collects L1 data from each trigger module and sends the summary of L1 data to MLC(Muon Logic Card) located on the surface. It actually receives two bits SCS from each module for each P_t category (up to 16), makes a summation and outputs the summary SCS with the same format. A TSE (Track Segment Encoder) picks up two track candidates with highest and 2nd highest P_t from the SCS summary sets and encode them to a set of 16 bits. This 16 bits will be transformed into serial data in order to be shipped to the MLC.

3.5 Summary of clock cycles

Following is the summary of clock cycles used for the formation of level 1 muon triggering underground :

cycle number	items
1	TSF clipping
2-4	TSF delayed signal wait #1-#3
5	TSF segment finding
6	TSF segment encoding
7-56	TSM drift time wait #1-#50 (mean timer)
57	TSM segment match finding

58	TSM segment encoding
59	TSC Pt decoding
60	TSC segment counting
61	TSC segment count set generation
62	TSS segment count summation
63	TSE MLC information encoding
64	EOC transmission to MLC

Therefore, we use up 14 clock cycles out of 20 allocated for L1 muon trigger formation. 6 cycles are left for the use of global L1 trigger at the surface, one of which is a consistency check in the number of track segments in chamber layers of BW1θ, BW1ϕ, BW2θ, BW3θ and BW3ϕ.

4. Level-2 trigger

Level-2 muon trigger is done by combination of microprocessors and specialized co-processors. Its architecture should be designed in order to maintain the maximum flexibility for trigger conditions. The level-2 trigger system utilizes outputs from L1 muon trigger. The system is composed of 5 different components (see Figs. A4.1,A4.3 and A4.4);

(1) L2 Buffer (L2PB)
L2B stores necessary data from L1TSM. Only data corresponding to accepted L1 trigger will be readout. Its outputs will also be sent to event builder.

(2) L2 Board Processor (L2BP)
This processor reads data of all L2B chips, does formatting and writes results on dual port memory on the same board. The memory will be readout by a crate processor through backplane bus.

(3) L2 Carte Processor (L2CP)
This processor collects data from all of the trigger boards and all of the TMC boards in the same crate through its backplane buses. It calculates track information based on these data for individual track candidates. The result will be transmitted to the sector processor on the surface via optical fibers.

(4) L2 Sector Processor (L2SP)
It collects data on track candidates and makes interconnections among tracks between superlayers. The results in θ and ϕ planes are checked against preloaded constraints on P_t and interaction points along the z axis.
Good candidates will be transferred to the master processor.

(5) L2 Master Processor (L2MP)
This processor receives data on track candidates from eight octants, forms their summary and sends the results to Global L2 trigger system. This system can serve as a master of subsystems for calibration runs.

5. Channel and module count

Table A3-1 is a summary of rough and approximate estimation of channels, modules, crates and cost for Level-1 muon trigger. The basic element costs assumed are \$100 per ASIC chip, \$2000 per crate for all parts except ASIC chips, and \$10,000 per crate for a crate, power supplies and associated processor boards.

	BW1-θ	BW1-ϕ	BW2-θ	BW2-s	BW3-ϕ	BW3-θ	total
sampling	6	6	6	4	6	6	34
cells	3367	2733	4467	3050	6433	4933	24983
sense wires	10100	8200	13400	6100	19300	14800	71900
TMC chips	2525	2050	3350	1525	4825	3700	17975
TMC boards	105	85	140	64	201	154	749
TMC crates	7	5	9	4	13	10	47
TMC cost (k$)	529	429	701	319	1010	775	3764
L1TSF chips	842	683	1117	0	1608	1233	5483
L1TSM chips	3367	2733	4467	0	6433	4933	21933
L1TRG boards	105	85	140	0	201	154	685
L1TRG crates	7	5	9	0	13	10	43
L1TRG cost (k$)	697	566	925	0	1332	1021	4541
L1 crates	13	11	17	4	25	19	90
L1 cost (k$)	1226	995	1626	319	2342	1796	8304

Table A3.1 Jet type muon chamber readout/trigger (option) electronics

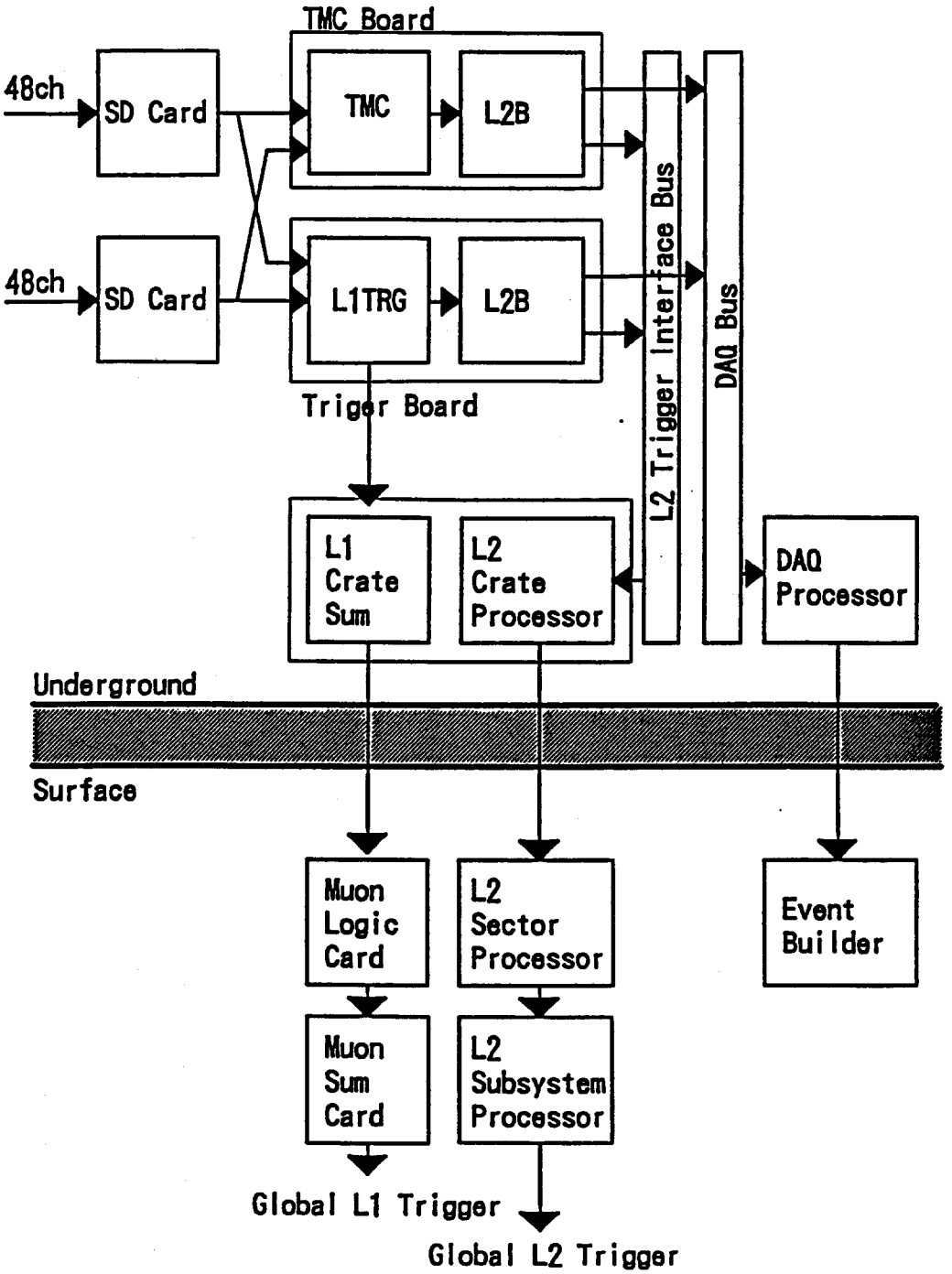

Fig. A4.1 Muon trigger system architecture

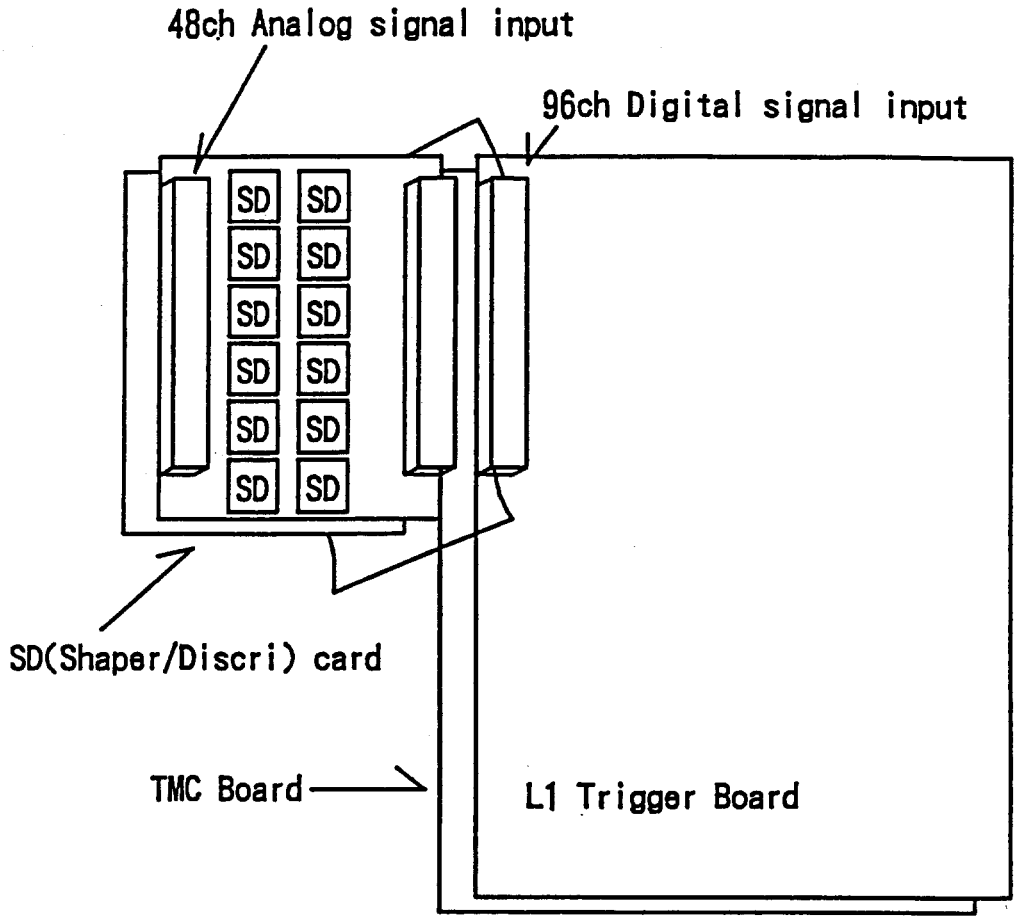

An SD card covers 48 channels from preamp.
TMC board and L1TRG board occupy adjacent 2 slots and share 96 digital inputs supplied by 2 SD cards behind the backplane.

Fig. A4.2 Connection of muon input signals

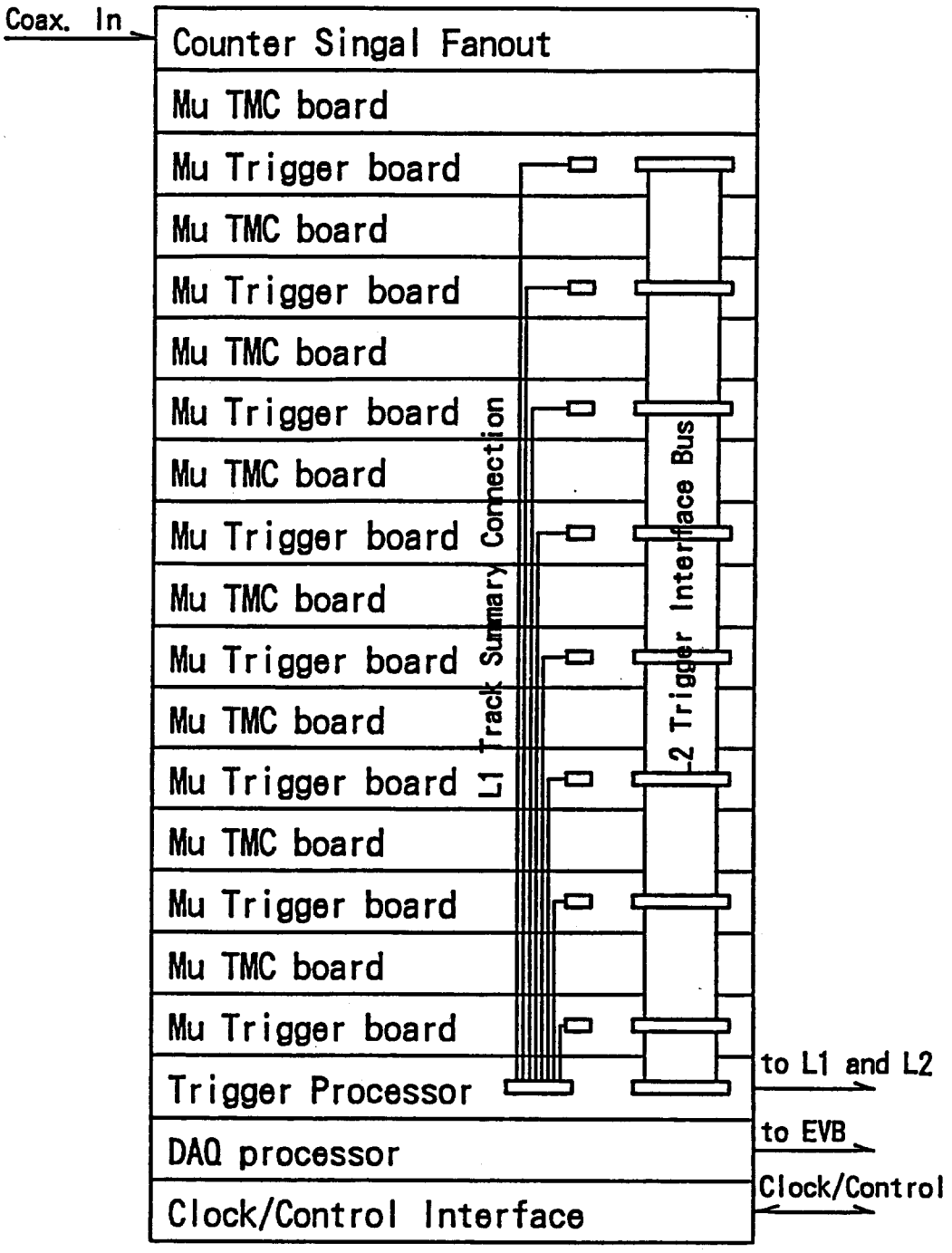

Fig. A4.3 Muon readout crate concept

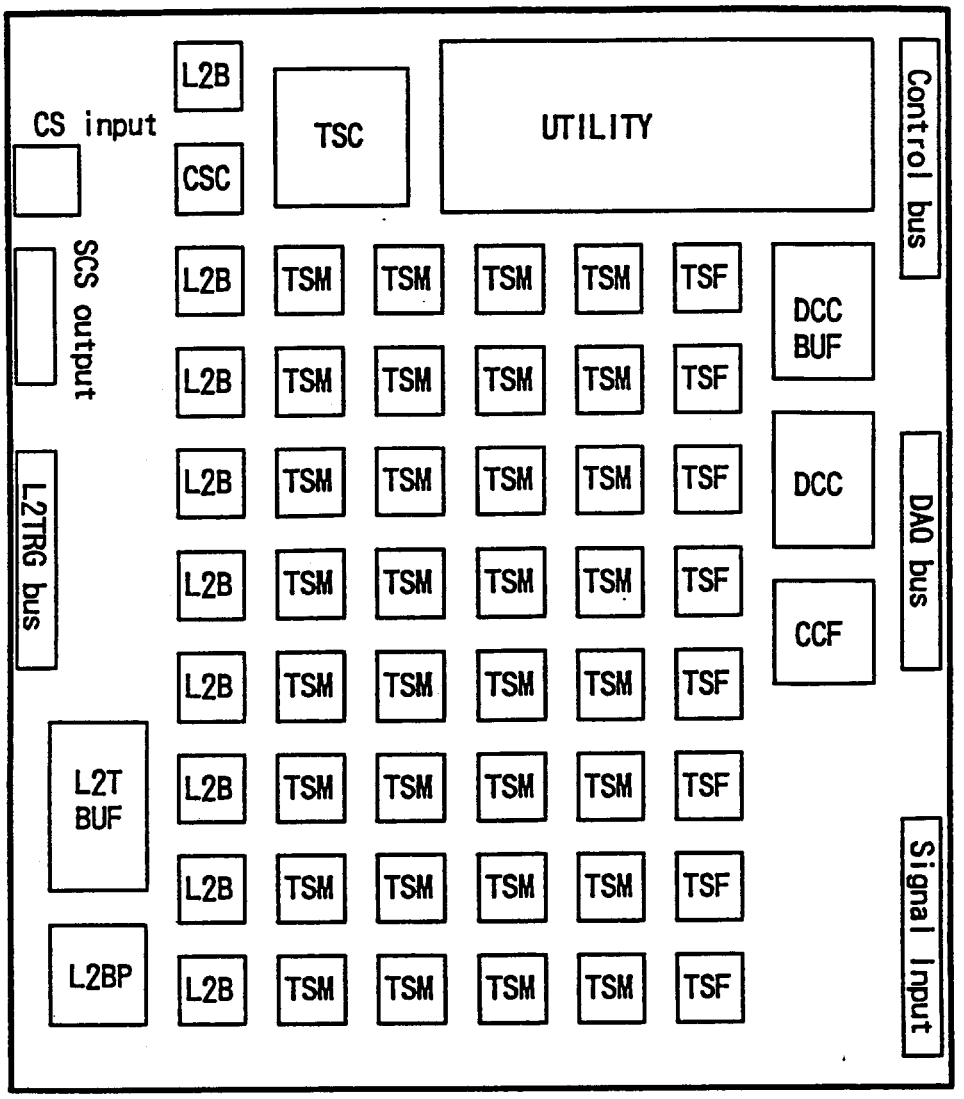

CCF: Clock and Control Fanout
CSC: Counter Signal Conditioner
DCC: Data Collection Chip
L2B: Level 2 Buffer
L2BP: Level 2 Board Processor
SCS: Track Segment Count Set
TSC: Track Segment Counter
TSF: Track Segment Finder
TSM: Track Segment Match Detector

Fig. A4.4 Muon trigger board concept

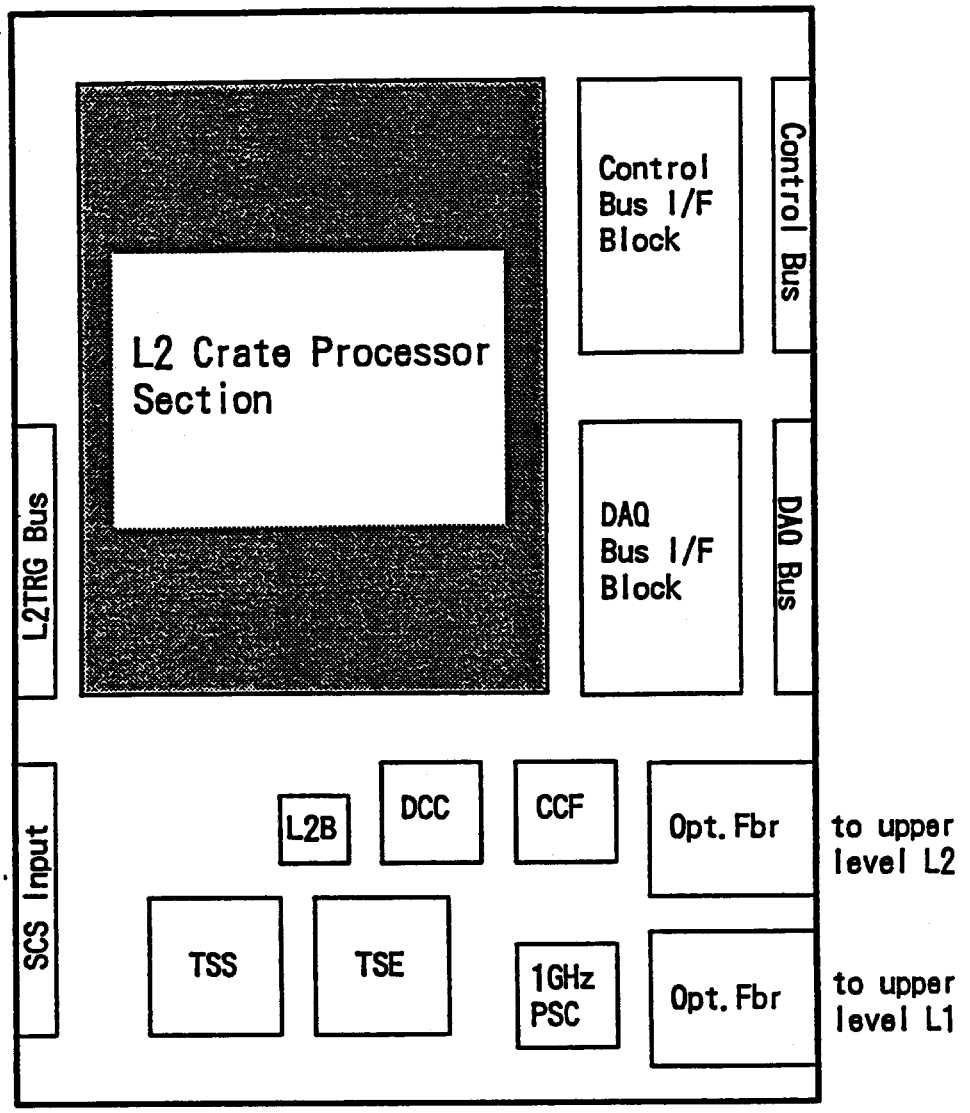

CCF: Clock and Control Fanout
DCC: Data Collection Chip
L2B: Level 2 Buffer
SCS: Track Segment Count Set
TSE: Track Segment Encoder
TSS: Track Segment Summation Circuit

Fig. A4.5 Muon crate trigger processor board

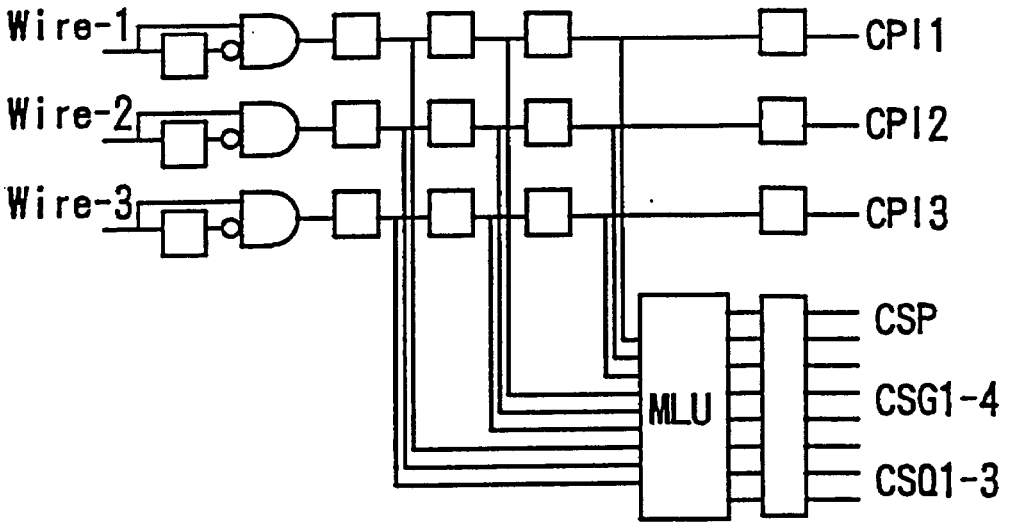

□ D-FF (clock = 16ns)

MLU Memory Lookup Unit

Fig. A4.6 Track segment finder (16 ns version)

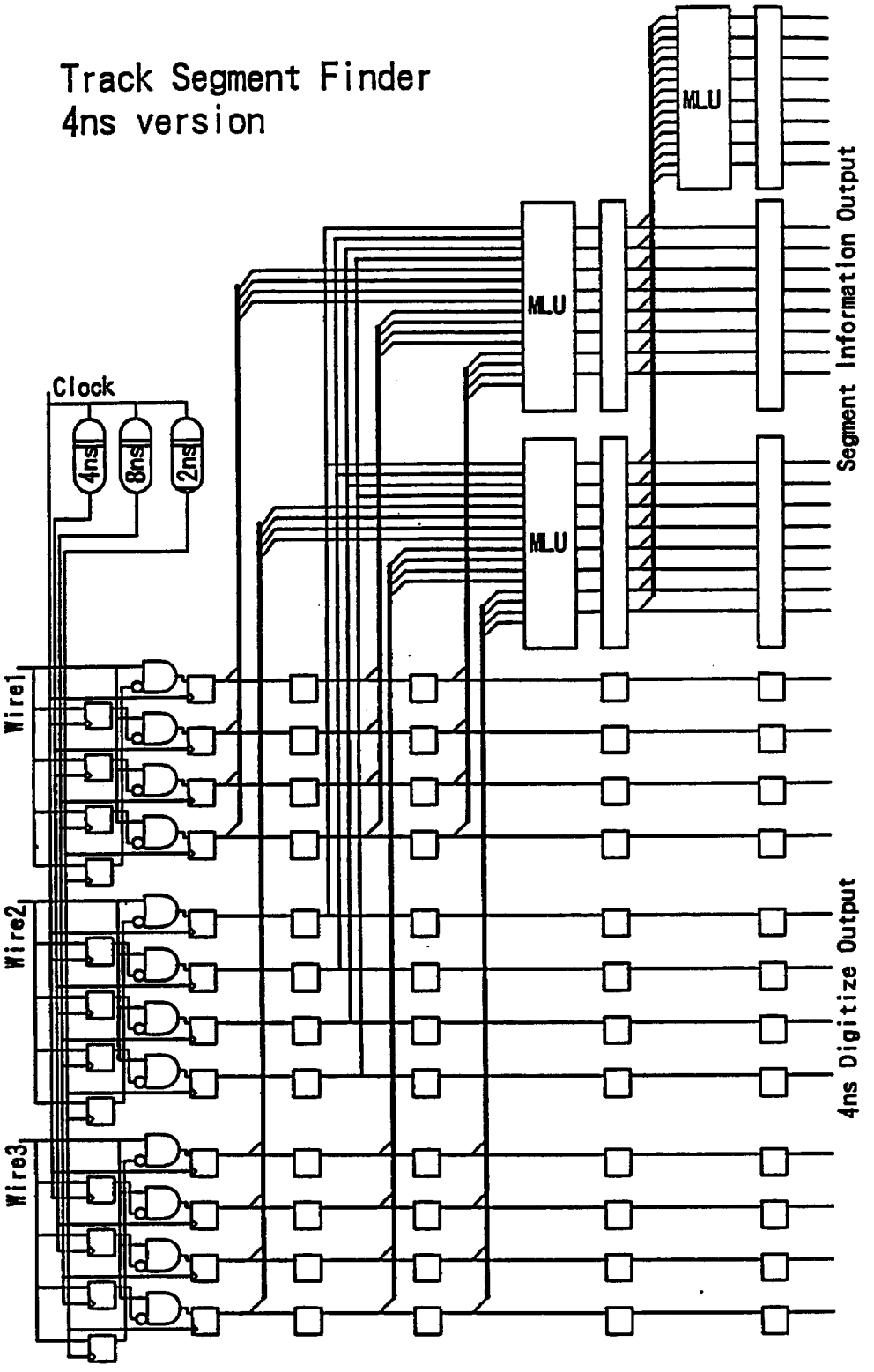

Fig. A4.7 Track segment finder (4 ns version)

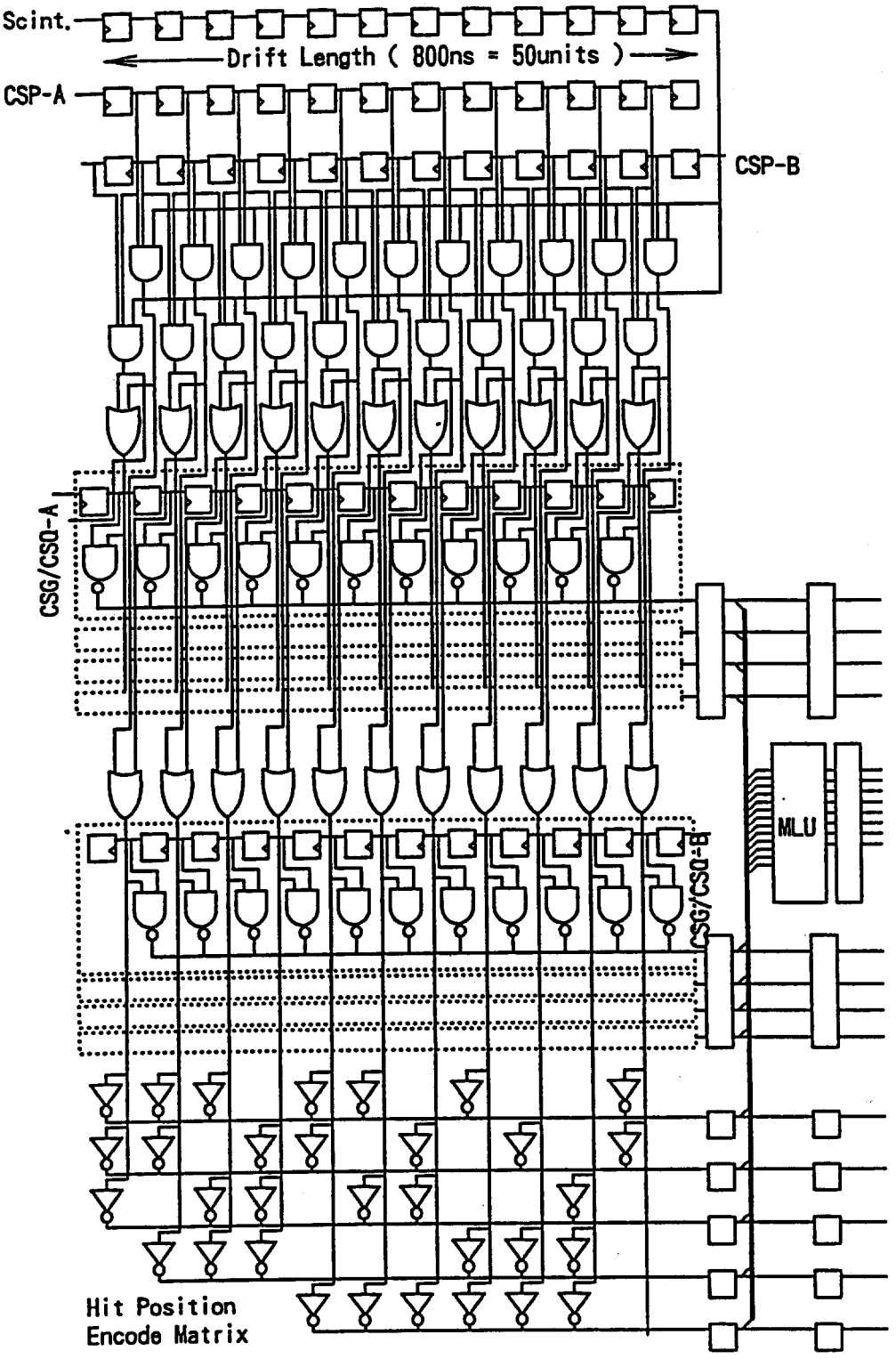

Fig. A4.8 Track segment match detector (TSM)